Master's thesis

NTNU
Norwegian University of Science and Technology
Faculty of Information Technology and Electrical Engineering
Department of Electric Power Engineering

Johannes Kalland Tjoland

Small-Signal Stability Enhancement by Wide-Area Damping Control Using a Battery Energy Storage System Emphasizing Selection of Device Location and Controller Input Signal

Master's thesis in Energy and Environmental Engineering
Supervisor: Kjetil Uhlen
June 2021

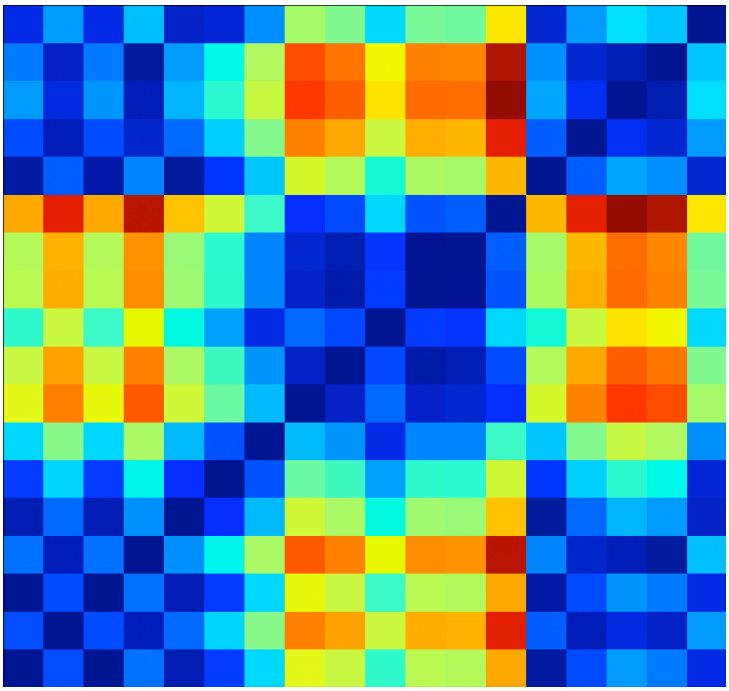

NTNU
Norwegian University of
Science and Technology

Johannes Kalland Tjoland

Small-Signal Stability Enhancement by Wide-Area Damping Control Using a Battery Energy Storage System Emphasizing Selection of Device Location and Controller Input Signal

Master's thesis in Energy and Environmental Engineering
Supervisor: Kjetil Uhlen
June 2021

Norwegian University of Science and Technology
Faculty of Information Technology and Electrical Engineering
Department of Electric Power Engineering

NTNU
Norwegian University of
Science and Technology

Preface

This thesis concludes the tenth and final semester as an Energy and Environmental Engineering student specializing in Electric Power Systems at the Norwegian University of Science and Technology. Working on this thesis has been challenging and fun and encouraged me to further work within power system operation and control.

I want to thank my supervisor, Professor Kjetil Uhlen, for the opportunity to work on this exciting and challenging topic. The weekly discussions throughout the past year have been appreciated. It has always been captivating and helpful when he has been sharing his comprehensive knowledge about power system analysis and control. Furthermore, I am grateful for him encouraging me to use Python instead of commercially available software, which made working on this thesis significantly more motivating while arguably providing a better learning outcome. His guidance has introduced me to a wide range of good topics, and his suggestions have been valuable for staking out the path of this thesis.

A huge thanks are also directed towards doctoral student Hallvar Haugdal willingly handing out the Python Dynamic Power System Simulation Software he has developed from scratch. His guidance, especially during the start of the autumn semester, has been helpful and motivating and created a foundation for developing new models, implementing code, and conducting simulations in a fun environment. The work done in this thesis would not have been as interesting and exciting if it were not for Haugdal creating and sharing the dynamic power simulation tool.

Lastly, I would like to thank fellow students, friends, and family for all the love and support. This degree would not have been possible without them.

Trondheim, June 2021

Johannes Kalland Tjoland

Abstract

Power systems throughout the world are, to a more prominent extent, getting interconnected. Together with a higher share of renewable generation sources, this is causing stability issues in the grids. The amount of inter-area oscillations in power systems are increasing, which historically have been the cause for several blackouts. New measurement units such as synchrophasors/PMUs are improving situational awareness. These are essential for enabling wide-area measurement systems and wide-area damping control schemes for mitigating arising problems. Utilizing these measurements for controlling energy storage systems are promising solutions for damping inter-area oscillations.

In this thesis, a Battery Energy Storage System (BESS) model is developed and implemented in the Python Dynamic Power System Simulator (DynPSSimpy) developed by PhD student Hallvar Haugdal at the Norwegian University of Science and Technology. The installed device's chosen control feedback signal and location considerably impact its performance and capability of providing power oscillation damping in the system. Using information about transfer function residues, observability, and controllability of a given mode, these can be selected optimally for providing the most extensive amount of damping in the pre-defined steady-state operation point of the system. In addition, the transfer function residues contain valuable information for appropriately determining the controller parameters. The performance and legitimacy of the method are through calculations and non-linear simulations in different versions of the Nordic 44 test network validated. The damping anticipated by the new modal positions coincides reasonably with the non-linear simulation results for small disturbances. However, for more immense disturbances, the properties of the linearized system do not accurately contain information about the actual response, as the internal power limitation of BESSs is not accounted for in the modal calculations.

Linear analysis is a valuable tool for selecting the feedback signal combinations and BESSs locations, and proves beneficial for controller selection and parameter tuning when maximizing the amount of damping is the objective. However, keeping in mind the constantly changing operating conditions of real-world systems and power limitations of BESSs is of uttermost importance. The results and conclusions have illustrated the importance of considering different aspects through simulations and the necessity for conducting non-linear simulations for verifying the linear results. Further development and research are needed, but the potential benefits for systems operators utilizing available wide-area measurements and properties of the linearized power system as a tool for controller selection are evident.

Sammendrag

Kraftsystemer over hele verden blir i mer fremtredende grad koblet sammen. I tillegg til en større andel fornybare generasjonskilder, forårsaker dette stabilitetsproblemer i nettene. Mengden oscillatoriske svingninger mellom ulike områder i kraftsystemene øker, noe som historisk har vært årsaken til flere strømavbrudd. Nye måleenheter som synkrofasorer/PMUer forbedrer situasjonsbevisstheten. Disse er avgjørende for å muliggjøre presise og nøyaktige systemmålinger og legger til rette for kontrollsystemer som kan redusere problemer i nettet. Å bruke disse målingene for å kontrollere energilagringssystemer er lovende for å dempe svingninger mellom ulike områder i nettet.

I denne oppgaven utvikles og implementeres et batterilagringssystem (BESS-modell) i en dynamisk kraftsystemsimulator (DynPSSimpy) utviklet av doktorgradsstudent Hallvar Haugdal ved Norges teknisk-naturvitenskapelige universitet i Python. Inngangssignalet til den installerte enhetens kotrollsystem og plassering av batterisystemet påvirker i stor grad ytelsen og evnen til å gi demping i systemet. Ved å bruke informasjon om åpen sløyfe transfer funksjoners residualverdier, samt observerbarhet og kontrollerbarhet for en gitt eigenverdi, kan disse velges optimalt for å gi best mulig demping i det forhåndsdefinerte operasjonspunktet til systemet. Metodens ytelse og legitimitet er gjennom beregninger og simuleringer i forskjellige versjoner av Nordic 44-testnettverket validert, og kontrollerparametrene velges basert på residual-verdiene. Resultatene blir videre bekreftet gjennom ikke-lineære simuleringer som replikerer tradisjonelle forstyrrelser i kraftsystemer. Dempingen som de nye posisjonene til eigenverdiene indikerer sammenfaller med de ikke-lineære simuleringsresultatene for små forstyrrelser. For større forstyrrelser inneholder derimot ikke egenskapene til det lineariserte systemet nøyaktig informasjon om den faktiske responsen, da den interne effektbegrensningen til BESSene ikke blir tatt hensyn til i de modale beregningene.

Lineær analyse er et verdifullt verktøy for valg av tilbakekoblingssignaler og plassering BESS i kraftsystemer for å effektivt bidra til demping, og viser seg gunstig for valg av kontrollere og parameterinnstillinger. Imidlertid er det ytterst viktig å huske på de stadig skiftende driftsforholdene til virkelige systemer og effektbegrensninger for BESSene. Resultatene har illustrert viktigheten av å vurdere ulike aspekter gjennom simuleringer og nødvendigheten av å gjennomføre ikke-lineære simuleringer for å verifisere de lineære resultatene. Det er behov for videre utvikling og forskning, men de potensielle fordelene for systemoperatører som bruker tilgjengelige målinger og informasjon om det lineære kraftsystemet som et verktøy for valg av kontrollere er tydelige.

Table of Contents

1 Introduction

The power grids throughout the world are transitioning into becoming smarter but more complex, and an essential element in this transition is the advancement of the Wide-Area Monitoring Systems (WAMS)[1]. Traditionally, the use of WAMS has been directed towards monitoring and situational awareness. However, the amount of research related to WAMS for automatic feedback control for meeting the requirements of the grids has increased in the past decades [2].

Higher utilization, secure operation, and more accurate control of power systems require monitoring system dynamics more precisely. An important element in this is the introduction of Phasor Measurement Units (PMUs), offering close to real-time synchronized measurements when deployed [3]. The technology behind PMUs was introduced in the mid-1980s but has lately gotten an increased focus due to prior blackouts [4] and operational requirements of modern power systems. PMUs are deployed for a wide range of applications such as monitoring, wide-area protection, Wide-Area Damping Control (WADC), and state estimation, all of which are essential when transitioning to a smarter grid [5]. While the traditional SCADA systems typically gather new measurements every 2-4 seconds, PMUs based on synchrophasor measurements time-stamped with clock signals obtained from Global Positioning Systems (GPS) are collected with a rate of 30-50 snapshots per second [6], making electromechanical frequency oscillations in the range 0.1 Hz to 2.0 Hz detectable and opening up for research utilizing these measurements for effective inter-area damping control [7]–[9].

Several types of technologies offer promising results in the field of WADC utilizing PMU measurements in the grid. Conventional FACTS-devices [10], HVDC-links [11]–[13] and demand response by actively participating loads [14] show promising results when deployed with ancillary controls for Power Oscillation Damping (POD). Modern power systems are characterized by bidirectional power flows and higher penetration of renewable energy sources. Energy storage systems are to a greater extent being installed in the grids to cope with the associated excess power production. The changes in modern power systems are causing new types of challenges and possibilities that need to be addressed for safe and efficient operation.

Mitigating the amount of low-frequency electromechanical oscillations between interconnected areas by utilizing phasor measurements for control of grid-connected Battery Energy Storage Systems (BESSs) is a promising solution for meeting the requirements of future power systems [15], [16]. Appropriately choosing the feedback signal from the available measurements and locating the BESS at a suitable location in the system is crucial for making it both economical and operationally beneficial [17].

1.1 Scope and Objective

Due to the importance of mitigating inter-area oscillations in modern and future power systems, using available devices and control systems present in power systems effectively are of great significance. Hence, the main objectives of this thesis are related to:

1. Selection of the optimal controller input signal and BESS location in a system for providing the largest dampening capabilities aiming at mitigating inter-area oscillations.
2. Appropriately deciding control parameters to make the overall system more stable and increase the capabilities of handling dynamic disturbances.

Doing so requires a fundamental literature review to obtain knowledge and inspiration based on previously conducted research on the topics and implement appropriate dynamic models relying on writing code for presenting the simulations results. This thesis can briefly be divided into four major parts, which essentially covers the scope; literature review, theoretical foundation, development and implementation of dynamic models, and simulations.

- Literature review for getting insights into the field of Wide-Area Monitoring and Control, working as a guideline, and staking out the path of the thesis.
- Based on the literature review, the theoretical foundation and background needed for implementation and analysis are established. The theory can be divided into several parts; linear analysis for modal analysis containing information about system response and mode excitation, control loop selection using transfer function residues and observability- and controllability properties of the linearized system. The transfer function residues provide information about mode sensitivity for different choices of feedback controllers, being suitable to use for controller parameter selection.
- The simulations and analysis heavily rely on Python implementations of the dynamic models, built upon the DynPSSimpy developed by doctoral student Hallvar Haugdal at NTNU. Instead of relying on commercially available software such as Simulink or PowerFactory, Python is chosen due to its flexibility allowing for custom-made dynamic simulations and providing the user/author with freedom and insights into the differential- and algebraic equations establishing the nature of the conducted simulations. Using Python instead of commercially available software increases the time spent working on simulations employing appropriate

dynamic models. However, it is deemed the most suitable solution as the learning outcome and intuitive understanding of power system operation and control are significantly increased, making working with this thesis more exciting and inspiring. A BESS model is implemented for providing ancillary control through a Power Oscillation Damper controller. Several other models suitable for providing grid-enhancing performance are created, some of which are provided and discussed in the Appendix. However, this thesis focuses on the BESS as the general results apply to various underlying physical models.

- Lastly, testing and simulations are conducted for verifying the obtained results in different versions of the Nordic 44 test network. Non-linear simulations are compared with the proposed system response received from the linear analysis and controller selection, aiming to exploit the proposed procedure's limitations and validate the optimality of the selected controller loop. Different types of common disturbances in power systems worldwide are investigated.

Hence, the main **contributions** of this thesis can be summarized as:

- Implementation of dynamic power system models suitable for use in Python or other open-source software.
- Application of transfer function residues for effectively selecting optimal feedback signals and locations of BESS devices for providing inter-area oscillation damping. In the literature, this has proved to be an effective tool for other devices in power systems, and to some extent, for energy storage devices. However, conducting the selection procedure in a Python environment using DynPSSimpy for different Nordic 44 test network versions is considered a distribution.
- Simultaneously, this thesis contributes to the selecting procedure of controller signals and location by a step-by-step approach presenting the needed theoretical background, using the theory for control loop selection in a straightforward way and, hopefully, suitable and easy to follow for students and researchers unfamiliar with the topic.

1.2 Outline of Thesis

The structure of the proceeding chapters of the thesis can roughly be described as follows.

Chapter 2 - *Background, Motivation and Literature Review*, serves as a foundation for introducing Wide-Area Monitoring and Control and presents relevant literature for

different devices used for providing oscillatory damping in Power Systems, and motivates the work to be conducted in the thesis.

Chapter 3 - *Theoretical Background*, provides the necessary theoretical foundation, with emphasis regarding linear theory and transfer function residues and their application to feedback controller design and parameter selection.

Chapter 4 - *Modelling and Implementation of Dynamic Models*, presents dynamic models utilized in the investigated test systems, including considerations and implementations regarding the BESS model and the underlying Battery model.

Chapter 5 - *Simulations and Results*, starts by presenting the initially unstable base case system, followed by the selection of the optimal feedback signal and BESS location based on the theory presented in Chapter 3. The controller parameters are determined, and non-linear simulations for performance validation are conducted. A final summarizing discussion of the main findings is provided in the end.

Chapters 6 - *Conclusion and Further Work*, concluding remarks on the findings in the thesis and suggestions for further work.

Appendix - *Appendix*, provides additional theoretical background and some considerations and examples of other models that are implemented but not used in the thesis. Lastly, calculations and simulations in other Nordic 44 test network versions are presented for further validation of the selection procedure.

The topics and research conducted for this thesis are based on a preceding specialization project conducted during the autumn semesters. Hence, parts of the introduction, literature review, theoretical background, and modeling are inspired and partly adopted from the project work.

2 Background, Motivation and Literature Review

Modern power systems use various control systems and devices to maintain safe operation and control of the systems. This section intends to briefly describe some usual compensation techniques and ways of integrating these to meet the requirements of future power systems. Some key technologies will be introduced, along with a literature review on modern research related to using available measurements to enhance grid stability. Emphasis is directed towards research conducted for using these technologies for wide-area damping control and mitigate frequency stability issues in power systems, especially regarding challenges related to low-frequency inter-area oscillations. Different methods for choosing control system signals and locations will be highlighted.

Although Battery Energy Storage Systems (BESSs) are the main focus of this thesis, research conducted for other devices related to oscillatory damping is covered. This is motivated by the fact that in terms of adding Power Oscillation Damping (POD) in power systems, the same principles and knowledge obtained for FACTS-devices, HVDC-links, and Demand Response schemes might be equally applicable for Energy Storage Systems.

Parts of this Chapter are based on and motivated by a literature review conducted for a preceding specialization project conducted during the autumn semester for getting familiar with the topics. Hence, citations and topics discussed coincides with the project work, but the presented literature review is restructured and rewritten for the topics covered in this thesis.

2.1 Research on Wide-Area Monitoring and Control

Research in wide-area monitoring and control has gotten increased focus after the introduction of synchrophasor-based measurement systems. The root cause of oscillations in electrical power systems is the mismatch between the instantaneous power demand and available power provided by generator sources at any given instant. Due to the increased complexity and distance between generators and loads in modern power systems, together with the reduction of inertia characterizing modern renewable power systems, the presence of low-frequency oscillations between interconnected areas are likely to increase [18].

By introducing PMUs, the situational awareness in the systems has improved significantly, but there are still challenges to overcome before fully utilizing the potential of these measurements. Chakrabortty and Khargonekar list fundamental research chal-

lenges for benefiting of wide-area measurement and control in future power systems [1]. The authors claim that the most important ones related to data handling are associated with the *scalability of the control systems*, *real-time processing of data* and *communication challenges related to distributed control system.* Other important challenges are utilizing these measurements for improving the operation and prevent outages in the systems. *Wide-area oscillation damping for providing damping of low frequency oscillations in the system*, *wide-area voltage control* and *wide-area disturbance localization* are mentioned as research topics of highest concern in the upcoming years [1].

A survey conducted in 2009 [19] showed that wide-area monitoring and control, and especially oscillation monitoring, were listed as the highest priority for most of the Nordic TSOs. Controller using local signals is easier to implement and works conveniently for appending damping to local modes, but are rather weak in detecting inter-area oscillations of low-frequency. Therefore, wide-area damping control have gotten increased focus lately [20].

2.2 Introduction to PMU technology

Phasor Measurement Units (PMUs) provides time-synchronized phasor information about voltages and currents in approximately real-time. With the measurement rate, they are highly preferred compared to traditional SCADA systems. They offer better monitoring and facilitate new ways of implementing control systems, especially related to the choice of input signals. There are major potential benefits for modern power grids when employing real-time measurement devices. Control systems no longer solely have to rely on local measurements, as the transmission rates of these signals promote the use of Wide-Area Measurements (WAMs) for accurate and potentially better control.

PMUs are making use of clock signals delivered by global positioning systems (GPS) for providing synchronized phase angle measurements and are often referred to as synchrophasors [21, p. 569]. The fundamental principles behind PMUs will be described in the following and are inspired by a paper written by Tsebia and Betarzi [22].

From introductory courses in electrical systems, one has that a pure sinusoidal waveform can be represented by a complex number, often referred to as a phasor [21], [23]. A pure sinusoidal voltage might be written as

$$v = V_m cos(\omega t + \phi), \tag{2.1}$$

where V_m is the voltage amplitude, ω is the frequency of the signal in radians per second, and ϕ is the phase angle determined by the magnitude of the sinusoidal voltage at t =

0. Making use of Euler's identity, $e^{j\theta} = cos\theta + jsin\theta$, Equation (2.1) is rewritten into

$$\begin{aligned} v &= V_m cos(\omega t + \phi) \\ &= V_m \Re\{e^{j(\omega t+\phi)}\} \\ &= \Re\{V_m e^{j\phi} e^{j\omega t}\}. \end{aligned} \tag{2.2}$$

The part $V_m e^{j\phi}$ is defined to be *the phasor transform* of the given time-varying sinusoidal voltage. The fundamental motivation for using phasors is that for an ideal system, everything varies with the same frequency, and accounting for the time-varying part, ωt, is unnecessary. What matters for power transfers in grids is system topologies, magnitudes, and relative angular differences between the different quantities, and the phasor representation captures the latter two. The magnitudes and relative angles of the currents and voltages in the systems are captured by the phasor representation and provide good system measurability when the deployment rate is satisfactory.

The fundamental idea behind the PMUs, sometimes referred to as *synchophasors* [24] and what makes it suitable for observability of power systems is the *synchronization with GPS*. Measurements are thus becoming reliable and obtainable in close to real-time. Furthermore, without proper synchronization between the measurement units, the phasors would not accurately describe the system. A more in-depth introduction of the PMUs can be found in the literature [22], including immaturity stage thoughts on the technology and its working principles discussed in 1994 [25].

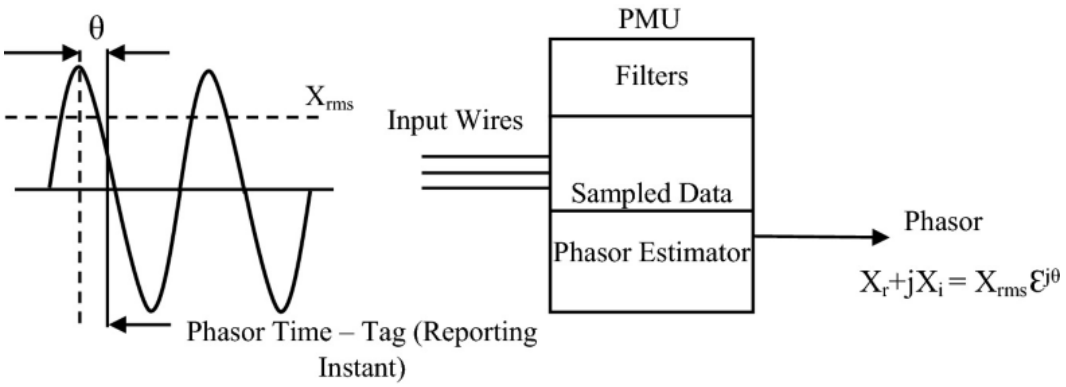

Figure 2.1: Basic components in PMU. GPS signal not included. Source: Adapted from [26].

The basic working principles of the PMU are presented in Figure 2.1. Several filters are included due to the input being discrete sampled measurement signals. The sampled data and the phasor estimator then provide a phasor estimate, which is the output measurement available for operators.

2.3 FACTS

Flexible Alternating Current Transmission Systems (FACTS) have in the last decades become predominant in the power systems [27]. These compensation devices are installed in transmission and distribution systems worldwide by injecting power to the grid to enhance grid performance and improve the operation. The main objective of FACTS has traditionally been to increase the useable power flow capacity of transmission lines and controlling the power transmission routes in the systems [27]. However, most of the available FACTS devices are not equipped with energy storage systems and are thus relying on injection of *reactive power* to the grid by the use of passive components such as inductors and capacitors [28]. These passive devices are generally bulky and require substantial space, especially if significant compensation is required in transmission systems.

2.3.1 Research on FACTS devices for oscillatory damping

In addition to conventional grid services such as increasing transfer capabilities, the FACTS devices can be controlled for dampening inter-area oscillations. Ramirez et al. [29] carried out an analysis on a linearized power system and concluded that the devices could, if properly controller, effectively provide damping and improve the transient stability of the system. However, they carefully mentioned that the control parameters should be chosen with care as certain choices of controller parameters could penalize other controllers in the system and make the overall system more unstable. Kazemi and Sohrforouzani [30] conducted simulations in the widely used Kundur's two-area system [31] with different types of FACTS-devices. Their results indicate that FACTS-devices injecting both active and reactive power can provide a greater amount of damping of inter-area oscillations than FACTS devices solely relying on reactive power injections. These results are further confirmed by Li et al. [10] who did an extensive review on input signal selection for wide-area damping control using FACTS and HVDC. In this paper, the damping assignment of each controller is chosen based on Residual Residue Ratios (RRR), which essentially says that if a controller and its location possesses a high value of RRR, it represents a high impact on this mode. The motivation behind this approach was to reduce the complexity of designing multiple controllers by not having to account for controller coordination, which might be a necessity if the RRR is low and interactions between control loops are significant. Their results suggest that whether one is having FACTS-based WADC or HVDC-WADC, effective damping of inter-area oscillations is enabled. The results were validated by conducting non-linear simulations for different disturbances such as load shedding, three-phase short-circuits events, and line outages, coinciding well with the linear results.

2.4 HVDC in Power Systems

Power systems worldwide are getting interconnected by using High Voltage Direct Current (HVDC) transmission lines, which could prove to have several advantages for satisfactory system operation. By intelligent and efficient monitoring and control, areas with high generation can send some of their excess energy to other regions lacking power. In addition to providing massive amounts of power with lower losses than the alternative AC lines, these high-power links can be equipped with ancillary control systems to offer grid-enhancing services to the interconnected systems.

2.4.1 Research on HVDC for Stability Enhancement

An extensive amount of research regarding ancillary control of HVDC-links for damping of inter-area oscillations has been conducted. Swathi and Poothullil [11] used speed deviation measurements for controlling the active power injection of an HVDC-link, and their results indicated that they could add damping to the inter-area oscillations. Similar research has been conducted by Harnefors et al. [12] using machine speed deviation as input signal for active-power modulation of HVDC-link aiming at dampening inter-area oscillations. Their initial guess suggested that choosing generators with small inertia should be a good candidate for feedback signals due to their sensitivity to changes in the system. However, their results demonstrated that choosing a feedback signal having the largest transfer function residue magnitude could be a preferable solution.

A paper submitted by Preece et al. [13] indicates that active power modulation of HVDC lines can effectively add damping to multiple inter-area modes within large networks by using power flows on selected lines as a feedback signal. For their simulation setup, the HVDC converter station was modeled as a current injection model connected in parallel to the AC-transmission line [13]. Zhang et al. [20] conducted case studies on a power system in China containing a large amount of Power System Stabilizers (PSSs) while still struggling with poorly damped inter-area modes. Different tests using an important HVDC link having frequency differences between remotely located areas as a feedback signal for the supplementary control were analyzed. Their results indicated that this had a massive positive impact on mitigating inter-area oscillations following different types of disturbances.

2.5 Actively Participating Loads by Demand Response

Already back in 1979, research was focused towards load-management for improving system stability and operation [32]. Controlling the load consumption was deemed a promising solution for reducing frequency deviations during disturbances. Trudnowski et al. [14] challenged the conventional power systems characterized by uncontrollable loads by proposing a much more active role for loads for providing frequency control and improving the dynamic stability of power systems. By a simple control rule where the loads are controlled proportionally to the local speed deviations in the system, their simulations showed a significant improvement in transient system stability. Although they are cautiously warning about generalizing from the obtained results, they demonstrated the potential for improving stability by using intelligent decentralized loads serving as a foundation for additional benefits such as cost-effective transmission systems and efficient operation of power plants [33].

There are several types of loads seen as ideal candidates for participating in frequency regulation and damping. Shi et al.. [34] used thermostatic (heating, ventilation, air-conditioning systems, and electric water heaters) load control for primary and secondary frequency regulation. Thermostatic loads are ideal candidates for such controls due to their high power ratings and thermal inertia [34]. Their simulations show that controlling the thermostatic loads improves the dynamic performance for systems containing a high share of renewable generation while having a negligible effect on customer comfort.

Jonsdottir et al. [35] aimed at providing damping in the Icelandic power system using a load control algorithm for industrial aluminum plants for providing Power Oscillation Damping (POD). The authors use Real-Time Hardware-In-the-Loop (RT-HIL) for testing the active load control algorithm, sending three-phase voltages and currents to the PMUs. Eight different signals obtained from the PMUs are tested as candidate input signals to the controller, ranging from active power transfer between the areas, positive sequence voltage magnitudes, and voltage angle differences in the system. Simulations are carried out in Real-Time Software-in-the-Loop (RT-SIL) and RT-HIL configurations, and for the latter case, one sees that the damping is reduced compared to RT-SIL, presumably due to time delays, scaling, and noise in the hardware setup. The authors conclude that for the different signals considered, voltage angle differences at the machine buses outperformed the other candidates in terms of damping.

2.6 Battery Energy Storage Systems

Battery Energy Storage Systems (BESSs) offers solutions to many operational problems in modern power system due to their fast-acting abilities. Other than providing peak-shaving and facilitate certain areas to be operated isolated from the central grid [36], these systems can participate in inter-area oscillations damping by properly designed controllers utilizing available phasor measurements.

2.6.1 Research on Battery Energy Storage Systems for Stability Enhancement

The location of BESSs and properly selecting controllers are essential considerations during the design and installation process. Tsang and Sutanto [15] conducted simulations using speed deviations for active power injection control and voltage magnitude deviations for reactive power compensation. To find the optimal placement of the BESS, the authors observed the movement of the eigenvalues for various locations in the system. The concluding remarks were that using speed deviation signals for both active and reactive power injection had the best damping abilities while using speed deviation as input for active power and voltage magnitude deviation for reactive power injection sacrificed a small amount of oscillatory damping in return for more stable terminal voltages. They also concluded that the optimal placement of the BESS, in general, will be dependent on the *type of input signal* used for the controller.

Some authors have compared STATCOMs with integrated energy storage performance in oscillatory damping against conventional STATCOMs [37]. The control of the energy storage is based on decoupled proportional-integral (PI) controllers, with a change in transmitted power taken as a feedback signal. The results show that having energy storage integrated into the STATCOM facilitates effective damping of the oscillations and avoids the sudden dip in voltage following disturbance.

There are several delays related to communication latency and the underlying physics of the system components for a real-world control system. Zhu et. al [16] are accounting for this by using a power reference signal to the BESS being proportional to the input signal and having the inner current loop modeled as a first-order time delay with a time constant of 0.02 seconds. In addition, the authors use a version of Mixed-Integer Particle Swarm Optimization (MIPSO) to select the BESS location and its corresponding controller parameters.

Batteries come in a wide range of sizes and ratings, having different performance characteristics. Neely et al.. [38] are focusing on inter-area oscillation damping using

ultra-capacitors/super-capacitors, which essentially is high power version of conventional BESSs [39]. Their simulations indicated the feasibility and potential value for power systems by the inclusion of a fast-acting energy storage damping controller. The damping provided increases for increasing proportional gain, but communication latency in the input signal might have a deteriorating effect.

2.7 Concluding Remarks on Feedback Signal Selection

Regarding controller design for inter-area oscillation damping, most authors emphasizes which kind of feedback signal they are utilizing for the controller. The chosen feedback signal should be selected based on the aim of the control system, and a feedback signal easily measurable in real-world systems is highly desired [40]. For the purpose of damping the oscillations in the system, a majority of the available literature are making use of speed measurements at different machines in the system [11], [12], [15], [20], some are using differences in terminal voltage angles [35], while others are making use of active power flow measurements available in the systems [13], [37].

Chompoobutrgool and Vanfretti [41] looked at different feedback signals for control of a PSS aiming at damping oscillations in the system. Their results indicated that *voltage angle difference was the most effective feedback signal* for the PSS and had superior damping performance compared to other signals such as voltage magnitudes and generators speeds.

Voltage angle differences might be a suitable feedback signal type, but selecting the most appropriate angles in the system is of major concern. Chompoobutrgool and Vanfretti [41] concluded that signals having a larger mode shape towards the given oscillatory mode achieved higher damping. This is also emphasized by Uhlen et al. [42] who conducted an actual implementation and testing of a Wide-Area Power Oscillation Damper (WAPOD) controlling a 180 MVar SVC installed in the Hasle substation of the Norwegian 420 kV transmission grid. The authors argue that for different PMU signals being candidates for feedback signal, those having good observability of inter-area modes can be advantageous to use, but further testing of the WAPOD using PMU signals with stronger observability will be helpful to illustrate the advantage of this approach clearer. Ge et al. [43] are using Damping Torque Analysis (DTA) for selecting feedback signals and controller location but argues that this approach is equivalent to using the residue magnitudes, which fundamentally is equivalent to using observability index and controllability index.

Although selecting the feedback signals based on the signal yielding the largest residue magnitude might be tempting, Ray et al. [44] highlights the importance of considering

the phase angle of the residues in addition to the magnitude. For some applications, especially in systems characterized by large eigenvalue movement from the different operating conditions, selecting feedback signals such that the residue angles do not vary significantly is preferred. Considerations are also undertaken by Li et al. [10] and Lin et al. [45] who selects the feedback signal by comparing the residue ratio for the different input signals, such that the chosen control loop does not influence other control loops in the system significantly.

2.8 Concluding Remarks on Control System Location Selection

From the variety of literature covering a wide range of devices aiming at providing damping of inter-area oscillations, it is evident that different authors utilize different methods for deciding the location of the controller. Whereas some authors are using eigenvalue movements [15] or more advanced methods based on observability and controllability index [46], Residual Residue Ratios or Relative Residue Index [10] and Mixed-Integer Particle Swarm Optimization [16] for determining optimal location, others are more focused towards finding a dominant path for placing the additional control system [47].

Xiao et al. [46] concluded that locating the controller based on controllability index yielded the largest additional damping of the mode of interest. A similar result is found by Aboul-Ela et al. [48] who emphasizes that a PSS aiming at damping inter-area oscillations of a given mode should be located nearby the machine having the largest residue value for the specific mode. This approach is also used by Prashash et al. [49] where the highest measure of joint controllability and observability is utilized for selecting the optimal feedback loop.

2.9 POD Controller Design

Whilst the actual physical devices may vary, most control systems providing POD to the grid are utilizing similar controller design. A *conventional design* consists of a *washout filter* for removing the impact of dc-signals and low-frequency oscillations and *lead-lag compensators* for providing the desired amount of phase compensation [45], [48], [50].

When designing controllers aiming at improving the reliability and performance of power systems, linear analysis is often used as a baseline. Uhlen et al. [51] concluded that linear techniques could be of great benefit when designing damping controllers for

larger power systems by comparing the results obtained for the linearized system with non-linear dynamic simulations.

Other authors are more specific in the POD design, showing how information about the residue for the chosen controller-loop can be used for tuning the lead-lag compensators of the PSS controller by applying an appropriate phase shift of the mode of interest [48]. This approach is not only applicable for the design of PSS, but might work equally well for the design of POD applied to FACTS-devices such as Static Voltage Compensators (SVCs) [50] and Unified Power Flow Controllers (UPFCs) [52].

Using information about the residue corresponding to the mode of interest for tuning the controller parameters seems to be the most common procedure for selecting controller parameters, although some authors are using more advanced schemes such as Particle Swarm Optimization Algorithms [16], [53]. However, a general trend is that regardless of the methods deployed for selecting controller parameters, most papers use information about the linearized system and the new positions of the system modes for determining whether the selected parameters is offering the desired amount of damping.

Adamczyk et al. [54] stress that when the residual method lays the foundation for parameter selection, the effective mode shift is not only dependent on the residue value but is affected by other system dynamics too. This is especially true when considerable gains are required, as the interactions between the different control loops in the system might be severe. Simulations carried out by et al. in [55] showed that the performance of the controller deteriorates considerably if the communication delay is greater than the time period of the oscillations of dominant modes in the system. Hence, when designing a controller for obtaining a specific amount of damping and phase compensations, checks should be undertaken to assure that the controller performs as expected.

2.10 Summary

It is evident that there are several ways of enhancing grid stability and provide additional damping to poorly damped modes in the system. There has been extensive research on more actively participating loads and ancillary controls of existing power system components such as FACTS-devices, HVDC-links, and Energy Storage for preserving system stability.

Several devices are suitable for providing POD to the systems. The design criterion in selecting optimal feedback signals and device locations seems similar for the different devices utilized in the literature. A common approach is to use transfer function residues to determine the signals and location. The selection of these has a significant

impact on the damping performance. Knowing the residues and their corresponding phase shifts, the controller parameters needed for obtaining the required phase compensation and gain can be determined satisfactorily. If the required controller gain is considerable, the interaction between different control loops in the system is significant, or communication delays in the system are an issue, considerations should be undertaken during design.

3 Theoretical Background

In order to create valuable simulations and interpreting results, a fundamental theoretical background is necessary. This chapter intends on presenting key theoretical foundations regarding the topics discussed in this thesis, and some deviations deemed important for intuitive understanding of the results and linear analysis are presented. Additional theory not being fundamental for the thesis, but still valuable, can be found in Appendix A.

Certain parts of the theoretical background are based on work from a preceding specialization project conducted during the autumn semester. This is especially related to state-space representation and modal analysis which are adopted, but rewritten and modified with the inclusion of illustrative figures.

3.1 Small Signal Stability and the Swing Equation

The swing equation is fundamental for understanding dynamics in power systems. Conventional generating units are traditionally based on some rotating masses, whether it is due to water flowing through pipes, burning of gas, or steam turbines. The swing equation contains information about how the angular speed of masses changes based on mechanical input power and electrical power. The common way of finding the associated equations starts by using Newton's second law for rotating mass. Assuming one has a generator and turbine with a total moment of inertia J and rotor shaft velocity ω_m, where the turbine is producing a torque τ_t, while having a counteracting electromagnetic torque τ_e, with a damping torque coefficient of D_d, one has [56]

$$J\frac{d\omega_m}{dt} = \tau_t - \tau_e - D_d\omega_m. \tag{3.1}$$

Making use of the fact that during a disturbance, one normally finds oneself in an operating state where the speed of the synchronous machine is close to the synchronous speed, and expressing the mechanical rotational speed and angle in terms of electrical quantities and deviations from steady-state, it can be shown that with a proper definition of M and D, Equation (3.1) can be rewritten as the following set of first-order equations

$$\begin{aligned} M\frac{d\Delta\omega}{dt} &= P_m - P_e - P_D = P_m - P_e - D\Delta\omega = P_{acc} \\ \frac{d\Delta\delta}{dt} &= \Delta\omega, \end{aligned} \tag{3.2}$$

which is also illustrated in the block diagram provided in Figure 3.1.

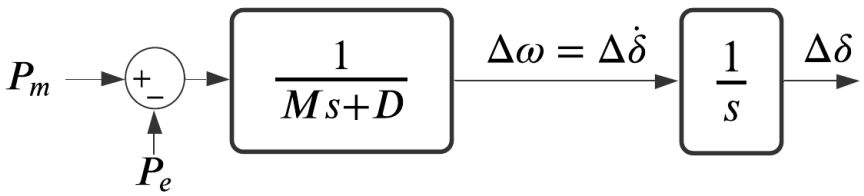

Figure 3.1: Block diagram describing the classical swing equation.

In Equation (3.2) and Figure 3.1, the variables are given as:

- P_m is the net shaft input power to the generator
- P_e the electrical air-gap power
- M is called the *inertia coefficient*
- D is the *damping coefficient*
- P_D is the damping power.
- $\Delta\omega$ is the deviation in rotor speed relative to steady-state speed, $\Delta\omega = \omega - \omega_0$
- $\Delta\delta$ is the deviation in rotor angle position, $\Delta\delta = \delta - \delta_0$

For the interested reader, the derivation of the equation can be found in Machowski [56, p. 169-172] and other typical textbooks within the field of power systems. This equation relates speed deviations in the generators, thereby frequency, to power imbalances in the grid. The change in rotor speed deviation depends on the accelerating power and the inertia coefficient M, where M is effectively a measure of rotational inertia present in the machine. A machine with large inertia will experience a lower change in frequency following disturbance than a machine with small inertia. This follows because large inertia essentially translates to a rotational mass containing a high amount of kinetic energy due to its rotational speed. Some of this kinetic energy is discharged during disturbance and reducing the rate of change of frequency. The term accounting for the damping power, P_D, is rather complex to express analytically as it relies on several assumptions. However, it is generally dependent on the rotor angle positions and damper winding reactances in the machine and the grid of which it is connected [56]. For many simulations, the influence of P_D is neglected in the analysis, but one should be aware of its presence.

The equilibrium point of a set of first-order differential equations is point where all the derivatives are zero [57] and the system is in a so-called steady-state operational point. By using the Swing Equation (3.2), one have that this will be a point yielding

net shaft input power equal to electrical air-gap power, as the damping power depends on the rotor speed deviation. If the resistance and shunt admittance's are neglected, the electrical power in steady-state for a salient pole machine is given by

$$P_e = P_{E_q} = \frac{E_q V_s}{x_d} sin(\delta) + \frac{V_s^2}{2} \frac{x_d - x_q}{x_q x_d} sin(2\delta), \tag{3.3}$$

where E_q is the internal generated emf within the generator E_f, V_s is the voltage at the connected bus, δ is the angle between these voltage phasors and x_d and x_q accounts for all the d- and q-components of reactances connected between the machine and the bus, given that one are representing the generator in an equivalent d-q-axis circuit diagram as done in [56, p. 87]. Assuming a round-rotor machine ($x_d = x_q$), the equation simplifies to the familiar relation for power transfer between two buses connected by an equivalent reactance

$$P_e(\delta) = P_{E_q}(\delta) = \frac{E_q V_s}{x_d} sin(\delta). \tag{3.4}$$

The maximum power transfer for this ideal case is found by setting $\delta = \pi/2$. Figure 3.2 shows the power output for round-rotor and salient pole machines, and the differences between them should be evident from the plot.

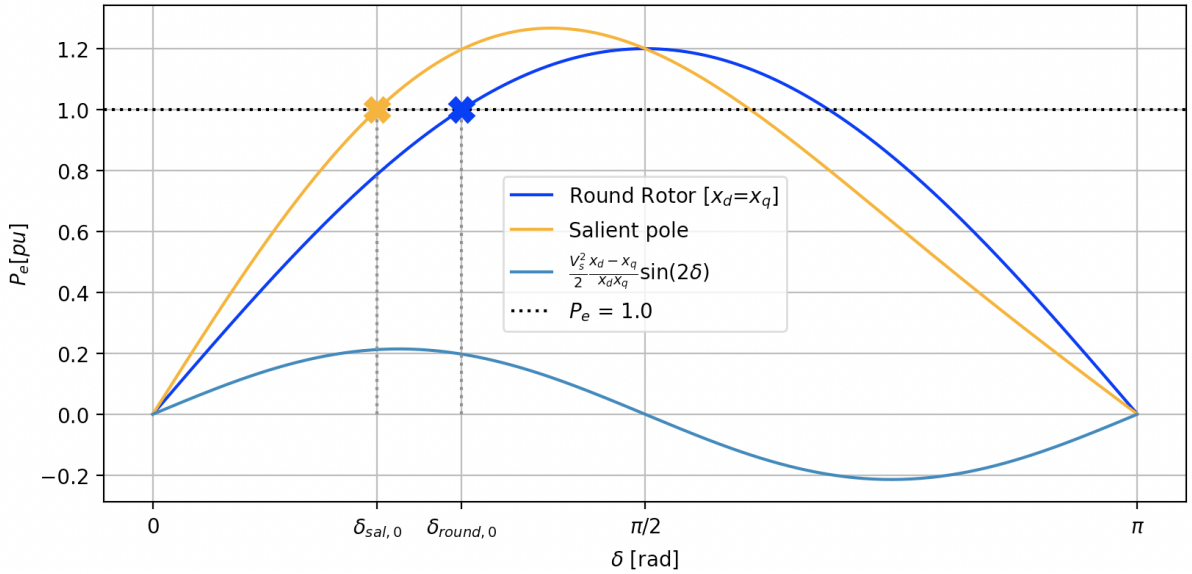

Figure 3.2: Electric Power output P_e for generators with different rotor configurations. The value of x_q is smaller than the value of x_d, such that the maximum power power output occurs at a smaller rotor angle for a salient pole machine compared to round rotor machines. Hence, for providing the same amount of electrical power, for instance $P_e = 1.0$ (dotted black horizontal line), the salient pole machine is operating at a smaller rotor angle $\delta_{sal,0}$.

The Electrical Power Equation (3.4) is sinusoidal which is also observable from the blue solid line in Figure 3.2, thus having two different angles in the interval $(0, \pi)$ yielding

the same electrical power P_e. It is highly desired to find oneself in an operating point lying the first quarter of the period. This will allow the system to fall back into a new steady-state after disturbance. A machine initially operating at a power angle δ in the range $[\frac{\pi}{2}, \pi]$ would lose synchronism with the rest of the grid following a small disturbance in the system as it would oscillate away from a steady-state point in case of an unregulated generator [56].

In terms of stability, the damping power plays a significant part. When a disturbance happens, speed deviations will be observable in the system. With damping power present, this will either decelerate or accelerate the system's response, essentially helping it reach a steady state much faster than cases without it. This is highly relatable to the theory presented for modal analysis (to be covered in Section 3.2.3), as the damping coefficient D is seen to account for the real part of the eigenvalues in terms of a simple Single-Machine Infinite Bus (SMIB) system. Without any damping present, the system would contain sustained oscillations after a disturbance.

3.2 Linear Theory

3.2.1 Linearising non-linear Systems

Modern power systems are non-linear dynamic systems in nature. Computing eigenvalues for determining dynamic response and analyzing system stability relies on a linear representation of the system. Linear analysis is well suited for accurately describing the dynamic response for small changes around a given operating point and is thus a useful tool for obtaining first-hand knowledge about system stability. However, a good practice is to validate the results obtained using linear analysis with a non-linear simulation as deviations between these will be present for larger system changes. A general description of a non-linear dynamic system can be given as

$$\dot{\boldsymbol{x}} = \boldsymbol{F}(\boldsymbol{x}, \boldsymbol{u}), \tag{3.5}$$

which says that the solution in time of a state variable $x_i(\mathrm{t})$ is given as a function of all the other state variables in the system. Several of the entries are zeros in most systems, as most states are only related to a couple of the other states in the system. Using Taylor series expansion for the purpose of *linearizing* the system around a given operating point $(\hat{\boldsymbol{x}}, \hat{\boldsymbol{u}})$ [57], and neglecting the higher order terms which are generally quite small yields the following system description for a small region around the defined operating point

$$\boldsymbol{\Delta}\dot{\boldsymbol{x}} = \boldsymbol{A}\boldsymbol{\Delta}\boldsymbol{x} + \boldsymbol{B}\boldsymbol{\Delta}\boldsymbol{u}, \tag{3.6}$$

where $\boldsymbol{\Delta}\boldsymbol{x} = \boldsymbol{x} - \hat{\boldsymbol{x}}$ and $\boldsymbol{A} = \partial\boldsymbol{F}/\partial\boldsymbol{x}$ is the Jacobi matrix. Similarly, the change in the input vector and input matrix are given by $\boldsymbol{\Delta}\boldsymbol{u} = \boldsymbol{u} - \hat{\boldsymbol{u}}$ and $\boldsymbol{B} = \partial\boldsymbol{F}/\partial\boldsymbol{u}$ respectively.

By this linearization, the state-matrix $\boldsymbol{A}$ and the linearized input matrix $\boldsymbol{B}$ for the system[3.1] is found to be [58]

$$\begin{aligned}\boldsymbol{A} &= \left.\frac{\partial \boldsymbol{f}}{\partial \boldsymbol{x}}\right|_{(\hat{\boldsymbol{x}},\hat{\boldsymbol{u}})} = \left.\begin{bmatrix} \frac{\partial f_1}{\partial x_1} & \frac{\partial f_1}{\partial x_2} & \cdots & \frac{\partial f_1}{\partial x_n} \\ \vdots & \vdots & \vdots & \vdots \\ \frac{\partial f_n}{\partial x_1} & \frac{\partial f_n}{\partial x_2} & \cdots & \frac{\partial f_n}{\partial x_n} \end{bmatrix}\right|_{(\hat{\boldsymbol{x}},\hat{\boldsymbol{u}})} \\ \boldsymbol{B} &= \left.\frac{\partial \boldsymbol{f}}{\partial \boldsymbol{u}}\right|_{(\hat{\boldsymbol{x}},\hat{\boldsymbol{u}})} = \left.\begin{bmatrix} \frac{\partial f_1}{\partial u_1} & \frac{\partial f_1}{\partial u_2} & \cdots & \frac{\partial f_1}{\partial u_n} \\ \vdots & \vdots & \vdots & \vdots \\ \frac{\partial f_n}{\partial u_1} & \frac{\partial f_n}{\partial u_2} & \cdots & \frac{\partial f_n}{\partial u_n} \end{bmatrix}\right|_{(\hat{\boldsymbol{x}},\hat{\boldsymbol{u}})}\end{aligned} \tag{3.7}$$

Notice that this system representation is basically the same as presented in section 3.2.2. The system matrix $\boldsymbol{A}$ will be essential in several parts of this report as this is the one containing information about eigenvalues and mode shapes which will be discussed further in the upcoming section. A numerical approach for calculating the system matrix $\boldsymbol{A}$ and input matrix $\boldsymbol{B}$ utilized for this report is provided in Appendix A.2.

It can be shown based on Lyapunov's first theorem that if the generally non-linear system described in Equation (3.5) can be approximated by the linear Equation (3.6), the system is asymptotically stable if all eigenvalues of state matrix $\boldsymbol{A}$ are located in the left half of the complex plane [56], that is

$$Re\{\lambda_i\} < 0 \quad \forall\{\lambda_i : det(\boldsymbol{A} - \lambda_i \boldsymbol{I}) = 0\}. \tag{3.8}$$

The eigenvalues contain significant information about the system stability. They are also used extensively when designing controllers for systems, as will be shown in the following section. Ogata includes a proof of this in his book "Modern Control Engineering" [40, pp. 241] utilizing residues[3.2] and other linear properties for deriving it.

3.2.2 State-space Representation

For a continuous time-invariant linear system a general representation of the system cab be written in the following form

$$\begin{aligned}\dot{\boldsymbol{x}}(t) &= \boldsymbol{A}\boldsymbol{x}(t) + \boldsymbol{B}\boldsymbol{u}(t) \\ \boldsymbol{y}(t) &= \boldsymbol{C}\boldsymbol{x}(t) + \boldsymbol{D}\boldsymbol{u}(t),\end{aligned} \tag{3.9}$$

which is also illustrated in the block diagram given in Figure 3.3, inspired by a Figure found in a course book in control system engineering [58, p. 92].

[3.1] By assuming there are n state variables in the system.
[3.2] Residues are covered in Section 3.3.1.

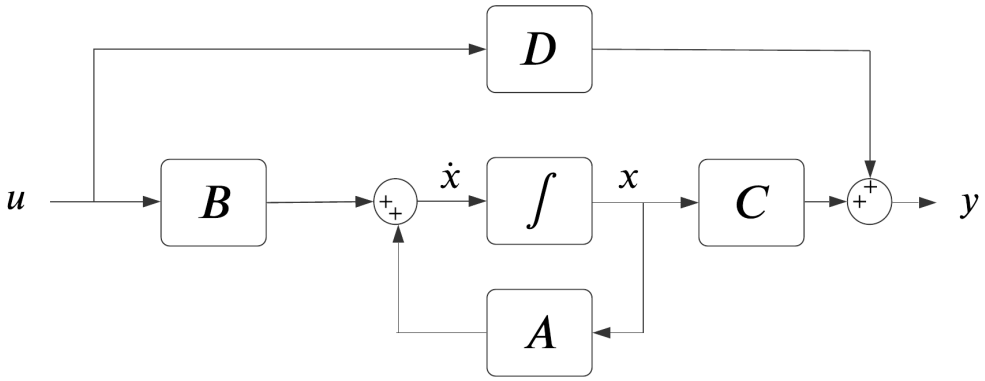

Figure 3.3: A general block diagram showcasing the state-space representation in Equation (3.9) for a continuous time-invariant linear system. The variables and notations used are described in the text and corresponds to commonly selected names in the literature.

This is referred to as the *State-space representation* of the system. The aforementioned representation has the following terms:

- $\boldsymbol{x}$ is the state-vector
- $\boldsymbol{y}$ is the output vector
- $\boldsymbol{u}$ is the input vector
- $\boldsymbol{A}$ is the system matrix
- $\boldsymbol{B}$ is the input matrix
- $\boldsymbol{C}$ is the output matrix
- $\boldsymbol{D}$ is the feed-forward matrix

The Laplace transform of such a system description will be valuable in terms of describing the concepts introduced in Section 3.3.1 and is thus given below:

$$\begin{aligned} s\boldsymbol{X}(\boldsymbol{s}) - \boldsymbol{x}(0) &= \boldsymbol{A}\boldsymbol{X}(s) + \boldsymbol{B}\boldsymbol{U}(s) \\ \boldsymbol{Y}(s) &= \boldsymbol{C}\boldsymbol{X}(s) + \boldsymbol{D}\boldsymbol{U}(s) \end{aligned} \tag{3.10}$$

Stability of such a linear time-invariant system can be studied from the eigenvalues of the system matrix (also called state-matrix). For a continuous linear time-invariant system as in (3.9) the eigenvalues λ are the values satisfying the characteristic equation

$$det(\boldsymbol{A} - \lambda \boldsymbol{I}) = 0. \tag{3.11}$$

For an extensive system, calculating the eigenvalues might be rather computational heavy and complex. However, with the development in computer power, this has become a manageable task.

3.2.3 Modal Analysis

This section is intended to provide the necessary background for doing and using modal analysis. The deviations are based on the work presented in [56]. Firstly, the theory is presented with some motivation behind the different steps before providing a small simulation highlighting the main observations is presented to validate the theory and show the power of modal analysis in power system dynamic analysis and control. This deviation might seem unnecessary to present in its entirety. However, due to the importance of the topic for the rest of the thesis, it was decided to give a complete overview of the steps as these contain much valuable information employed for the rest of the report. Textbooks and literature often provide a rather theoretical view on this topic, for instance, Machowski [56], some figures showing how to interpret modal analysis and the information contained in it is included in Section 3.2.5 to illustrate the concepts for the unfamiliar reader and provide an intuitive first-hand visualization of the interpretation.

In the following, the Δ-notation is removed from Equation (3.6) for simplicity and the part related to the input $\boldsymbol{B\Delta u}$ is set to zero, yielding the matrix form of the linear differential homogeneous equation as

$$\dot{\boldsymbol{x}} = \boldsymbol{A}\boldsymbol{x}, \tag{3.12}$$

where $\boldsymbol{x}$ is denoted the state vector and $\boldsymbol{A}$ is called the state matrix. This system representation can, for instance, be thought about as a linearization of a dynamic system around a steady-state operating point. The following deviations will be a good approximation for the system's dynamic behavior for small changes away from this operating point. The main advantage of the following deviation is to be able to represent the generally infinitely high order system as a linear combination of decoupled first- and second-order systems, which simplifies the system analysis significantly [58].

An eigenvalue of matrix $\boldsymbol{A}$ is a value λ_i satisfying the following equation for a nonzero eigenvector .

$$\boldsymbol{A}\boldsymbol{\phi_i} = \boldsymbol{\phi_i}\lambda_i, \tag{3.13}$$

where $\boldsymbol{\phi_i}$ is the right eigenvector corresponding to eigenvalue λ_i Using Equation (3.13) for every pair of eigenvalues and eigenvectors in the system, one can write

$$\begin{aligned} \boldsymbol{A\Phi} &= \boldsymbol{\Phi\Lambda} \\ \boldsymbol{\Lambda} &= \boldsymbol{\Phi^{-1}A\Phi} \end{aligned} \tag{3.14}$$

where the matrix $\boldsymbol{\Phi}$ is a matrix whose columns are the right eigenvectors of the state matrix $\boldsymbol{A}$ structured as

$$\boldsymbol{\Phi} = \begin{bmatrix} \phi_1 & \phi_2 & \dots & \phi_n \end{bmatrix}, \tag{3.15}$$

and ϕ_i is the right eigenvector corresponding to eigenvalue λ_i. The matrix $\mathbf{\Lambda}$ is a square diagonal matrix containing all the eigenvalues in the system such that

$$\mathbf{\Lambda} = \begin{bmatrix} \lambda_1 & 0 & \dots & 0 \\ 0 & \lambda_2 & & 0 \\ 0 & \dots & \ddots & 0 \\ 0 & \dots & \dots & \lambda_n \end{bmatrix}. \tag{3.16}$$

This idea of factorizing $\boldsymbol{A}$ such that it can be presented as Equation (3.14) is fundamental in several applications of linear algebra and are a useful way to analyze dynamic systems [59]. Using a linear transformation of the state vector in Equation (3.12) and transforming the state vector into a new state vector with a linear transformation based on the relation shown in Equation (3.14), one gets

$$\boldsymbol{x} = \mathbf{\Phi}\boldsymbol{z}, \tag{3.17}$$

The vector z is contains the *modal variables* or simply *modes* in the system. One could, in principle, use all thinkable invertible matrices satisfying the dimensions of the original system for this transformation. However, the choice of using the matrix $\boldsymbol{W}$ whose columns are the right eigenvectors in the system is not arbitrary, as will be made clear in the following. Defining the inverse matrix of $\mathbf{\Phi}$ as $\mathbf{\Psi}$, one sees that the new state vector $\boldsymbol{z}$ can be written as

$$\boldsymbol{z} = \mathbf{\Psi}\boldsymbol{x}. \tag{3.18}$$

It can be shown that the matrix $\mathbf{\Psi}$ contains the left eigenvectors, defined similarly as the right eigenvectors presented in Equation (3.14),

$$\mathbf{\Psi}\boldsymbol{A} = \mathbf{\Psi}\mathbf{\Lambda}, \tag{3.19}$$

but structured like

$$\mathbf{\Psi} = \begin{bmatrix} \psi_1^T & \psi_2^T & \dots & \psi_n^T \end{bmatrix}, \tag{3.20}$$

where ψ_i^T is the transposed left eigenvector corresponding to the i-th eigenvalue. Using the Equation (3.18) in equation 3.12 describing the system, one gets

$$\dot{\boldsymbol{z}} = \mathbf{\Phi^{-1}}\boldsymbol{A}\mathbf{\Phi}\boldsymbol{z} = \mathbf{\Psi}\boldsymbol{A}\mathbf{\Phi}\boldsymbol{z}. \tag{3.21}$$

The last expression is rather tedious to work with, but making use of the relation found in Equation (3.14) into Equation (3.21), it is evident this can be rewritten as

$$\dot{\boldsymbol{z}} = \mathbf{\Lambda}\boldsymbol{z}. \tag{3.22}$$

This representation is often simply referred to as the *modal form* of the state equation presented in Equation (3.12) [56]. The system is significantly simplified due to $\mathbf{\Lambda}$ being a diagonal-matrix (whose off-diagonal elements are zero). In contrast, the original

system relied on matrix $\boldsymbol{A}$ which in principle could contain non-zero elements in every entry. Equation (3.22) is called decoupled since none of the modal variables solutions depends on the dynamics of the other modes, which comes as a consequence of the diagonal matrix off-diagonal zeros. The derivative of the new state vectors does only depend on their own corresponding state variable

$$\dot{z}_i = \lambda_i z_i, \tag{3.23}$$

which makes this a system of first-order differential equations on arguably on of the simpler forms[3.3], having the solution

$$z_i(t) = e^{\lambda_i t} z_{i0}, \tag{3.24}$$

where z_{i0} is the initial value of this modal variable i. The above is valid for a specific modal variable z_i, but it is straightforward to express it for the whole system by defining a new matrix

$$\boldsymbol{e}^{\boldsymbol{\Lambda} t} = \begin{bmatrix} e^{\lambda_1 t} & 0 & \dots & 0 \\ 0 & e^{\lambda_2 t} & \dots & 0 \\ \vdots & \vdots & \ddots & \vdots \\ 0 & 0 & \dots & e^{\lambda_n t} \end{bmatrix}, \tag{3.25}$$

which yields the following solution in time for the overall system

$$\boldsymbol{z}(t) = \boldsymbol{e}^{\boldsymbol{\Lambda} t} \boldsymbol{z_0} \tag{3.26}$$

The state vector $\boldsymbol{x}$ and modal vector $\boldsymbol{z}$ are related by the linear transformation given in Equation (3.17), such that by combining equation (3.17) and (3.24) the state variable time responses are given by

$$\boldsymbol{x} = \boldsymbol{\Phi} \boldsymbol{e}^{\boldsymbol{\Lambda} t} \boldsymbol{z_0}. \tag{3.27}$$

or, when written it in a less compact form

$$\begin{aligned} \begin{bmatrix} x_1(t) \\ . \\ . \\ . \\ x_n(t) \end{bmatrix} &= \begin{bmatrix} \phi_{11} & \phi_{12} & \phi_{13} & ... & \phi_{1n} \\ . & . & . & . & . \\ . & . & . & . & . \\ . & . & . & . & . \\ \phi_{n1} & \phi_{n2} & \phi_{n3} & . & \phi_{nn} \end{bmatrix} \begin{bmatrix} e^{\lambda_1 t} & 0 & 0 & ... & 0 \\ 0 & e^{\lambda_2 t} & 0 & ... & 0 \\ 0 & 0 & e^{\lambda_3 t} & ... & 0 \\ 0 & 0 & 0 & ... & 0 \\ 0 & 0 & 0 & ... & e^{\lambda_n t} \end{bmatrix} \begin{bmatrix} z_{10} \\ . \\ . \\ . \\ z_{n0} \end{bmatrix} \\ &= \begin{bmatrix} \phi_{11} e^{\lambda_1 t} & \phi_{12} e^{\lambda_2 t} & ... & \phi_{1n} e^{\lambda_n t} \\ . & . & . & . \\ . & . & . & . \\ . & . & . & . \\ \phi_{n1} e^{\lambda_1 t} & \phi_{n2} e^{\lambda_2 t} & ... & \phi_{nn} e^{\lambda_n t} \end{bmatrix} \begin{bmatrix} z_{10} \\ . \\ . \\ . \\ z_{n0} \end{bmatrix} \end{aligned} \tag{3.28}$$

[3.3] A first order differential equation being presented in the form $\dot{x} = \lambda x$ is usually the first type of equation one look at when studying differential equations [57].

From the above equation, one sees that for a given state variable x_k, its dynamics is described by

$$x_k(t) = \phi_{11} z_{10} e^{\lambda_1 t} + \phi_{12} z_{20} e^{\lambda 2t} + ... + \phi_{1n} z_{n0} e^{\lambda nt}. \tag{3.29}$$

That is, the response of a state variable $x_k(t)$ is a linear combination of the modal variables in the system. The vector of initial conditions of the vector $\boldsymbol{z_0}$ can be found by using Equation (3.18).

From Equation (3.18), it can be seen that equivalently to the state variables in the system being described as a linear combination of the modal variables as in (3.29), the modal variable z_i can be expressed as a linear combination of the state variables in the system

$$z_i(t) = \sum_{j=1}^{n} \psi_{ij} x_j(t), \tag{3.30}$$

where ψ_{ij} is an entry in the matrix $\boldsymbol{\Psi}$ containing the left eigenvectors. By expanding the sum in (3.30)

$$z_i(t) = \psi_{i1} x_1(t) + \psi_{i2} x_2(t) + ... + \psi_{in} x_n(t) \tag{3.31}$$

It is evident from Equation (3.31) that each state variable x_k is having an impact on the value of the modal variable z_i, and to which extent being dependent ψ_{ik}. As discussed previously, the entries in $\boldsymbol{\Psi}$ are the left eigenvectors entries. It is therefore said that the left eigenvectors contain information about the *controllability* of a given modal variable by individual state variables. In other words, how much will the modal variable z_i be changed by controlling the state variable x_k. If ψ_{ik} is approximately zero, controlling x_k will have a negligible impact on the modal variable z_i. The left-eigenvectors turn out to have essential properties when defining control systems.

Another way to make observations about this system is to look at equation (3.29), which describes how the modal variables affect the dynamics of the state variables. Each modal variable z_i is contributing to the state variable x_k, and to which extent is given by the entry of the right eigenvectors corresponding to this modal variable, ϕ_{ki}. As the state variables are a linear combination of the modal variables, it can be said that the modal variables are *observed* in the state variables. Thus, the right eigenvectors carry information about the *observability* of the different modal variables in the state variables. By normalizing the eigenvectors, ϕ_{ki}, which generally is a complex value determining the magnitude and phase of the share of modal variable z_i(t) in state variable x_k. The latter is often referred to as *mode shape* [56] and plays a major part in the stability analysis of power systems as it shows to which extent the oscillatory modes influence the dynamic behaviors of individual states. The relations between state variables and modal variables together with left- and right-eigenvectors presented here will be of great importance for the rest of this thesis when determ-

ining control systems' locations and making qualified guesses to the system response following different disturbances.

3.2.4 Damping and Frequency of Oscillatory Modes

The state variables contained in the state vector $\boldsymbol{x}$ is defining the dynamics of the system. From the deviations above, it is made clear that the solution in the time domain of a state variable $x_k(\mathrm{t})$ depends on the initial conditions of all modes $\boldsymbol{z_0}$ as well as the coefficients obtained from the right eigenvectors. An important point to take on from this is that if the system contains complex eigenvalues, they appear in pairs as complex conjugates. As a result, these complex pairs of eigenvalues $\lambda_i = \alpha_i \pm j\omega_i$ introduces a response to state variable $x_k(\mathrm{t})$, which depending on the values of the corresponding eigenvectors, is proportional to $e^{\alpha_i t}cos(\omega_i t + \theta_{ki})$. The real part of the eigenvalue α_i should be less than zero for the oscillatory mode to be stable as per (3.8). The frequency of oscillations for the i-th mode is given by the imaginary part of the mode, $\omega_i = \Im(\lambda_i)$, given in rad/s. As all the oscillatory modes ($\lambda \in \boldsymbol{\Lambda} \mid \Im(\lambda) \neq 0$) in the system appears in pairs, a common approach is to perform analysis for the modes having $\Im(\lambda_i) > 0$, as positive frequencies have a physical intuitive interpretation.

The relative damping ratio of the modes provides information about how fast the oscillatory responses for the given modal variables decays towards zero and is normally expressed as

$$\zeta_i = \frac{-\alpha_i}{|\lambda_i|} = \frac{-\alpha_i}{\sqrt{\alpha_i^2 + \omega_i^2}}, \tag{3.32}$$

whereas the frequency of the oscillatory mode in expressed in Hz is given by

$$f_i = \frac{\omega_i}{2\pi}. \tag{3.33}$$

A negative sign is included in Equation (3.32) such that damping is defined as positive if the eigenvalue is located in the left-half plane, whereas, for an asymptotically unstable operating condition, at least one of the eigenvalues (two if the eigenvalues appear as complex pairs) is defined to be negatively damped; thus (3.8) is not satisfied.

Figure 3.4 shows the fundamentals behind the different dynamics associated with a given eigenvalue λ_i. There are several ways to compute the relative damping of the eigenvalue/mode. However, all of them are essentially a measure of the angular displacement of the eigenvalue from the imaginary axis. In Figure 3.4, this angular displacement is denoted ψ_i, and the larger the angle, the greater is the relative damping of the corresponding mode.

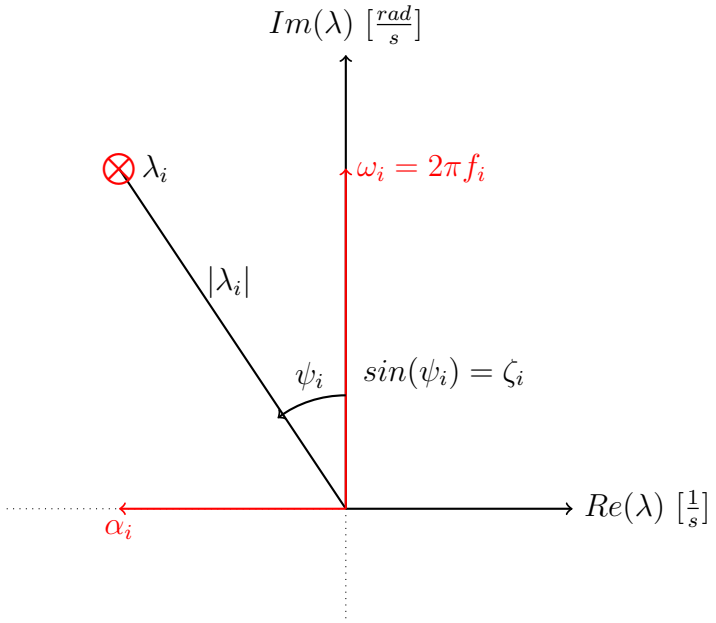

Figure 3.4: Graphical interpretation of the eigenvalue $\lambda_i = \alpha_i + j\omega_i$.

It should be noted that since the relative damping ratio in (3.32) depends on the angular frequency of the mode[3.4], two modes having the same relative damping ζ, will correspond to a response where the oscillatory mode having the largest frequency dies out faster. Thus, in terms of oscillations in a system, the lowest frequency mode is more severe to take care of, as the associated oscillations are sustained longer. These low-frequency modes often turn out to be inter-area modes, making it clearer why these modes are of deepest concern in power system operation. This is illustrated by a simple example in Figure 3.5.

[3.4]Therefore called *relative* damping ratio.

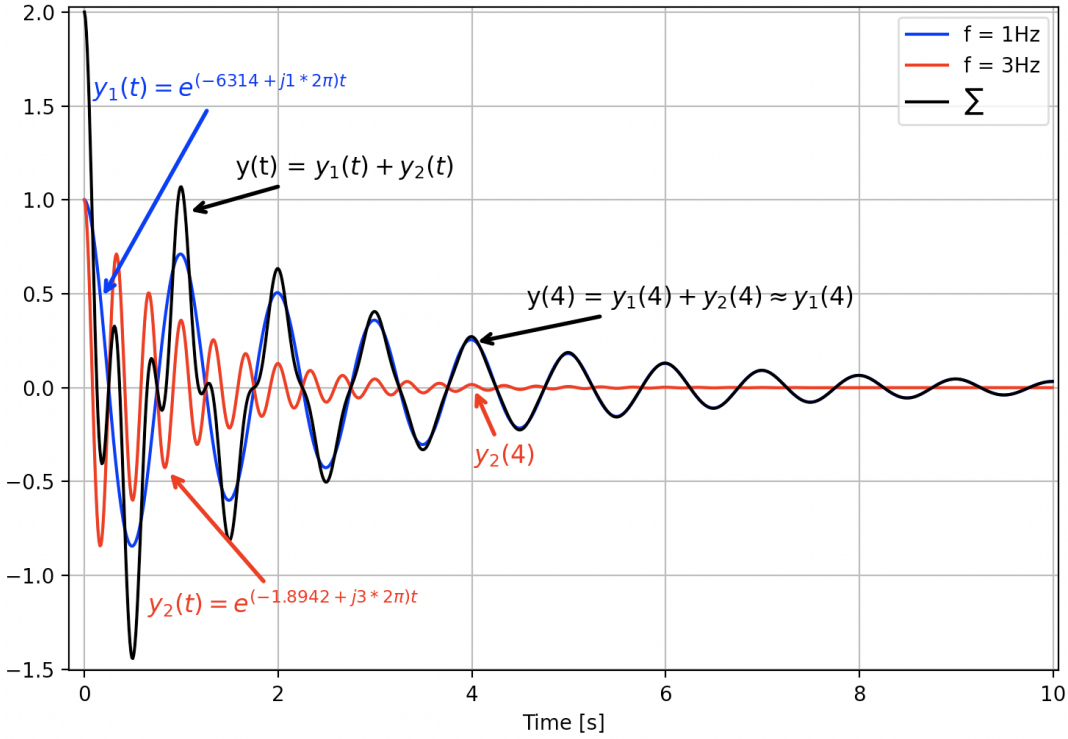

Figure 3.5: Illustrative example showing that for two eigenvalues having the same relative damping, the oscillation originating from the eigenvalue having the lowest frequency will sustain for a longer period of time.

The problems related to low-frequency oscillations should be clear from Figure 3.5. The output signal, $y(t)$ is the sum of two signals originating from eigenvalues having a frequency of 1 Hz and 3 Hz, respectively. Both eigenvalues have the same relative damping of 5%. However, the oscillations due to the lowest frequency mode are sustained for a longer time.

3.2.5 Example showing the Interpretation of Modal Analysis

The theory presented here might be pretty tedious to look at theoretically. Therefore, a small example is included below by conducting a simulation in Kundur's two-area system further described in Section 4.3.1. The motivation behind this is to visualize the theory presented here and thereby have an increased understanding of the fundamental principles and modal analysis power as a tool for investigating system stability. The example is focused on readers not familiar with the modal analysis.

The results from the modal analysis are first presented. Then a discussion is made on the eigenvalues and right eigenvectors in the system to estimate the speed responses in the system, solely relying on the linearised properties of the system. Then, the actual speed responses from the system are shown, showing that knowledge of modal proper-

ties is quite robust in terms of small-signal system response assessments. Compared to the default representation of the system given in Appendix C.1, inertia constant H at Generator 4 was halved, while AVRs and PSS's was disconnected to better highlight the theory by having eigenvalues that are easily distinguishable—running the simulation yields to following eigenvalues and mode shapes (normalized right-eigenvector) in the system.

Table 1: Eigenvalues in the system having frequency in the range 0.5 Hz to 1.5 Hz.

Eig	**Frequency [Hz]**	**Damping ratio**	**Type**
-0.35 $\pm j3.97$	0.63	0.088	Inter-area
-0.25 $\pm j5.37$	0.85	0.046	Local area 1
-0.88 $\pm j9.41$	1.50	0.093	Local area 2

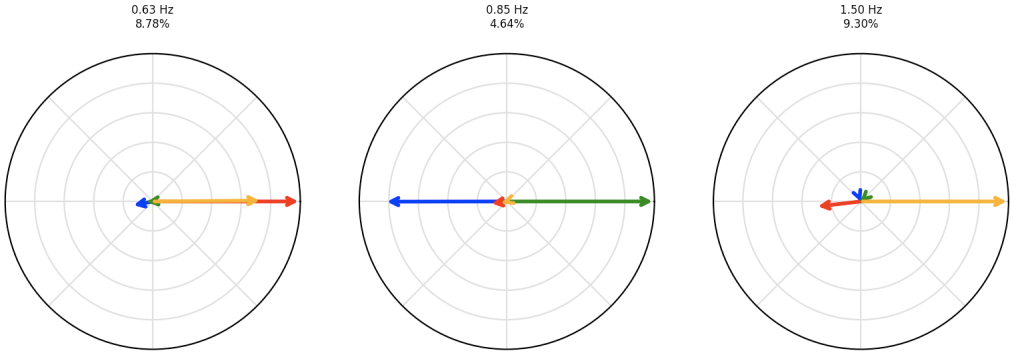

Figure 3.6: Mode shapes corresponding to the eigenvalues presented in Table 1. The state variables corresponding to the considered mode shapes are generator speeds. Blue: G1. Green: G2. Red: G3. Orange: G4

Based on the theory presented above, one should, in principle, be able to say something about the dynamic behavior of the system following a small disturbance by looking at Table 1 and Figure 3.6. One would expect that the 0.63 Hz oscillatory mode is almost negligible in Area 1 (Generator 1 and Generator 2), while being more observable in Generator 3 than Generator 4, as the mode shape length has a greater magnitude. The oscillatory mode corresponding to 0.85 Hz should, in theory, be visible in both Generator 1 and Generator 2 to approximately the same extent. At the same time, the small damping ratio would make it last for quite a few cycles before eventually dying out. With the given mode shapes for the eigenvalue having a frequency of 1.5 Hz, one should expect that this oscillatory mode will only be present in the state variable corresponding to speed at Generator 4. Figure 3.7 shows the actual speed responses in the systems when running the simulation.

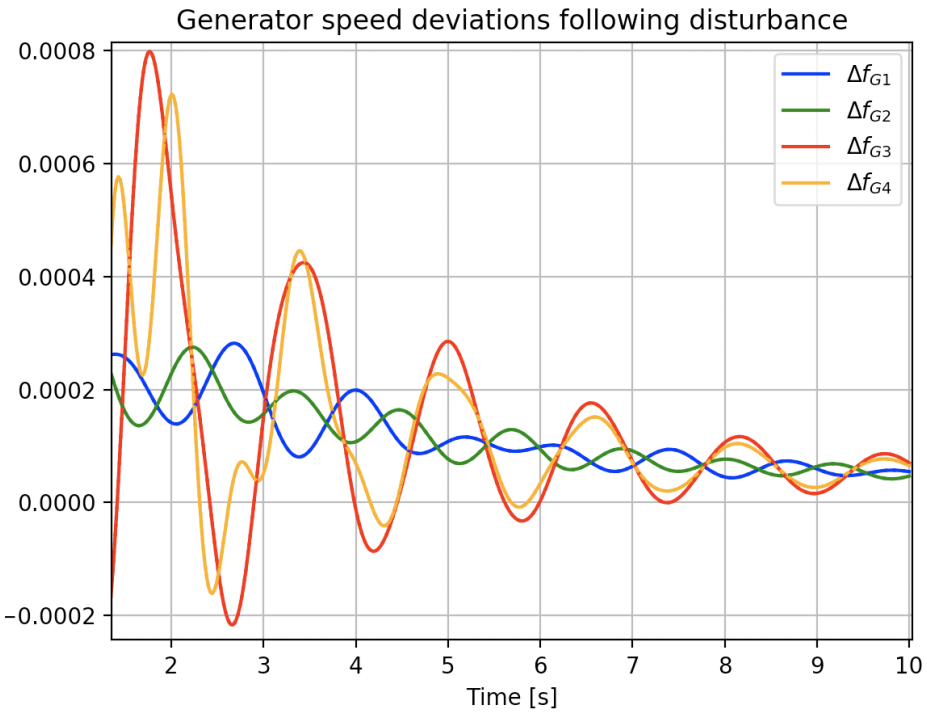

Figure 3.7: Generator speed responses. The system parameters are chosen to showcase how the linearized properties such as mode shapes and eigenvalues can be used to anticipate the system's small-signal response. By using Figure 3.6 one recognizes the oscillatory modes anticipated by the mode shapes in the speed/frequency deviations at the different generators.

Looking at the actual speed response from the simulation in Figure 3.7, it is clear that the anticipated response when looking at the eigenvalues and corresponding mode shapes accurately describes the dynamic behavior of the system. Keep in mind that the eigenvalues and mode shapes are all calculated at a steady-state at t = 0; nevertheless, they contain a significant amount of information about what happens when a small disturbance is applied, which shows the power of modal analysis. For instance, one observes that the oscillations between speed deviation at Generator 1 and Generator 2 have a period of a little bit more than 1 second. Measuring the time taken between two consecutive maximum values of the oscillations of, for instance, Generator 1, one can see that this correspond to oscillation with a frequency of 0.85 Hz, which was the same as was presumed by looking at the eigenvalues and mode shapes in Figure 3.6. The damping ratios are also observable, as the oscillatory mode corresponding to eigenvalue with frequency 0.63 Hz decays significantly faster than the oscillations in Generator 1 and Generator 2.

3.2.6 Participation Factors

From Section 3.2.3, it should be clear that the matrices $\mathbf{\Phi}$ and $\mathbf{\Psi}$ containing the right and left eigenvectors plays an essential role in the small-signal stability of power systems. Knowledge of these matrices allows for determining the sensitivity of a given modal variable $z_i(\mathrm{t})$ based on system parameters [56]. This is especially relevant when choosing the parameters of controllers in the system, and it could also be beneficial to use it for the optimal placement of power system stability-enhancing devices. Looking at one specific eigenvalue λ_i of the matrix $\boldsymbol{A}$, with the associated right and left eigenvectors $\boldsymbol{\phi_i}$ and $\boldsymbol{\psi_i}$, one have by combining Equation (3.21) and (3.22) that this eigenvalue can be expressed as

$$\lambda_i = \boldsymbol{\psi}_i \boldsymbol{A} \boldsymbol{\phi}_i \tag{3.34}$$

Now let β be a parameter in the system, for instance an inertia constant at a generator or a line reactance between two connected buses. In this deviation, the goal is to say something about the sensitivity towards certain system parameters, which naturally includes some derivative

$$\frac{\partial \lambda_i}{\partial \beta} = \boldsymbol{\psi}_i \frac{\partial \boldsymbol{A}}{\partial \beta} \boldsymbol{\phi}_i. \tag{3.35}$$

The value of $\partial \boldsymbol{A}/\partial \beta$ yields information about whether or not a given change in system parameter β yields better damping in the system, thereby improving the stability. Taking the system parameter β to be equal to a diagonal element of the system matrix, $\beta = A_{kk}$,

$$\frac{\partial \lambda_i}{\partial A_{kk}} = \boldsymbol{\psi}_i \frac{\partial \boldsymbol{A}}{\partial A_{kk}} \boldsymbol{\phi}_i = \begin{bmatrix} \psi_{i1} & \dots & \psi_{ik} & \dots \end{bmatrix} \begin{bmatrix} 0 & \dots & 0 & \dots \\ . & . & . & . \\ 0 & \dots & 1 & . \\ . & . & . & . \end{bmatrix} \begin{bmatrix} \phi_{1i} \\ . \\ \phi_{ki} \\ . \end{bmatrix} = \psi_{ik}\phi_{ki} = p_{ki}, \tag{3.36}$$

where p_{ki} is referred to as the participation factors. Thus, the participation factor contains information about the sensitivity of eigenvalue λ_i to the k'th diagonal element of the state matrix $\boldsymbol{A}$. Since the participation factors are a product of elements from both right and left eigenvector corresponding to the eigenvalue, they provide a good measure of the correlation between modal variable z_i and state variable x_k. Normally system enhancing controllers such as a stabilizer, damping controller, or a battery energy storage system is best located where modal variables associated with a given eigenvalue to a certain amount are both observable and controllable, which is essentially what the participation factors measures. Several previous papers have used participation factors for determining the optimal placement of PSSs in power systems [60], [61], and this will also be investigated further in this report. One could argue that looking at the controllability matrix would be sufficient in terms of determining the location of a control system. However, then one is not getting the effect of which state variables related to this location contain the oscillatory modes of interest as the

observability matrix measures. Thereby, suppose local measurements are used as feedback signals. In that case, even if the controllability matrix contains large values, there will be little interaction between the controller and the system as the mode of interest is almost non-observable at that location when observability entries are small. Thus, as the participation factors provide a measure of both of these simultaneously, they can be a valuable tool for determining controller locations, especially for controllers acting on local signals. For wide-area controllers acting on global signals, the participation factors do not necessarily contain that much information. For such cases, other procedures could prove to be a more valuable tool, for instance, the use of *Transfer Function Residues* which will be discussed in Section 3.3.1.

3.3 Transfer Function Residues and Applications

3.3.1 Transfer Function Residues in MIMO-systems

Using the state-space representation presented in Section 3.2.2 and including the input matrix $\boldsymbol{B}$, the output matrix $\boldsymbol{C}$ and the feedforward matrix $\boldsymbol{D}$, the diagonalized system in terms of modal variables might be written[3.5]

$$\begin{aligned} \dot{\boldsymbol{z}}(t) &= \boldsymbol{\Lambda z}(t) + \boldsymbol{\Psi B u}(t) \\ \boldsymbol{y}(t) &= \boldsymbol{C\Phi z}(t) + \boldsymbol{D u}(t), \end{aligned} \tag{3.37}$$

which when doing a Laplace transformation can be written

$$\begin{aligned} s\boldsymbol{Z}(s) - \boldsymbol{z}(0) &= \boldsymbol{\Lambda Z}(s) + \boldsymbol{\Psi B U}(s) \\ \boldsymbol{Y} &= \boldsymbol{C\Phi Z}(s) + \boldsymbol{D U}(s) \end{aligned} \tag{3.38}$$

A convenient tool for designing controllers is the concept of residues. From section 3.2.3 it can be seen that since $\boldsymbol{\Lambda}$ is a diagonal matrix, one has that ψB_i measures how much the k-th mode is excited by the i-th input. Analogously $C_j \phi_i$ measures the visibility of k-th mode in the j-th output, and therefore noted controllability and observability matrices respectively [54].

By ignoring the steady-state term $\boldsymbol{z}(0)$ and rearranging the first line of Equation (3.38) before inserting it into the second line, one have that the output matrix $\boldsymbol{Y}(s)$ is related

[3.5] Using the Laplace-transform of state-space system presented in (3.10) and rewriting to modal variables, $x(t) \rightarrow z(t)$, by making use of the right- and left-eigenvector matrices presented in Section 3.2.3.

to the input matrix $\boldsymbol{U}(s)$ such that

$$\begin{aligned}\frac{\boldsymbol{Y}(s)}{\boldsymbol{U}(s)} &= \boldsymbol{C\Phi}(s\boldsymbol{I}-\boldsymbol{\Lambda})^{-1}\boldsymbol{\Psi B}+\boldsymbol{D}\\ &= \boldsymbol{C\Phi}\begin{bmatrix}\frac{1}{s-\lambda_1} & 0 & \dots & 0\\ 0 & \frac{1}{s-\lambda_2} & & \vdots\\ \vdots & & \ddots & \\ 0 & \dots & & \frac{1}{s-\lambda_n}\end{bmatrix}\boldsymbol{\Psi B}+\boldsymbol{D}\\ &= \boldsymbol{G}(s),\end{aligned} \tag{3.39}$$

where $\boldsymbol{G}(s)$ is the transfer function matrix connecting the inputs and outputs in the system. The relationship between the input variables and output variables for such a system is illustrated in Figure 3.8.

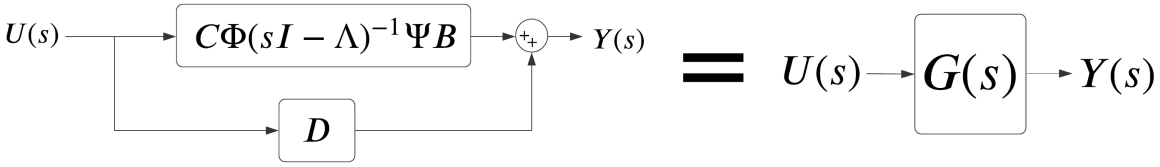

Figure 3.8: Multiple-input-multiple-output (MIMO) diagonalized compact representation.

Looking at one specific input and output combination from Equation (3.39), the open loop transfer function between the i-th input and j-th output is given by

$$\frac{Y_j(s)}{U_i(s)} = G_{ij}(s) = D_{ij} + \sum_{k=1}^{n}\frac{\boldsymbol{c_j}^T\boldsymbol{\phi_k}\boldsymbol{\psi_k}^T\boldsymbol{b_i}}{s-\lambda_k} = D_{ij} + \sum_{k=1}^{n}\frac{R_{ij,k}}{s-\lambda_k}, \tag{3.40}$$

which is graphically presented in Figure 3.9.

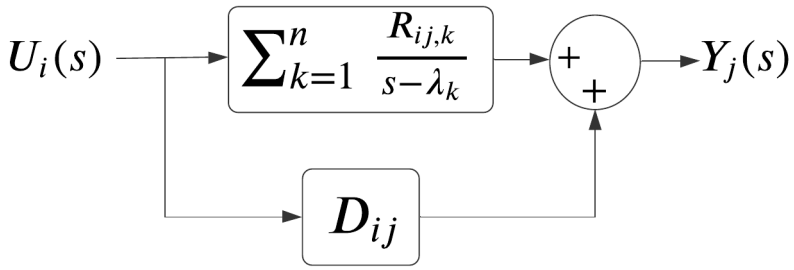

Figure 3.9: Open-loop transfer function G_{ij} between an input U_i and output Y_j expressed in terms of the system modes and residues.

The term $R_{ij,k}$ is the *transfer function residue* of the open-loop transfer function between the i-th input and j-th output in the system corresponding to eigenvalue λ_k. Hereinafter, the transfer function residue will be referred to as the *residue* for simplicity. Generally, the residue is a complex scalar value which can be seen by looking

at the dimensions of the vectors included in the computation of the residue $R_{ij,k}$ in Equation (3.40). This is presented below.

$$\underset{(1\times1)}{R_{ij,k}} = \underset{(1\times n)}{\boldsymbol{c_j}^T} \underset{(n\times1)}{\boldsymbol{\phi_k}} \underset{(1\times n)}{\boldsymbol{\psi_k}^T} \underset{(n\times1)}{\boldsymbol{b_i}} = \underset{(1\times1)}{\boldsymbol{c_j}^T\boldsymbol{\phi_k}} \underset{(1\times1)}{\boldsymbol{\psi_k}^T\boldsymbol{b_i}}$$

Therefore, for having a complete mapping of the residues in the system, this will be a three-dimensional structure with the dimensions being input signal, output signal, and mode numbering, respectively.

3.3.2 Residues for Feedback-Controller Design

The fundamental reason for discussing residues and including these in this thesis is that the k-th residue $R_{ij,k}$ mapping the i-th input to the j-th output contains information about the sensitivity of the k-th mode to a proportional gain feedback controller. *Having calculated the residue, one possesses information about the mode shift of the k-th mode given that one are assuming proportional feedback control from the j-th output to the i-th input*, thereby being valuable in terms of designing feedback controllers in the system with desired phase compensation for the mode of interest. Hence, feedback controllers can be designed based on this theoretical foundation for increasing the damping of specific modes in the system.

When the input-output combination is decided, and the mode of interest is determined, a feedback controller $H(s)$ can be inserted to the system for obtaining the desired gain and phase shift. Such a configuration is shown in Figure 3.10.

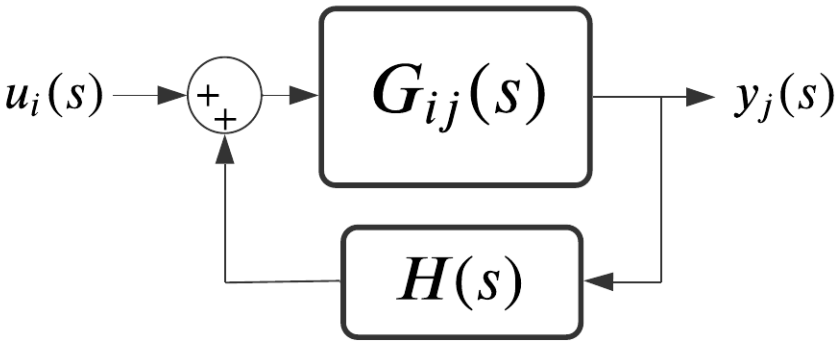

Figure 3.10: Open-loop transfer function $G_{ij}(s)$ and the tunable feedback-controller H(s) between the input u_i and output y_j.

The eigenvalue phase shift and amplitude for small feedback gains can be shown to be

$$\Delta\lambda_r = H(j\omega_r)R_r = |H(j\omega_r)|\angle H(j\omega_r)|R_r|\angle R_r. \tag{3.41}$$

Hence, by properly tuning the feedback controller, one could provide additional damping to mode of interest in the system. The mode shift when an arbitrary feedback controller aiming at adding damping to mode λ_r is used is illustrated in Figure 3.11.

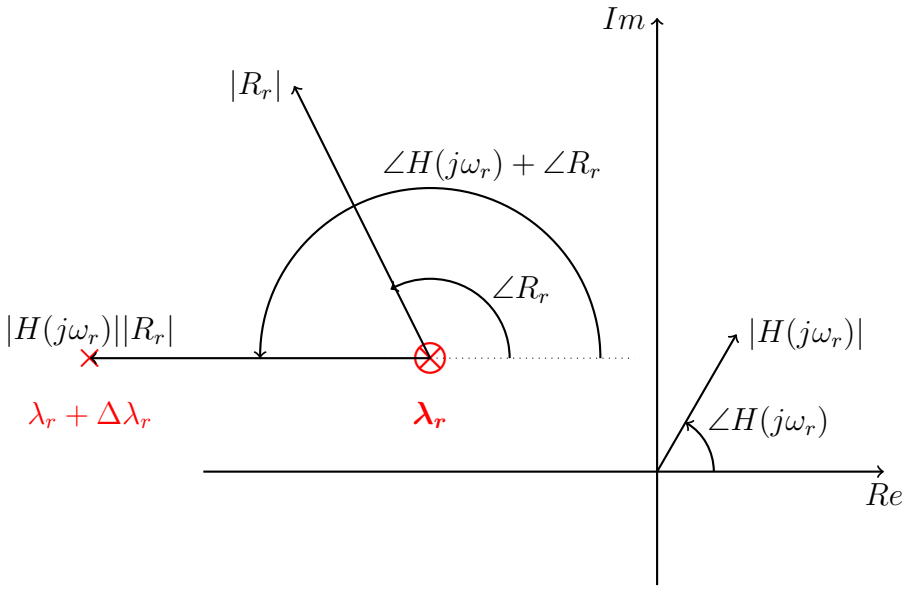

Figure 3.11: The basic principles behind design of feedback controller $H(j\omega_r)$ using the residue angle $\angle R_r$ for obtaining the desired shift of the mode of interest λ_r. This figure is essentially a visualization of equation 3.41.

To obtain the desired gain response, the proportional gain should be chosen such that the desired mode shift is obtained. Looking at the magnitude of change in Equation (3.41) and extracting the proportional gain constant out of the controller $H(s)$, one have that the gain constant should be chosen as

$$K_p = \left|\frac{\lambda_{id} - \lambda_i}{R_i H(\lambda_i)}\right|, \tag{3.42}$$

where λ_{id} denotes the desired position of the mode and λ_i is the original mode position. It is usually a requirement and good practice to not alter significantly with mode frequency as this may effect several other control loops in the system. Consequently, the imaginary parts in the nominator of (3.42) cancels out. The same thing happens with the denominator when the feedback controller $H(s)$ is tuned based on (3.61) for moving the eigenvalue in a straight line leftwards in the complex plane, and the gain constant K_p can thus be chosen

$$K_p = \frac{\Delta\lambda_i}{|R_i||H(\omega_i)|}, \tag{3.43}$$

where $\Delta\lambda_i$ is the change in the eigenvalue needed for moving the eigenvalue by an appropriate amount left-wards in the complex plane.

Proof of Residue Sensitivity for Feedback Controller Design

Due to the significance of residue direction related to the scope of this thesis, a short proof is provided to justify the mode sensitivity. This proof is based on the work done by [62, p. 83-84]. The angle of the k-th residue indicates the direction of the k-th mode when assuming a proportional feedback controller with sufficiently small gain. By inserting a feedback controller in the system and changing the proportional feedback gain, the mode is expected to follow the direction indicated by the residue in the complex plane. To derive this, a SISO system with input $u_i = Ky_j$ can be considered which is shown in Figure 3.12.

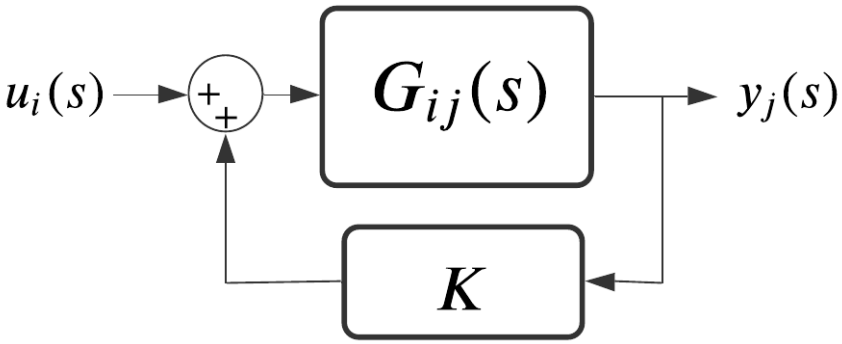

Figure 3.12: Open-loop transfer function $G_{ij}(s)$ and the proportional feedback controller between the input u_i and output y_j.

This input signal u_i is chosen such that it effectively accounts for a scalar feedback from the output y_j to the input u_i with the proportional feedback gain being K. From (3.40), the Laplace domain response $y_j(s)$ is found, when replacing D_{ij} by D and $R_{ij,k}$ by R_i

$$y_j(s) = G_{ij}(s)u_i(s) = (\sum_{i=1}^{n} \frac{R_i}{s-\lambda_i} + D)u_i(s) = (\sum_{i=1}^{n} \frac{R_i}{s-\lambda_i} + D)Ky_j(s). \tag{3.44}$$

Dividing by $y_j(s)$ on both sides, and rearranging yields

$$1 - (\sum_{i=1}^{n} \frac{R_i}{s-\lambda_i} + D)K = 0. \tag{3.45}$$

Applying a small change to the r-th eigenvalue, such that the new value is $\lambda_r + \Delta_r$, and substituting $s = \lambda_r + \Delta\lambda_r$ into Equation (3.45)

$$1 - (\sum_{i=1}^{n} \frac{R_i}{\lambda_r + \Delta_r - \lambda_i} + D)K = 0. \tag{3.46}$$

Assuming distinct eigenvalues in the system ($\lambda_i \neq \lambda_r \; \forall \; i \neq r$) and taking the limit of this equation as the change in the eigenvalue $\Delta\lambda_r$ and proportional gain K goes to

zero, one gets:

$$1 - \lim_{\Delta\lambda_r, K\to(0,0)}[(\sum_{i=1}^{n} \frac{R_i}{\lambda_r + \Delta\lambda_r - \lambda_i} + D)K] = 1 - \lim_{\Delta\lambda_r, K\to(0,0)}[\frac{R_r}{\Delta\lambda_r}K] = 1 - \frac{R_r}{\Delta\lambda_r}K = 0. \tag{3.47}$$

Hence, by making use of the last expression, one sees that the change in the r-th eigenvalue, or the sensitivity of this, is given by

$$\Delta\lambda_r = R_r K. \tag{3.48}$$

Consequently, it can be seen that for a scalar feedback from output y_j to input u_i, the residue contains information about the sensitivity of the r-th eigenvalue, and is valid for small scalar gains. This can purposely be used for designing desired feedback controllers in the control system.

This deviation is not only valid for proportional feedback controllers as will be seen. Suppose one are designing a feedback controller $H(j\omega)$ as in Figure 3.10 for targeting a specific eigenvalue with frequency ω_r. Then, by replacing K by $H(j\omega_i)$, Equation (3.44) might be rewritten as

$$y_j(s) = [\sum_{i=1}^{n}(\frac{R_i}{s - \lambda_i} + D)H(j\omega_i)]y_j(s), \tag{3.49}$$

where ω_i is the frequency of the i-th mode. Taking the limit as the feedback controller gain $|H(j\omega_r)|$ and $\Delta\lambda_r$ goes to zero yields

$$\Delta\lambda_r = H(j\omega_r)R_r = |H(j\omega_r)|\angle H(j\omega_r)|R_r|\angle R_r,$$

which is the same as presented in Equation (3.41). Thus, by adjusting the feedback controller gain and phase shift at the frequency of interest ω_r, one are able to change the eigenvalue of interest with an appropriate length and phase. The general idea behind Equation (3.41) is graphically provided in Figure 3.11. This derivation is undertaken by making the change in eigenvalue and controller gain go towards zero. Hence, Equation (3.41) is only valid for small controller gains, and care should be taken when using it using large gain values as the interaction between the different control loops in the system might be significant.

3.3.3 Residues for Determining Small Signal Time-Domain Responses

From Equation (3.44) it is clear that by neglecting the feed-forward term D, having the input u being a dirac pulse for simplicity, the Laplace domain signal of the output $y(s)$ can be written as:

$$y(s) = (\sum_{i=1}^{n} \frac{R_i}{s - \lambda_i})U(s) = (\frac{R_1}{s - \lambda_1} + \frac{R_2}{s - \lambda_2} + ... + \frac{R_n}{s - \lambda_n}), \tag{3.50}$$

where one take advantage of the fact that the Laplace transform of a dirac pulse is a constant. Thus, by using that

$$\mathscr{L}\{Ce^{-at}\} = C\mathscr{L}\{e^{-at}\} = C\frac{1}{s+a},$$

where C is a constant value, one have

$$y(t) = \mathscr{L}^{-1}\{y(s)\} = R_1e^{\lambda_1} + R_2e^{\lambda_2} + ... + R_ne^{\lambda_n}. \tag{3.51}$$

The time-domain response of the output variable will be a sum of exponentials weighted (and phase-shifted) by the corresponding residue, and the amount of oscillations depends on the damping and frequency of the corresponding eigenvalue. This correlates well with the theory presented in section 3.2.3, as it essentially is two different ways of looking at the same thing. This can be applied for simplifying the analysis significantly. Larger systems generally tend to yield computationally burdens for longer simulations. Hence, extracting the transfer function from a chosen input to output by calculating the residues as in section 3.3.1, one can efficiently run simulations to give a preliminary understanding of how a system input will affect a specific output of the system.

To further simplify the problems related to this, one could use the fact that, in reality, most of the residues turn out to have a value close to zero. Thus, by neglecting terms having an absolute value of residues lower than the desired threshold while neglecting terms corresponding to eigenvalues with high damping[3.6], one could significantly reduce the complexity of a system and still being able to run valuable simulations.

3.4 Feedback Controller Signal and Location Selection

When it comes to local Power Oscillations Controllers (PODs) such as conventional PSSs, the participation factors discussed in Section 3.2.6 provide knowledge of which locations in the system are suitable for applying damping to specific modes. However, the participation factor approach assumes local control with local input signals. Thus, it is a suitable tool for these purposes, but it does not necessarily indicate the optimal feedback signals and controller location when global signals are to be used.

When it comes to wide-area measurement and controllers, one could take advantage of the fundamental theory for local controllers and somehow extend this further. For a BESS installment in the system or any POD controller in general, a major design criterion would be to minimize the installed batteries' total capacity while still providing a satisfactory amount of damping in the system. Hence, selecting the feedback signal and location based on maximizing the residue value for the mode of interest should, in

[3.6] Responses originating from eigenvalues with high relative damping die out quickly.

theory, yield the largest magnitude change of the mode as per Equation (3.3.2) and the required feedback controller gain (or BESS capacity) needed for obtaining a desired amount of shift is reduced.

Since the BESS is injecting/subtracting power from the power system, this is essentially the same as modifying the y-bus in the system. Thus, by choosing the system input to be a change in y-bus, calculating the corresponding $\boldsymbol{B}$-matrix (which will be a vector when SISO-systems are considered), and then choosing the system output (feedback signal to the controller) to be some combination of the state variables in the system, a suitable selection of feedback signal and controller location should be possible to obtain.

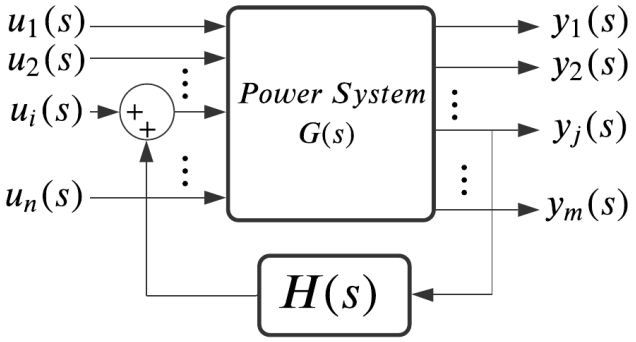

Figure 3.13: Multiple-input multiple-output (MIMO) power system with feedback controller between the j-th output and the i-th input. The general idea behind location and feedback signal selection is to choose the i-th input and j-th output yielding the largest residue magnitude for the mode of interest, such that the gain of the feedback controller (equivalent to the BESS capacity) can be minimized as per Equation (3.3.2).

This is illustrated briefly in Figure 3.13. It is generally a good practice to select feedback signals that are easily measurable in real-world systems [40]. Thus, the voltage angles at the buses in the system is considered for most of this thesis, as these are to a greater extent becoming available with the introduction of PMUs in the modern power systems as discussed in Section 2.2. One could potentially use several voltage angles as the feedback signals, but to limit the scope and not introduce further complexity, voltage angle deviations between two different buses in the system are considered. This is deemed to yield a satisfactory result. Hence, when seen in relation to the MIMO-system shown in Figure 3.13, the different outputs y_k correspond to different combinations of voltage angle deviations in the system. The inputs u_l corresponds to change in active power injection at different buses in the system. The objective would then be to find the combination of the input signal and feedback signal yielding the largest residue value for the mode of interest. This would minimize the needed BESS capacity installment for obtaining increased damping of the mode.

The voltage angles in the system are heavily correlated with the active power flows in the system (3.4) and should thereby be a good candidate for feedback signal aiming at controlling the active power injection at a given bus. It should be noted that the terminal voltage angles are not a state variable in the present configuration of the system. However, these correlate with the generator angles (state variables) in the system to a great extent. These prove to give a similar performance in terms of additional damping and phase shift. Therefore, using the generator angles for analysis purposes could be justified. Furthermore, the feedback signal could be changed to bus voltage angles when the actual batteries are implemented and non-linear simulations are performed. This is done in order to remove some of the complexity in building up the C-matrix (or vector for SISO-systems) when calculating the modal properties discussed in Section 3.2.3. A deviation showing the correlation between generator voltage angle $\Delta\delta$ and terminal voltage angle $\Delta\theta$ is provided in Appendix A.4 together with a short simulation showcasing how these angles are essentially having the same response following a disturbance.

3.4.1 Feedback Signal Selection

Denoting the vector storing the state variables in the system as $\boldsymbol{x}$ and having $\mathbb{X}_{\delta,idx}$ being the set of indexes corresponding to generator angle state variables in the state variable vector $\boldsymbol{x}$, a good choice of feedback signal would be a difference in generator angles satisfying

$$\begin{aligned} \max_{(j,\hat{j})} \quad & |R_{i,(j,\hat{j}),k}| = |\boldsymbol{c_{(j,\hat{j})}}^T \boldsymbol{\phi_k} \boldsymbol{\psi_k}^T \boldsymbol{b_i}| \\ \text{s.t.} \quad & j \in \mathbb{X}_{\delta,idx} \\ & \hat{j} \in \mathbb{X}_{\delta,idx} \\ & \boldsymbol{c}^T(j) = 1 \\ & \boldsymbol{c}^T(\hat{j}) = -1 \\ & \boldsymbol{c}^T(l) = 0 \quad \forall \quad l \neq j, l \neq \hat{j} \end{aligned} \tag{3.52}$$

where the k-th mode is the mode of interest (usually the lowest damped mode in the system), $\boldsymbol{b_i}$ is the linearized b-vector in the system (the values depend on where which entries in y-bus is modified in the system), j is the index of of the generator angle in the system included positively as feedback signal, and $\hat{j}$ is the index of the generator angle in the system included negatively as feedback signal to the controller. The last constraints of Equation (3.52) assures that one are taking the difference between two signals in the system, which is shown to more easily capture the inter-area oscillation in the system compared to cases using local signal only. Since Equation (3.52) essentially is a multiplication of the controllability and observability, one could further reduce the

size of this objective function as will be shown.

Writing out the residue computation for a arbitrarily chosen index of j and $\hat{j}$, one have

$$R_k = \begin{bmatrix} 0 & \dots & 1 & \dots & -1 & \dots \end{bmatrix} \begin{bmatrix} \phi_{k,1} \\ \vdots \\ \phi_{k,j} \\ \vdots \\ \phi_{k,\hat{j}} \\ \vdots \end{bmatrix} \begin{bmatrix} \psi_{k,1} & \dots & \psi_{k,j} & \dots & \psi_{k,\hat{j}} & \dots \end{bmatrix} \begin{bmatrix} b_1 \\ \vdots \\ b_j \\ \vdots \\ b_{\hat{j}} \\ \vdots \end{bmatrix} \tag{3.53}$$

where $\phi_{k,1}$ is the first entry in the right eigenvector corresponding to the k-th eigenvalue, and $\psi_{k,1}$ is the first entry of left-eigenvector. Carrying out the multiplication in (3.53) and rewriting into a suitable compact representation one have

$$R_k = (\phi_{k,j} - \phi_{k,\hat{j}}) \boldsymbol{\psi_k}^T \boldsymbol{b}. \tag{3.54}$$

Hence, by using fundamental properties from linear algebra [59] one have that for a given input signal selection (j, $\hat{j}$), the residue magnitude and phase shift is found by

$$|R_k| = |\phi_{k,j} - \phi_{k,\hat{j}}||\boldsymbol{\psi_k}^T \boldsymbol{b}| \tag{3.55}$$

$$\angle R_k = \angle(\phi_{k,j} - \phi_{k,\hat{j}}) + \angle(\boldsymbol{\psi_k}^T \boldsymbol{b}). \tag{3.56}$$

This relation can be interpreted in different ways, but for this purpose, as the BESS location is held constant, the term $|\boldsymbol{\psi_k}^T \boldsymbol{b}|$ is the same for all candidates of feedback signal combinations. Consequently, as the objective in Equation (3.52) is to select signals yielding the largest residue magnitude, the problem reduces so simply looking at which combination of feedback signals yields the highest absolute value of the difference between right eigenvector entries related to the k-th mode, $|\phi_{k,j} - \phi_{k,\hat{j}}|$, fundamentally being the same as choosing the difference between two mode shapes (discussed in Section 3.2.3) yielding the vector of largest magnitude. Thus, the objective function in Equation (3.52) could naturally be reduced to

$$\begin{aligned} \max_{(j,\hat{j})} \quad & |\boldsymbol{c_{(j,\hat{j})}}^T \boldsymbol{\phi_k}| \\ \text{s.t.} \quad & j \in \mathbb{X}_{\delta,idx} \\ & \hat{j} \in \mathbb{X}_{\delta,idx} \\ & \boldsymbol{c}^T(j) = 1 \\ & \boldsymbol{c}^T(\hat{j}) = -1 \\ & \boldsymbol{c}^T(l) = 0 \quad \forall \quad l \neq j, l \neq \hat{j} \end{aligned} \tag{3.57}$$

which simplifies the optimization problem quite significantly. To summarize, by using the objective stated in (3.57), one are able to determine the feedback signal combination yielding the largest magnitude of the residue and thereby maximizing the mode

shift seen in (3.3.2) without having to take into consideration the controller location. However, the important information about the residue angle for the optimal case is lost when using Equation (3.57), but it allows for deciding the feedback signal and location independently.

3.4.2 BESS Location Selection

When the feedback signal is chosen based on the previously discussed optimization problem, the natural next step would be to determine the optimal placement of the BESS. The same procedure used for the optimal feedback signal could be used. Similarly as for the feedback signal, one could use the residue approach as in (3.52) However, as the term $|\phi_{k,j} - \phi_{k,\hat{j}}|$ is fixed, one could remove the necessity of using residues, as the required information would be stored in the the complex scalar value $\boldsymbol{\psi_k}^T \boldsymbol{b}$. Denoting $\mathbb{B}$ to be a set of the buses in the system and the vector b_i being the linearized input vector calculated when y-bus is modified at the i-th bus, the objective to solve in terms of deciding the optimal placement of the battery could be written

$$\begin{aligned} \max_i \quad & |\boldsymbol{\psi_k}^T \boldsymbol{b_i}| \\ \text{s.t.} \quad & i \in \mathbb{B} \\ \text{where} \quad & \mathbb{B} \text{ is the set of buses in the system.} \end{aligned} \tag{3.58}$$

The optimal location of the BESS is decided based on the amplitude of $\boldsymbol{\psi_k}^T \boldsymbol{b_i}$ and the term that is getting maximized is the controllability of mode k from the j-th bus/generator in the system. It should be made clear that $\boldsymbol{b_i}$ does not solely consist of zeros and ones in general as was the case for the output vector $\boldsymbol{c}^T$ in (3.57), but it is found by calculating the value of $\boldsymbol{B} = \partial \boldsymbol{f} / \partial \boldsymbol{u}|_{(\hat{\boldsymbol{x}}, \hat{\boldsymbol{u}})}$ as in Equation (3.7) for every input location i being considered.

3.5 Tuning of Lead-Lag Filters

Lead-lag blocks are commonly used when designing control systems in power systems, especially for applications regarding Power Oscillation Damping. The lead-lag blocks offer tunable phase shifts in controller design. They can easily be cascaded for achieving desired phase shift at the frequencies of interest. A figure showing a proposed POD controller for the BESS is given in Figure 3.14.

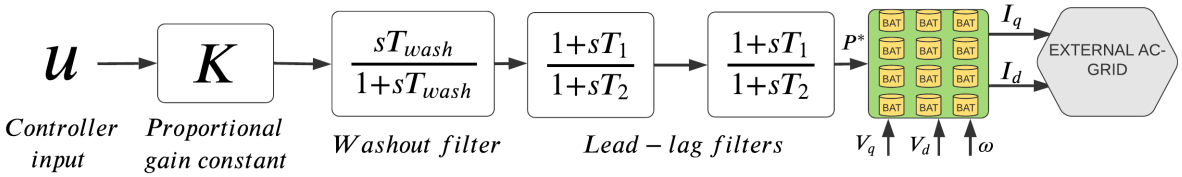

Figure 3.14: A BESS connected to an external AC-system deployed with the proposed controller. The different variables in the figures should be clear from the labelling.

When it comes to tuning of the lead-lag blocks, a reasonable procedure is to look at these blocks separately, without considering the washout filter in the control system in Figure 3.14. This is justified by the small phase shift originating from the washout filter at the frequencies of interest. The desired phase shift appended by the lead-lag blocks could be chosen to account for this. The general algebraic representation of m series-connected lead-lag blocks employed with a proportional gain factor K_p can be written out in the Laplace domain as

$$H(s)_{lead,lag,m} = K_p \left(\frac{1 + sT_1}{1 + sT_2} \right)^m \tag{3.59}$$

The proportional gain constant K_p have major impact on the transfer functions gain response $|H(s)|$, but does not influence the phase shift of the transfer function [58]. The amplitude response of the lead-lag blocks is then found to be

$$|H_{lead-lag,m}| = \left| \left(\frac{1 + sT_1}{1 + sT_2} \right) \right|^m, \tag{3.60}$$

where m denotes total number of lead-lag blocks with the same parameters. Hence, based on the desired phase shift ϕ_{comp} to be applied in the control structure and the frequency of interest (the frequency of the mode one are aiming to damp), ω_i, the parameters can be selected as

$$\begin{aligned} \alpha &= \frac{1 + sin(\frac{\phi_{comp}}{m})}{1 - sin(\frac{\phi_{comp}}{m})} \\ T_2 &= \frac{1}{\omega_i \sqrt{\alpha}} \\ T_1 &= \alpha T_2. \end{aligned} \tag{3.61}$$

Choosing the lead-lag parameters based on (3.61) assures that the desired phase shift is applied at the frequency of interest, but does not account take care of providing the desired gain response. However, it should be mentioned that several authors are expressing α in Equation (3.61) inversely [63], [64], such that $\alpha = (1-sin(\phi_{comp}/m))/(1+sin(\phi_{comp}/m))$, but this is simply a matter of which sign one applies to the desired phase shift ϕ_{comp}, and both approaches could be used as long as one are confident in the angular direction of movement of the eigenvalue. If in doubt, it is straightforward to get a visual representation of the BODE-plot of the transfer function $H(s)$ to see whether or not the desired phase shift at the frequency of interest is obtained.

3.6 Numerical Identification of Modes of Interest when System Topology and Parameters Change

When new control systems are inserted into the system, the eigenvalues in the system will change slightly, reflecting that the damping of the system and frequency of the different modes are changing slightly. Hence, some problems may arise in determining the correlation between the no-controlled-system eigenvalues and the eigenvalues when new controllers are deployed. Large systems contain a significant amount of eigenvalues, and determining the movement of the eigenvalues based on controller parameters is useful when designing control systems.

Suppose that one is interested in a specific poorly damped inter-area mode in the system, especially the movement of this mode when system parameters change. The most accurate way of doing so could potentially be to look at the participation factors discussed in Section 3.2.6, but this is a rather time-consuming way of recognizing the inter-area mode. A more suitable and numerically fast way of doing so in a programmable environment is to look at a small region around the initial position of the eigenvalue by assuming that the frequency and damping do not change too significantly.

Choosing the region around the initial eigenvalue position to be sufficiently small yields a fast-way of overcoming this problem, and is seen to be very effective unless two-eigenvalues are overlapping. This method is inspired by the criterion Perić and Vanfretti used for selecting the appropriate mode for a similar application [65]. Making eigenvalue λ_{k0} have an initial frequency of ω_{k0} and relative damping ζ_{k0}, the check to be undertaken could be summarized in the following set of equations

$$\begin{aligned} \omega_{k0} - \epsilon_\omega < \omega_k < \omega_{k0} + \epsilon_\omega \\ \zeta_{k0} - \epsilon_\zeta < \zeta_k < \zeta_{k0} + \epsilon_\zeta, \end{aligned} \tag{3.62}$$

where ϵ_ω and ϵ_ζ is a sufficiently small change in frequency and relative damping respectively. The eigenvalue in the "new system" satisfying (3.62) is λ_k, being the new/updated value of the eigenvalue originally being λ_{k0}. During the work with this thesis, this numerical way of determining the new modal positions have been utilized to a great extent, proving to yield good results for all modes being of interest. The method is illustrated for a specific more of interest in Figure 3.15.

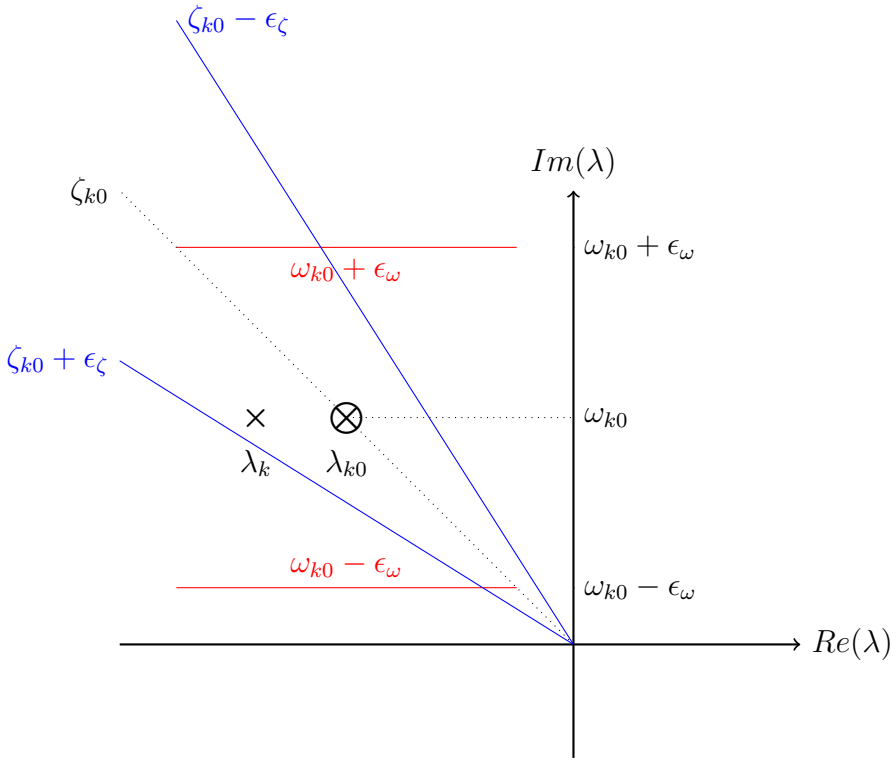

Figure 3.15: Illustration of how to appropriately select the desired mode when system parameters have changed. The initial position of the mode is λ_{k0}, and since λ_k is located within the dotted red and blue lines indicating the allowed shift in frequency and relative damping respectively, this is the new position of the mode. This way of searching for the mode produces accurate results when ϵ_ω and ϵ_ζ are chosen sufficiently small, and the mode of interest does not overlap with other modes in the system.

4 Modelling and Implementation of Dynamic Models

Regardless of the software being used, the different components present in the system and their implementation creates the foundation for the results. Capturing the essential dynamics seen in real-world systems requires accurate modeling of the essential components. This section is intended to introduce the Python Dynamic Power System Simulation, considerations to be taken when implementing different control blocks, presentation of the test systems used in this thesis, and discussions on different dynamic models employed for crucial components in the systems. Parts of this chapter are based on and adapted from the modeling conducted for the preceding specialization project.

4.1 Python Dynamic Power System Simulator (DynPSSimpy)

A Python Dynamic Power System Simulator (DynPSSimpy) developed by PhD student Hallvar Haugdal at the Norwegian University of Science and Technology is used to perform calculations, develop and implement dynamic models, and perform power system simulations. This section will serve as a brief introduction to the Python package and are based on a paper written by Haugdal and Uhlen [66] describing the working principles of the software, together with the author's consideration after working with the package for nine months.

DynPSSimpy is an open-source package for performing dynamic RMS simulations of preferably small to medium-sized power systems. Using DynPSSimpy instead of commercially available software such as PowerFactory or Simulink was chosen due to its flexibility, transparency, and expandability, facilitating the deployment of custom-made dynamic models. Thus, the package could arguably prove beneficial for researchers and students, creating a foundation for developing an intuitive understanding of power system operation and control due to the necessity of creating self-made models, requiring a real-time interaction and a fundamental understanding of their operation. Furthermore, the package is entirely built within a Python environment, promoting the use of built-in Python packages and libraries, which proves to be tedious and complicated to interact with for other available software [66]. Hence, this allows for straightforward implementation of appropriate dynamic models while allowing the user to create custom-made plots suitable for the research being conducted.

The package relies on Differential-Algebraic Equations (DEAs) describing the dynamics of the system. It is further based on solving linear equations on the form $\boldsymbol{YV} = \boldsymbol{I_{inj}}$,

where $\boldsymbol{Y}$ is the system admittance matrix, $\boldsymbol{V}$ is bus voltages and $\boldsymbol{I_{inj}}$ is the injected bus currents. Therefore, current injection models are preferred/suitable due to their simplicity in interacting with the rest of the systems. On the other hand, the dynamic simulations rely on solving Ordinary Differential Equations (ODEs) and facilitating the use of any suitable integration method, allowing the user to decide on the trade-off between computational burden and solving accuracy by selecting appropriate solvers in the Python environment, or using self-created solvers if that is preferred. Most of this thesis is utilizing an older version of the package (August 2020), being slightly unorganized and not structured as clearly as the new version. However, in the new version available [67], the dynamic models are represented by classes, significantly simplifying the implantation of new models and providing a more transparent and intuitive structure.

In order to validate the performance of DynPSSimpy, Haugdal conducted simulations in the Kundur Two-Area system using the Python package and compared the results with results obtained by the use of PowerFactory [66]. The results correlated well and showcased that simulations conducted in DynPSSimpy could reproduce results from commercially available software.

4.2 Block Diagrams to Differential Equations

When it comes to implementing different models and controllers in dynamic simulation tools, some key points are to be aware of, which will be presented here. This section is intended to give a fundamental introduction and possibly inspiration to future students on how the block diagrams and their dynamics might be implemented when writing code.

The design and structure of control systems and power system components are commonly given in the Laplace domain. However, in terms of implementing it in software, understanding and knowledge of how to go from Laplace-domain blocks to differential equations in time-domain are necessary[4.1]. These are the bottom layer of the implementations of all the models and control systems, and doing this correctly is of significant concern for representing the systems as intended.

A general control block $H_i(s)$ is shown in Figure 4.1. The controller input and output are denoted $u_i(s)$ and $y_i(s)$ respectively. The dotted lines and other variables named $u_{(.)}$ and $y_{(.)}$ represents other inputs and outputs in the overall system.

[4.1] Laplace transforms, and their inverses are covered in introductory courses in Mathematics and Control System Engineering and will thus not be covered in this thesis. For the interested reader, this can be found in Kreyszig [57].

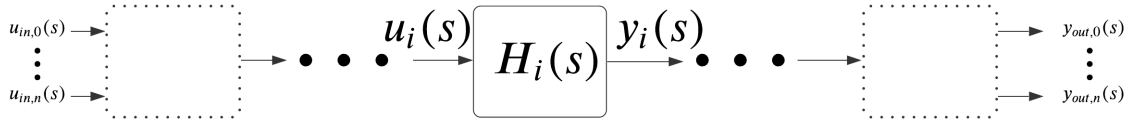

Figure 4.1: A general control block $H_i(s)$ being a part of a larger system. The variables subscripted with 'i' corresponds to the block of interest, and the block one are supposed to implement in a differential equation solver.

The three expressions needed for implementing $H_i(s)$ into the dynamic equations that the DynPSSimpy is built upon are listed below:

1. An expression for the change in the state variable, $\dot{\boldsymbol{x}}(\boldsymbol{t})$. Most of the commercially available software in the field of power system dynamics relies on solving a set of differential equations, and $\dot{x}(t)$ contains information about the change of the state variable for every consecutive step in the simulation.
2. The output from the control block, $\boldsymbol{y}(\boldsymbol{t})$. A large power system model consists of blocks connected, and the output from one block might be the input to another block and vice versa.
3. The initial value of the output from the block, $\boldsymbol{y_0 = y(t = 0)}$. This value holds the steady-state value of the output from the block, thus being important as solutions of differential equations rely on the initial values [57].

As an introductory example, a relatively simple block corresponding to a first-order time delay is considered. The transfer function together with its associated input and output is given in Figure 4.2a).

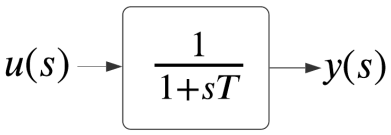

(a) Compact representation.

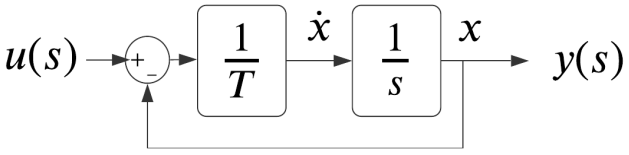

(b) Enlarged version for facilitating extraction of the information about the state variable derivative and block output.

Figure 4.2: Block diagram of a first-order low-pass filter in compact and enlarged versions.

For instance, this block could represent a time delay in a controller or a low-pass filter aiming at removing high-frequency input signals and is one of the most basic control

blocks. It can be seen that the block contains a Laplace-variable s, hence introducing a new state variable in the system [58]. Thus, to find expressions for the derivative of the state variable, a general procedure would be to enlarge the block diagram such that the derivative can more easily be obtained. One have that

$$y(s) = \frac{1}{1+sT}u(s), \tag{4.1}$$

where y(s) is the block output, $1/(1+sT)$ is the transfer function associated with the block, and $u(s)$ is the block input. Thus, by taking the inverse Laplace of both sides of the equation, one gets

$$\begin{aligned} \mathscr{L}^{-1}\{u(s)\} &= \mathscr{L}^{-1}\{(1+sT)y(s)\} = \mathscr{L}^{-1}\{y(s)\} + T\mathscr{L}^{-1}\{sy(s)\} \\ u(t) &= y(t) + T\dot{y}(t). \end{aligned} \tag{4.2}$$

Having the output correspond to the state variable, such that $y = x$, the block diagram shown in Figure 4.2a) can be redrawn into Figure 4.2b). By reading and interpreting the figure, one sees that the set of equations describing the system is found to be

$$\begin{aligned} \dot{x}(t) &= \frac{1}{T}(u(t) - x(t)) \\ y(t) &= x(t) \\ y_0 &= \mathscr{L}^{-1}\left\{ \frac{1}{1+sT}\bigg|_{s=0} u_0 \right\} = u_0 \end{aligned} \tag{4.3}$$

When the equations in (4.3) are established, one has the information necessary for defining this control block in the power system simulator tool.

The previous block might be relatively simple to implement, and other blocks might not be as trivial. Such blocks might require more extensive block diagram manipulation in order to develop the necessary expressions. An example of this is the lead-lag block, commonly used in AVRs, PSSs, and PODs applications, hence being a fundamental block for the topics covered in this thesis. A lead-lag block on its classical form is shown in Figure 4.3a).

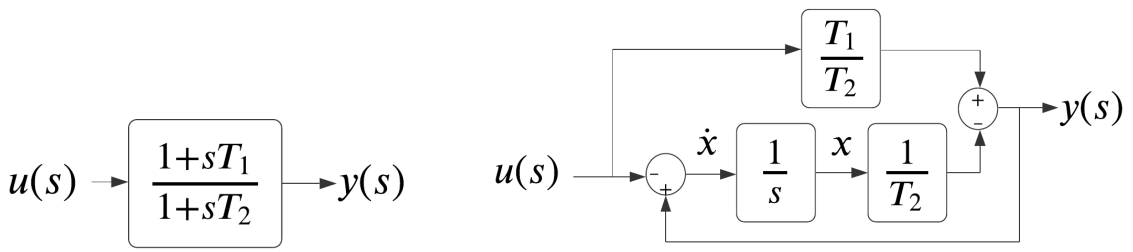

(a) Compact representation.

(b) Enlarged representation.

Figure 4.3: Block diagram of a lead-lag block in compact and enlarged version.

For such a block, one have from Figure 4.3a)

$$y(s) = \frac{1 + sT_1}{1 + sT_2} u(s). \tag{4.4}$$

Rearranging and dividing by sT_2 yields

$$y(s)\left(\frac{1}{sT_2} + 1\right) = u(s)\left(\frac{1}{sT_2} + \frac{T_1}{T_2}\right), \tag{4.5}$$

which can be further simplified to

$$y(s) = u(s)\frac{T_1}{T_2} - \frac{1}{sT_2}[y(s) - u(s)]. \tag{4.6}$$

Hence, by interpreting (4.6), it should be clear that the lead-lag block can be represented as in Figure 4.3b). Similarly as was the case for the simpler first-order low-pass filter block discussed in the start of the section, it simply is a matter of manipulating the original block diagram and transfer function in an attempt to make it more readable in terms of extracting the necessary equations to be implemented. From Figure 4.3b), the following relations are found

$$\begin{aligned} \dot{x}(t) &= y(t) - u(t) \\ y(t) &= u(t)\frac{T_1}{T_2} - \frac{1}{T_2}x(t) \\ y_0 &= \mathscr{L}^{-1}\left\{ \frac{1 + sT_1}{1 + sT_2}\bigg|_{s=0} u_0 \right\} = u_0, \end{aligned} \tag{4.7}$$

which are the three expressions needed for implementing the lead-lag block into the dynamical system.

Similar procedures are used for the other types of control blocks. Knowledge of how to implement the lead-lag blocks makes implementing other control blocks relatively straightforward by using the same procedure. As it turns out, the different control blocks used for implementing models and control systems in power system models are usually similar among the different models, and having a good understanding of a few of the fundamental blocks seems to be sufficient for most applications. However, it could be seen that the implementation of the lead-lag block was not as easily observable from the initial block diagram representation. Therefore, it should be mentioned that MATHWORKS is providing the differential equations and initial conditions necessary for several common control blocks and filters [68].

4.3 Test Networks

When designing components and controls that could have a real impact on the operation of modern power systems, the test networks used, or system models, are of

great importance. A common hypothetical and simple power system model that is used for a wide range of research related to operation and control is the Kundur two-area system, originally developed by Kundur in 1991 for simulating the interactions between different areas connected by weak grids [31]. This system is rather small and consists of two areas separated by a long tie-line, where each area are employed with two generators. Through numerous research papers, it has become clear that the dynamics and responses obtained for this system gives accurate first-hand knowledge of how different controllers will behave in a larger systems. Thus, due to its simplicity and capabilities in terms of providing valuable information scalable to larger system, its widely being used in the literature [31], [61], [63], [69]–[71]. Consequently, a common procedure when designing new control systems is to validate the results through simulations in this simple system, before testing it in a larger and more realistic system.

For this thesis, the larger system is chosen to be a version of the Nordic 44 system [72]. This system is more complex than Kundurs system, and aims at replicating load demand, generating units and power lines in the Nordic power system. Its not necessarily true that it is accurately describing the real-life power system for all operating conditions, but the size of it is sufficiently big such that it should work as intended for validating control systems and models. Both systems will be described more deeply in the following.

4.3.1 Kundur's Two-Area System

The original Klein-Rogers-Kundur system, or commonly referred to as Kundur's two-area system, [31] was modified slightly in this report, and the parameters used can be found in Appendix C.1. If not otherwise stated, all of the controls are active, and the parameters are as shown in the tables. The slightly modified version[4.2] of the system is shown in Figure 4.4. The BESS could, in principle, represent any component having a controllable current injection to the grid. For this thesis, this system will mostly be used for testing purposes, and for simulations verifying the implemented models.

[4.2] The modification is essentially the BESS connected in Area 2.

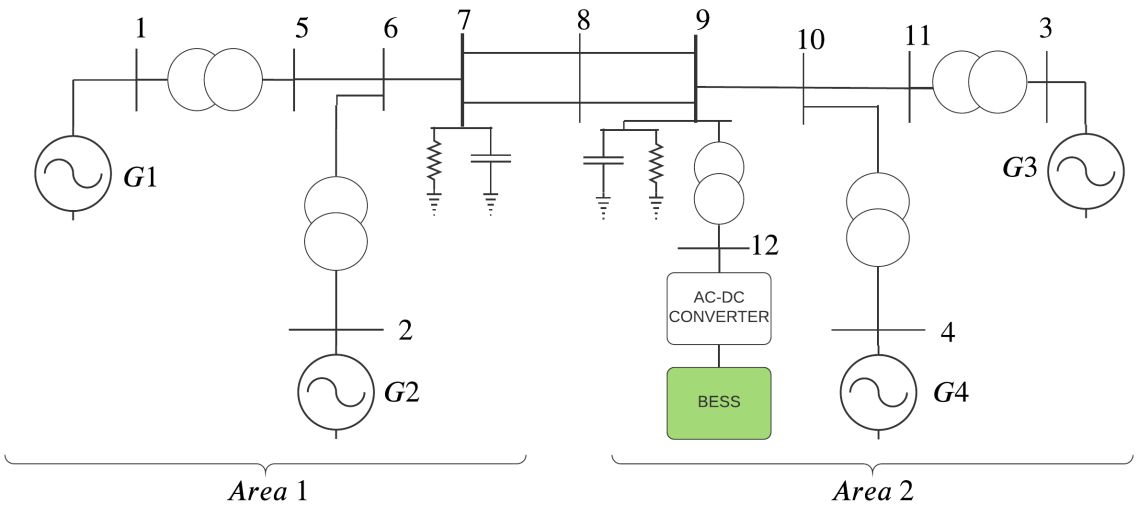

Figure 4.4: Kundur's two-area system with Battery Energy Storage System (BESS) connected at the load bus in Area 2 through a transformer. System parameters used when conducting simulations in this network can be found in Appendix C.1.

From the parameter list in Appendix C.1, one notices that the droop constants of the different governors might be a little high. These are chosen solely as they proved to showcase the oscillations of interest for this thesis more clearly when performing simulations. This could easily be adjusted if more realistic simulations are needed for future work. The inertia constants for generators located in the same area are the same but slightly modified compared to the original system [31]. This was purposely done in order to be able to distinguish the local area modes corresponding to Area 1 and Area 2, which are highly dependent on the inertia constants. The transformer connected between the BESS and its converter to the external AC-system is somehow arbitrary and does not influence the simulations extensively as it is made modeled to be lossless in this thesis. Therefore, it is omitted for most of the simulations but included in Figure 4.4 to represent a more realistic real-world connection of BESS to an ac-system.

4.3.2 Nordic 44

A version of the Nordic 44 system is used for validating the controllers and models in different types of simulations. The model is inspired by previous work of Jacobsen [73], and the system parameters used for this thesis can be found in Appendix C.2. Not all generators are installed with governors and AVRs, and for those with these control systems, they will be the same for all generators. This is rather unrealistic, but generalizable results are still obtainable. More realistic values and control systems could be employed for future simulations if deemed necessary, but the fundamental results are still valid for this setup. The last claim is justified by running a large number of simulations in different system configurations. The system is shown in Figure 4.5 and

a larger version is provided in Appendix C.2 in Figure C.1 to facilitate reading of the bus names.

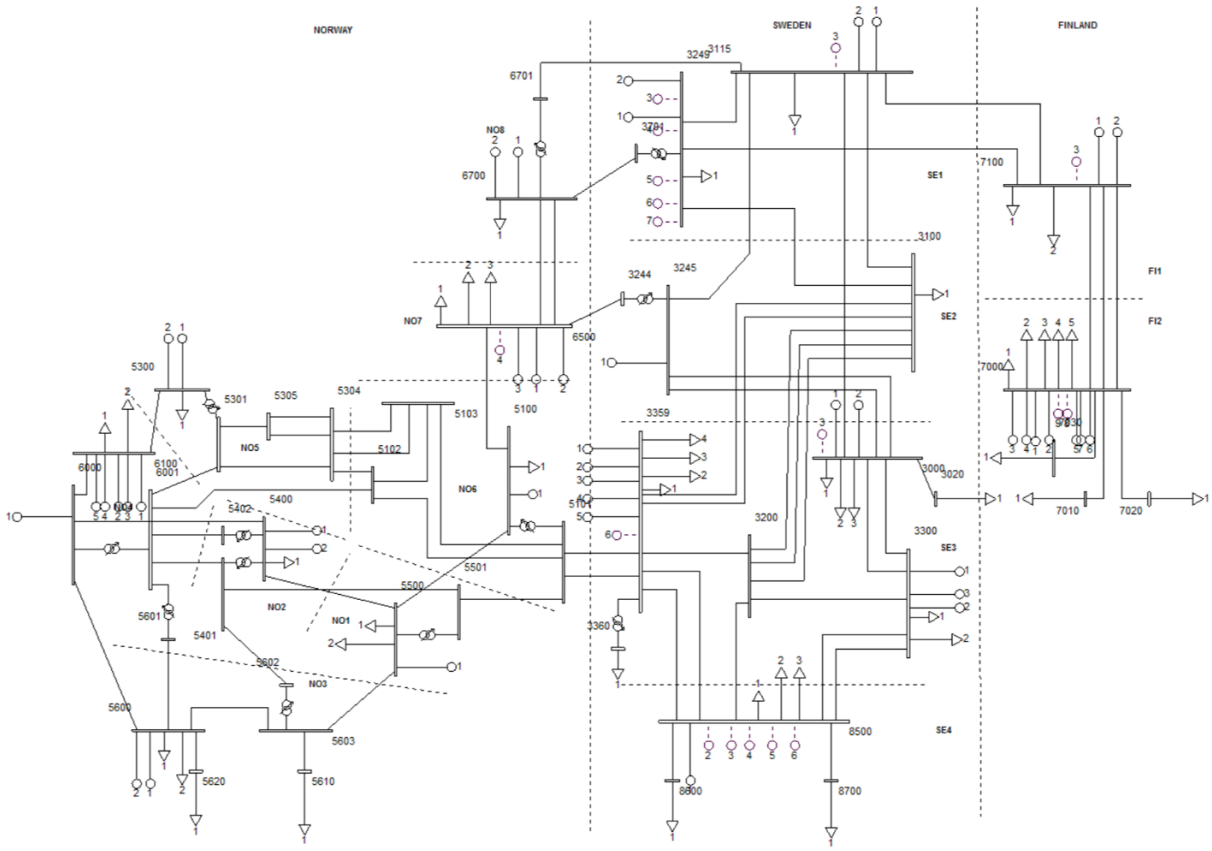

Figure 4.5: The Nordic 44 test network. System parameters used (if not otherwise stated) in the simulations are listed in tabular forms in Appendix C.2, in addition to a larger figure (Figure C.1) showing the system for easifying the reading of the bus names. Source: Adapted from [74].

The test network is employed to see the performance of the different implemented units in a larger and more complex system than the hypothetical and straightforward Kundur's two-area system. For this thesis, the main purpose of the system network is to carry out dynamical simulations and analyze the performance and characteristics of different models and controls. Hence, more information about the development of the system is out of the scope for this thesis, but detailed information about the development of the test network written by Jacobsen and Solvang is available for the interested reader [72].

4.4 Generator Models

Accurate simulations and analysis in power systems are greatly affected by the generator models, as these are of uttermost concern regarding the system dynamics. Thus,

this section intends to give a brief introduction to two commonly used approached for modelling the generators. The first one being the classical generator model commonly used for theoretical deviations and for obtaining general knowledge about the system dynamics. A more detailed model is the sixth-order generator model, which more accurately captures the dynamics within the generator, hence more modelling real-world generators more detailed and accurately.

4.4.1 Classical Model

Several theoretical deviations, simplifications, and system reductions make use of the classical generator model, which is noticeably simpler than the sixth-order model. In the classical generator model, two differential equations containing information about the rotor angle and speed dynamics are represented in the generator dynamics. This model is developed by assuming that the d-axis armature current and the internal emf remain constant during simulations. Hence, a model represented by a constant emf behind the transient d-axis reactance X'_d is used. The set of first-order differential equations for the generator are fundamentally the same as the swing equation (3.2) and are given by

$$\begin{aligned} M\Delta\dot{\omega} &= P_m - P_e - D\Delta\omega \\ \dot{\delta} &= \Delta\omega. \end{aligned} \tag{4.8}$$

The algebraic equations describing the relationship between the d- and q-axes currents and voltages are found by utilizing assumptions given in Machowski [56, p. 457]. By having the phasor quantities written in bold names, one have

$$\begin{aligned} \boldsymbol{I_g} &= I_q + jI_d \\ \boldsymbol{E_f} &= E_q + jI_d \\ \boldsymbol{V_g} &= V_q + jI_d, \end{aligned} \tag{4.9}$$

where $\boldsymbol{I_g}$ is the generator current, $\boldsymbol{E_f}$ is the generator internal emf and $\boldsymbol{V_g}$ is the generator terminal voltage. Subscript d and q represent d-axis and q-axis components respectively, where the axis are defined based on internal generator voltage angle δ_g. Therefore, by choosing the axis alignment such that the d-axis internal emf component is 0, one have that $\boldsymbol{E_f} = E_q$. The internal emf can then be found by

$$\boldsymbol{E_f} = \boldsymbol{V_g} + jX_dI_d + jX_qI_q + R\boldsymbol{I_g}. \tag{4.10}$$

Assuming the generator is lossless by having $R = 0$ and using the expression for current in (4.9) into (4.10), one have by rearranging

$$\begin{aligned} \boldsymbol{E_f} &= \boldsymbol{V_g} + jX_q\boldsymbol{I} + j(X_d - X_q)I_d \\ &= \boldsymbol{E_Q} + j(X_d - X_q)I_d, \end{aligned} \tag{4.11}$$

where $\boldsymbol{E_Q}$ is a new phasor defined for the sole purpose of having an easy expression for the generator voltage angle, δ_g. Since the d- and q-axis alignment is chosen such that $E_d = 0$ and these axes are separated 90 degrees apart, the quantity $j(X_d - X_q)I_d$ corresponds to a phasor in the same direction as the q-axis in the system. Consequently, the generator voltage angle δ_g can be found based on the newly defined phasor $\boldsymbol{E_Q}$ such that

$$\delta_g = \angle \boldsymbol{E_f} = \angle E_Q = \angle(\boldsymbol{V_g} + jX_q\boldsymbol{I}). \tag{4.12}$$

Hence, it is sufficient to have information about generator terminal voltage, generator current, and generator q-axis reactance to calculate the generator voltage angle. This process and the relationship between the different quantities are illustrated in Figure A.2.

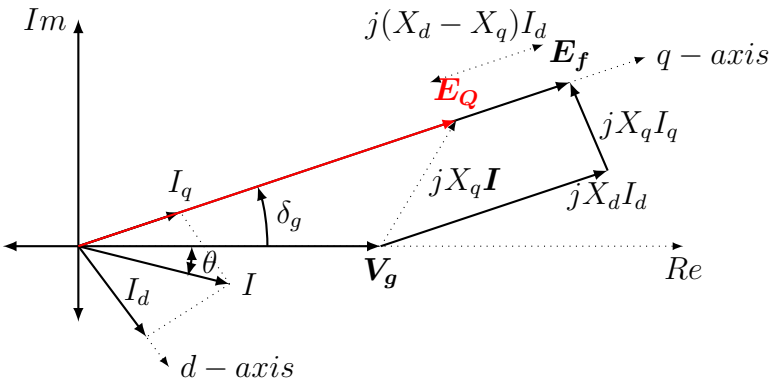

Figure 4.6: Illustrative example of how the different quantities in the generator model are related to one another. Special emphasizes is given towards the procedure behind algebraically finding the generator voltage angle δ_g

4.4.2 Sixth Order Model

For this thesis, a more advanced model is used. As a result, the simulations will be closer to what is being observed in the real world, and more details are captured. Although the generator actions are not of the most significant interest in this thesis, having an accurate generator model will be crucial. One of the most fundamental, if not the most fundamental, component in power systems are the generators. There are several way to model these generators which yields a different results in terms of model accuracy and simulation computational time. Without going to deep into the theory on the generator models, the basic equations are presented here. The dynamic simulator used in Python are based on the sixth-order generator model [56, p. 454]. The sixth-order model contains six state variables and six differential equations describing its dynamics, hence the name. This model is represented by sub-transient dq-axis emf's

behind sub-transient reactaces X''_d and X''_q which is compactly written in the form

$$\begin{bmatrix} V_d \\ V_q \end{bmatrix} = \begin{bmatrix} E''_d \\ E''_q \end{bmatrix} - \begin{bmatrix} R & X''_q \\ -X''_d & R \end{bmatrix} \begin{bmatrix} I_d \\ I_q \end{bmatrix} \tag{4.13}$$

The set of first-order differential equations describing the generators dynamics, $\dot{\boldsymbol{x}}_{\boldsymbol{gen}} = \boldsymbol{F}(\boldsymbol{x}_{\boldsymbol{gen}})$, are then found to be

$$\begin{aligned} M\Delta\dot{\omega} &= P_m - Pe \\ \dot{\delta} &= \Delta\omega \\ T'_{d0}\dot{E}'_q &= E_f - E'_q + I_d(X_d - X'_d) \\ T'_{q0}\dot{E}'_d &= -E'_d - I_q(X_q - X'_q) \\ T''_{d0}\dot{E}''_q &= E'_q - E''_q + I_d(X'_d - X''_d) \\ T''_{q0}\dot{E}''_d &= E'_d - E''_d - I_q(X'_q - X''_q), \end{aligned} \tag{4.14}$$

One recognizes that the two first differential equations are essentially the swing equation in it's simplest form as in (3.2). The implementation of the generator models is written in Python by Hallvar Haugdal, and is shown in Figure 4.7

```
self.p_m = self.P_m * self.S_n_gen/self.s_n
self.t_m = self.p_m / (1 + self.speed)
self.T_m = self.P_m / (1 + self.speed)
for i, dm in enumerate(self.gen_mdls):
    dx[dm.idx] = [
        1/(2*dm.par['H'])*(self.T_m[i] - self.P_e[i] - dm.par['D'] * x[dm.states['speed']]),
        x[dm.states['speed']]*2*np.pi*self.f,
        1/(dm.par['T_d0_t'])*(self.e_q[i] + self.v_aux[i] - x[dm.states['e_q_t']] - self.I_d[i] * (self.X_d[i] - self.X_d_t[i])),
        1/(dm.par['T_q0_t'])*(-x[dm.states['e_d_t']] + self.I_q[i] * (self.X_q[i] - self.X_q_t[i])),
        1/(dm.par['T_d0_st']) * (x[dm.states['e_q_t']] - x[dm.states['e_q_st']] - self.I_d[i] * (self.X_d_t[i] - self.X_d_st[i])),
        1/(dm.par['T_q0_st']) * (x[dm.states['e_d_t']] - x[dm.states['e_d_st']] + self.I_q[i] * (self.X_q_t[i] - self.X_q_st[i])),
    ]
```

Figure 4.7: Sixth-order model DynPSSimpy (version August 2020) implementation.

Comparing the Python implementation in Figure 4.7 with the system described in Machowski and rewritten in Equation (4.14), it is clear that these are essentially the same. The only noticeable difference is that the Python implementation is making use of the fact that in p.u. values, one have $M = 2H$, while the damping term from the Swing Equation (3.2) is included in the Python code. However, if not stated otherwise, $D = 0$ in simulations conducted for this thesis.

4.5 Battery Energy Storage System Model

The number of storage devices installed in the power systems is constantly increasing. Traditionally, Battery Energy Storage Systems (BESSs) have been used for peak shaving, storing excess power from renewable energy sources, and helping the grid during critical operating conditions [75]. When installed, these installations could also provide a significant amount of ancillary support to the transmission system operators. With

the increased focus on wide-area measurement systems throughout the world, utilizing the available data for grid-critical operation support and especially inter-area oscillation damping through the use of storage systems is promising.

Therefore, a BESS model was implemented in the dynamic power system simulator in Python. A significant number of analyses were performed to validate the implemented model and see how it could be controlled to improve the dynamic stability in power systems. A typical grid storage solution consists of a DC-system, a power conversion system, and a grid connection [75]. Hence, a diagram showing the general principles being considered for the implementation of the BESS model is shown in Figure 4.8, were arbitrarily chosen buses present in the Kundur's system presented in Section 4.3.1 and seen in Figure 4.4 are chosen as the location of the BESS.

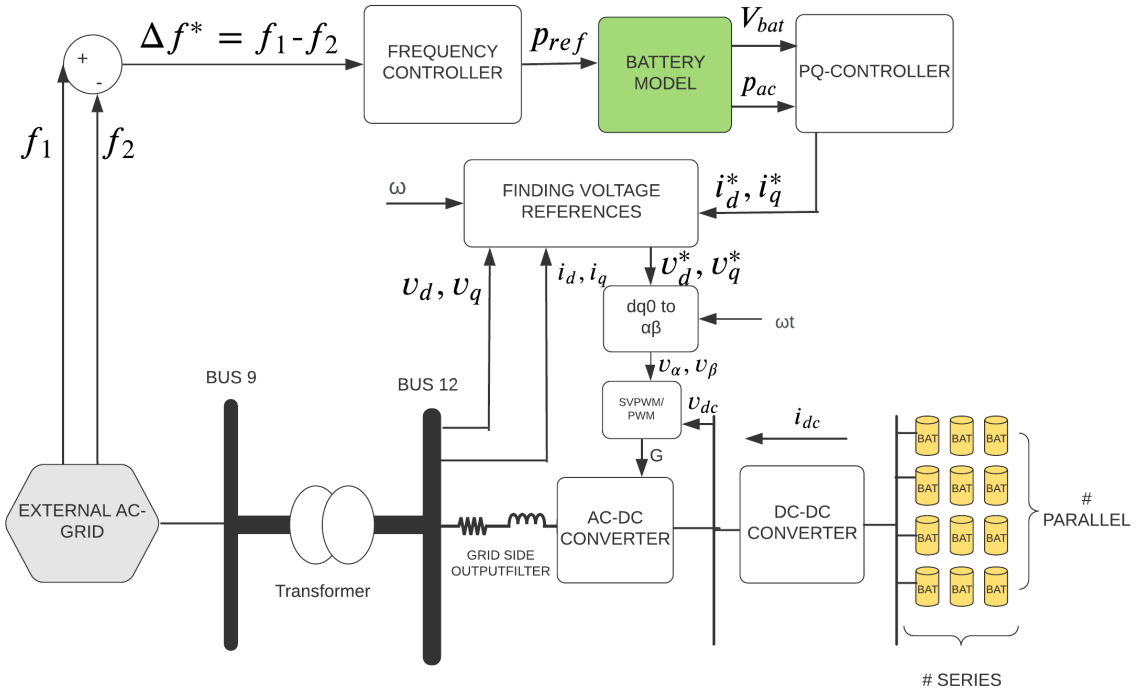

Figure 4.8: AC-system with grid connected BESS. A Phase-Locked-Loop (PLL) control system is usually employed for real-world systems, but is not included in the figure due to space limitations.

From Figure 4.8 it is evident that there is a lot of complexity and consideration to be taken when implementing a BESS model. A significant challenge to be addressed is the conversion between the AC- and DC-system and whether or not the DC-DC converter employed for some storage systems is to be included. When doing dynamic simulations in Python, most of the underlying dynamics in the battery, including the associated converters, can arguably be approximated by simplifications, as these dynamics are not of concern for system performance regarding damping of the oscillatory modes. However, when developing models, there is always a tradeoff between the model accuracy

and computational time [75]. Including the switching dynamics of the converters might be a necessity for future research but is deemed out of scope for this thesis.

Simplifications have been undertaken to remove some of the underlying dynamics present in Figure 4.8, and a simpler BESS model suitable for the work conducted in this thesis is presented in Figure 4.9.

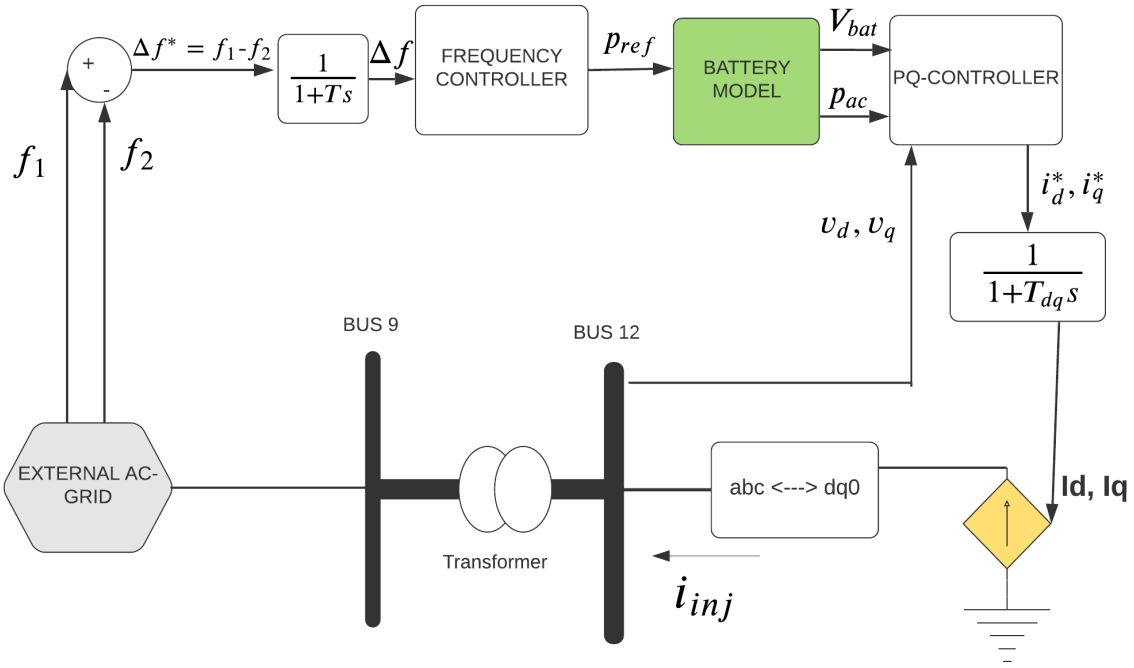

Figure 4.9: Overview of simplified BESS model implemented in Python. The converters from Figure 4.8 are replaced by first-order time-delays as the underlying dynamics is out of the scope for this thesis. This simplified representation allows for a decreased computational time when conducting analysis, but the most important dynamics for the work of this thesis are still present.

A first-order time delay with a time constant T is included for the input signal in an attempt to account for communication delays in the input signal, which is often of concern for Wide-Area Measurements applications [55]. However, this time constant is kept at a value close to zero for the simulations conducted in this report if not otherwise stated. The converter dynamics are replaced by first-order time delays represented by the block $1/(1 + T_{dq}s)$, where the time constant T_{dq} account for the time of which the underlying switching dynamics present in real-world converter uses for making the currents corresponds to the controller reference values. The next section covers the underlying battery model represented by the green rectangle in Figure 4.9.

4.5.1 Battery Model Considerations

While modeling the battery, some challenges had to be overcome. A significant amount of work was conducted to interconnect it with the rest of the power system in a desirable way and represent real-world batteries accurately.

The battery model accounts for losses by the inclusion of an internal resistance in each battery, while also accounting for discharge/charging dynamics by considering the state-of-charge (SOC) of the battery. One could argue that a the BESS is supposed to be deployed for damping of inter-area oscillations in the system over a relatively short duration, the SOC could in principle be made constant, as most battery systems installed in the grids uses hours to discharge fully/charge [76].

The battery model implementation in Python is to a great extent motivated by the BESS implementation found in DigSilent PowerFactory [77]. Generally, the available power to be extracted from a battery is dependent on the rate at which the battery is being charged and discharged [78], and the amount of available energy follows Peukerts law

$$C = I^k t, \tag{4.15}$$

where C is the battery capacity at 1 Ah discharge rate, I is the current of which the battery is discharged, k is Peukert's constant having different values for different battery technologies [79], and t is time in hours of which the battery is discharged. Battery ratings are usually given by producers in Ah-ratings together with a specified time of full discharge. A battery rated 200 Ah with a given discharge time of 20 hours can provide 10 A for 20 hours which is its rated condition [21, p. 370]. This would correspond to a C-rate of C/20 with the given terminology. Peukert's law says that for *Peukert constants* larger than 1, which is generally true for most technologies available [79], the available power to be extracted from the battery decreases with increasing current discharge rates. Although this is true for batteries, this is not specifically accounted for in the proposed battery model, but the internal losses increase when the discharge/charging rate is high, yielding a decrease in the power output.

In this model, it is assumed that the SOC will not be allowed to drop lower than 20%, and the voltage can then be assumed to be linearly dependent on the SOC [80]. These ensure that if the SOC drops to 20%, it will not provide more power and keeps the batteries within a safe operational region [81]. Although this is not of significant concern for this thesis due to the small changes seen in the SOC for short-simulations, this might be of concern if the battery model is used for replicating, for instance, a super-capacitor which exhibits higher rates of charge/discharge [39].

The dynamics regarding the SOC of the battery is modeled by the following relation

$$SOC(t) = SOC_0 - \frac{1}{C}\int_0^t Idt, \tag{4.16}$$

which can also be found in other papers [82]. The variable SOC_0 is the initial state-of-charge, I is the battery cell current, and C is the battery's capacity. If not stated otherwise, the SOC_0 is initialized to 0.5 for the simulations conducted in this thesis. This allows the BESS to extract and inject power while keeping it away from the SOC limits presented above. The internal voltage in the cell is assumed to be linearly dependent on the SOC, and by including an internal resistance replicating losses, one has

$$V_{cell} = V_{max}SOC + V_{min}(1 - SOC) - r_{cell}I_{cell}. \tag{4.17}$$

The finalized BESS model, not including the simplifications made for representing the converter dynamics, together with a proportional controller is shown in Figure 4.10.

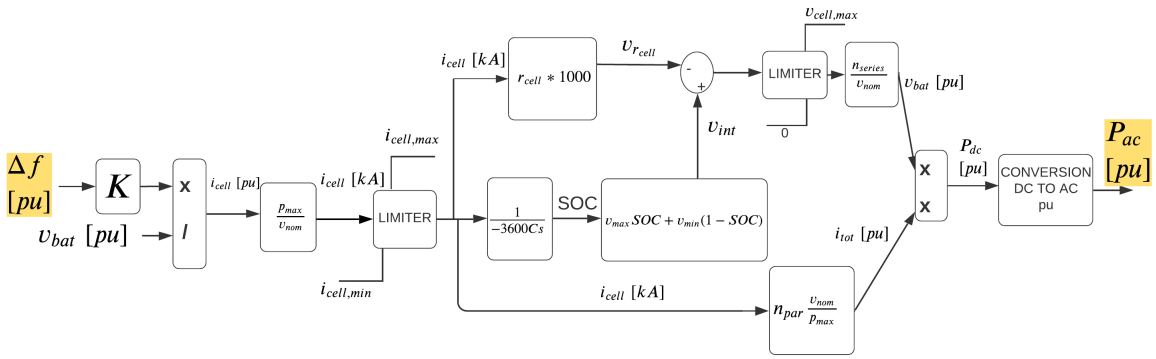

Figure 4.10: The implemented BESS model being made up by $n_{par} * n_{series}$ equivalent battery models together with a proportional controller acting on the arbitrarily selected input signal Δf. Some limiters are included to assure that the battery is not operating above its rated conditions. Internal resistance is included to represent a more realistic scenario, while the state-of-charge (SOC) ensures that each battery has limited storage capacity.

The BESS model presented in Figure 4.10 consists of the input controller and a total of $n_{par} * n_{series}$ equivalent underlying battery models connected together. It is assumed that each battery holds the same cell voltage and provides the same current. Making the AC-side power coincide with the provided power on the DC-side is taken care of by the block "Conversion DC to AC" which essentially is a conversion between the per unit systems. The output of the block diagram is denoted P_{AC}, being the reference power to be provided by the BESS into the external AC system.

The converter switching dynamics are simplified and approximated by first-order time delays with time constants T_{dq}, such that the reference power to be provided by the

BESS is delayed when interacting with the external system. Utilizing this, the current control scheme presented in Figure 4.11 are proposed.

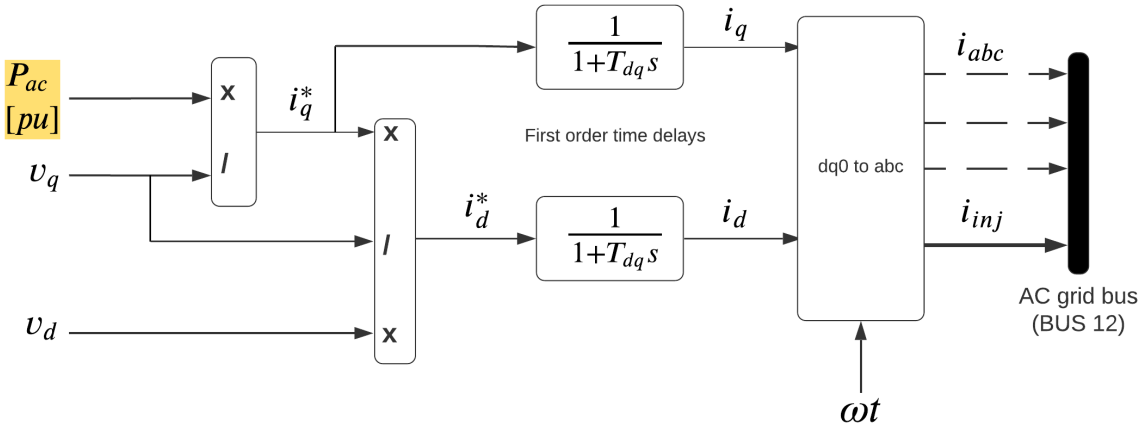

Figure 4.11: The current dynamics in the controlled current source injection within the given BESS model. The ability of the currents to follow their references values are modelled by a first order time delays with time constants T_{dq}.

This controller takes the power output P_{AC} from the BESS as input and then calculates the corresponding reference currents to be provided to the external grid. When using dq-reference frame of currents and voltages it can be shown [83], [84] for a balanced three-phase systems that the powers (excluding the scalar factors needed for certain varieties for the transform) can be calculated as

$$P = v_d i_d + v_q i_q \approx v_q i_q \tag{4.18a}$$

$$Q = v_q i_d - v_d i_q \approx v_q i_d. \tag{4.18b}$$

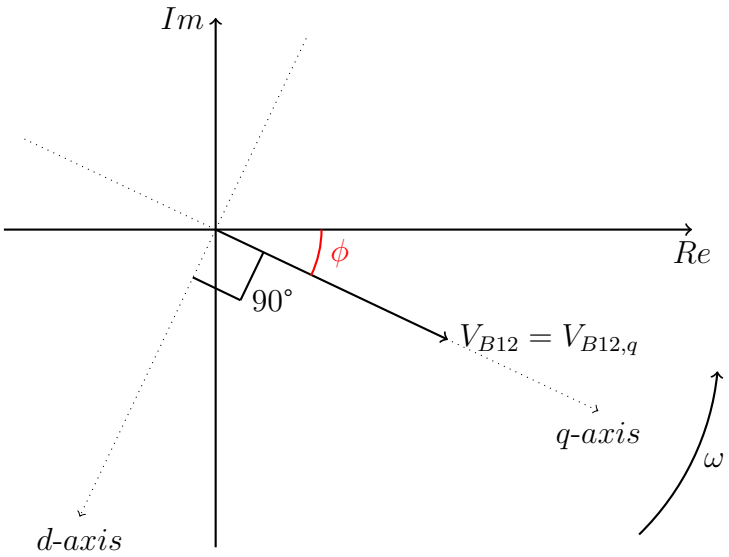

Figure 4.12: Reference frame alignment used for the battery model. For this illustration it is assumed that the BESS is connected to bus 12 in the system, but this could be chosen as any arbitrary bus in the system. For the conducted simulations, the dq-components of the voltage will be dependent on the bus of which the BESS is connected.

With the reference frame aligned such that $v_d \approx 0.0$ as illustrated in Figure 4.12, one have that the reference q-component of the current, i_q*, can be calculated by $i_q* = p/v_q$, which is essentially what the control system in Figure 4.11 does. The regulator also contains regulation for the d-component of the current, although this is approximately zero throughout this thesis. In the end, the obtained dq-component of the currents are transformed back into abc-representation, such that the injected current components are appropriately interacting with the power system.

4.5.2 Simulation Showing the Power and Current Dynamics

The consequences of introducing a first-order time delay on the injected currents are shown by a simulation conducted in Kundur's two-area system. The time delay was set to a value of $T_{dq} = 0.2$ seconds, which is significantly higher than the ones that will be used for the other simulations. This is solely set so for illustrating the concepts and effects of including the first-order time delays. The other parameters used in the Kundur system are similar to the values found in Appendix C.1.

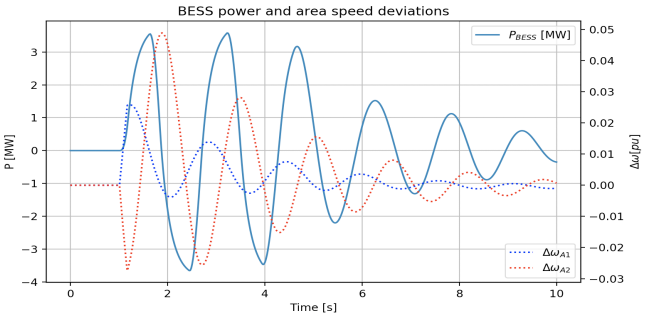

(a) Power provided by the BESS (solid blue) and speed deviations in Area 1 (dotted blue) and Area 2 (red).

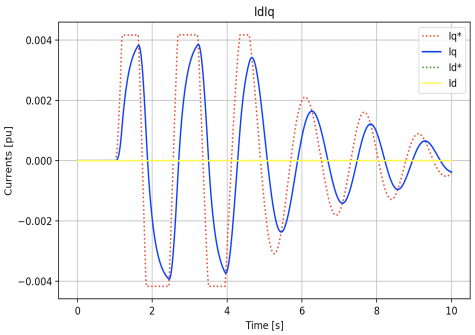

(b) Current components and their reference values. I_d* is kept at zero, while the I_q component are following its reference value I_q*.

Figure 4.13: Time-domain simulation with first-order time delay on current controls. T_{dq} is set to 0.2 seconds, which is significantly larger than real-world dynamics, but used for illustration purpose.

From Figure 4.13 one observes that the q-component of the current is not able to reach its reference value fast enough, consequently limiting the power output of the BESS and its ability to provide dampening. Nevertheless, these controls will naturally include some time delay in a real-world system, assuring a more accurate representation. A value of 0.02 seconds is usually representing real-world inner current controls quite accurately [16], which is ten times smaller than the one used for obtaining the results in Figure 4.13. One also sees that the d-component of the current stays approximately zero throughout due to the reference frame alignment described and illustrated in Figure 4.12. Suppose the time constant is set to 0.02 seconds instead, the q-component of the current is more or less a square wave initially following the disturbance, as I_q and I_q* would essentially be overlapping.

4.5.3 Effective Gain of the BESS Model

The BESS model presented in Figure 4.10 included an arbitrarily chosen input signal Δf and a proportional controller with gain K. When further simulations are conducted for providing damping to critical modes in the system, the internal gain of the BESS model will be of great importance. Thus, having a fundamental idea of how the different parameters in the BESS model influence its capability of providing damping is needed.

Assuming one are not exceeding the current limits of the batteries, having the internal resistance of each individual cell set to zero and approximating the SOC to be constant which is a valid assumption for short-duration simulations, one sees that the

output of the block diagram in Figure 4.10 yields

$$\begin{aligned} \Delta P_{DC} &= K\Delta f n_{par} n_{series} \\ \Delta P_{AC} &= \Delta P_{DC} \frac{P_{battery}}{S_{AC}} = K n_{par} n_{series} \frac{P_{battery}}{S_{AC}} \Delta f = K k_{bess} \Delta f \end{aligned} \tag{4.19}$$

where ΔP_{DC} is the total dc-side power in per unit, P_{AC} is the per unit value of the AC-side power provided by the BESS. $P_{battery}$ and S_{ac} is the power rating of one battery unit and apparent power base value in the external power system respectively, and K is the gain constant used in the arbitrarily chosen proportional controller. The fraction fraction P_{bess}/S_{ac} is converting the power provided by the BESS to p.u. power values in the AC-system, represented by the block *conversion DC to AC pu* in Figure 4.10. Hence, one have that for the given assumptions, the BESS model internal gain is found to be

$$k_{bess} = n_{par} n_{series} \frac{P_{bess}}{S_{AC}} \tag{4.20}$$

Thus, when looking at the effective gain of a feedback loop utilizing the BESS model, having in mind that Equation (4.20) contains an approximate value of the internal gain of the BESS model will be crucial. For instance, if the proportional gain controller K is replaced by a general controller $H(s)$, the total effective gain of the feedback loop is $|H(s)|k_{bess}$.

5 Controller Selection, Simulations and Results

5.1 Base Case System Response

Stability issues in power systems can often be addressed by calculating the eigenvalues/modes for a given steady-state operational point. For this thesis, a marginally unstable version of the Nordic 44 test system is chosen as the base case, and the system parameters are given in Appendix C.2. By linearizing the system around the pre-defined operating point, it is seen that it contains a pair of eigenvalues barely inside the right-half of the complex plane, indicating oscillatory responses with increasing amplitudes following a disturbance. Figure 5.1 shows the eigenvalues having an imaginary part/frequency greater than or equal to zero, and real part greater than -5.

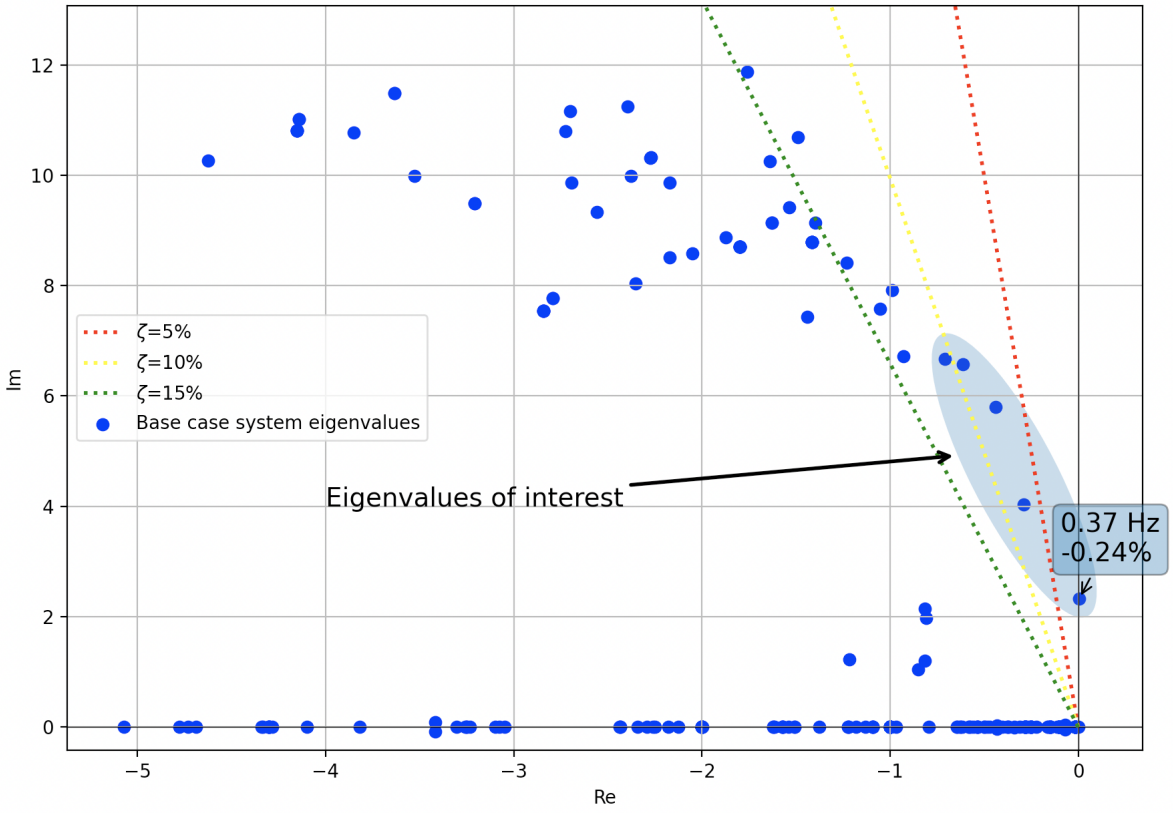

Figure 5.1: Eigenvalues in the base case system. The region marked with "Eigenvalues of interest" corresponds to the five lowest damped modes in the system, and the dotted lines indicates constant relative damping lines. The poorest damped mode, marked with (0.37 Hz, -0.24%), have a value of $\lambda_{ia,0} = 0.005695 + j2.3257$.

Although the presented eigenvalues are not showing all of the eigenvalues in the sys-

tem[5.1], it is clear that the system contains a large number of eigenvalues[5.2]. Most eigenvalues are satisfactorily damped, but five of the eigenvalues contain relative damping of approximately 10% or smaller. These eigenvalues are highlighted in the blue region Figure 5.1. The most noticeable eigenvalue is the one slightly to the right of the imaginary axis, having a frequency of $f = 0.37Hz$ and relative damping ζ = -0.24%. In order to have a stable operating point and safe operation of the power system, somehow shifting this eigenvalue leftwards in the complex plane will be of uttermost importance. Without addressing this, any small disturbance in the system will eventually make the system unstable.

The right- and left-eigenvectors corresponding the five poorliest damped modes and generator speeds in the system is provided in Figure 5.2 and 5.3 respectively. The participation factors[5.3], which essentially is a measure of both right- and left-eigenvectors, is presented in Figure 5.4. The coloring of the arrows in the eigenvector plots are corresponding to the colors used in the participation factor plots. That is, a red arrow in one of the eigenvector plots will correspond to generator 6100 which is the generator colored red in the participation factor plot in Figure 5.4.

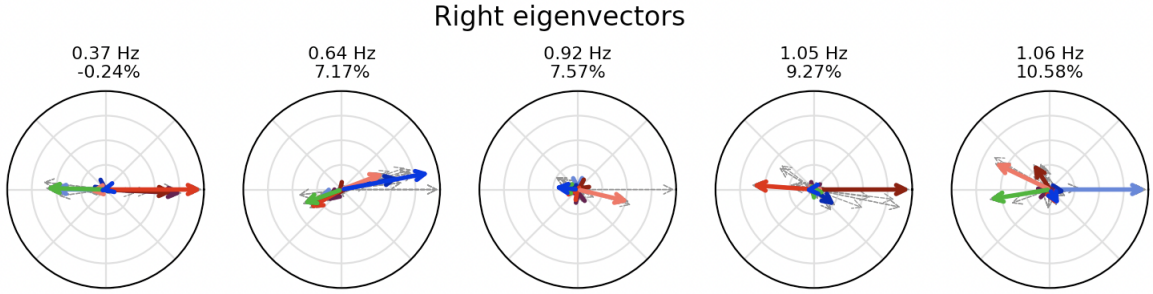

Figure 5.2: Right eigenvectors (mode shapes or observability) in the base case system. The coloring complies with the coloring used in Figure 5.4

[5.1] The eigenvalue plot is zoomed in, thus not showing the eigenvalues containing a negative real part with large magnitudes or eigenvalues with imaginary part less than zero (this will only be a mirrored image of the eigenvalue having a positive imaginary part).

[5.2] Number of eigenvalues equals number of state variables in the system, in the region of 400-500 for this system configuration.

[5.3] Participation factors are presented in Section 3.2.3.

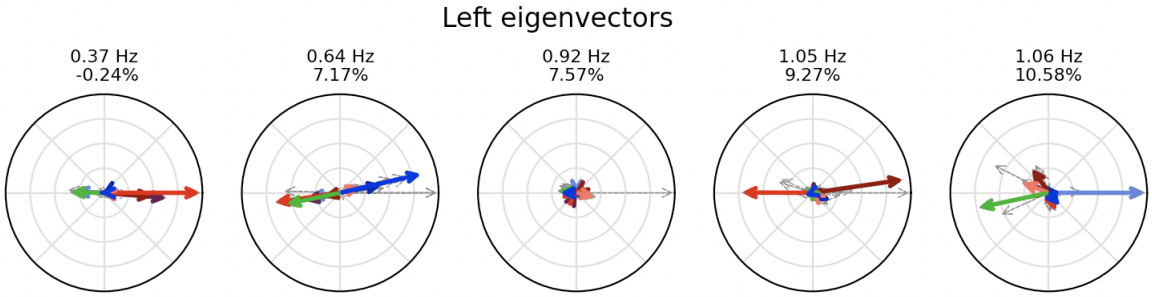

Figure 5.3: Left eigenvectors (controllability) in the base case system. The coloring complies with the coloring used in Figure 5.4.

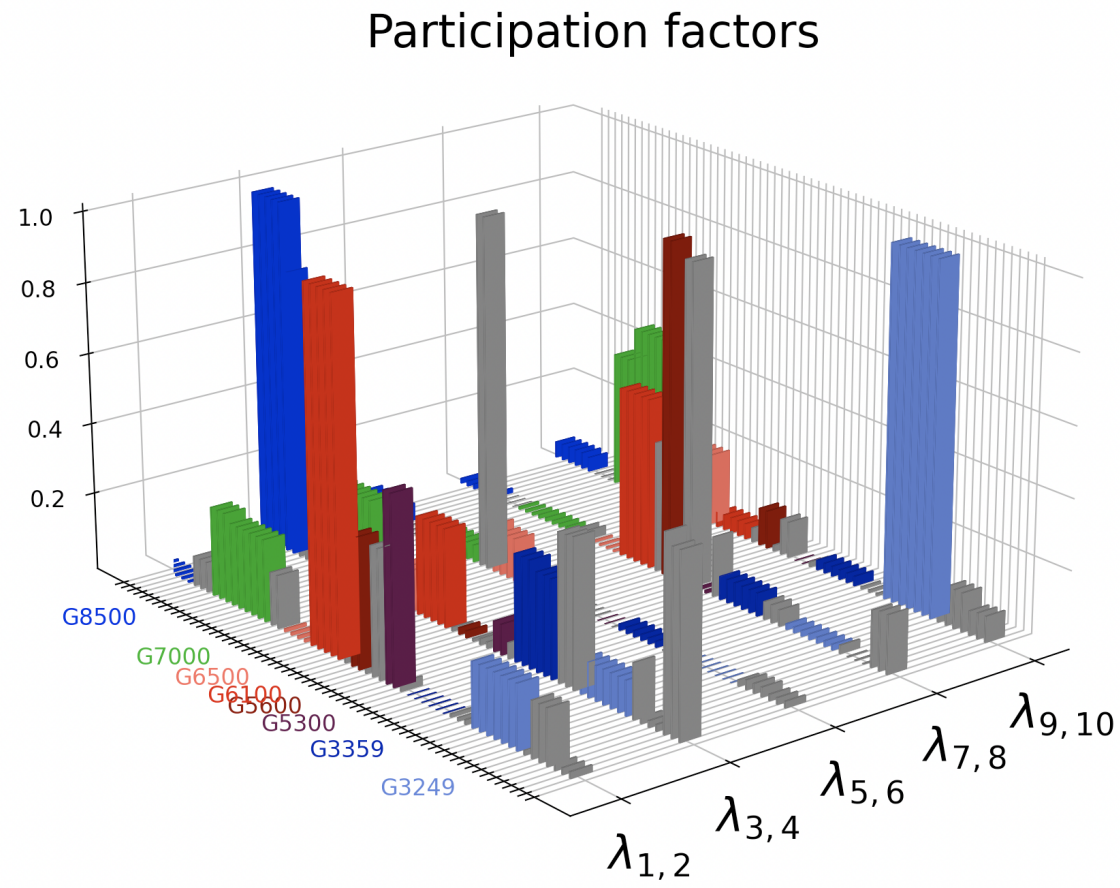

Figure 5.4: Magnitudes of the participation factors for the base case system. The numbering of the eigenvalues are ordered from lowest to highest damping ratio of the five eigenvalues of interest. The subscripts contain two indexes indicating that the eigenvalues appear in complex pairs, but only the positive frequency eigenvalues are shown in Figure 5.1.

From the theory presented in Section 3.2.3, one have that the right eigenvectors or mode shapes contains information about the observability of certain modes in the spe-

cific state variables. Thus, by interpreting Figure 5.2, one should expect the oscillatory mode of 0.37 Hz (lowest damped) to be mostly observable in the speed response of generator 6100, followed by generator 5300. As the green arrow (G7000) is essentially 180° shifted compared to the red arrow (G6100), one should expect the oscillatory response of speed at G7000 to be out of phase with the response in G6100. Thus, it should be clear that the poorliest damped mode having a frequency of 0.37 Hz is an inter-area mode as the west-coast of Norway will be oscillating against Finland[5.4]. In contrast, the mode having a frequency of 1.05Hz is a local area mode, as two generators (G6100 and G5600) being geographically in the same region (see Figure 4.5) is oscillating against one another.

Looking at the left-eigenvectors, it is evident that G6100 is not only the most observable generator, but also the most controllable. Thus, it should intuitively be clear from the theory in Section 3.2.3 that the participation factor corresponding to this generator for the mode of 0.37 Hz will be the largest for the mode of interest. This is observed in the participation factor plot in Figure 5.4. Hence, if only local controllers using local measurements were to be applied in the system, placing it close to G6100 should, in theory, have the largest dampening capabilities on this mode.

A simulation is conducted by increasing the load demand at load L6100-1 by 100MW at 1.0 seconds. It then decreases by the same amount at 1.05 seconds to showcase the troubles associated with this negatively damped eigenvalue. The sole purpose of the disturbance is to excite the oscillatory modes[5.5]. The speed responses of a few selected generators in the system are presented in Figure 5.5.

[5.4] Take a look at the system presented in Figure 4.5 to see the approximate geographical locations of the different buses in the system, alternatively in Appendix C.2 where a larger version of the system is presented in Figure C.1.

[5.5] Exciting the system for illustrating the response could in principle be done by any disturbance, for instance, a generator outage or short-circuit, but a load-change lasting for a short duration is seen to illustrate the general oscillatory response clearly.

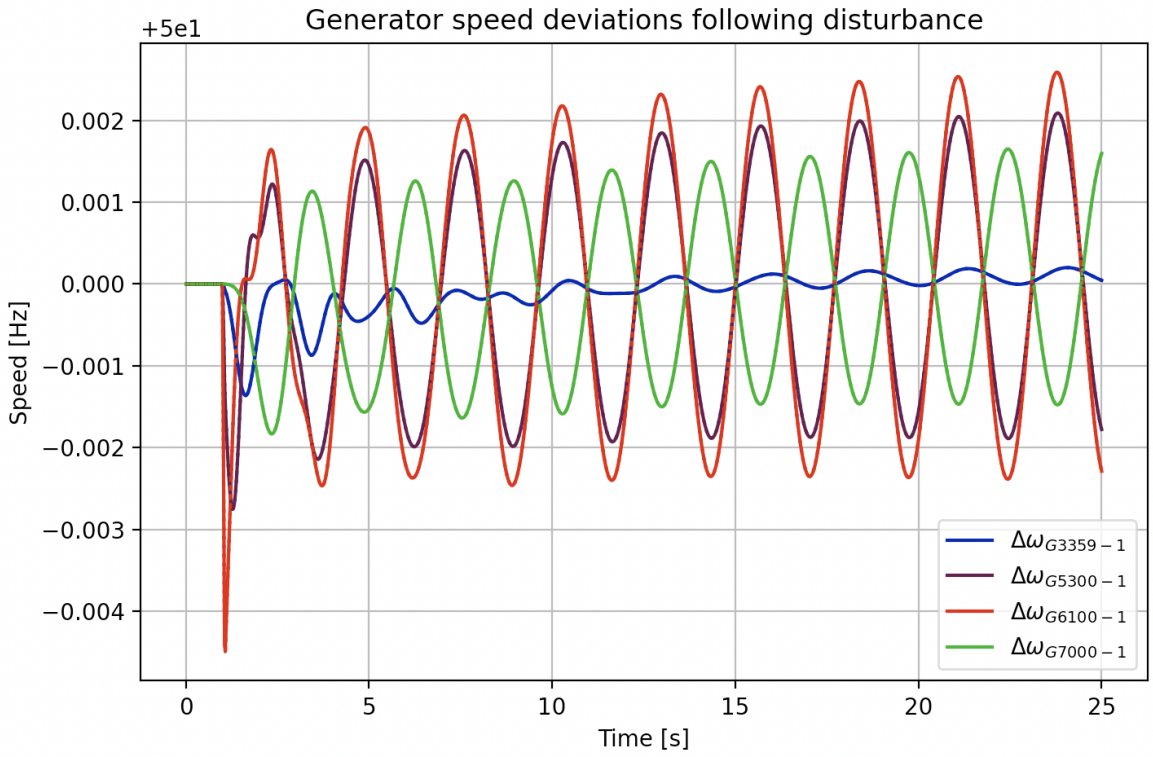

Figure 5.5: Speed response in the system for a few chosen generators following the disturbance.

From the simulation results presented in Figure 5.5 it is evident that the disturbance is exciting the system. Before the load change is applied ($t < 1.0$ seconds), the speeds of the selected generators are constant, reflecting the fact that the system is initially in a steady-state equilibrium point. After the load events are applied at $t = 1.0$ seconds and $t = 1.05$ seconds, the speed responses can be seen to be somehow distorted, reflecting the fact that it consists of the sum of all of the oscillatory modes with different frequencies. Eventually, most of these frequency components die out due to the amount of damping present at most eigenvalues in the system. Approximately at t = 5.0 seconds, the only noticeable frequency of oscillation left in the system is found to be 0.37 Hz. This frequency component is slightly increasing[5.6] during the entire duration of the simulation, which should be anticipated when knowing that the corresponding eigenvalue is located marginally right of the imaginary axis in the eigenvalue plot. Hence, the system will not return to the steady-state operational point, nor will it find a new operational point before the overall system collapses due to failure. The amplitude of the oscillations of the speed of G6100-1 is slightly larger than the amplitude of oscillations at G5300-1. This could be foreseen from the right eigenvector plot in Figure 5.2, as the arrow corresponding to G6100-1 is slightly larger than the arrow corresponding to G5300-1. The 180° phase shift between the speed at G6100-1 and G7000-1 anticip-

[5.6]The response is close to standing oscillations. Damping of 0.0% would correspond to standing oscillations. However, this eigenvalue is marginally in the right-half of the complex plane, thereby giving rise to moderately increasing system response.

ated by the mode shapes is also evidently seen in the speed responses present in as these are oscillating in counter phase. Notice how the speed response of G3359-1 stays relatively constant towards the end of the simulation after the majority of the excited modes have decayed to zero. This could be anticipated by the participation factor plot in Figure 5.4 together with the mode shape for this generator[5.7] in Figure 5.2, implying that the observability of the 0.37 Hz is almost non-observable at this generator.

The 0.37 Hz mode in the system response is also present in the power flows between different buses in the system. Figure 5.6 shows the power flowing between an important connection between Eastern Norway (bus 5101) and Western Sweden (bus 3359).

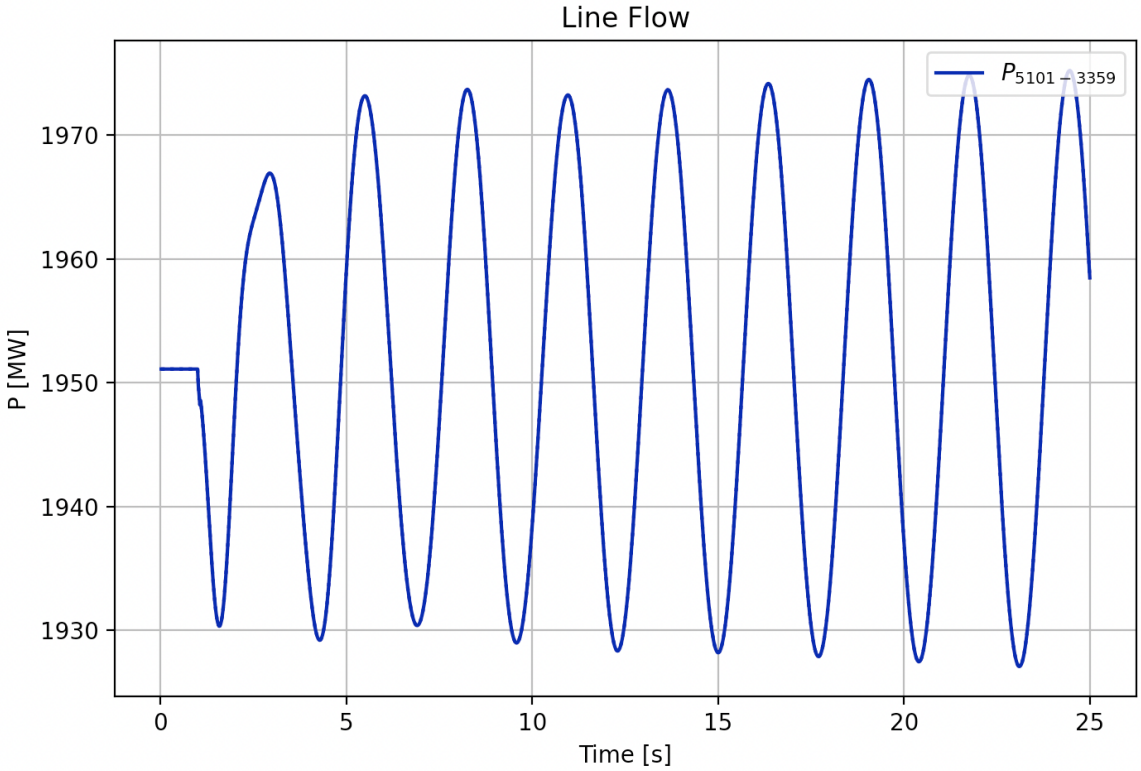

Figure 5.6: Power flow between bus 5101 (east Norway) and bus 3359 (west Sweden).

Similarly, as for the speed responses, the magnitude of oscillations in power flows increases when a pair of eigenvalues is located in the right half of the complex plane. Again, for a real-world system, this could relatively fast prove to exceed the thermal limitations in the power lines, potentially causing catastrophic results.

Based on the eigenvalues and the linear properties of this system, together with the non-linear simulation carried out, it should be clear that one is in desperate need of addressing the problem related to the poorly located pair of eigenvalues. Thus, the rest of this thesis will be focused on figuring out a good choice of BESS location, together

[5.7] The mode shape for this generator for the 0.37 Hz mode is close to zero, being the "arrow" located at the origo of the polar plot.

with an appropriate BESS controller feedback signal and controller parameter selection in an attempt to dampen out these oscillations. The theory presented in Section 3 will serve as a foundation for doing so, especially the theory covering the linearized properties of the system and transfer function residues. Therefore, the next section attempts to validate the residue implementation in Python to confirm that the implementation and corresponding results are as expected.

5.2 Validation of Transfer Function Residue Implementation

For the rest of the thesis, the transfer function residues will be of significant importance. Having this implemented correctly is of the most profound concern. To see whether the residue-way of finding the open-loop transfer function between an input u_i and output y_j in the system (discussed in Section 3.3.1) is implemented correctly, linear simulations based on calculated open-loop transfer functions are compared with non-linear simulation results. A linear simulation based on open-loop transfer functions should in theory correspond well with non-linear simulations for small disturbances from Equation (3.51). Therefore, if the linear simulations coincide desirably with the non-linear simulations, one could arguably conclude that the implementation of the transfer function residues is working as intended.

The simulations are conducted in Kundor's two-area system, where the input is chosen to be a load change at L2, P_{L2}, and the output is the terminal voltage at the corresponding bus θ_{B3}. An additional simulation including a feedback-loop connected BESS with arbitrarily chosen parameters using the terminal voltage angle θ_{B3} as feedback signal is included to see whether the transfer function residues calculation works as intended for changing system topologies. The setups without BESS and with BESS are shown in Figure 5.7a) and 5.7b) respectively.

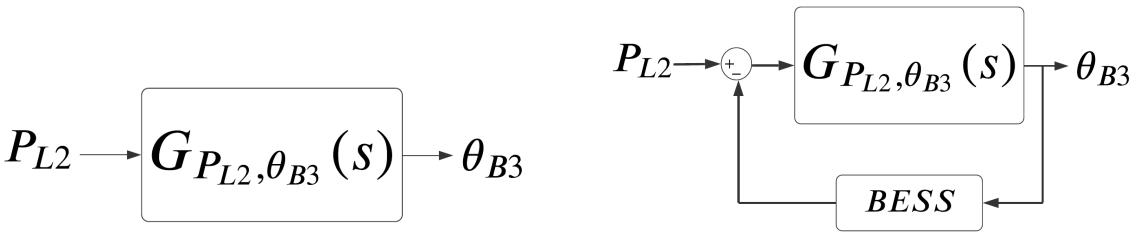

(a) Open-loop transfer function without any external feedback controllers.

(b) Transfer function from input to output with a BESS feedback controller.

Figure 5.7: The setup for the different simulations carried out for verifying the implementation of the residues by comparing linearized system response by the use of calculated open-loop transfer functions with non-linear simulation results.

Calculating the open-loop transfer function from the input to the output for the two different cases (without and with BESS) yields transfer functions of order 40, thus not given here[5.8]. Hence, to check whether these transfer functions accurately describe the dynamics between the input and output, a small step change is applied at L2 at t = 1.0 seconds before a new oppositely directed change is applied at t = 1.1 seconds, essentially being a small-signal disturbance in the system. Results for the linear simulations (dotted lines) and non-linear simulations (solid lines) are presented in Figure 5.8.

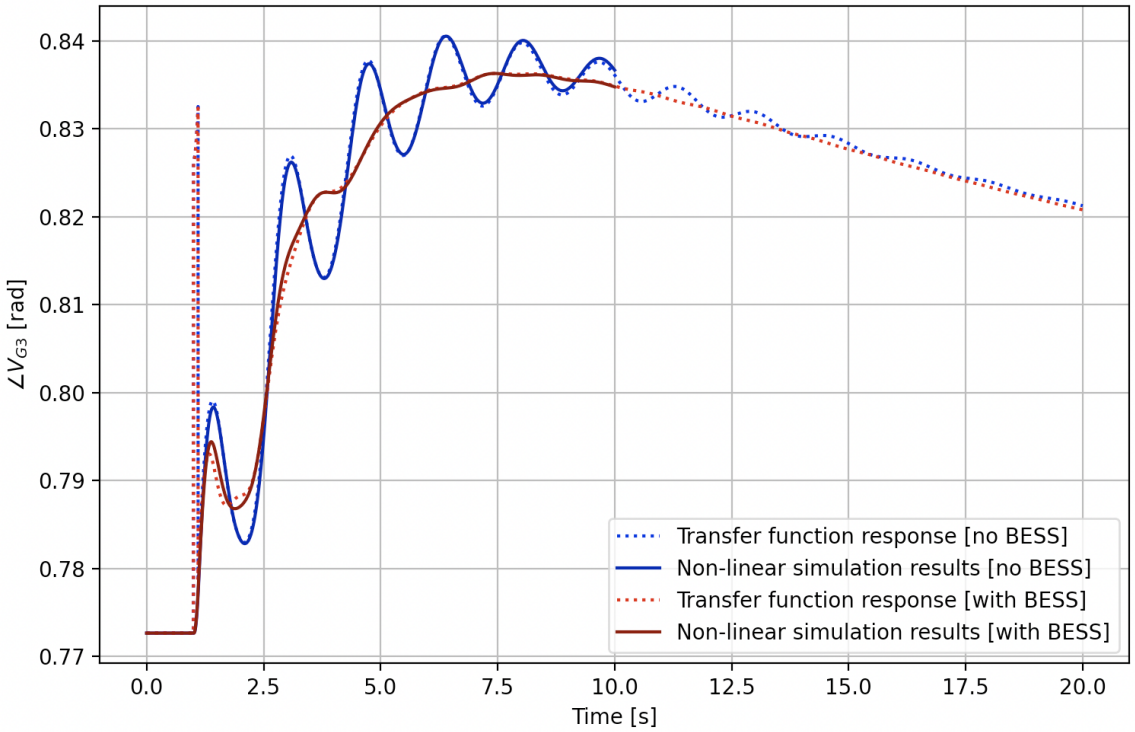

Figure 5.8: The time-domain simulation results for both non-linear simulations and simulations solely using the calculated open-loop transfer functions, both with and without BESS. The transfer function-based simulations are carried out twice the length of the non-linear simulations. It is evident that they can predict non-linear simulation responses.

Neglecting the responses during the time of disturbance from t = 1.0 to t = 1.1 seconds, one sees that the transfer function-based linear simulations coincide well with the non-linear simulations. This is the case both when BESS is included in the system and without BESS. Thus, as the solid blue line and the blue dotted line is overlapping, which is also true for the red lines, it is evident that the calculation of the transfer function between the input and output P_{L2} and θ_{B3} yields the expected response in the system when a small-signal disturbance is applied. Consequently, *the residue im-*

[5.8]The order of the open-loop transfer function is the same as the number of state variables in the system.

plementation works as intended.

When the transfer function is calculated, one also notices that this could effectively be used for having first-hand knowledge of the system response for a longer simulation period than what is being carried out in the non-linear simulations. Non-linear simulations use extensively longer computational time as these rely upon solving the entire set of differential and algebraic equations characterizing the system. Thus, the transfer function approach could be suitable if more extended simulations are required and limited computational resources are available. This last claim could especially be relevant to use for larger systems that use significantly longer time to compute if only some specific outputs are of interest for the user.

5.3 Feedback Signal and BESS Location Selection

5.3.1 Signal Selection

The residue implementation is now validated by the simulation carried out in Section 5.2[5.9]. The feedback signal selection is crucial to get the most out of the BESS to be installed. Assuming PMUs are installed in the system and all bus voltages in the system are measurable, the feedback signal is determined to be a difference between two terminal voltage angles in the system, $(\theta_x\text{-}\theta_y)$[5.10], as Jonsdottir et al. [35] found that voltage angles gave the best damping performance of the candidate feedback signals, while also being obtainable from PMUs. *The calculations carried out in this section and the next section for the base case system, aiming to select the optimal feedback signal and BESS location, are also carried out in two different versions of the Nordic 44 test network, and is provided in Appendix D.2 and Appendix D.3.*

In an attempt to select the optimal voltage angles in the system, the general procedure discussed in Section 3.4.1 would be to calculate the residue corresponding to the mode of interest for the different combinations of angles in the system. From the theory presented in Section 3.4.1, the feedback signal can be selected independently from the input location, as long as the same input location is considered for the different candidate feedback signals. Therefore, the input is simply denoted P_i, where P_i in principle could be the power input to any bus present in the system. The general procedure can be summarized by the Figure 5.9 and 5.10.

[5.9] A large number of additional simulations are carried out for verifying the implementation of the residues and the corresponding transfer functions due to the significance regarding feedback signal and location selection.

[5.10] The notation of j and $\hat{j}$ is switched with x and y for simplicity for this case, while also yielding more intuitive reading of the provided plot as will be seen.

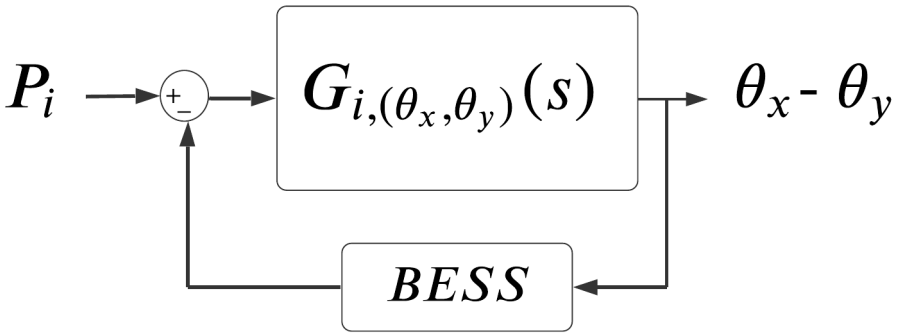

Figure 5.9: Open-loop transfer function $G_{i,(\theta_x,\theta_y)}(s)$ between an arbitrarily chosen bus power input P_i and output θ_x-θ_y, with a feedback controller named BESS.

The total open-loop transfer function $G_{i,(\theta_x,\theta_y)}(s)$ is excessive when deciding the optimal feedback signal. The important part, as discussed in the optimization problem given in (3.52), is to figure out which combination of voltage angles θ_x-θ_y yields the largest residue magnitude for the mode of interest, λ_{ia}. Hence, Figure 5.9 could be enlarged and represented as in Figure 5.10, where the part of concern is highlighted in a yellow rectangle.

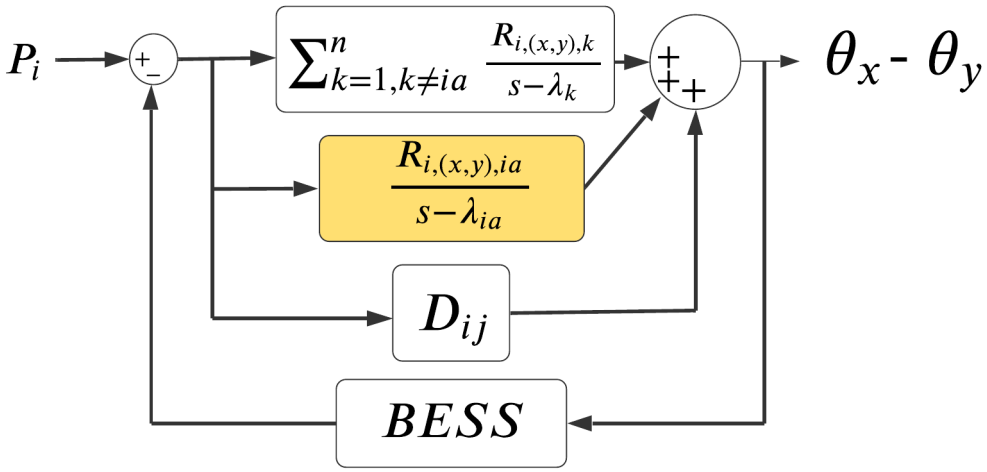

Figure 5.10: Transfer function between the input P_i and output θ_x-θ_y in an enlarged version. The yellow box is denoting the block associated with the mode of interest, λ_{ia}, and the feedback signal θ_x-θ_y maximizing $R_{i,(x,y),ia}$ is whats being looked after.

Thus, the objective is to maximize the residue related to the mode of interest $R_{i,(x,y),ia}$, by systematically checking the residues for the possible combinations of terminal voltage angles in the system for the given arbitrarily chosen input signal. The number of combinations to be checked will correspond to the number of generators in the system squared and then divided by two[5.11].

[5.11]Divided by two since taking the absolute values of $R_{i,(x,y),ia}$ and $R_{i,(y,x),ia}$ is the same, but the phases are 180° shifted.

The different feedback signal combinations with the calculated residue amplitude corresponding to the mode of interest (0.37 Hz) are shown in Figure 5.11. A colormap representation is chosen, as this allows for a simple, intuitive comparison of the residue magnitudes.

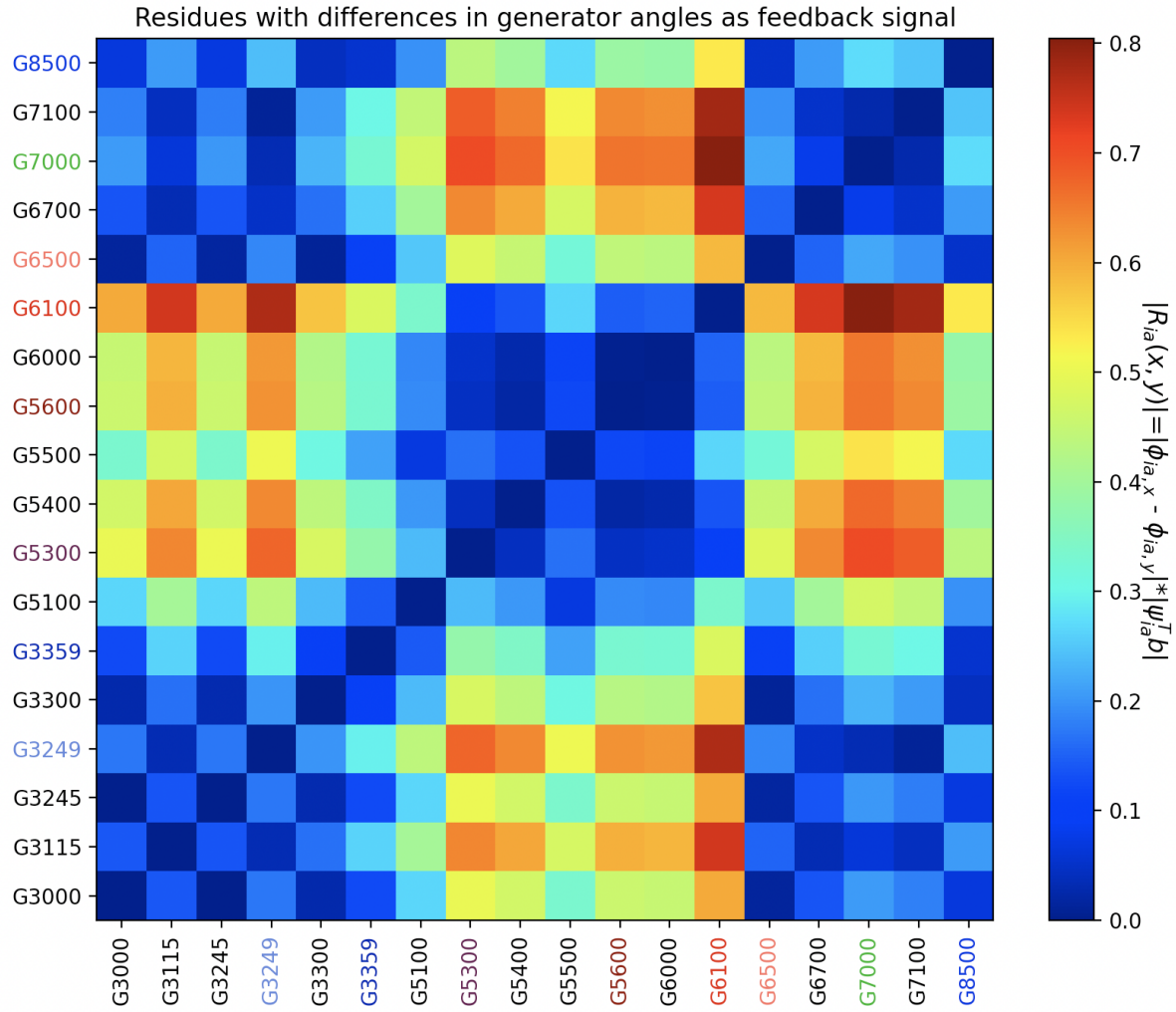

Figure 5.11: Colormap showing the residue magnitude for different feedback signal combinations, θ_x-θ_y. The combination giving the highest residue magnitude is a good choice of the feedback signal to the BESS. Buses containing more than one generator are represented by the first generator at this bus (for instance, *G*6100 is representing G6100-1) to reduce the size of the plot. This does not alter the results.[1]

[1] This does not influence the final result and has been validated by considering every single combination of generators. Buses containing several generators have essentially the same generator parameters as can be seen in the parameters presented in Appendix C.2

By interpreting the results presented in Figure 5.11, it is evident that using the difference between the voltage angle at bus 6100 and bus 7000, $\pm(\theta_{B6100} - \theta_{B7000})$, is a good choice of feedback signal as this corresponds to the difference in angles yielding the largest magnitude of the residue of interest. One also notices that the largest residues

generally tend to correspond to voltage angle combinations related to different areas in the system. This is expected, as the mode of interest, in this case, is an inter-area mode, and using signals from different areas tends to be good candidates for influencing such modes [64]. The plot presented in Figure 5.11 is symmetrically around the diagonal line going from lower left to upper right, whereas the amplitude of the diagonal elements is zero[5.12].

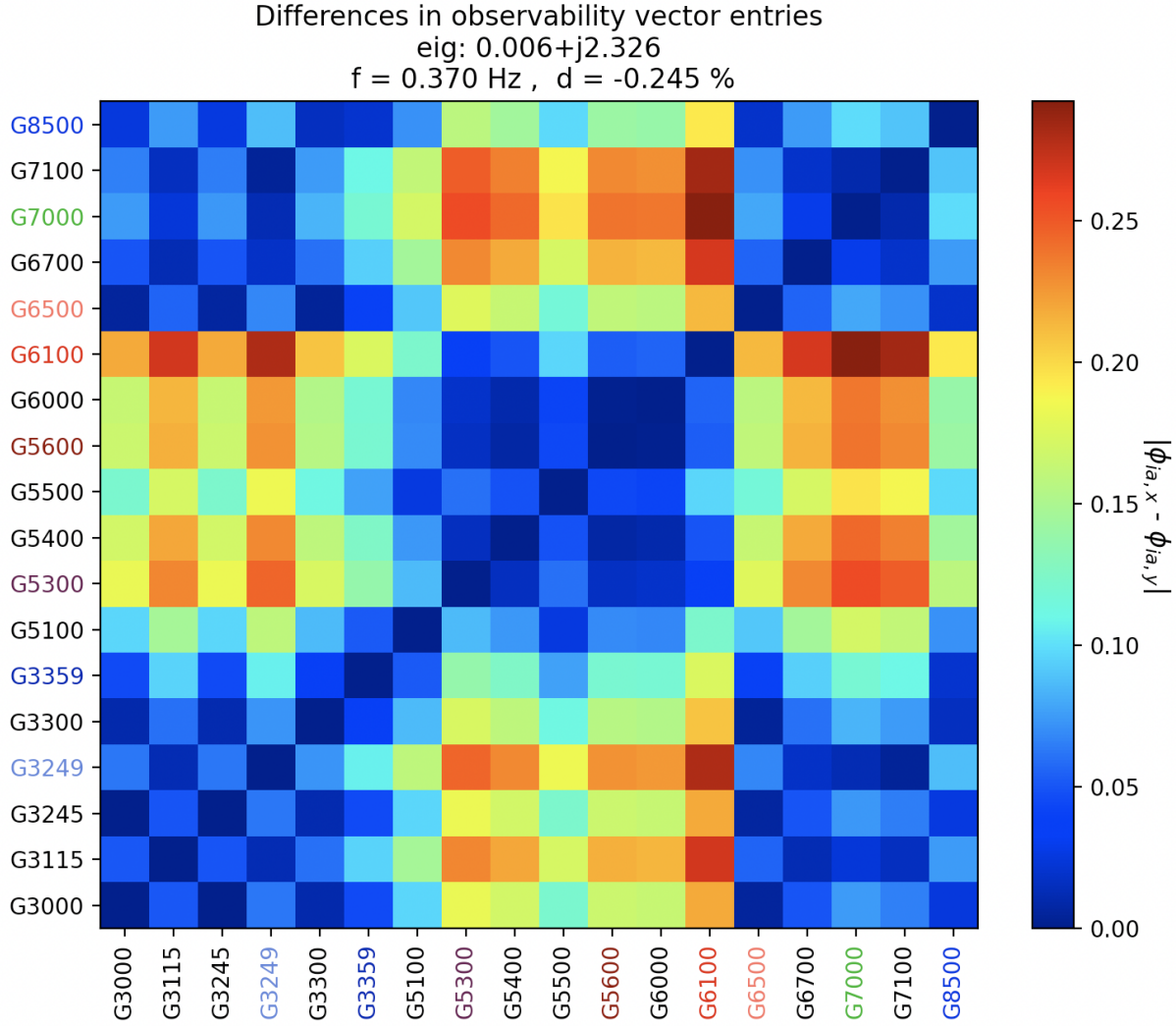

Figure 5.12: Colormap showing the absolute value of differences in observability vector (mode shape) entries.

A plot is also provided for differences in observability vector entries without considering the effect of controllability and input location to show that the simplification made in the theory section is valid. This is presented in Figure 5.12, which visually is exactly the same as residue magnitude plot Figure 5.11, but with different scaling. This is in accordance with the theory presented in 3.4.1, namely that accounting for the location of the BESS, represented by P_i, scales all the residues by the same amount, thus not

[5.12]Since the diagonal elements correspond to taking the angle at one bus and subtracting the same angle, for instance, θ_{G3000}-$\theta_{G3000} = 0$.

altering the relative differences between the magnitudes of the residues for the different feedback signals. Therefore, looking at differences in observability vector entries yields the same conclusion as the residue approach in deciding the optimal feedback signal based on maximizing the magnitude of the residue.

In a general case, one could be interested in selecting feedback signal combinations for other modes, for instance, a local-area mode. An example of this is provided in Appendix D.1.1, where the largest residues are strongly correlated with two specific buses in the system where the local-area mode are mostly observable.

5.3.2 Location Selection

The optimal feedback signal combination is selected in Section 5.3.1 to be a difference between the voltage angle at bus 6100 and bus 7000. A natural next step would be to determine a suitable location of the BESS to have it as effective as possible in terms of adding damping to the inter-area mode. The theory behind this, and the proposed optimization problem is presented in Equation (3.58) in Section 3.4.2.

Similarly, as for the feedback signal selection, this relies on changing the BESS location iteratively around in the system, and figuring out which open-loop transfer function between the input P_x and output θ_{6100}-θ_{7000} are having the largest magnitude of the residue corresponding to the inter-area mode, λ_{ia}. Hence, the feedback signal combination is fixed, and the problem reduces to determining the optimal location, P_x, where x denotes a bus in the system. The setup for this problem is similar to the problem considered in Section 5.3.1, and is presented in Figure 5.13.

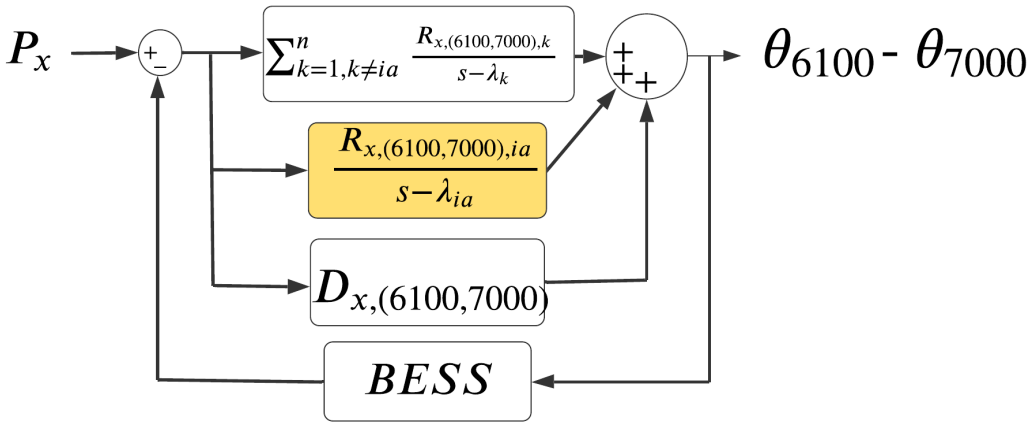

Figure 5.13: Setup for selecting the optimal BESS location. The feedback signal θ_{6100}-θ_{7000} is fixed, and the optimization problem aims at finding the location x such that the residue $R_{x,(6100,7000),ia}$ is maximized.

Considering the generator buses in the system[5.13], the result presented in Figure 5.14 is obtained:

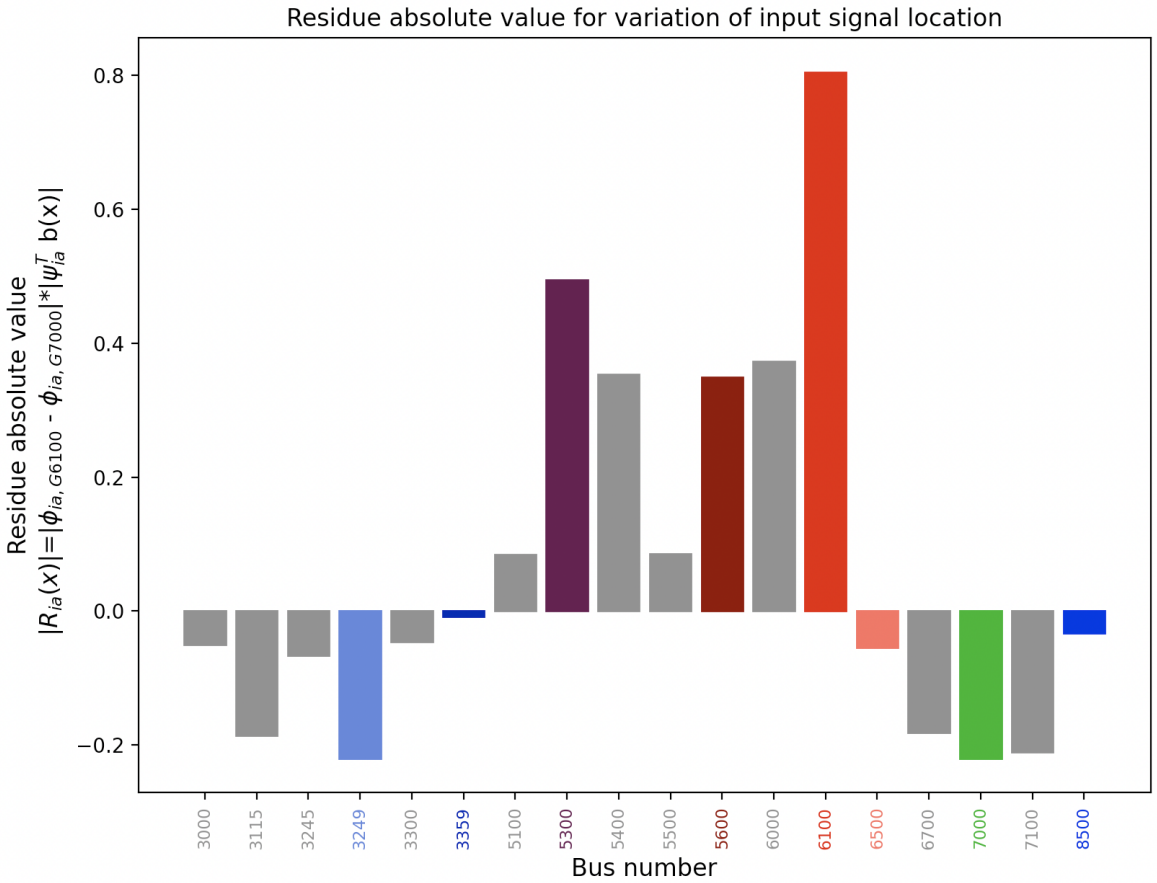

Figure 5.14: Residue magnitude related to the inter-area mode λ_{ia} for variations in BESS location. The vector b(x) (present in the y-axis label) is denoting the input vector b for BESS located at bus x in the system calculated by using Equation (3.7). The residues directed in the positive direction are in phase with the largest residue, whereas the negatively directed residues are oppositely directed in the complex plane.

Hence, it is evident that by using the optimal feedback signal found in Section 5.3.1, the optimal location of the BESS will be at bus 6100. Thus, two major things are now determined, stated below for easily being readable and also illustrated in Figure 5.15:

1. **Optimal feedback signal combination**: θ_{6100}-θ_{7000}.
2. **Optimal BESS location:** Bus 6100.

[5.13]Selecting the BESS location is a one-dimensional problem when the feedback signal is determined. When selecting feedback signals in Section 5.3.1, a difference between two signals were considered, thereby yielding a two-dimensional solution space.

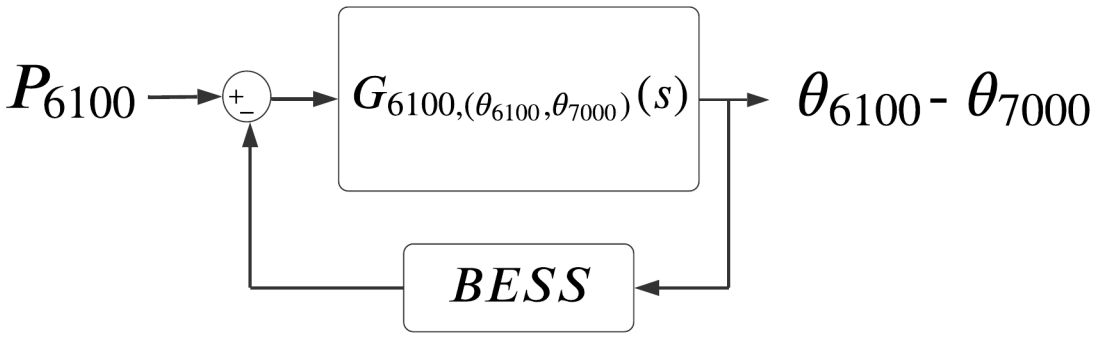

Figure 5.15: Block diagram illustrating the optimal feedback signal combination θ_{6100}-θ_{7000} and location bus 6100. The BESS-block is accounting for both the BESS-model transfer function and the associated control system.

When both the feedback signal combination and BESS location are determined, a natural way to proceed would be to account for the actual residue amplitude and phase shift to design an appropriate controller. The directions and magnitudes of the residues for the different candidate locations are presented in Figure 5.16.

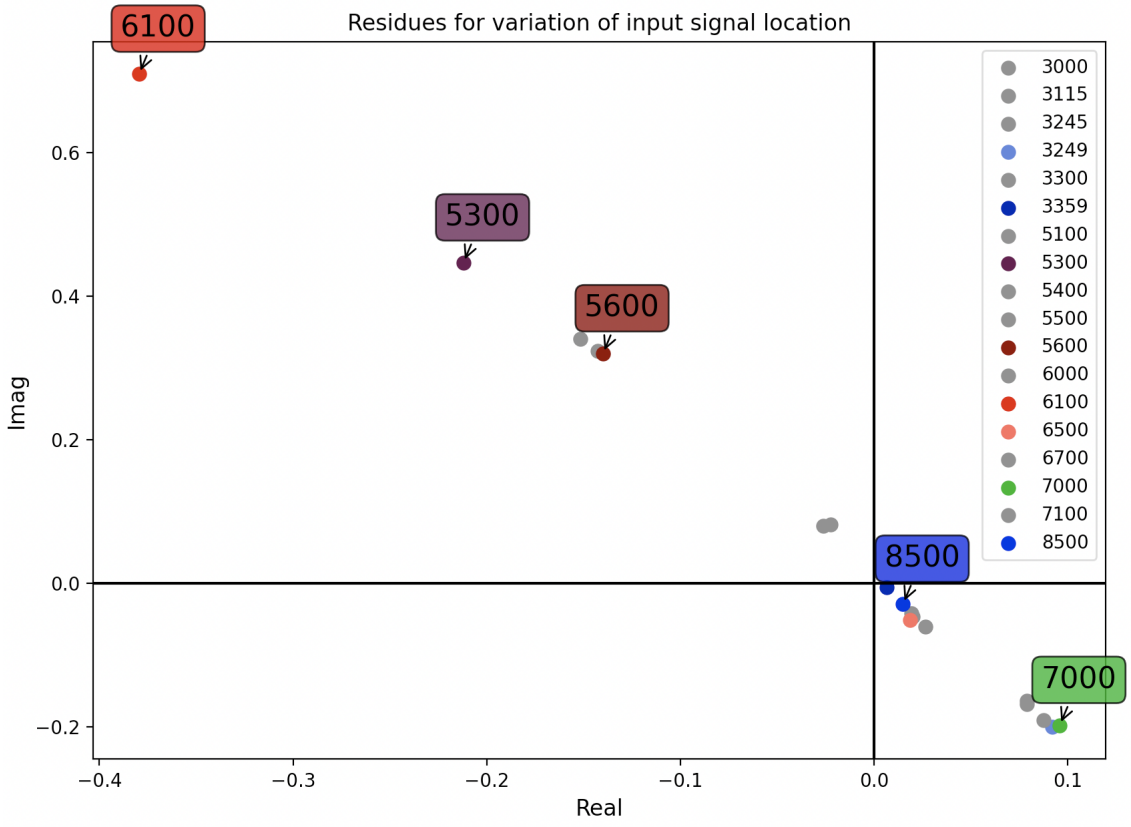

Figure 5.16: Residue variations in the complex plane for different BESS locations when the feedback signal (θ_{6100}-θ_{7000}) is fixed, containing information about residue magnitudes and phase shifts.

From Figure 5.16, one have that the largest residue (BESS at Bus 6100) is directed

left-wards in the complex plane. Hence, based on the theory presented in Section 3.3.2, a proportional feedback controller would move the mode of 0.37 Hz in the direction anticipated by the red dot. Therefore, as it is generally undesirable to alter the frequency of the oscillatory mode[5.14], phase compensation is needed in the feedback controller for moving the mode straight left-wards in the complex plane, which will be considered in the upcoming section.

5.4 Feedback Controller Parameters Tuning

At this point, both the feedback signal combination and BESS location is determined. Hence, the next step would be to decide the controller parameters needed in order to move the eigenvalue leftwards in the complex plane. The overall control loop is given in Figure 5.17.

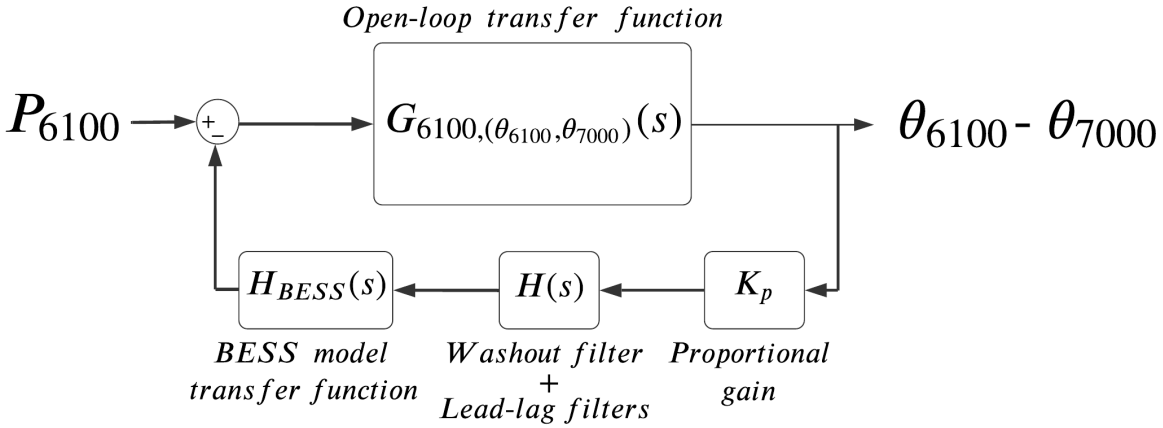

Figure 5.17: Battery controller and BESS-model in the feedback loop from the selected feedback signal and location determined in Section 5.3.1 and Section 5.3.2, respectively. The Figure is essentially the same as Figure 5.15, but the BESS-block is enlarged to illustrate the BESS-model and the associated controller independently. The proportional gain factor K_p is given as an individual block as it does not influence the phase shift of the controller [58], hence this value will be determined separately.

5.4.1 Selection of BESS Parameters

The BESS parameters used while conducting simulations are important and heavily influence the amount of damping obtainable from the BESS as seen in Equation 4.20. For this thesis, the effects of the different BESS model parameters are not covered

[5.14] A change in the imaginary part of the mode corresponds to change in modal frequency as per Equation (3.33).

deeply, as this is conducted in the preceeding spezialization project, and will essentially only cause slightly different choices of controller parameters. Hence, the parameters are pre-determined, and the essential ones are set as follows:

Table 2: Fixed BESS parameters

p_{max} [kW]	n_{par}	n_{series}	T [sec]	T_{dq} [sec]
245	12	1	0.035	0.035

The parameters are described in Section 4.5, but essentially p_{max} is the power rating of the individual batteries chosen in the power region of commercially available Tesla Powerpacks [76], n_{par} and n_{series} are number of parallel- and series-connected batteries in the BESS model, respectively. Consequently, the total rating of the BESS affecting the feedback loop gain response is close to 3 MW, but the available power depends on the state-of-charge. Furthermore, due to the time constants representing delays in the input signal, T, and converter dynamics, T_{dq}, some internal phase shifts of the BESS model should be expected and thereby accounted for when designing the feedback controller.

5.4.2 Parameter Tuning for Desired Phase Compensation

A conventional control system for providing Power Oscillation Damping (POD) to power systems are utilizing a washout filter, lead-lag compensates and a proportional gain constant [45], [48], [50]. The washout filter, $sT_{wash}/(1 + sT_{wash})$ is included to remove the steady-state and low-frequency signal inputs to the controller. A common choice of the parameter T_{wash} is 10 seconds when considering inter-area oscillations [85], which will also be used for this controller, even though other values in the region 1-20 seconds might be suitable [86]. Thus, as the inter-area mode of interest has a frequency of 0.37Hz, the washout filter will only have minimal effect on the gain and phase shift.

$$\begin{aligned} H_{wash}(s) &= \frac{sT_{wash}}{1 + sT_{wash}} \\ |H_{wash}(j2\pi 0.37Hz)| &= \frac{2\pi 0.37Hz * 10s}{\sqrt{1 + (2\pi 0.37Hz * 10s)^2}} \approx 1 \\ \angle H_{wash}(j2\pi 0.37Hz) &= 90° - 87.54° = 2.46° \approx 0° \end{aligned} \tag{5.1}$$

The BESS model itself is responsible for some phase shifts. This is related to the first-order time-delays incorporated in the input signal and current components injected into the grid, which can be seen from the BESS model implementation presented in Section 4.5. Hence, when plotting the eigenvalues for different phase shifts, the straight

lines indicating a constant phase shift are accounting for this internal shift in the BESS model. *That is, the line indicating* 0° *phase shift does not exactly correspond to the residue direction but is slightly skewed to account for the inner dynamics present in the BESS-model.* This is done in order to see the relative accuracy of the estimated phase shifts for different targeted phase shift by having a starting point that falls exactly on the 0°-line for small gains. For a proportional gain value of $K_p = 2.0$ and having the lead-lag blocks, $(1 + sT_1)/(1 + sT_2)$, using parameters such that there is no additional phase shift ($T_1 = T_2 \approx 0$), the internal phase shift is found to be 5.05°, which is how much the original residue direction is shifted. Doing an iterative simulation where the feedback controller gain at the frequency of interest ($K_p|H(j2\pi0.37)|$) is held constant for different targeted phase shifts (or different values of T_1 and T_2), the results provided in Figure 5.18 is obtained.

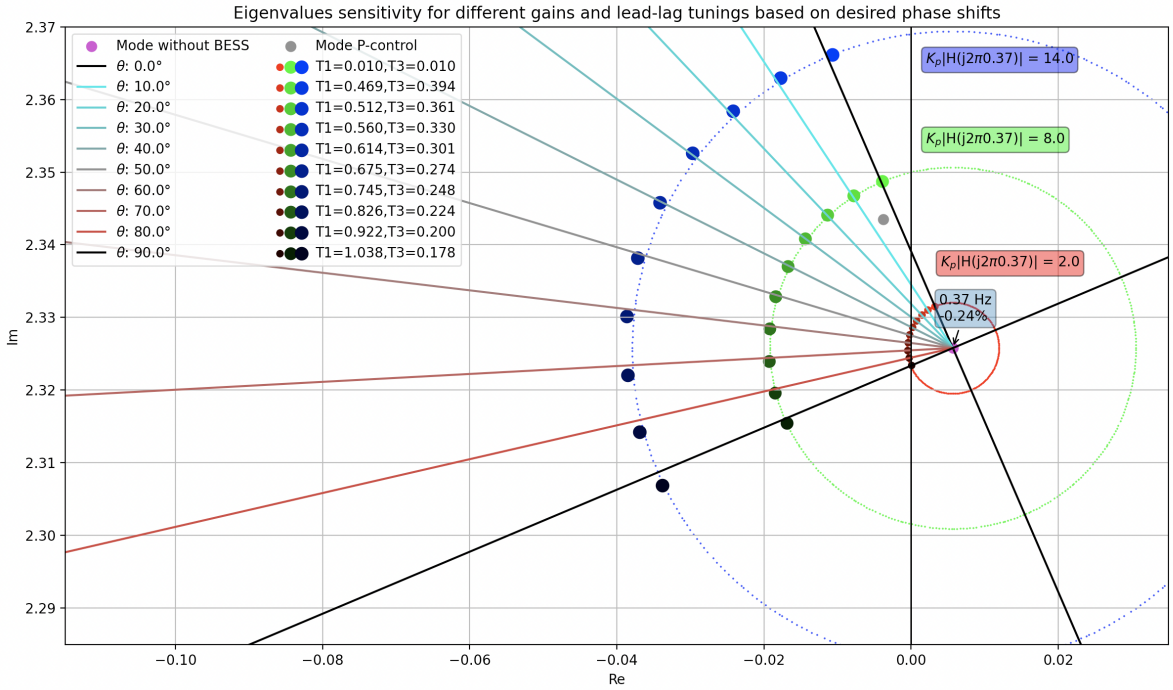

Figure 5.18: Eigenvalues for different controller gains and targeted phase shifts. The colored circles surrounding the initial mode position indicates points where the controller gain $K_p|H(j2\pi0.37)|$ is held constant. The original direction anticipated by the residue is shown as a gray dot indicates the mode movement if a simple proportional feedback controller is used, without accounting for the inner dynamics of the BESS-model and the associated phase shifts. This dot/direction is the same as the residue direction of BESS at Bus 6100 from Figure 5.16.

It is clear that for different gain values (although all of them are in principle very small), the different phase shifts targeted by the tuning of the lead-lag blocks is well capable of predicting the new modal position. Ideally, all the blue dots (mode positions for the largest gain) would fall on the dotted blue circle (constant gain) and the targeted

phase shift straight lines, and the same thing goes for the green and red modes. This is somehow accurate but not necessarily perfectly fitting. To illustrate this more clearly, a plot is provided in Figure 5.19 to see the relation between the targeted and actual phase shifts.

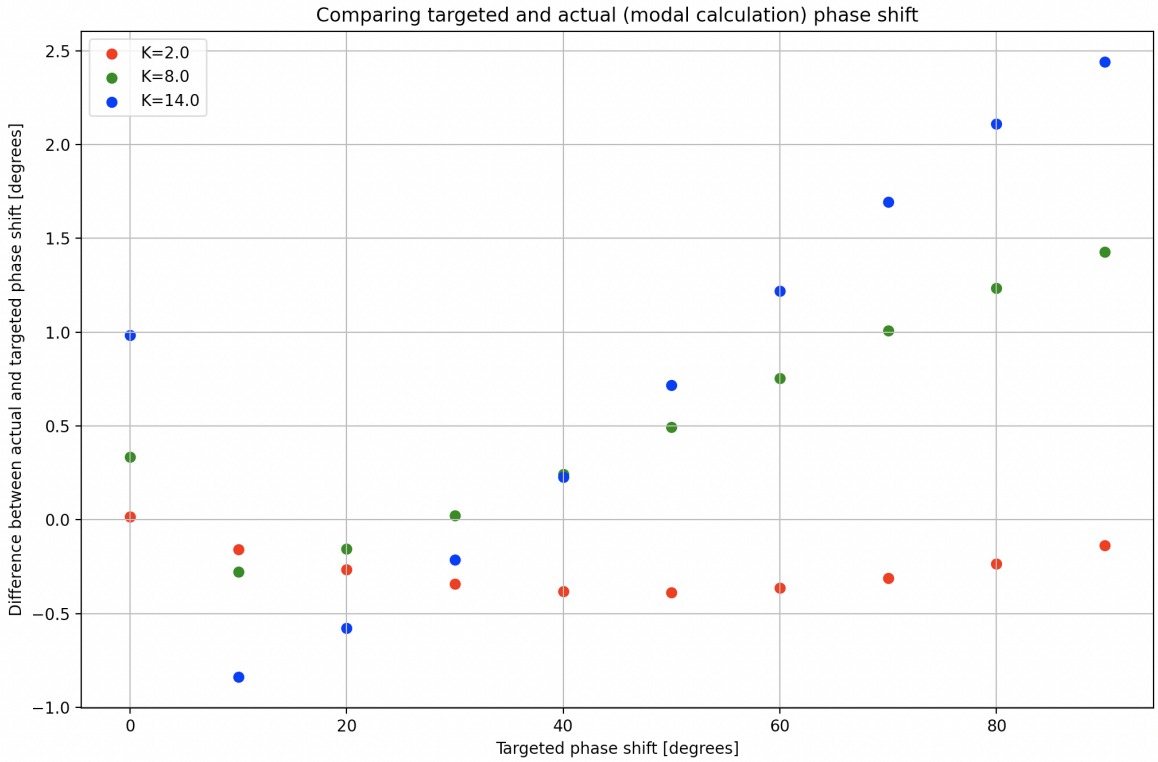

Figure 5.19: Difference between the targeted and actual phase shift for different parameter gains and targeted phase shifts (x-axis). Notice how the difference between actual and targeted phase shift for K=2 and targeted phase shift of 0° is 0°, as this is made the relative starting position of the 0°-line in Figure 5.18 to account for the internal BESS model phase shifts.

It is evident that the targeted phase shift and actual phase shift are correlating significantly better when the lowest gain is used, and the deviation between these increases for higher gains and larger targeted phase shifts. This corresponds well with the theory behind residue sensitivity provided in Section 3.3.2, which states that the mode movement given a feedback control is valid for small gains only, and deviations should be expected for larger gains.

To further investigate the results from Figure 5.18, a BODE-diagram is provided in Figure 5.20 where the mode shift from large gains is plotted in the phase response of the BODE-diagram too see how well it corresponds with the phase compensation of the controller.

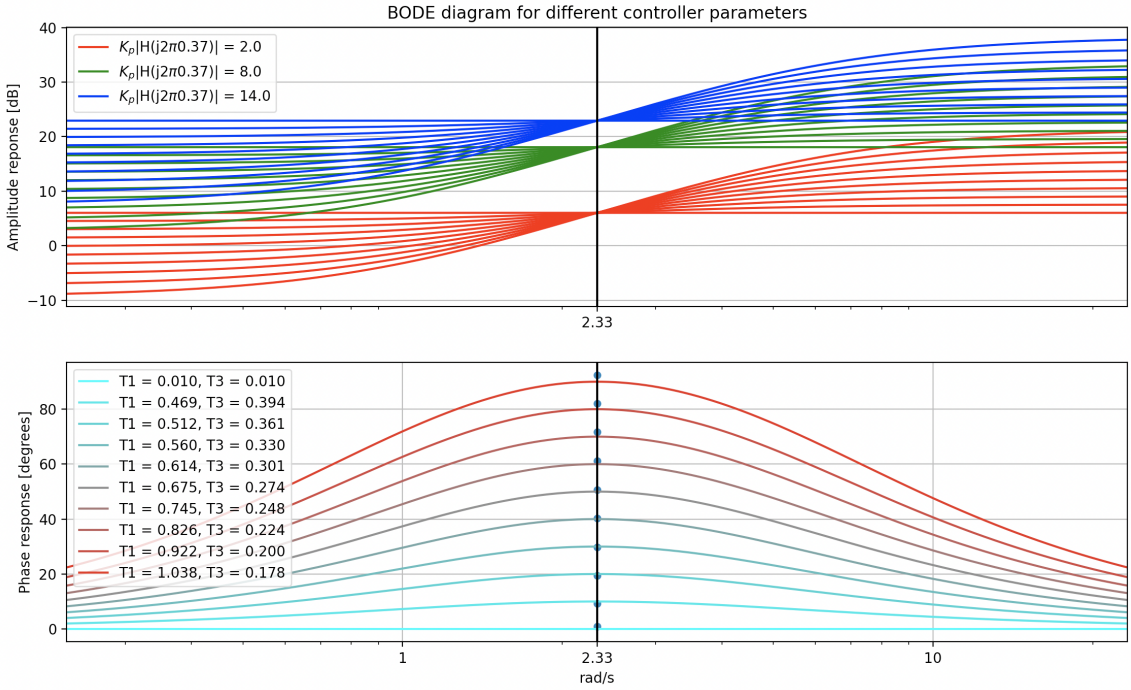

Figure 5.20: BODE-diagram for different parameters of the lead-lag filters and proportional gain constant K_p. The product $K_p|H(j2\pi0.37)|$ is held constant for the three different gains considered, such that regardless of the desired phase shift of a given gain, the gain response at 0.37Hz (2.33 rad/s) is the same. This should be seen in relation to the colored circles in Figure 5.18, indicating constant controller gains. The dots in the phase response indicates the actual phase shift for the given mode for the largest investigated gain, which can be seen to fall approximately on the desired phase shifts indicated by the points of which the curves cross the vertical line at 2.33 rad/s (0.37Hz).

From the BODE-diagram given in Figure 5.20 it is clear that the amplitude/gain response collapses at the frequency of the inter-area mode, 2.33 rad/s, which essentially was a criterion made when selecting the parameters and especially the proportional gain constant K_p for creating the plot shown in Figure 5.18, such that all modes would end up approximately the same Euclidean distance away from the original modal positions. It should be evident that the tuning of the lead-lag blocks presented in Section 3.5 together with the information about the residue presented in Section 3.3.1 is capable of moving the critical mode away from its initial position by appropriately selecting the feedback controller parameters based on the desired phase shift, but some inaccuracy is seen for larger gains.

In terms of deciding the actual parameters to be used for the BESS-controller, a closer look should be taken into Figure 5.18. For the given system, the chosen BESS-location and feedback signal, it can be seen that in order to move the mode leftwards in the complex plane, a phase shift somewhere in the region of 60° to 70° relative to the

initial direction suggested by the residue should yield a satisfactory result. However, this will depend on the amount of damping which is desired, as it could be seen in Figure 5.19 that the accuracy of the proposed tuning method depends on the desired gain. Choosing a phase shift of 60° initially, and then moving on by figuring out the amount of gain needed.

5.4.3 Proportional Gain Parameter for Obtaining a 5% Damping of the Critical Mode

By Equation (3.3.2), the change in the eigenvalue will be a product of the total feedback transfer function and the residue related to the mode of interest for the analysis. The total feedback transfer function will consist of both the internal BESS-model transfer function, the feedback controller aiming at a desired phase shift $H(s)$ and the proportional gain factor K_p, where the latter one is the one to be determined for obtaining the desired eigenvalue movement in the system. Since the phase shift needed for shifting it leftwards is determined, one are only interested in the magnitude of change as of now. By using Equation (3.42) and rewriting the term $H(\omega_i)$ to include the different controller blocks present in the feedback controller seen in Figure 5.17, one have

$$|\Delta\lambda_{ia}| = K_p|H_{bess}(s)||R_{ia}|\left|\frac{sT_{wash}}{1+sT_{wash}}\right|\left|\left(\frac{1+sT_1}{1+sT_2}\right)\right|^2\Bigg|_{s=j2\pi 0.37}, \tag{5.2}$$

where R_{ia} is the residue value for the chosen loop for the given inter-area mode, K_p is the proportional gain to be determined, $|H_{bess}(s)|$ is the gain due to the inner dynamics of the battery model discussed in Section 4.5 and the two last expressions are the washout and lead-lag compensators amplitude gains at the frequency of interest, respectively. Rearranging gives that for a desired change in the eigenvalue, the proportional gain parameter can be determined by

$$K_p = \frac{|\Delta\lambda_{ia}|}{|H_{bess}(s)||R_{ia}|\left|\frac{sT_{wash}}{1+sT_{wash}}\right|\left|\left(\frac{1+sT_1}{1+sT_2}\right)\right|^2\Big|_{s=j2\pi 0.37}} \tag{5.3}$$

For many applications it is desirable to have at least 5% damping of the critical mode, as this yields satisfactory damping for most systems while providing some margins in the system [54]. This will be the chosen damping to aim for in this application too. Consequently, as the initial value of the mode is $\lambda_{ia,0} = \alpha_{ia,0} + j\omega_{ia,0} = 0.005695 + j2.3257$, the real value of the new modal position can be found by using Equation (3.32) and having the imaginary part (frequency) of the mode to be constant

$$\alpha_{ia} = -\sqrt{\frac{\zeta^2\omega_{ia,0}^2}{\sqrt{1-\zeta^2}}} = -\frac{0.05 * 2.3257}{\sqrt{1-0.05^2}} = -0.116, \tag{5.4}$$

where the negative solution of the square-root equation is used as the mode is intended to be moved to the left-half of the complex plane. This corresponds to a change in the mode of

$$|\Delta\lambda_{ia}| = |\lambda_{ia} - \lambda_{ia,0}| = |\alpha_{ia} - \alpha_{ia,0}| = 0.1218. \tag{5.5}$$

- The desired mode change is established, and from (5.1) one have that the washout block contributes to a gain of approximately 1.0 at the given frequency when $\underline{T_{wash} = 10 \text{ sec}}$.
- For an **initially chosen**[5.15] phase shift of 60°, the lead-lag parameters can be found from Figure 5.18 to be $\underline{T_1 = 0.745}$ and $\underline{T_2 = 0.248}$. Thus, the two lead-lag blocks contributes to a total gain of 3.0 at the given frequency by using Equation (3.60) with $m = 2$.
- The residue value $|R_{ia}|$ can be read from Figure 5.14 to be $\underline{|R_{ia}| = 0.804}$.
- Lastly, one need to determine the value of $|H_{bess}(j2\pi 0.37)|$. As can be seen in Section 4.5.3, this value will depend on the individual battery ratings, the number of batteries series and parallel connections, the apparent power rating in the system, and the scheduled voltage (in p.u.) at the bus of which the BESS is connected. One could utilize the formula presented in the battery section if accounting for the apparent generator ratings of the generators connected at the bus of which the BESS is connected (Bus 6100). For convenience, this conversion factor is found by running a simulation and using the fraction of the battery power signal relative to the battery input signal of the BESS. Doing so, this value is found to be $\underline{|H_{bess}(j2\pi 0.37| = 0.00402}$. This value might seem low initially, but remember that the power system base rating is 1000 MVA, and the batteries are only rated a couple of hundreds kW. And, currently, the BESS system consists of an equivalent of 12 parallel connected batteries, such that this conversion factor should be reasonable.
- For a 5% targeted damping having the lead-lag parameters tuned to give a phase shift of 60°, the proportional gain factor K_p is calculated to be $\underline{K_p = 12.56}$ by Equation (5.3) for this specific operating point of the system.

In order to see how well this targeted gain shift is predicting the new position of the mode, the K_p values is calculated for targeting 1% and 3% damping in addition to the desired damping of 5%, giving the values of $K_p = 2.98$ and $K_p = 7.67$ by using Equation (5.3) and (5.4). The simulation is carried out for phase shift targets in the region $[60°, 70°]$ with steps of 2°, and the results can be seen in Figure 5.21.

[5.15] Will be slightly changed later to account for the deviations between the actual and desired phase shifts at the chosen gain.

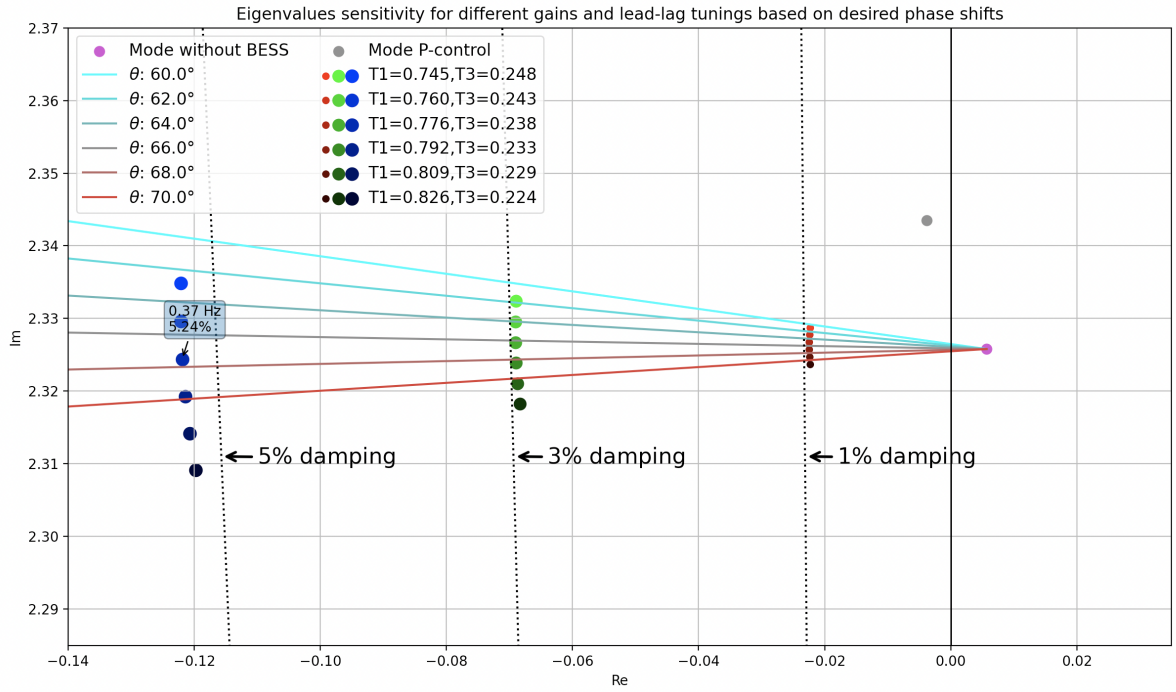

Figure 5.21: The new modal positions for proportional gain factors calculated to be $K_p = [2.98, 7.67, 12.56]$ for targeting a damping of 1%, 3% and 5% respectively based on Equation (3.42). The results are shown for different phase shifts and the proportional gain is slightly adjusted for each simulation to account for the increased gain response of the lead-lag blocks when parameters are selected for providing larger phase shifts.

From the results seen in Figure 5.21, it is evident that the proposed way of deciding the proportional gain parameter seems to yield a suitable solution. For all three of the targeted dampings (1%, 3% and 5%), deciding K_p in the proposed way yields decently accurate results. However, it can be seen that when 5% damping is desired, the K_p parameter is slightly underestimating the mode shift, causing marginally better damping than anticipated. This is not of major concern, as larger damping is generally desired, and the deviation between the targeted and actual damping is thus deemed insignificant. One also notices that the deviation between the phase shift that is being aimed for and the actual phase shift is larger the greater the gain is. The errors between the targeted and actual phase shift for different phase shifts and amplitude gains is shown in Figure 5.22.

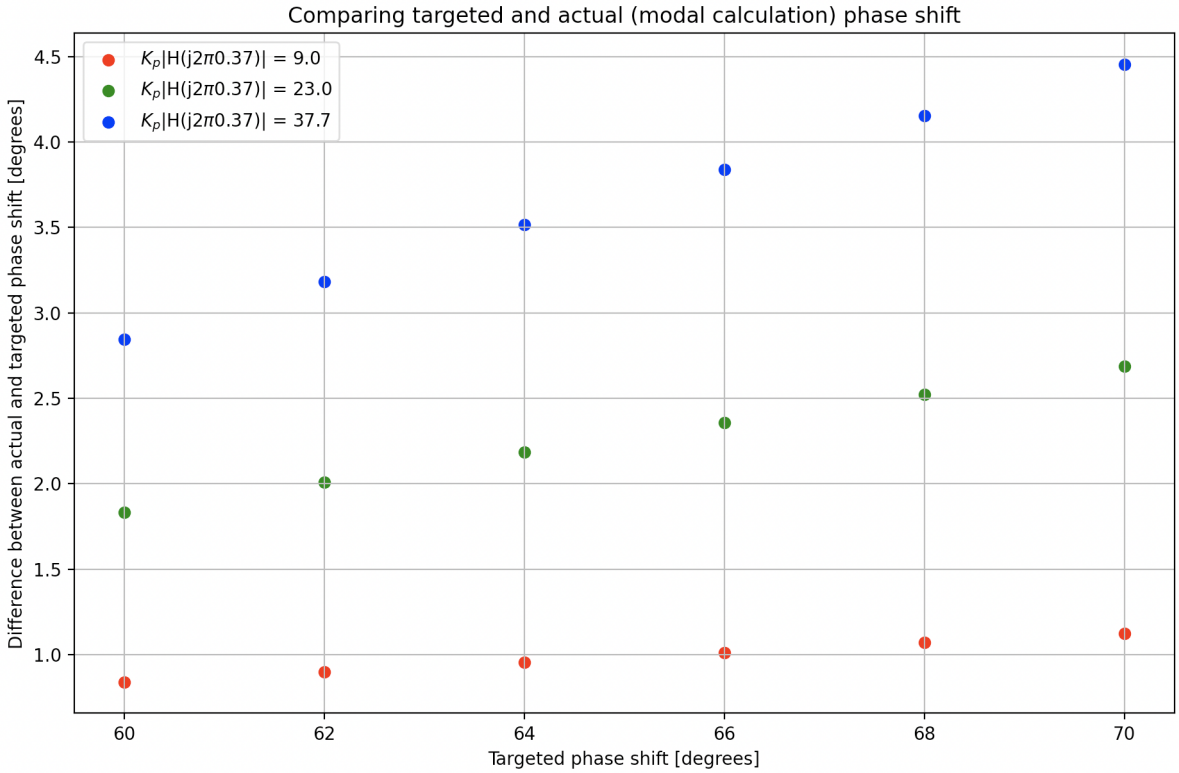

Figure 5.22: The difference between the targeted and actual phase shift for different proportional gain constants aiming for 1%, 3% and 5% damping. The larger the proportional gain (and thereby desired damping), the larger is the error in the targeted phase shift.

One of the modes in Figure 5.21 is marked with a text-box stating (0.37Hz, 5.24%). Relative to the initial position of the mode, this mode is seen to be located approximately at the same imaginary value (frequency), but moved by a desirable amount left-wards in the complex plane. Therefore, as this mode is mode number three when counted downwards (the blue modes), this corresponds to a phase shift of 64°. For a 64° targeted phase compensation of the lead-lag blocks, the actual compensation is found to be 68.5° by adding the difference between targeted and actual phase compensation in Figure 5.22 at a target of 64° and damping approximately equal to 5%. The lead-lag block is yielding a slightly higher amplitude gain for larger phase shifts[5.16], hence the original proportional gain constant $K_p = 12.56$ would have to be modified slightly to

[5.16] See Equation (3.60).

account for this.

$$\begin{aligned} K_{p,final} &= K_{p,0} \frac{\left|\left(\frac{1+sT_1}{1+sT_2}\right)\right|^2\Big|_{60°, s=j2\pi 0.37}}{\left|\left(\frac{1+sT_1}{1+sT_2}\right)\right|^2\Big|_{64°, s=j2\pi 0.37}} \\ &= 12.56 \frac{\left|\left(\frac{1+s0.745}{1+s0.248}\right)\right|^2\Big|_{s=j2\pi 0.37}}{\left|\left(\frac{1+s0.776}{1+s0.238}\right)\right|^2\Big|_{s=j2\pi 0.37}} \\ &= 11.56 \end{aligned} \tag{5.6}$$

Thus, the proportional gain should be chosen to $\underline{K_p = 11.56}$ when a phase compensation of 64° is to be appended by the lead-lag blocks.

To further showcase how the residue sensitivity approach fails when gains get large, the feedback controller gain is changed in steps from 0 to 50, where $K_p = 11.56$ is the value chosen for this application and the lead-lag filters are fixed to provide 64° phase compensation. The results are shown in Figure 5.23.

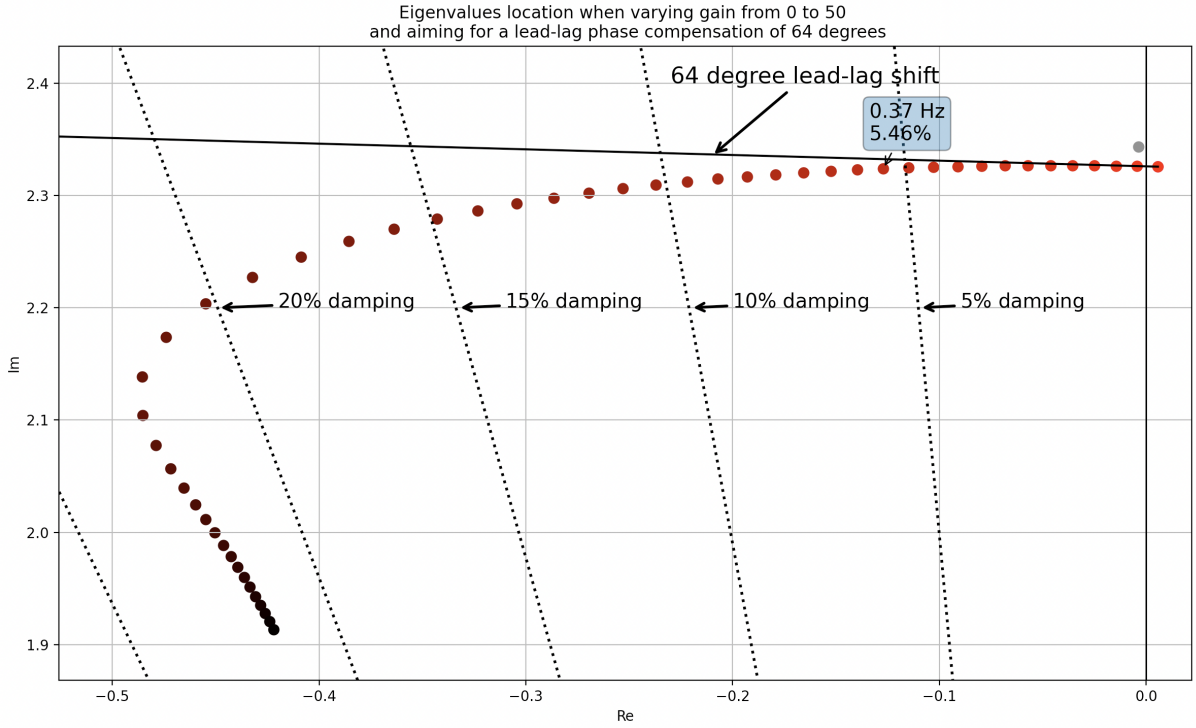

Figure 5.23: Inter-area mode of interest for different proportional gain constants K_p in the region [0, 50]. For small gains, the modes is located relatively accurately on the straight line anticipating the phase compensation of the controller. However, for larger gains, the mode movement is not following the anticipated direction of 64∘ relative to the residue direction, as the assumptions used for deriving Equation (3.41) ($K_p \to 0$) is not valid for such cases. The mode marked with a text-box (0.37Hz, 5.46%) corresponds to $K_p = 12$, which is close to the chosen value of $K_p = 11.56$.

From Figure 5.23 it is clear that for the larger gains the residue approach fails, and the method should be used with caution if large relative movement of the modal position is required. Nevertheless, for a targeted damping close to 5%, it is seen to perform desirably in this system.

5.4.4 Validating the Controller Parameters

The final values for the controller parameters is listed in Table 3.

Table 3: Final choices of the BESS controller parameters to increase the damping of the poorest damped mode

Proportional gain	**Washout filter**	**2nd order lead-lag**	
K_p	T_{wash} **[sec]**	T_1 **[sec]**	T_2 **[sec]**
11.56	10	0.776	0.238

To have an initial validation of the BESS performance, a short simulation is carried out where a BESS using the controller parameters listed in Table 3 is included. Figure 5.24 shows some of the eigenvalues in the system for such a case, both with and without the BESS included.

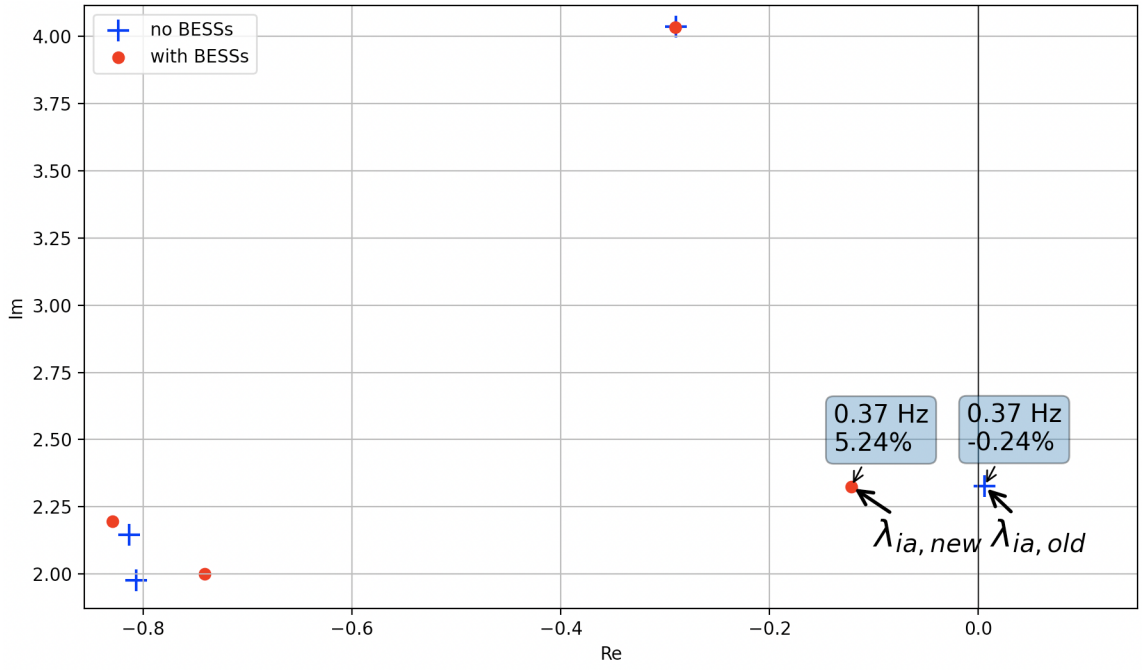

Figure 5.24: Eigenvalues in the system (zoomed-in) both with and without the BESS using the controller defined in Table 3. The mode of interest, λ_{ia}, is changed desirably, whereas the other observable modes in the plot are affected to a low-extent, which is also confirmed for modes not shown in the figure.

When looking at these linearized properties, it is seen that the controller is operating desirably, namely by imposing a straight horizontal left-wards shift on the mode of interest and reaching a new position of approximately 5% damping. Hence, the finalized parameters of the controllers work as intended for this linear analysis. Non-linear simulations will be looked more into at a later point to validate the controller performance for different types of faults. Figure 5.25 shows the different input signals and output signals to the blocks used in the controller[5.17] for a small load disturbance lasting 0.05 seconds. For simplifying the reading, a block diagram showing where the different signals in Figure 5.25 are measured is provided in Figure 5.26.

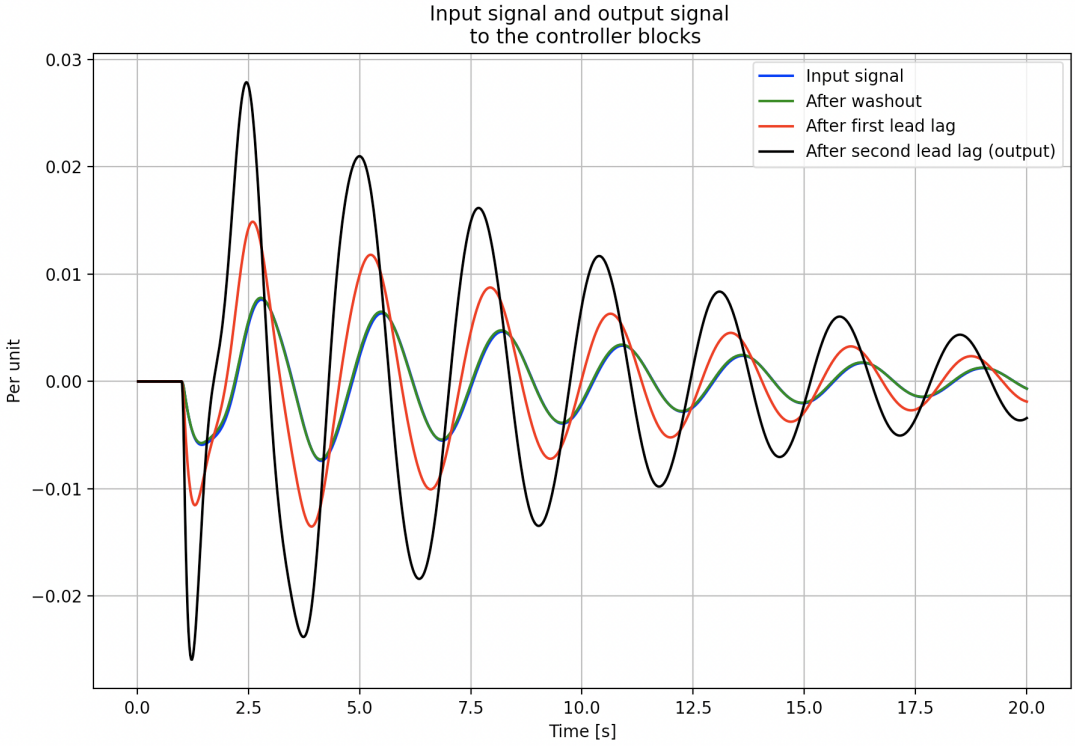

Figure 5.25: Input and output signals for the different controller blocks in the system. An illustration showing where the different signals are measured during the dynamical simulation is given in Figure 5.26.

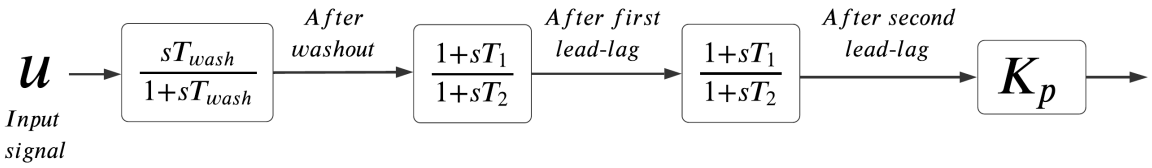

Figure 5.26: Block diagram showing where the different signals in Figure 5.25 are measured during the simulation.

[5.17] Excluding the impact of the proportional gain (which will only act as a scaling factor)

From Figure 5.25 some of the properties of the different controller blocks can be observed.

1. The input signal, and the signal measured after the washout filter are essentially overlapping. This is as expected, since the amplitude gain of the washout filter was seen to be approximately 1.0 at the frequency of interest, while providing a phase shift close to zero from (5.1).

2. The first lead-lag block is imposing a phase shift on the signal, as well as an amplitude gain[5.18].

3. Similarly, *the second lead-lag block*, which is tuned with the same parameters as the first one, imposes an equal phase shift on the signal and increases the amplitude of the signal by the same factor as the first lead-lag block.

4. By looking at the time of which a local maximum value happens on the output signal and input signal, it can be seen that the time differences between these tops are found to be approximate $\Delta t = 0.5275$ seconds (towards the end of the simulation). The inter-area mode of interest is having a frequency of approximately 0.37 Hz, such that the overall phase shift from the input signal and output signal can be found to be, $\phi = \frac{\Delta t}{1/f_{ia}} 360° = 70.26°$.

5. Having in mind that the tuning of the lead-lag blocks aims at applying a phase compensation of 64°, while also having a few degrees deviation due to the relatively large proportional gain and accounting for the small phase shift imposed by the washout filter, a 70.26° phase shift from input to output seems reasonable.

5.4.5 Validating the Optimality of the Selected Signal and Location

Up until this point, the feedback signals and BESS location is chosen as the optimal combination based on the theory presented in Section 3.4.1 and 3.4.2. However, no analysis has been conducted for validating that the chosen location and feedback signal actually yields the best solution for the given system. Thus, this section is investigating this further by comparing the mode shift and additional damping applied to the mode of interest for different combinations of BESS location and feedback signals. The feedback signal and BESS location selection procedure is also conducted for two other versions of the Nordic 44 test network, and can be found in Appendix D.2 and Appendix D.3.

For the base case system, the optimal feedback signal presumably is $\pm(\theta_{6100}\text{-}\theta_{7000})$

[5.18] Which is expected when looking at the Equation for amplitude response of lead-lag filters (3.60) and $T_1 > T_2$.

from the results presented in Figure 5.11. However, the residue obtained by choosing the feedback signal as $\pm(\theta_{6100}\text{-}\theta_{3249})$ is also having a large value and could potentially be a good solution. Additionally, the feedback signal $\pm(\theta_{5300}\text{-}\theta_{3249})$ yields a relatively large value of the residue from the residue plot and is thus worth looking further into. Hence, choosing these three feedback signal combinations to look further into in an attempt to justify the improved performance when using the suggested optimal feedback signal.

The residue values for different BESS locations in the system, given that the feedback signal is chosen to be $\theta_{6100}\text{-}\theta_{7000}$, are shown in Figure 5.14. The three different locations to be investigated are chosen as the optimally selected location $B6100$, the supposedly next best location $B5300$, and, lastly, $B3249$, which corresponds to the maximum residue location in the opposite half of the complex plane. It should be made clear that in a general case, one would have to adjust the controller parameters, especially related to the phase compensation of the lead-lag filters. However, it was seen in Figure 5.16 that the residues for different BESS locations are located approximately on a straight line through origo, such that the desired phase compensation for the different BESS locations is approximately the same, or 180° shifted if the residue is located in the opposite half of the complex plane (which is the case for $B3249$). The BESS with fixed controller parameters are given in Table 3 is thus deployed for all three of these locations, together with the three aforementioned feedback signal combinations, and the results are presented in Table 4.

Table 4: Frequency and relative damping of the inter-area mode for different locations of the BESS using different feedback signals. Without BESS in the system, the eigenvalue is having a frequency of 0.37 Hz and relative damping of -0.24%. The new frequency and relative damping of the inter-area mode are given by f_{ia} and ζ_{ia}, respectively, and $\Delta\zeta_{ia}$ is the change in relative damping compared to the base case system.

BESS LOCATION	FEEDBACK SIGNAL	f_{ia}	ζ_{ia}	$\Delta\zeta_{ia}$
B6100	$\theta_{6100}\text{-}\theta_{7000}$	0.37 Hz	5.24 %	5.49 %
	$\theta_{6100}\text{-}\theta_{3249}$	0.37 Hz	4.99 %	5.24 %
	$\theta_{5300}\text{-}\theta_{3249}$	0.37 Hz	3.50 %	3.75 %
B5300	$\theta_{6100}\text{-}\theta_{7000}$	0.37 Hz	4.52 %	4.77 %
	$\theta_{6100}\text{-}\theta_{3249}$	0.37 Hz	4.32 %	4.57 %
	$\theta_{5300}\text{-}\theta_{3249}$	0.37 Hz	2.74 %	2.99 %
B3249	$-(\theta_{6100}\text{-}\theta_{7000})$	0.37 Hz	1.24 %	1.49 %
	$-(\theta_{6100}\text{-}\theta_{3249})$	0.37 Hz	0.91 %	1.16 %
	$-(\theta_{5300}\text{-}\theta_{3249})$	0.37 Hz	0.76 %	1.01 %

The ordering of the table is chosen based on the presumably best solution. That is, the location apparently having the largest effect on the mode ($B6100$) is placed at the top, followed by $B5300$ and then lastly $B3249$. From the absolute value of the residues provided in Figure 5.14, one should expect that for the same feedback signal at these three locations, the top one ($B6100$) should provide the largest amount of damping, followed by the second ($B5300$), and then the smallest amount of damping provided by the BESS located at $B3249$. By reading the tables for the different locations and feedback signals, one sees that this is true for all of the three feedback signals considered.

The different values of the residues for different feedback signal combinations is provided in Figure 5.11. Similarly as for the different locations, the feedback signals analyzed (θ_{6100}-θ_{7000}, θ_{6100}-θ_{3249}, θ_{5300}-θ_{3249}) are ordered based on the presumed effect they would have on the mode of interest as read from the residue plot in Figure 5.11. For each of the different locations, one observes that the change in the relative damping $\Delta\zeta_{ia}$ is larger the greater the value of the residue for the corresponding feedback signal is. Thus, it seems evident that the chosen BESS location and feedback signal combination does, in fact, correspond to the optimal solution for this system[5.19].

In an attempt to validate the selection procedure and optimally of the selected input/output combinations, the same method employed for this system is conducted in two other versions of the Nordic 44 system. These results are presented in Appendix D.2 and D.3, and for both of those systems, being fundamentally different from the base case system, the results indicates that the procedure is proficient at accurately selecting the optimal feedback signal and BESS location, yielding different results compared to the base case system, as one would expect when system topologies are heavily modified.

5.5 System Disturbance Selection Based on Mode Excitation

For power system analysis, the disturbance location significantly impacts the extent to which the modes are being excited. Thus, before performing the non-linear analysis for validating the performance of the selected BESS with its corresponding location and input signal, first-hand knowledge about the disturbance locations having the highest impact on the system excitation seems necessary. From Equation (3.37) one have[5.20] that the derivative of the change in the modal variables is given by $\Delta\dot{z} = \Lambda\Delta z + \Psi B\Delta u$. Thus, the product $\Psi B\Delta u$ contains information about the excitation of the modal vari-

[5.19] Numerous other combinations are considered too, all of them providing a smaller amount of damping compared to the chosen solution. The procedure is also conducted for other version of the Nordic 44 system, which can be found in Appendix D.2 and Appendix D.3.

[5.20] By including the Δ notation which is dropped for simplicity in Equation (3.37).

ables.

In an attempt to figure out the most critical disturbance locations in the system, an iteration is performed through the different generator buses in the system. For each of the considered buses, the product ΨB is calculated, where the B-matrix (which is a vector as *only one input* is considered in each iteration) is calculated for each iteration by using Equation (3.7). The element of the vector ΨB corresponding to the mode of interest is thus extracted for each iteration (using Equation (3.62) from Section 3.6 when searching for the index of the mode of interest), and the magnitude of this element for the different locations is presented in Figure 5.27.

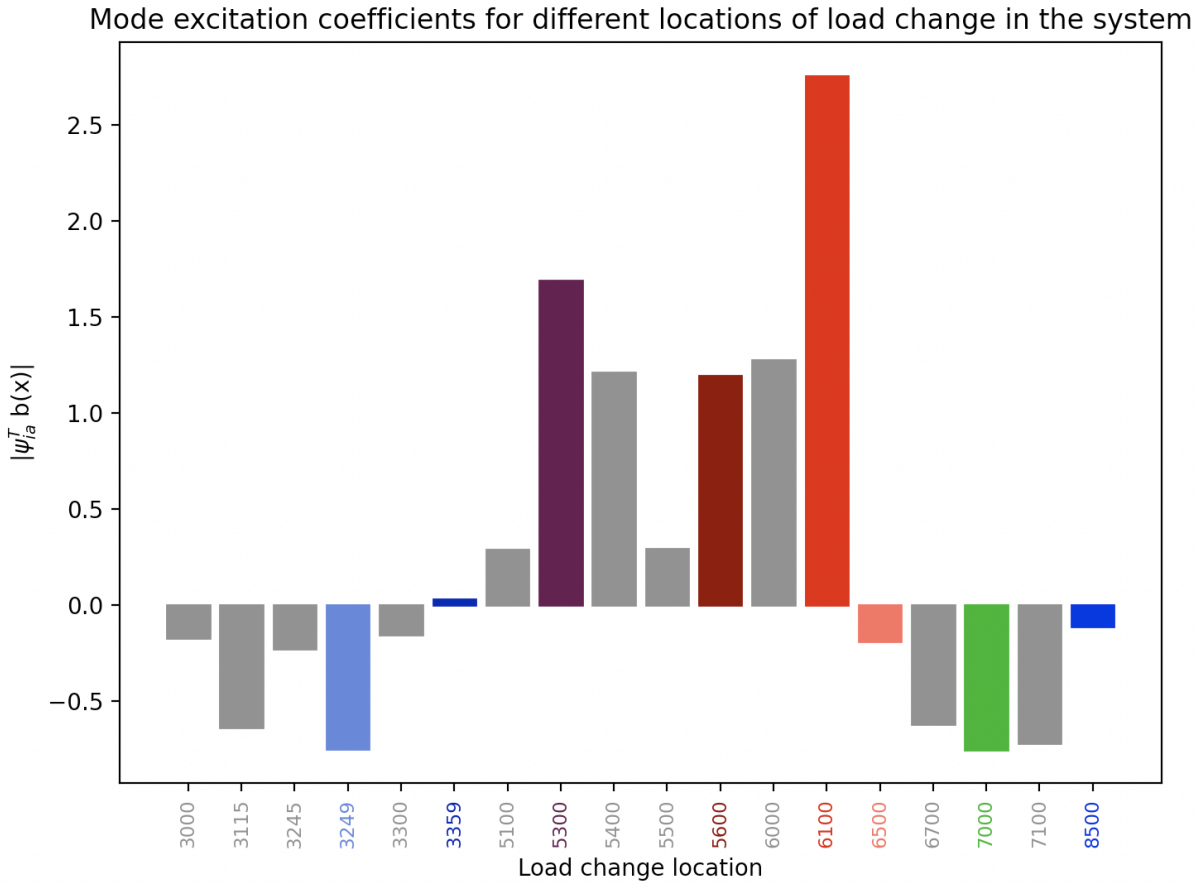

Figure 5.27: Excitation of the mode of interest for different locations of disturbances in the system.

The y-axis contains the magnitude of the product ΨB on the element position corresponding to the mode of interest. The plot should be interpreted such that the bar containing the largest magnitude will excite the modal variable of interest the most. Notice how the plot is fundamentally the same as Figure 5.14 used for selecting the optimal BESS location, the only difference being the scaling of the y-axis. This should be anticipated due to the chosen feedback signal used for obtaining Figure 5.14 is seen to only provide scaling of all elements in ΨB. This was also discussed in theory presented

in Section 3.4.2, where it was stated that the optimal BESS location could be determined independently of the chosen feedback signal. Intuitively, it seems reasonable that the location being most critical in terms of disturbances in the system is simultaneously the location best suited for adding system stability improvement controllers.

To validate that the modal excitations for different disturbance locations in the system are depending on the magnitude of the bars presented in Figure 5.27, a simulation is carried out where four different small-signal load events lasting 0.05 seconds are applied to the system. Firstly, a load-change is applied at B6100 (presumably being the location exciting the mode the most). When the oscillations eventually die out, the load-change is applied at B5300, which in theory should excite the mode quite a bit, but not as much as the first one. Thirdly, a load-event is happening at B3249, which should cause lower excitation than the previous two events. Lastly, the load-event is applied at B8500, which from Figure 5.27 should correspond to an almost negligible amount of excitation for the given mode. All of the load events are of the exact same magnitude ($\pm$ 10MW). The signals associated with the controller are the results being presented since only the excitation of the mode of interest (0.37 Hz) is what's of interest. Some of the locations might excite other modes in the system by a great amount, thereby being hard to distinguish in, for instance, the generator speed response[5.21]. The proportional gain factor determined in Section 5.4 to being 11.56 (targeting 5% damping) is increased without loss of generality, simply to let the oscillations following the different events die out faster, such that a reasonable steady-state is obtained before a new load-change is happening. The simulation results are presented in Figure 5.28.

[5.21] Various locations will cause high excitation of other modes in the system, such that for instance the speed response will be very distorted and not being meaningful in terms of analyzing the amount of excitation for the mode of interest.

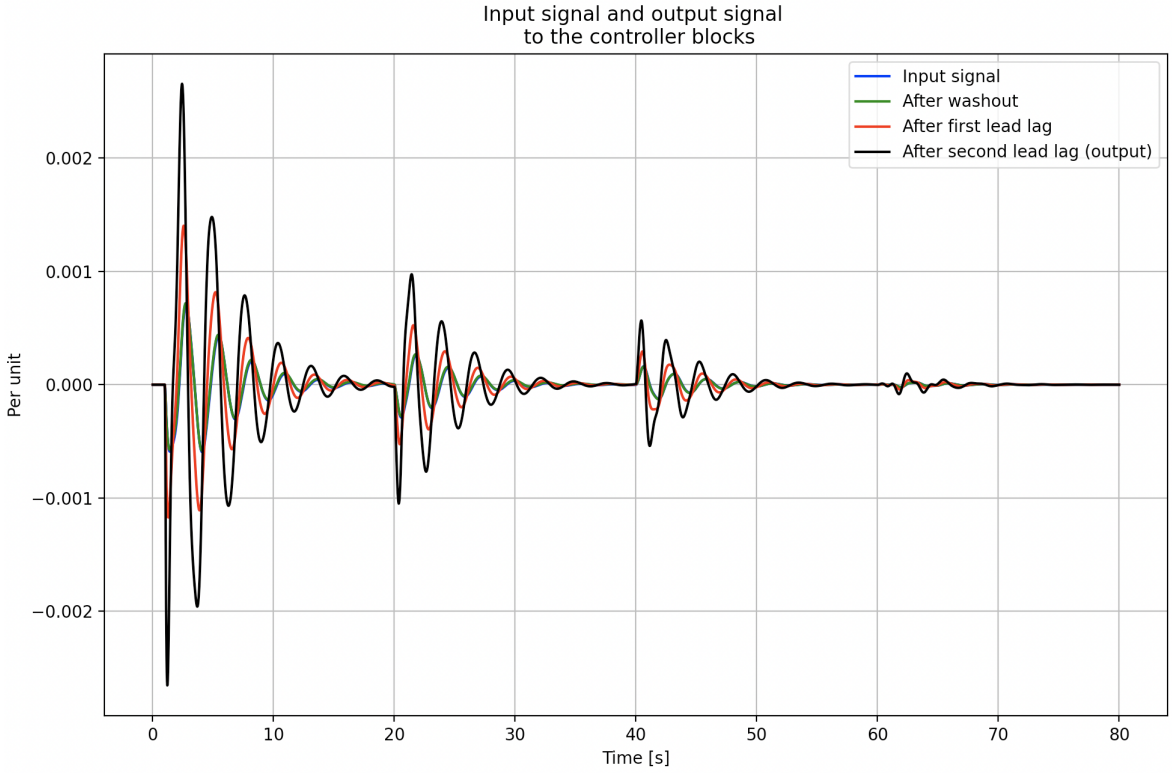

Figure 5.28: BESS controller signals for four different load events of 10MW, each lasting 0.05 seconds. The different load event locations are based on descending magnitudes from Figure 5.27 and in the order [B6100, B5300, B3249, B8500].

As anticipated, output signals from the controller are highest when the load event happens at B6100 containing the largest magnitude from Figure 5.28, and decreases based on the magnitudes seen in this figure. The output signal of the controller is correlated and almost proportional to the input signal to the BESS controller[5.22], thereby being a useful signal to measure when looking at the actual modal excitation. Due to the filtering and BESS targeting damping of the mode having a frequency of 0.37 Hz, this signal is a great measure for looking at the excitation of the mode of interest without having to consider the excitation of all other modes in the system. Therefore, when performing non-linear simulations validating the controller, a useful approach would be to have in mind Figure 5.28 when selecting disturbance locations in the system; for instance, a load-change at B8500 would have minimal impact on the mode of interest.

5.6 Non-linear Simulations for Verifying the Performance of the Selected Controller

The BESS controller signals, locations and parameters are now selected, the validity of the suggested optimal solution is discussed in Section 5.4.5 and the modal excitation

[5.22]Some phase shifts and filtering are included.

for different fault/disturbance location is presented in Section 5.5. Thus, up until this point, most of the simulations and selections are based on linearized properties of the system around the given operational point in the system. In order to validate the controller, non-linear simulations will be conducted in this Section to see the performance of the BESS and whether or not the anticipated responses from the linear system can be seen. The design of the BESS controller has been fundamentally based on the linearized properties of the system, hence presumably being well able to handle small signal stability issues. During larger disturbances such as line- and generator outages, what happens is not described accurately through linear analysis.

5.6.1 Switching to Bus Voltage Angle Signals

Firstly, one seemingly major change will be done to the BESS controller signals. Up until this point, when talking about differences in angles regarding the feedback signal, one has been utilizing the generator angle for the different generators in the system. However, for a real-world system, the measurable angles in the system are related to the terminal voltage angles in the system. Using generator angles instead of terminal voltage angles simplified the calculation of the Eigen-properties of the system significantly. Appendix A.4 provides a deviation and includes an illustrative example of why these quantities are closely related, essentially providing the same signal under some given assumptions. These assumptions are not met for a large system like Nordic 44 using the sixth-order generator model. Therefore, before completely exchanging the generator angle signals with bus terminal voltage angles, a closer look into the eigenvalues for the different cases is undertaken. For the given selected controller parameters selected in Section 5.4 and presented in Table 3, the new modal position of the mode of interest ended up being at 0.37 Hz with a damping of 5.24%. If the mode of interest is located approximately at the same location when switching to terminal voltage angles, keeping the controller parameters at the chosen values is justified.

Computing the eigenvalues in the system without BESS, with BESS utilizing generator angle differences and a BESS utilizing the difference in bus voltage angles, yields the plot shown in Figure 5.29.

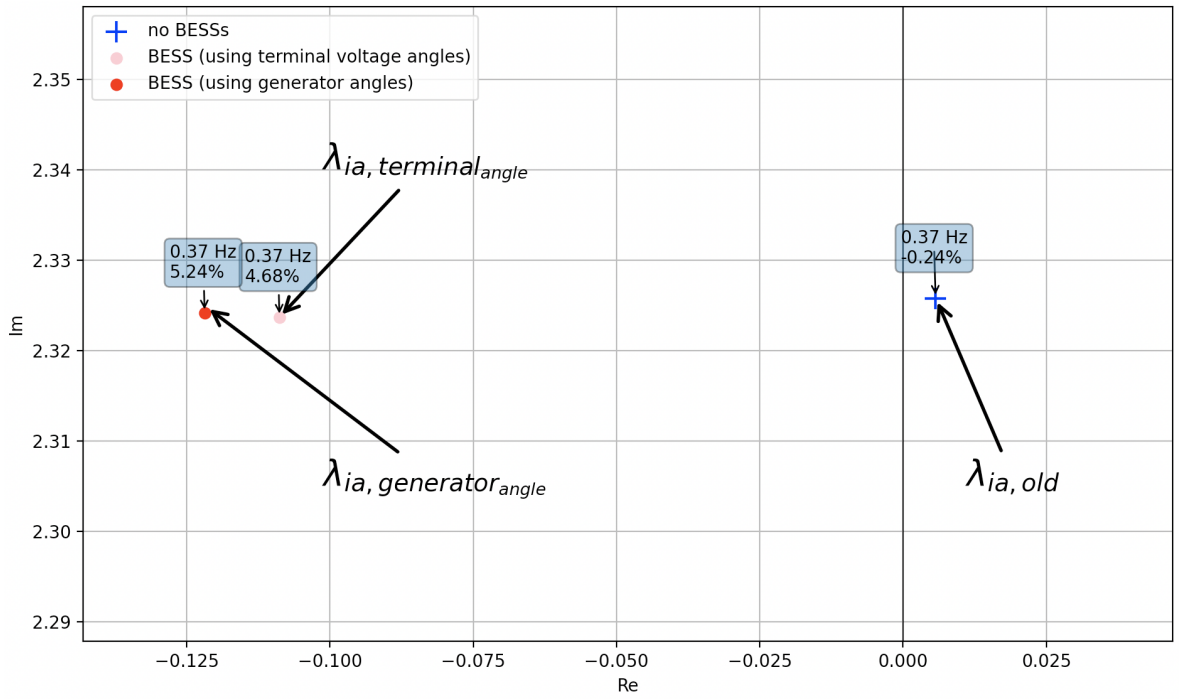

Figure 5.29: The mode of interest for three different cases: No BESS, BESS utilizing terminal voltage angles and BESS using generator voltage angles.

From the plot, one observes that when the feedback signals are switched to being differences in terminal voltage angles at B6100 and B7000, the damping of the mode of interest is marginally reduced compared to the case employing differences in generator angles. Nevertheless, the phase compensation designed for the controller using generator angle is seemingly a good choice when using terminal voltage angles too. Therefore, keeping the parameters are the previously determined values is reasonable. Hence, the non-linear simulations conducted for the rest of this section utilize the real-world measurable bus voltage angles replicating PMU installed in the actual grid.

5.6.2 Load Change Events

Small Period Lasting Load Change

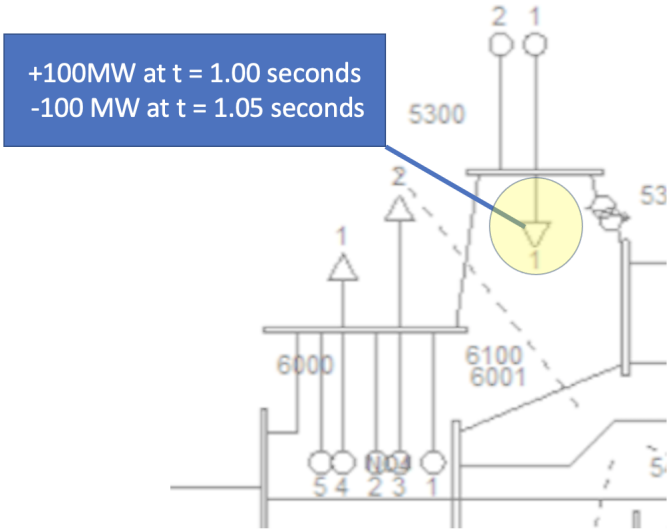

Figure 5.30: Illustration showing the load change of 100MW lasting 0.05 seconds at L5300-1.

The first type of disturbance to be checked is a load change applied at Bus 5300. Based on the result found in Section 5.5 and presented in Figure 5.27, applying a change at Bus 6100 would have the largest effect on the excitation of the mode of interest. However, as this coincides with the BESS location, the disturbance is applied at Bus 5300 instead, such that the disturbance location is somehow remotely located[5.23] seen from the BESS bus. Running the simulation by applying a *100MW load increase at 1.0 seconds*, and 100MW load *decrease at 1.05 seconds* as illustrated in Figure 5.30, the results presented in Figure 5.31 and 5.32 is obtained.

[5.23]Bus 6100 and Bus 5300 are relatively close geographically, though.

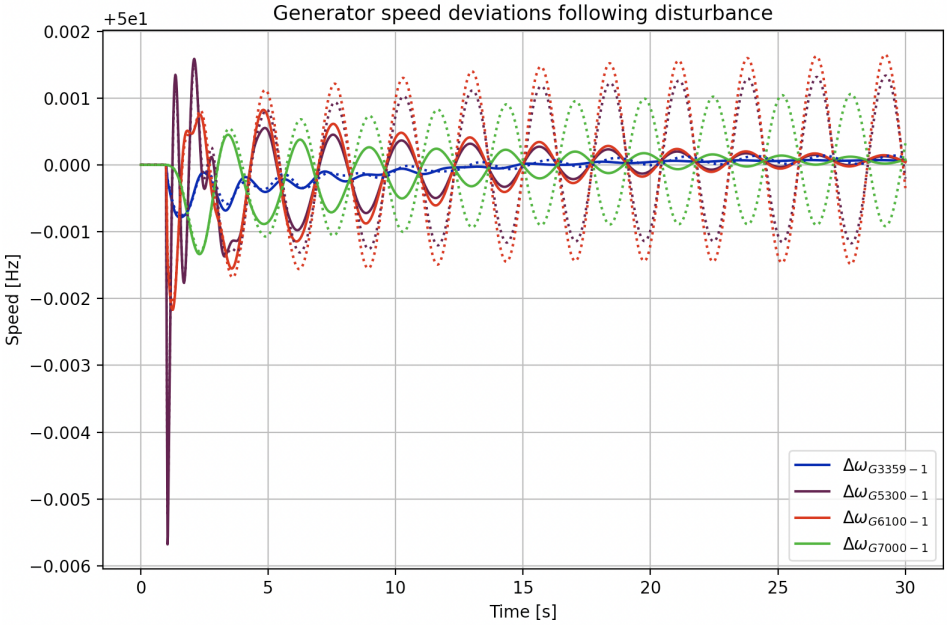

Figure 5.31: Speed response in the system following the load change of 100MW at L5300-1 lasting 0.05 seconds. Solid lines is the responses when the BESS is included, whereas the dotted lines indicates the base case system (no BESS) response.

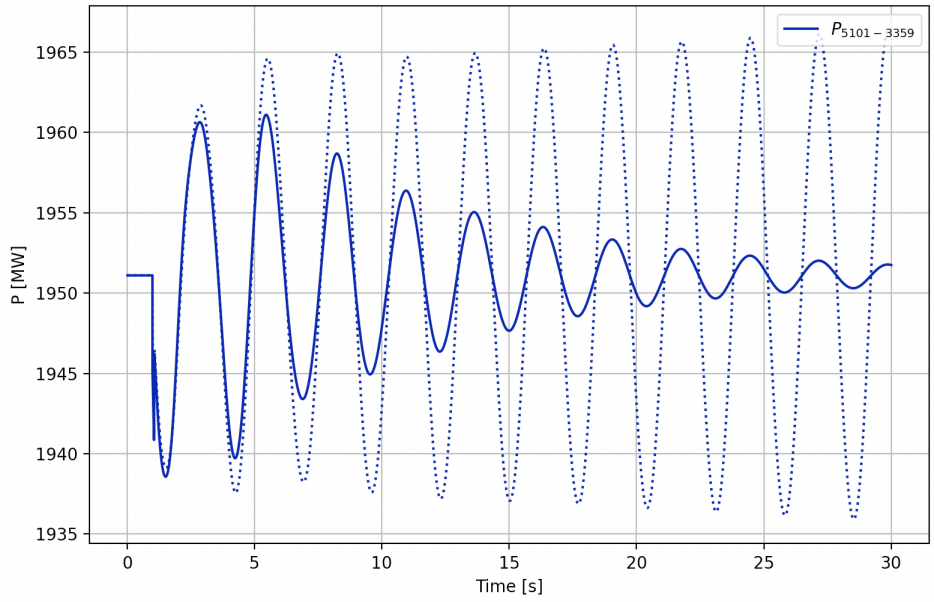

Figure 5.32: Power flow between Bus 5101 and B3359 connected between Norway and Sweden following load change of 100MW at L5300-1 lasting 0.05 seconds with (solid line) and without (dotted line) BESS included in the system.

The frequency starts dropping (especially for G5300-1 being connected to the bus of which the disturbance happens) immediately after 1.0 seconds, before increasing again when the same amount reduces the load after 1.05 seconds. This response could be anticipated by the Swing Equation (3.2), and the oscillatory response of approximately 0.37 Hz strongly suggests excitation of the mode of interest.

Suppose the BESS is not included (dotted lines). In that case, the amplitude of the oscillations will marginally increase during the simulation. It will not be able to return to a steady state, and the system is thus unstable. When the BESS is included (solid lines), the opposite effect can be seen. The oscillations of the speed deviations in the system decrease during the simulation period and almost reach a steady equilibrium point towards the end of the simulation. These results could be anticipated by only having information about the system modes obtained from the linear analysis. The effect of the BESS might be most easily seen from the power flowing between Bus 5101 and Bus 3359. When the load change of 100MW is only lasting 0.05 seconds, this essentially translates to a small disturbance in the system, which correlates well with the type of faults where the linearized theory is somehow accurately estimating the system response.

Sustained Load Change in the System

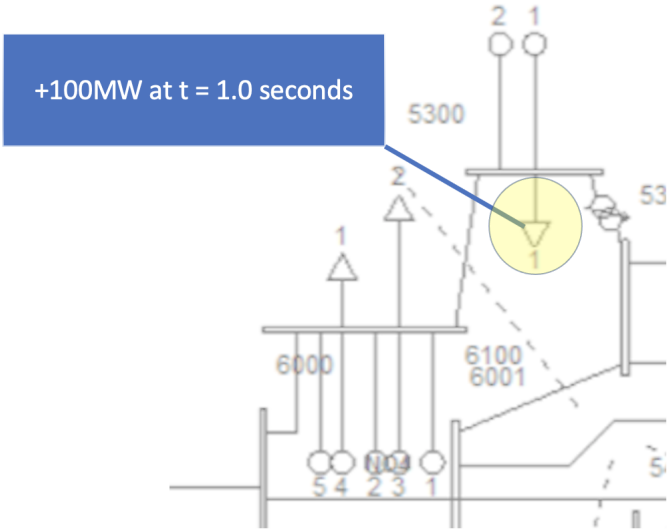

Figure 5.33: Illustration showing where the sustained load-change is applied.

The simulation mentioned above included a load decrease of 100MW at 1.05 seconds. The disturbance in the system is only active for a short duration of 0.05 seconds. However, if one carry one with the same type of simulation, but this time the load increase of 100MW is sustained as seen in Figure 5.33, one should expect from the theory presented in Section 3.1 and Appendix A.1 that the steady-state frequency in the system will change compared to the initial value. For such a case, the loading in the system is suddenly increased. From the Swing Equation (3.2), the new steady-state frequency should be slightly lower than the scheduled frequency in the system. The

simulation results are presented in the Figures below.

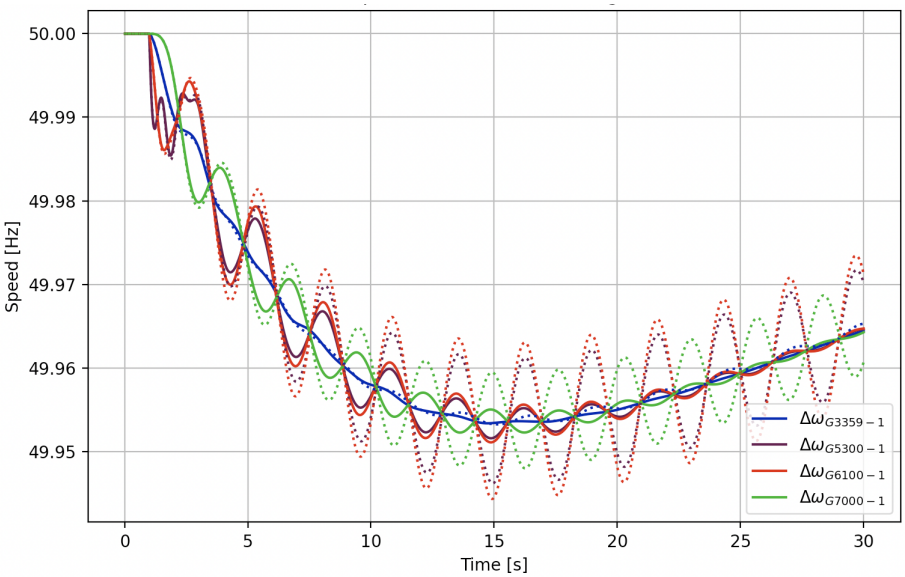

Figure 5.34: Speed response for a few selected generators when a load increase at L5300-1 of 100MW is applied. Solid lines is the responses when the BESS is included, whereas the dotted lines indicates the base case system (no BESS) response.

The speed response in Figure 5.34 is somehow as anticipated. When the load is increased, one has from the Swing Equation (3.2) that the frequency in the system will decrease. This is true both for the case using BESS (solid lines) and the case without (dotted lines) as the BESS controller is not aiming at reducing the frequency drop in the system but dampening the oscillations following disturbances; the latter is evident from the response in Figure 5.34. If the BESS is not included, the system will not return to a steady-state, and approximately standing oscillations are observed.

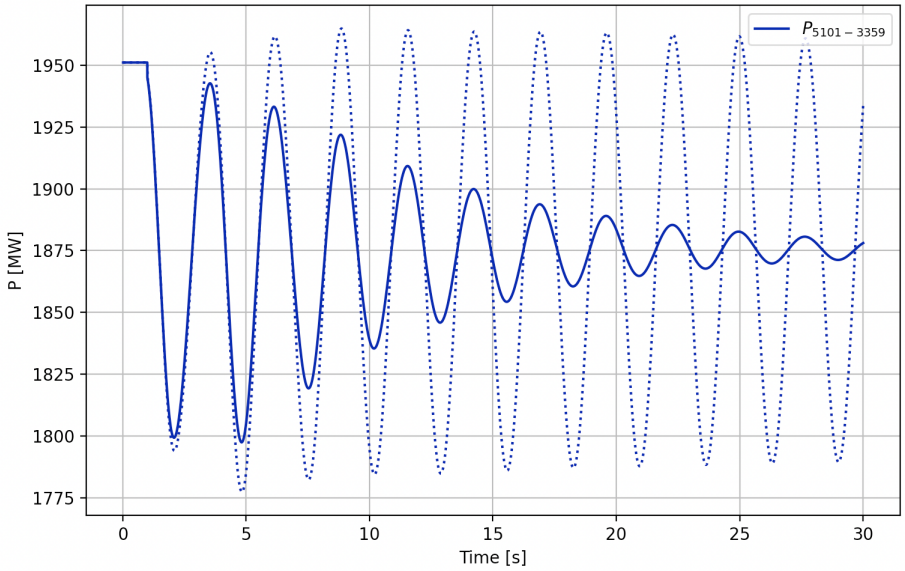

Figure 5.35: Power flowing from B5101 to B3359 when load L5300-1 increases by 100MW at 1.0 second. Solid lines is the responses when the BESS is included, whereas the dotted lines indicates the base case system (no BESS) response.

Following the disturbance, there will be a mismatch between power production and power demand in Norway. Thus, the power flowing from Norway to Sweden will decrease slightly to account for this, as can be observed from the power flow presented in Figure 5.35, but the oscillatory damping imposed by the BESS is evident.

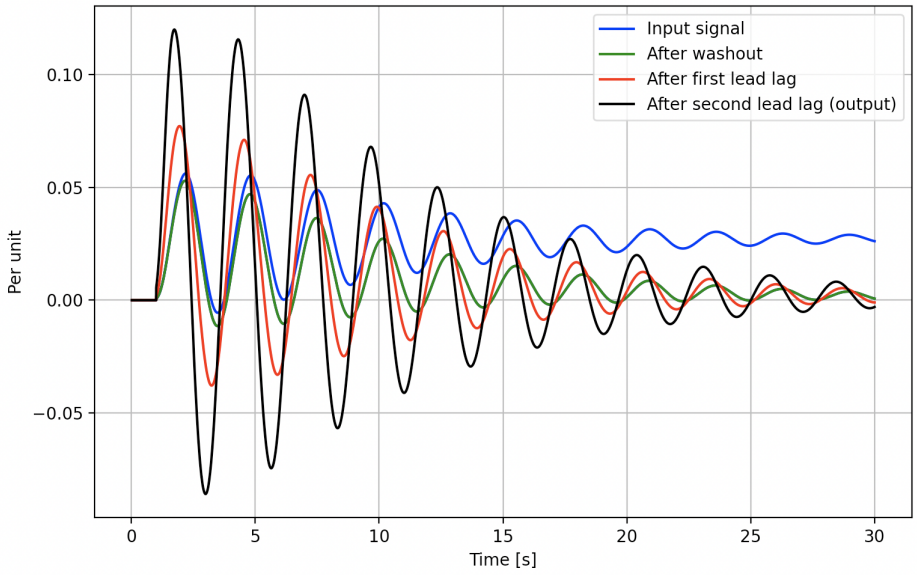

Figure 5.36: BESS controller signals when load L5300-1 increases by 100MW at 1.0 seconds.

Some interesting things can be seen when looking at the different signals associated with the BESS controller in Figure 5.36. Towards the end of the simulation, one sees that the input signal has an offset from the initial angular difference between the

terminal voltages at B6100 and B7000. However, the controller's output signals (black line) are not making controller actions based on this. This follows because the washout filter is employed in the BESS controller to remove the impact of low-frequency (and zero frequency DC-signals) input to the controller.

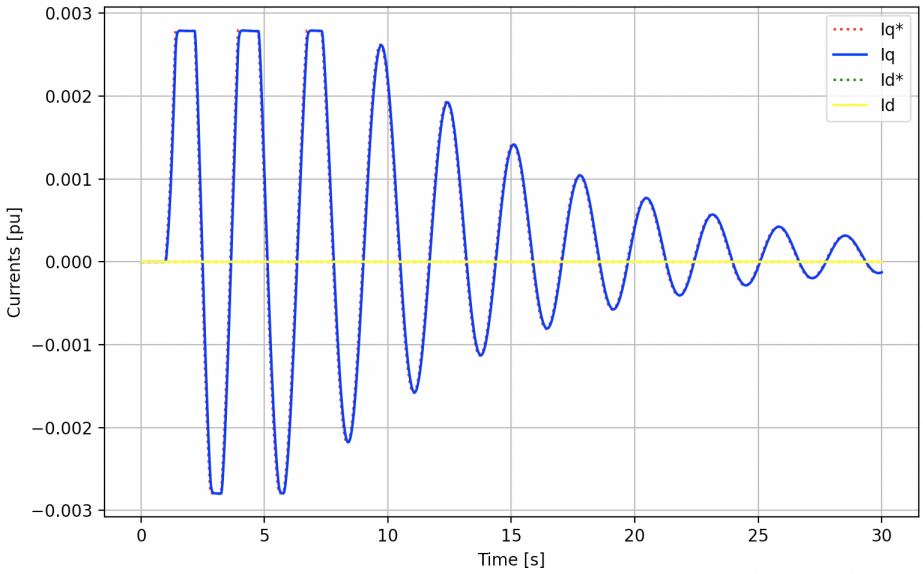

Figure 5.37: Current components ($I_d = 0$) injected by the BESS when load L5300-1 increases by 100MW at 1.0 seconds.

By looking at the dq-components[5.24] of the current injected into the system by the BESS in Figure 5.37 one notices a response similar to responses seen in the literature for devices having internal limitations [42], [54]. Due to the power limitations in the BESS system, the injected current component (I_q) initially looks like a square wave for the first few periodic cycles. As the amplitude of the oscillations and the magnitude of the controller input signal decreases, the current injected into the grid is more or less becoming a sinusoidal wave having the frequency of the mode of interest, namely 0.37 Hz. The first-order time-delay included representing the delay associated with real-world converters is having a time constant of 0.035 seconds. Therefore, for a simulation time of 30 seconds, the differences between the reference value of the current component (I_q*) and the actual current component injected to the grid (I_q) is almost non-observable, but can be observed when zooming in on the plot.

[5.24] $I_d = 0$ by design.

5.6.3 Short-Circuit Events

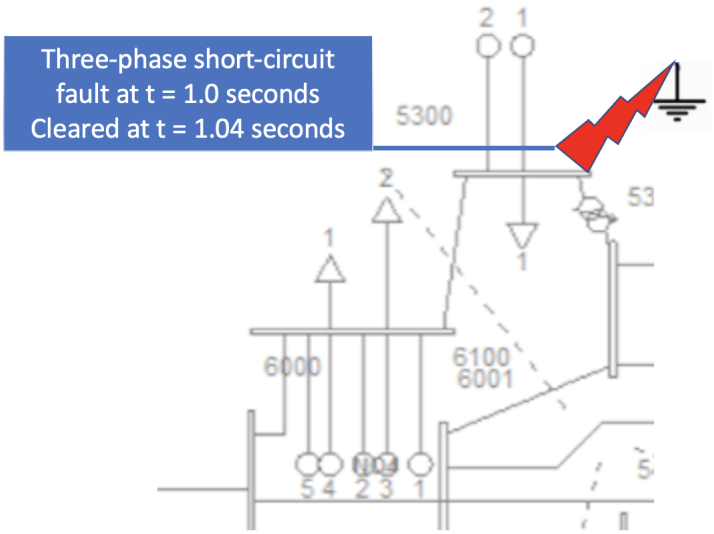

Figure 5.38: Illustration showing the short-circuit event initiated at Bus 5300 after 1.0 seconds before being cleared at 1.04 seconds.

Short-circuit Event with *Base Case BESS Power Rating*

Short-circuits happens from time to time in the power system. These are often cleared rather quickly but cause excitation of the equipment installed in the system. For this Section, a short-circuit event lasting 0.04 seconds before clearance is being investigated. Due to the small duration of the fault, one should expect a similar response as when the load was increased for a short period of time. However, the system's excitation is presumed to be significantly increased in the case of a short-circuit event compared to a relatively small load-change event previously simulated. The short-circuit is applied at Bus 5300, which from Figure 5.27 could be seen to yield a high excitation of the mode of interest. The setup for this simulation is illustrated in Figure 5.38 and the results are presented in Figure 5.39 and 5.40.

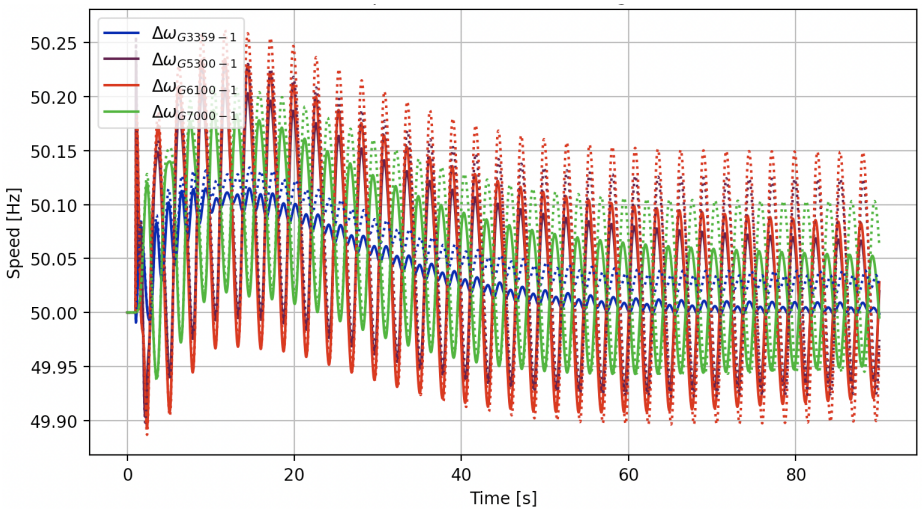

Figure 5.39: Speed response in the system following the short-circuit event at Bus 5300. Solid lines is the responses when the BESS is included, whereas the dotted lines indicates the base case system (no BESS) response.

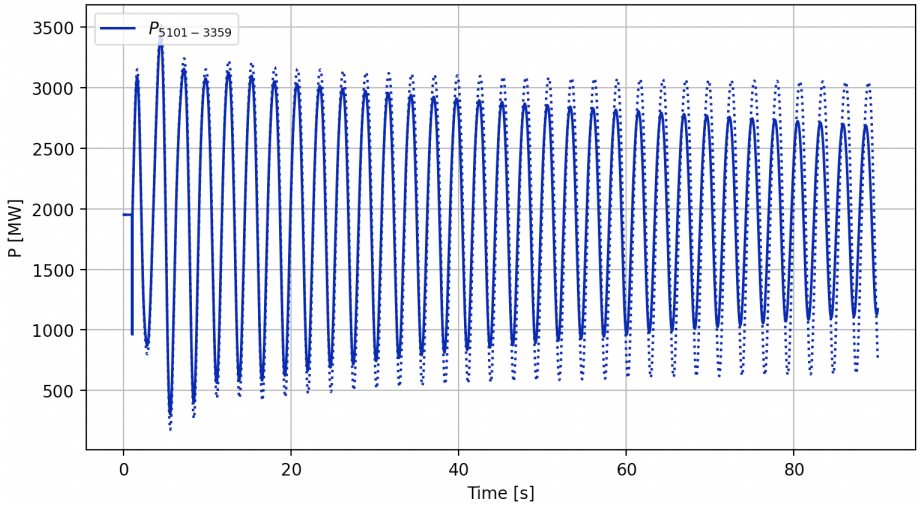

Figure 5.40: Line flowing from Bus 5101 to Bus 3359 following the short-circuit event at Bus 5300. Solid lines is the responses when the BESS is included, whereas the dotted lines indicates the base case system (no BESS) response.

One sees that a short-circuit event, even when lasting only 0.04 seconds, excites the system significantly. The simulation period is increased for this simulation due to the slow decay of the responses. Although only marginally, the BESS responses (solid lines in both figures) prove to dampen the responses. For instance, by looking at the speed response in Figure 5.39, the system not equipped with the BESS are reaching approximately 50.15Hz as the maximum value of frequency towards the end of the simulation. For the system equipped with BESS, this value is "only" 50.08Hz towards the end. Nevertheless, the amount of damping is not necessarily satisfactory, as these oscillations withstand for a prolonged period. Looking at the current injected by the

BESS[5.25], the BESS limit is reached every cycle during the simulation period. Hence, one could naturally deduce that increasing the BESS capacity by a certain amount could be beneficial.

Short-circuit Event with *Increased BESS Power Rating*

Therefore, the BESS capacity is increased from about 3 MW to 18 MW before the same simulation is conducted once more. The results are presented in Figure 5.41, 5.42 and 5.43, and the simulation period is reduced to 60 seconds to have a better overview of the interesting parts of the response. The simulation not including BESS (dotted lines) is only carried out for 30 seconds this time, but the response is exactly the same as was seen in the dotted lines of Figure 5.39 and Figure 5.40 .

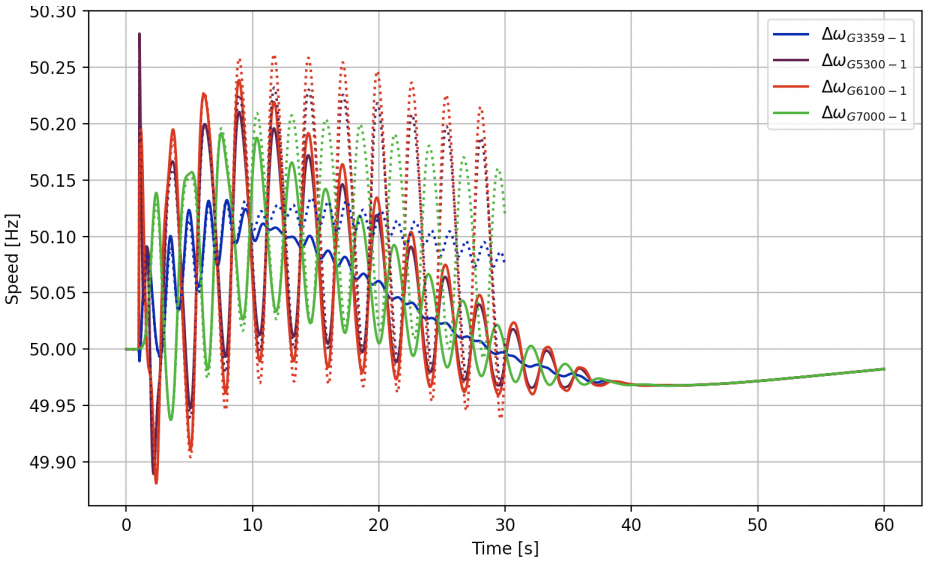

Figure 5.41: Speed response in the system following the short-circuit event when the BESS power rating is increased by a factor of six. Solid lines is the responses when the BESS is included, whereas the dotted lines indicates the base case system (no BESS) response.

[5.25]The plot is not provided in this thesis for simplicity, but it is essentially the same as the first half of Figure 5.43.

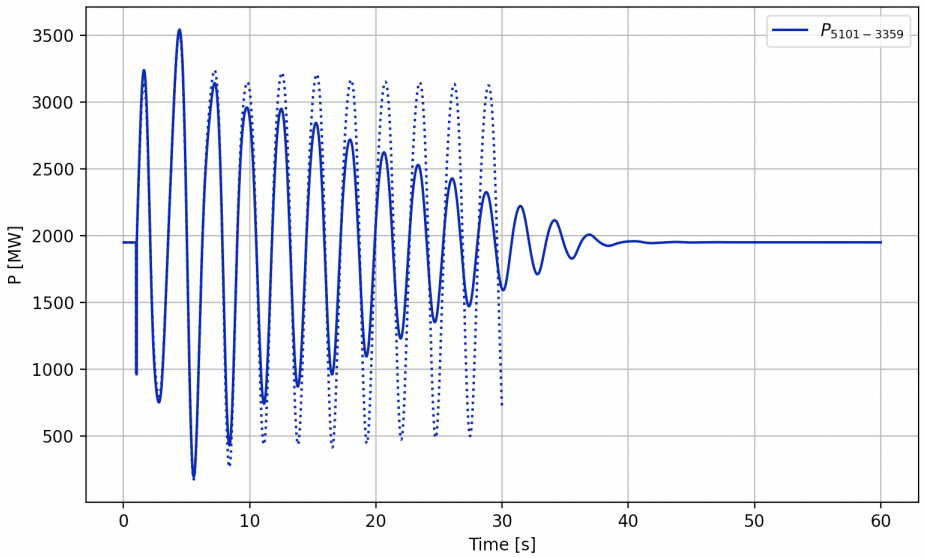

Figure 5.42: Line flowing from Bus 5101 to Bus 3359 following the short-circuit event when the BESS power rating is increased by a factor of six. Solid lines is the responses when the BESS is included, whereas the dotted lines indicates the base case system (no BESS) response.

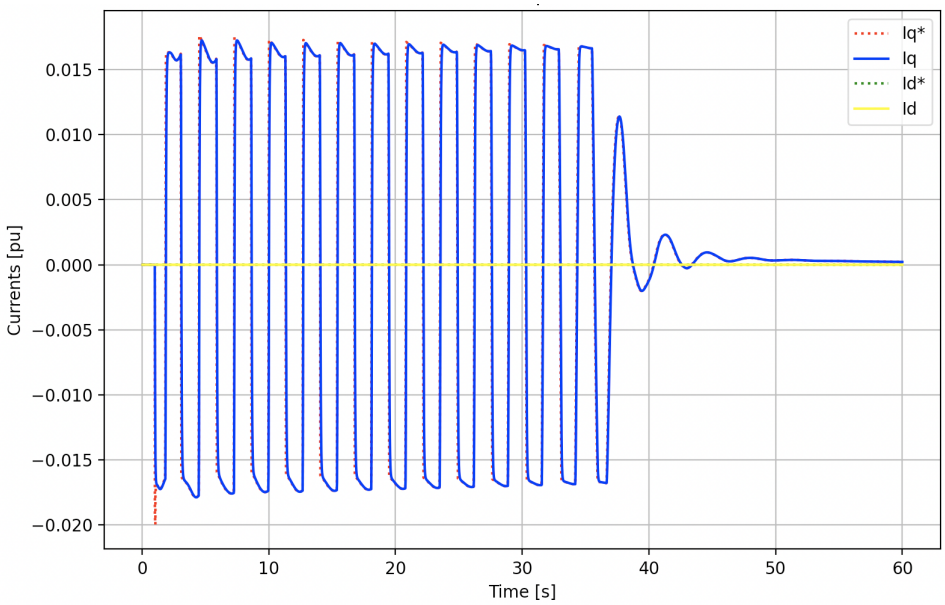

Figure 5.43: Current components injected by the BESS when the BESS power rating is 18 MW.

From the presented figures, it should be evident that increasing the BESS power rating does significantly better in terms of dampening the oscillations. When the BESS was only rated 3 MW, one could still see a marginally dampening effect. However, when the rated power is increased till 18 MW, the dampening effect is much more evident, especially when looking at the power flow in Figure 5.42. Up until about 35 seconds, the BESS reaches its rated power for each oscillation which can be seen in Figure 5.43. After this, the controller input signal (difference in voltage angles at Bus 6100 and

Bus 7000) is sufficiently small, keeping the BESSS within its power limits. Therefore, the oscillations can be seen to fade out rather quickly after this. Hence, as long as the input signal is making the controller provide a power reference within the rated capacity of the BESS, the dampening effect can be observed to a great extent. As a consequence, one observes that the power flow oscillations in Figure 5.42 decay with the same rate from about 5.0 seconds until 35 seconds, before eventually disappearing rather quickly around 40 seconds, which coincides with the point in time of which the power signal to the BESS is within its limits.

Short-Circuit event at *Less Critical Bus*

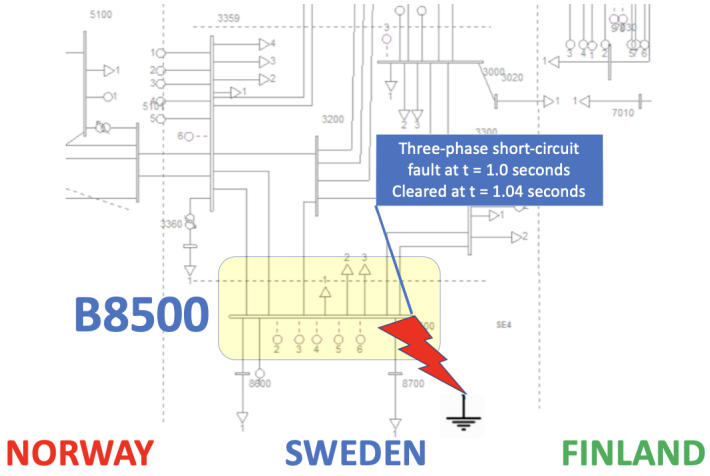

Figure 5.44: Short-circuit event at a less critical Bus based on the results presented in Section 5.5.

It was previously seen in Section 5.5 that the fault or disturbance location plays a significant role in terms of looking at the excitation of the modal variables. The short-circuit event previously shown was initiated at Bus 5300, which excites the mode of interest the most (when looking apart from Bus 6100, of which the BESS is connected). Therefore, the short-circuit event previously looked at is a somehow worst-case scenario, and increased BESS capacity was needed to see a significant effect in the oscillatory damping. However, if the short-circuit happens at other buses in the system, the original BESS capacity of 3 MW might be sufficient. Therefore, a short-circuit is conducted at Bus 8500, which from Figure 5.27 could be seen to have minimal impact on the excitation of the 0.37 Hz mode. The results are presented in Figure 5.45 and Figure 5.46.

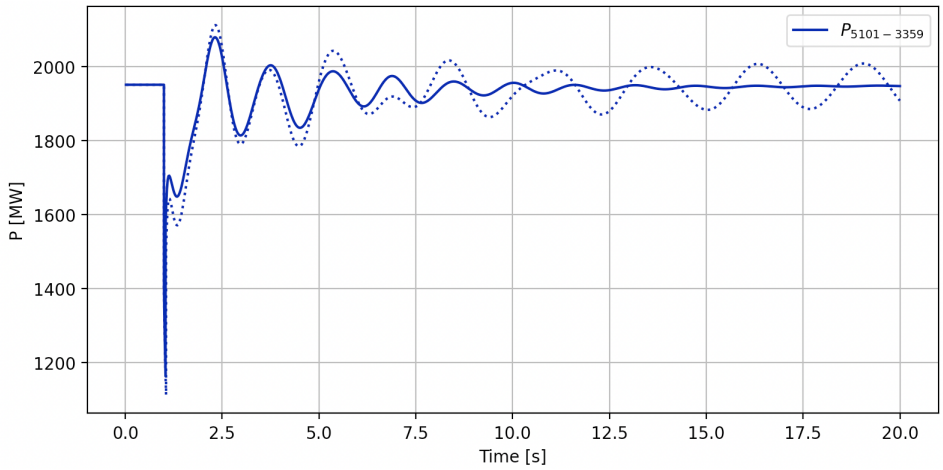

Figure 5.45: Line flow following the short-circuit event at Bus 8500. Solid lines is the responses when the BESS is included, whereas the dotted lines indicates the base case system (no BESS) response.

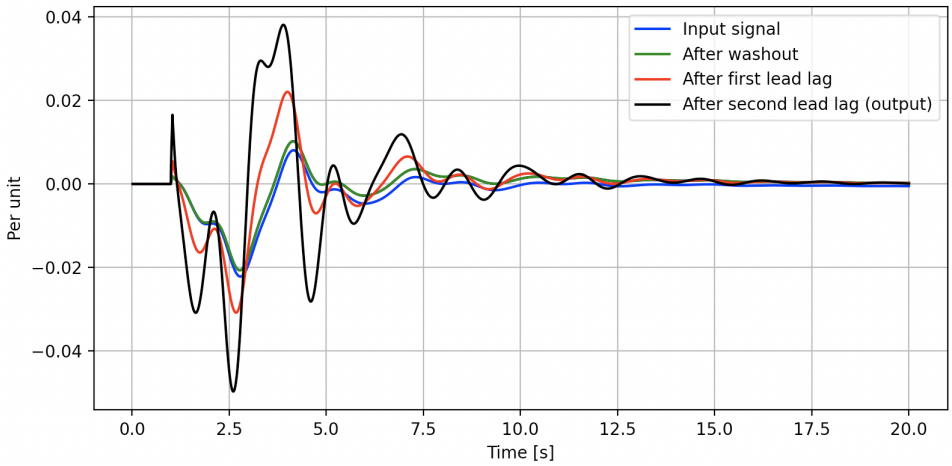

Figure 5.46: Controller signals following the short-circuit event at Bus 8500. Notice how the signals are more distorted compared to the previous simulations due to higher excitation of other modes in the system.

The controller signals are shown instead of frequency/speed in the system for this case. The reason being that from the controller signals, it is evident that the signal is more distorted for this case due to the amount of excitation of other modes in the system. For the previous simulations, it could be seen that the oscillatory responses in the system almost only consisted of the 0.37 Hz frequency component. In contrast, for this disturbance, other modes are being excited by a more significant amount. However, it can be seen from the power flow in Figure 5.46 that the BESS is helping out significantly. The oscillations in the system are almost non-observable (solid lines) after 15 seconds. When the BESS is not included (dotted lines), one sees that the oscillations are slightly increasing towards the end of the simulation period, reflecting that one has a pair of modes located marginally inside the right-half of the complex plane.

5.6.4 Line Outage

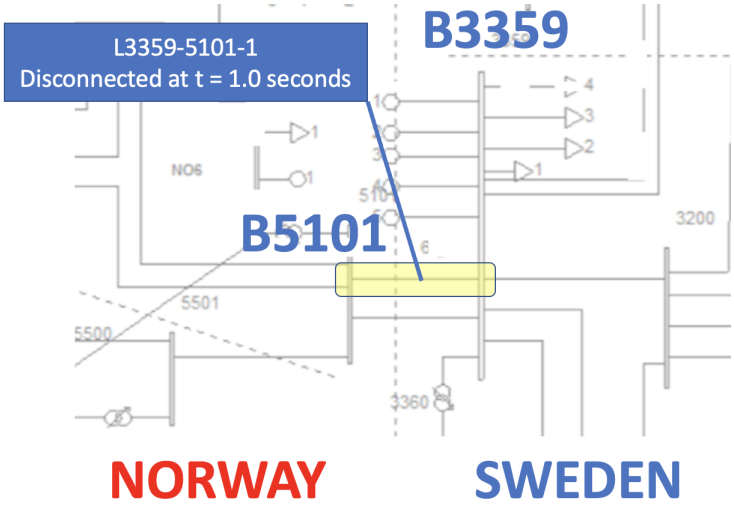

Figure 5.47: Illustration showing the line outaging of L3359-5101-1 at 1.0 seconds in Nordic 44.

The lines connecting Norway and Sweden through the southeast part of Norway and the West part of Sweden are represented by the two lines connected between B5101 and B3359. These are the lines on which the power flow is plotted for the various simulations conducted in this thesis. It can be seen from previous simulations that the power flowing between these lines are close to being 2000MW (for instance, in Figure 5.46), thus being a connection of significant concern. For the case of a real-world system, one could potentially find oneself in a situation where one of these lines is having an outage. Consequently, a line outage of one of these key lines is presumed to impact the system's stability significantly.

Line Outage with *Base Case BESS Power Rating*

Keeping the BESS and its corresponding control system as it is, and having a line outage of L3359-5101-1 at 1.0 seconds, the results presented in Figure 5.48 and 5.49 are obtained.

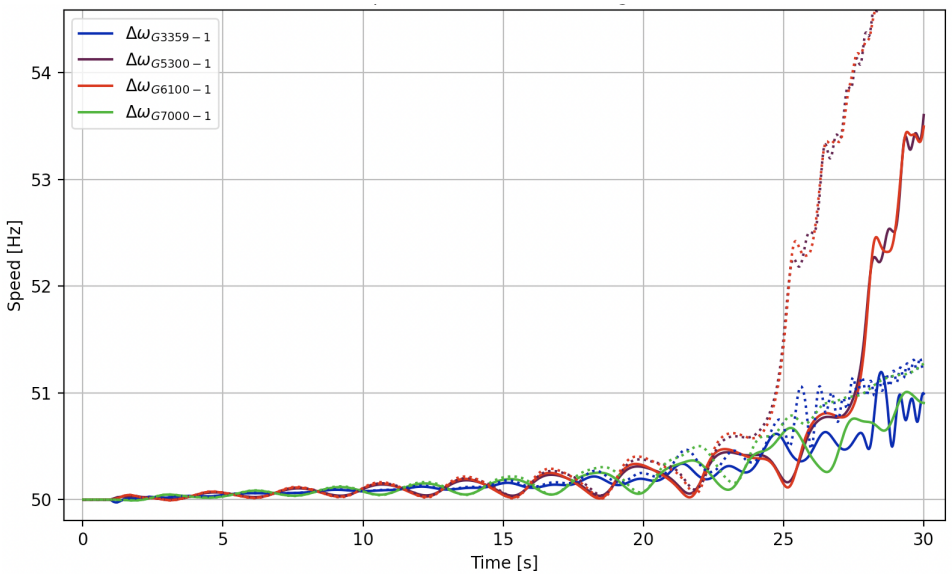

Figure 5.48: Speed response in the system for a few selected generators following a disconnection of L3359-5101-1 at 1.0 seconds. Solid lines is the responses when the BESS is included, whereas the dotted lines indicates the base case system (no BESS) response.

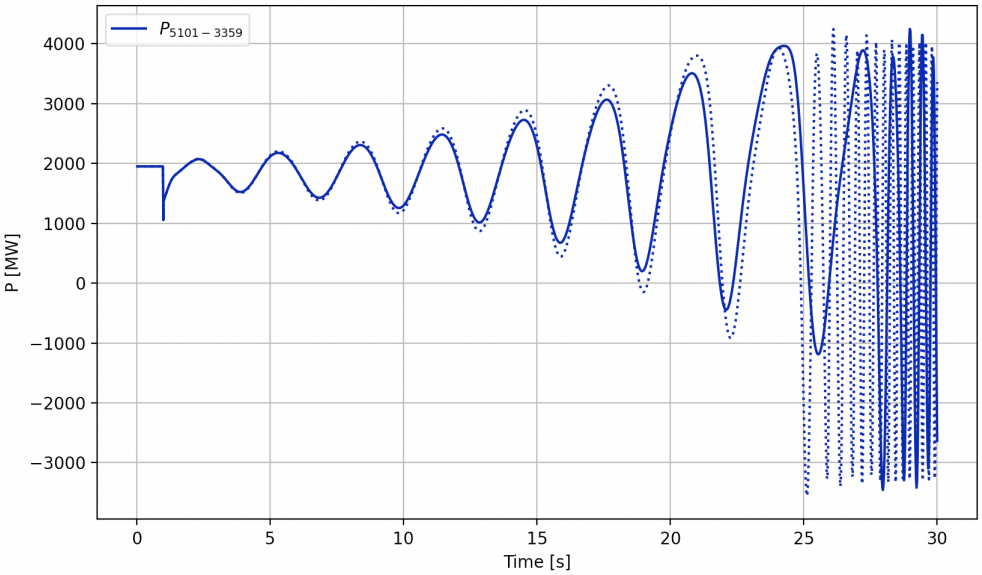

Figure 5.49: Power flow between Bus 5101 and Bus 3359 following a disconnection of L3359-5101-1 at 1.0 seconds. Solid lines is the responses when the BESS is included, whereas the dotted lines indicates the base case system (no BESS) response.

Both the system containing BESS (solid lines) and the system not employed with BESS (dotted lines) cannot return to a new steady-state. The line outage causes instability for both cases. The disturbance has a noticeable impact on the system, and the BESS system having a rating of around 3 MW cannot prevent a disaster. Although, it can be seen that the solid lines (response when BESS is employed) are somehow delaying the time of which the instability is present the most. Hence, one could naturally presume

that a larger BESS power rating could somehow help out for this situation, similarily as was the case for the short-circuit event discussed previously.

Line Outage with *Increased BESS Power Rating*

Changing the proportional gain factor K_p of the BESS controller might initially seem like a good choice, but this would not have any noticeable effect due to the power limitations of the internal BESS system. Therefore, the simulation is conducted once more. However, this time the BESS power rating is increased by a factor of six, almost reaching 18 MW. This new rating is still a realistic BESS power rating for real-world power systems [87]. Conducting the same simulation with this higher rated BESS containing the exact same controller parameters as previously, the results seen in Figure 5.50 and 5.51 is found.

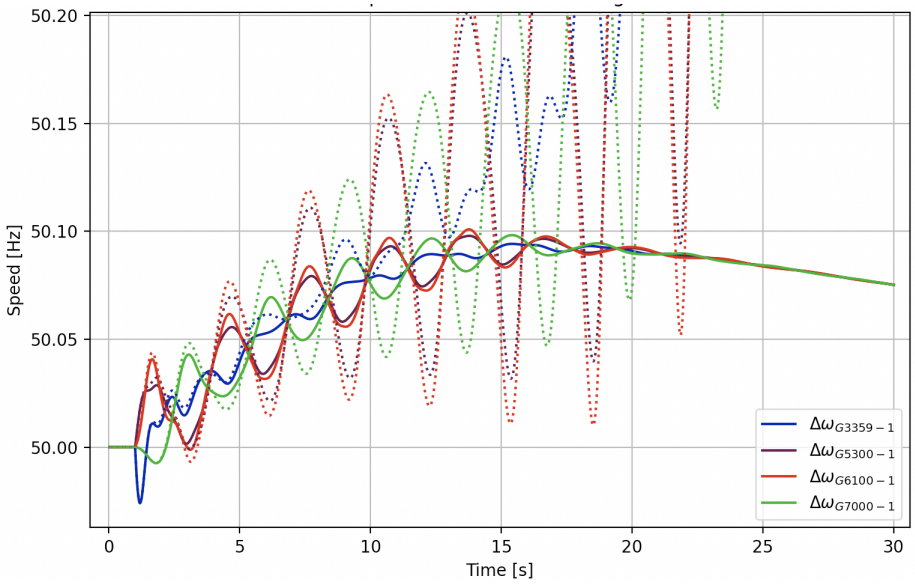

Figure 5.50: Speed response in the system for a few selected generators following a disconnection of L3359-5101-1 at 1.0 seconds, with BESS power capacity of 18 MW installed. Solid lines is the responses when the BESS is included, whereas the dotted lines indicates the base case system (no BESS) response.

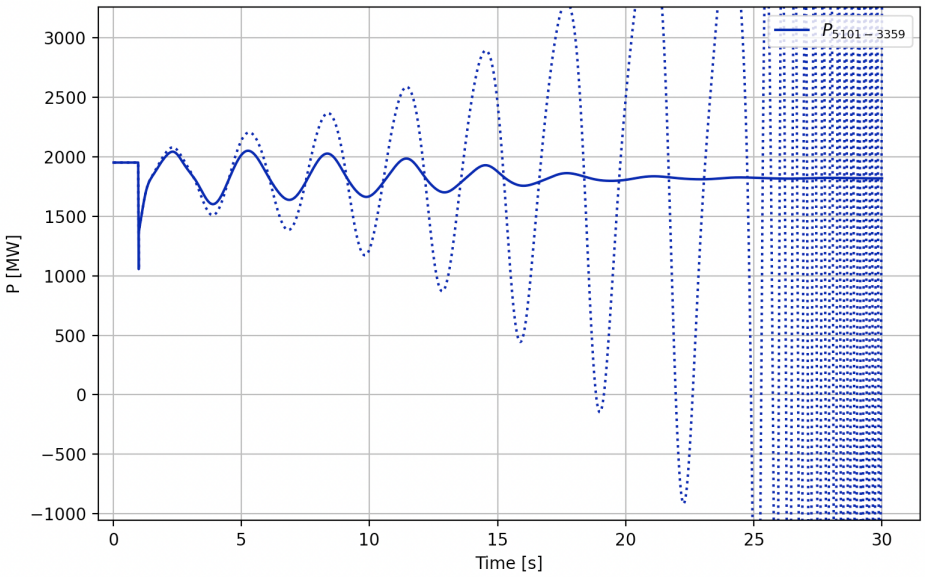

Figure 5.51: Power flow between Bus 5101 and Bus 3359 following a disconnection of L3359-5101-1 at 1.0 seconds when the BESS power rating is increased, with BESS power capacity of 18 9MW installed. Solid lines is the responses when the BESS is included, whereas the dotted lines indicates the base case system (no BESS) response.

It should be noted that the dotted lines in Figure 5.50 and Figure 5.51 exactly matches the dotted lines in Figure 5.48 and 5.49 respectively, as this is the system response without BESS for both cases. When this higher-rated BESS is utilized, it is evident that the response with BESS (solid lines) can damp out the oscillations in the system. The system is thus stable and able to withstand the large disturbance of the line outage is. The BESS capacity and rating will have a major impact on how the BESS can provide grid enhancing performance for larger systems during large disturbances. By having a sufficiently large power rating, it might be able to perform satisfactorily.

5.7 Discussion and Remarks

Non-linear simulations have been conducted to verify the results based on linear analysis for feedback controller design and tuning. However, certain things should be clarified, and this section aims at discussing and summarize findings from the results and simulations.

Remarks on BESS model Implementation

Python has enabled the study of a self-defined BESS model to replicate dynamics associated with grid-connected Energy Storage systems. The BESS model works as intended for analyzing small-signal stability and inter-area oscillation damping. Still, some simplifications were utilized to represent the inverter/converter switching dynamics appropriately for this thesis. Including the first-order time-delays for representing

these is deemed satisfactory without influencing the final results significantly. For the conducted simulations, the actual power provided by the BESS is carefully checked to assure that the implementation does not allow the BESS model to operate outside of its rated conditions, and having the power on the DC-side of the model coincides with the AC-power injected to the grid as the converter are modeled lossless. For possible future research on the actual BESS model and its operation, a more detailed model might be desired, but the proposed model sufficient when analyzing the grid-enhancing performance in larger systems when system stability is the main topic.

Optimality of Selected Feedback Signal and BESS location

Using the transfer function residues given by observability and controllability for determining the optimal feedback signal and BESS location respectively arguably works as intended to provide the largest amount of damping to the poorliest damped mode in the system for the given operating condition. Given that the feedback signal is predetermined to be a difference between the terminal voltage angle signals that are easily measurable if PMUs installments in the system are located appropriately, selecting the combination of voltage angles yielding the largest residue value (or equivalently, the difference in observability vector entries) selects the most suitable combination having the largest effect on the mode of interest for the given operating condition.

Generalizing the obtained results should be done with caution if applied in a real-world system where the operation condition of the grid is constantly changing. Therefore, measures should be taken to account for different characteristic operation conditions. The performance obtained by using other input signal types (for instance, power flows or speed measurements) has not been looked into in this thesis. This could prove to yield satisfactory results, and more research seems necessary. One could also argue that considering several voltage angles (not only the difference between two distinct voltage angles) could prove to be suitable.

Tuning of Controller Parameters based on Residue Approach

The selection of the controller parameters based on the residue approach yields accurate results when small gains and low phase compensation are required. For more considerable gains and phase shifts, errors between the targeted and actual compensation increases, especially for large gains, the mode movement anticipated by the residue and feedback controller has its shortcomings.

Besides looking at modal plots for the initial mode positions and their new positions after the BESS is installed, little effort is undertaken regarding the interaction between the different control loops in the system. For the different versions of the Nordic 44 systems investigated, it could be seen that some of the other modes in the system are

getting influenced by the BESS installment. However, except for the critical mode, none of the other poorly damped modes (having approximately 10% relative damping) was affected significantly by the introduction of BESS. For other systems containing a more significant amount of sophisticated control systems, the interaction between the different control loops might be predominant, and measures such as relative residue index (see Appendix A.3) or similar might be appropriate to utilize when selecting feedback signal and BESS location.

Non-linear Simulations compared with Linear Analysis

For small-signal disturbances, such as relatively small load changes, the linear analysis accurately contains information about the system response following the events. However, for more considerable disturbances (short-circuit events and line outages) that significantly impact the system and excitation of the modes, the 5% damping proposed by the linear analysis is not seen. When calculating the modes in the system, the limitations of the system components, devices, and controllers are not accounted for due to the small perturbation applied in the modal calculation process. Hence, the modes are not accurately representing the amount of damping present when the power limitations of system components are reached. However, a certain amount of damping might be observed anyhow. Consequently, it is shown through simulations that if the power rating of the BESS installment is increased, still being within the range of conventional energy storage systems in real-world power systems, the BESS handles a wide range of disturbances satisfactorily if ancillary control providing POD is employed.

6 Conclusion and Further Work

6.1 Conclusion

Through a literature review, development and implementation of a Battery Energy Storage System (BESS) model and other system components, together with dynamic simulations conducted in Python, this thesis has illustrated the grid-enhancing performance obtainable by appropriately selecting feedback signal and BESS location for effectively providing inter-area oscillation damping in power systems.

A promising solution for adding damping to power systems is using available phasor measurements obtainable through PMUs in the system. Information about the open-loop transfer functions in the system can effectively be used as a decision criterion for appropriately selecting the optimal terminal voltage angles to be used as the input signal to the controller and optimal BESS location for power oscillation damping. The proposed method is based on maximizing the transfer function residue corresponding to the mode of interest, usually the poorest damped inter-area mode. The controller selection procedure is verified through analyses conducted in different versions of the Nordic 44 test network. Each version yields slight variations in the optimal feedback signal and BESS location, further strengthening the procedure's validity.

The transfer function residues facilitate the selection and tuning of the POD-controller parameters as they contain information about the mode sensitivity for a proportional feedback controller, being generalizable to an arbitrarily chosen feedback controller. However, the accuracy of the tuning procedure worsens when considerable gains and phase compensations are required.

The performance of the installed BESSs is validated through numerous non-linear simulations taking into consideration the differential- and algebraic equations describing the dynamics of the system. For small-signal disturbances, the damping proposed by the modal analysis is observed in the simulations, and the BESSs are performing as anticipated from the linear analysis. The limitations of the power system components are not accounted for in the modal calculations, causing deviations between the linear and non-linear results for more immense disturbances, which further promotes the necessity of using non-linear simulations for exploiting drawbacks and shortcomings of the linearized model.

Linear analysis is a valuable tool for selecting the feedback signal and BESS locations and proves beneficial for controller parameter tuning. However, the constantly changing operating conditions of the systems and the power limitations of BESSs should be accounted for when employed for real-world applications. Further development and

research are needed, but the potential benefits for systems operators utilizing available phasor measurements and properties of the linearized power system as a tool for controller selection are evident.

6.2 Further Work

Although the study indicates the possibilities of using transfer function residues and available phasor measurements for appropriately selecting feedback signal and BESS location, further work is needed to verify the selection procedure and exploit the proposed method's possibilities and shortcomings for different operating conditions. Hence, suggestions on further work to be conducted for increasing the knowledge and utilizing available measurements effectively for real-world applications are identified.

- Look further into **different controller input signal types**, or possibly a combination of more than two voltage angles.
- Enhance the Nordic 44 model by a more accurate model, representing the real-world system in more detail. Although the results in this thesis are validated for different versions of the Nordic 44 test network, **a more realistic system** might prove to exploit some shortcomings not captured by the results in this thesis.
- Specifically, more **sophisticated load models** could conveniently be implemented and used for capturing real-world dynamics more accurately. This thesis relies on constant impedance load models having shortcomings in representing a non-negligible amount of real-world loads dynamic behaviors.
- The optimal feedback signal and BESS location are in this thesis selected based on a pre-defined given operating condition of the test network. However, real-world systems have constantly varying power demand and thus production, and more research is needed for validating the selection procedure of the **optimal control loop for changing operating conditions of the grid**. Adaptive controller parameter tuning might be a suitable way to cope with this to obtain the desired amount of phase compensations and better handle grid uncertainty and changing system topologies.
- A significant concern is the **interaction between the different control loops** in the system, which for the investigated systems in this thesis did not accompany any significant problems. However, for other systems containing a greater amount of local controllers, measures of interaction should be investigated and possibly used together with maximizing the residues for appropriately selecting the damper control loops.
- Using remote phasor measurement signals naturally exhibits **communication delays**. Further research seems necessary to understand how the uncertainty in communication systems affects the performance of the selected feedback signals.

Appendix

A Supplementary Theory and Deviations

A.1 Frequency Stability and Control

Suppose a sudden disturbance happens in a power system. In that case, there will be a power imbalance in the system, and as a consequence, the frequency in the system will change [56]. This change in frequency is often divided into several stages describing the different characteristic steps of the frequency response. The rotational speed of a generator is proportional to frequency, such that if the speed of the generator rises, so does the frequency in the system [88]. A turbine-governor control system ensures that load fluctuations in the system only cause low speed changes $\Delta\omega$. Figure A.1 shows the system response with and without governors[A.1] in the system following a load increase of 0.05 p.u. of load located in area 1 based on a base of 900 MVA. The system parameters can be found in Appendix C.1.

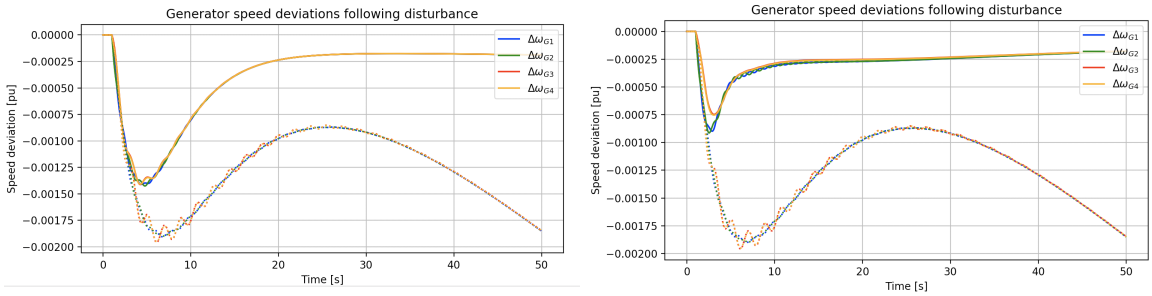

(a) $R_{G1} = R_{G2} = 0.06$, $R_{G3} = R_{G4} = 0.12$

(b) $R_{G1} = R_{G2} = R_{G3} = R_{G4} = 0.02$

Figure A.1: Simulations conducted for different governor droop constants. Dotted lines shows the system response if governors are not included in the system. One observes that having governors employed (solid lines) yields a new steady-state frequency in the system, whereas smaller droop constants (Figure **??**) reduces the initial drop in frequencies due to faster changes of generator power reference set-points.

One observes that in the case of governors included in the system, the frequency drop is less significant compared to the case without governors. The generators are able to adjust their power outputs based on the power imbalance and thereby speed deviations in the system. The amount of speed drops would change if other droop values where used. When the valve position c of the generator is assumed to vary linearly between 0 (fully closed) and 1 (fully open), the change in valve position given a change in

[A.1] Governors is described more detailed in Section B.1.1, but is essentially a controller that adjusts the mechanical power reference of the generators.

generator speed can be expressed as $\Delta c = -\Delta\omega/R$, where R is noted the droop if taken in per units of nominal speed, that is, $R[pu] = R/\omega_n$, which is often denoted ρ [56]. The idealized speed-droop characteristics can then be shown to be

$$\frac{\Delta\omega}{\omega_n} = -\rho\frac{\Delta P_m}{P_n}, \tag{A.1}$$

where subscript n indicate nominal values. This equation simply says that if the valve gating position c is linearized between 0 and 1, there will be a linear relationship between speed deviation and power imbalance in the system. If the power demand is increased in the system, the speeds and thereby frequency, will drop. The latter comes as a consequence of the swing equation discussed in Section 3.1. Generalizing Equation (A.1) to account for all generators i in the system N_G, where the total power change in the system is denoted ΔP_T one may write

$$\Delta P_T = \sum_{i=1}^{N_G} \Delta P_{mi} = -\frac{\Delta f}{f_n}\sum_{i=1}^{N_G}\frac{P_{ni}}{\rho_i} = -\Delta f\sum_{i=1}^{N_G}\frac{P_{ni}}{\rho_i f_n}. \tag{A.2}$$

This equation defines the total system ability to account for power imbalances at the cost of deviation in system frequency Δf. Equation (A.2) essentially says that it is a sum of the power regulations capabilities of the individual generators present in the system, which from a physical aspect seems reasonable.

Some important definitions of the different stages of frequency control are needed. From Machowski, one reads that

> "The action of turbine governors due to frequency changes when reference values of regulators are kept constant is referred to as *primary frequency control*." [56, p. 340]

This is basically what is shown by Equation (A.2). However, when the generators are already operating at the maximum power output, they cannot participate in primary frequency control. In a real-world power system, it is of uttermost importance to assure that the system always has some spare capacity available as the total load in the system is constantly changing [89]. This additional capacity is often referred to as *spinning reserves*, and system operators need a sufficient amount of this in order to have a satisfactory system operation. Although out of the scope of this report, it is worth mentioning that with an increasing share of renewable generation in the power system, there is less conventional inertia in the system. Research is being done into how these new generation types can participate in primary frequency control, for instance, by the introduction of auxiliary control systems providing virtual inertia to power system components [90].

From Figure A.1 one notices that although the generators can adjust their power output for compensating for the load increase, a steady-state error in terms of the frequency is observed. In order to account for this, additional controllers providing *secondary control*, aiming at removing this steady-state deviation, is needed. This corresponds to changing the frequency-power linear characteristics upwards or downwards, depending on the sign of frequency deviation in the system. In interconnected areas, such additional control would have to be centralized as there are several different control areas, and decentralized secondary control would cause undesirable changes on power tie-lien flows [56]. Without going further into detail, such controllers are usually based on PI regulators. The change in reference power settings is adjusted based on tie-line flows and frequency error in the system, aiming at removing steady-state errors. Secondary control is out of the scope for the topics covered in this thesis. However, a secondary control system utilizing local measurements and tie-line flows was developed during the work with this thesis and is provided for the interested reader in Appendix B.3.

The slowest working, and last step of frequency control, is referred to as *tertiary control*. This control step is often based on economic dispatch and optimal power flow, such that the generation in the system is redistributed based on some external control signals while still maintaining the system frequency at its reference value. This control can either be done manually or automatically and changes the different generator setpoints based on specific standards such as maintaining enough spinning reserves, optimal dispatch of units participating in secondary control, and maintaining a satisfactory amount of secondary control reserves in the system [56].

A.2 Numerical calculation of state-matrix $\boldsymbol{A}$

The way this matrix is calculated in the Python simulator used for this thesis is by the use of difference equations [57]. A short description of this is provided here. It is essential to calculate modal properties in the system and thus be fundamentally important for the conducted simulations and analysis. A derivative of a multi-variable function $f(x, y)$ is a point ($x = a, y = b$ is by definition given by

$$\frac{\partial f}{\partial x}(a, b) = \lim_{h \to 0} \frac{f(a + h, b) - f(a, b)}{h}. \tag{A.3}$$

By using a difference equation which can be proved by the use of Taylor series expansion and neglecting higher-order terms [57], one obtains a decently accurate representation of the derivative at a given operating point

$$\frac{\partial f_k}{\partial x_i}(\hat{\boldsymbol{x}}, \hat{\boldsymbol{u}}) \approx \frac{f_k(\hat{x}_1, ..., \hat{x}_i + \epsilon, ..., \hat{x}_n, \hat{u}_1, ..., \hat{u}_n) - f_k(\hat{x}_1, ..., \hat{x}_i - \epsilon, ..., \hat{x}_n, \hat{u}_1, ..., \hat{u}_n)}{2\epsilon}. \tag{A.4}$$

Choosing ϵ small enough allows for accurately finding the linearized system matrix numerically. Thus, by simply adding and subtracting ϵ on the index corresponding to the i'th state variable in the state variable vector and computing the difference from Equation (A.4), an accurate estimation of the partial derivative terms can be found numerically. The derivative terms associated with the input, $\frac{\partial f_k}{\partial u_i}(\hat{\boldsymbol{x}}, \hat{\boldsymbol{u}})$, is calculated in the same way.

A.3 Relative Residue Index

When the open-loop transfer functions between inputs and outputs in the system are computed using the residue method, one obtains multiple residue values. For most purposes covered in this thesis, one is mostly interested in the residue corresponding to the mode of interest, usually the weakest damped mode in the system. Most of the analysis and parameter tuning is based on the value of this residue. However, when a WADC is deployed in the system, the controller loop will be influenced by the interaction of the WADC and other modes in the system [86]. The larger the RI is, the weaker is the interaction between the WADC and the other modes in the system, and the higher is the accuracy of the controller tuning. For an input u_i, output y_j and mode of interest λ_k, the RI can be defined as [86]:

$$RI = \frac{|R_{ij,k|}}{\sum_{t=1,t\neq k} |R_{ij,t}|}, \tag{A.5}$$

where $R_{ij,k}$ is the residue in the open-loop transfer function between the input u_i and output y_j corresponding to the k-th mode.

A.4 Generator Angle and Terminal Angle Correlation

As the linear analysis and the linear theory is mostly built up by using state variables and other quantities in the system, a justification of why the terminal voltage angle follows the generator voltage angle is given. This is of major importance in this thesis, as the analysis and discussion is based on using generator voltage angle (state-variable in the system) as feedback signal, whereas from PMUs, the available measurement is terminal voltage angles. It is confirmed through simulations that one gets satisfactory results by doing it this way, with some small deviations in the results, but an analytical approach seems necessary in order to justify the structure and analysis performed in this thesis. Hence, the motivation behind this deviation is to showcase that under some assumptions, the generator voltage angle follow the generator terminal voltage angle such that the relationship

$$\delta = \delta_0 + \Delta\delta = \delta_0 + \Delta\theta \tag{A.6}$$

is valid, where δ is the generator voltage angle, δ_0 is the steady-state value of the generator voltage angle relative to the generator terminal, $\Delta\delta$ is the change in generator voltage angle and $\Delta\theta$ is the change is generator terminal voltage change. That is, the generator voltage angle follows the changes in the generator terminal voltage angle such that for a change in terminal angle $\Delta\theta$, one observes a change in generator voltage angle $\Delta\delta$ satisfying $\Delta\delta = \Delta\theta$. This relationship is shown in Figure A.2.

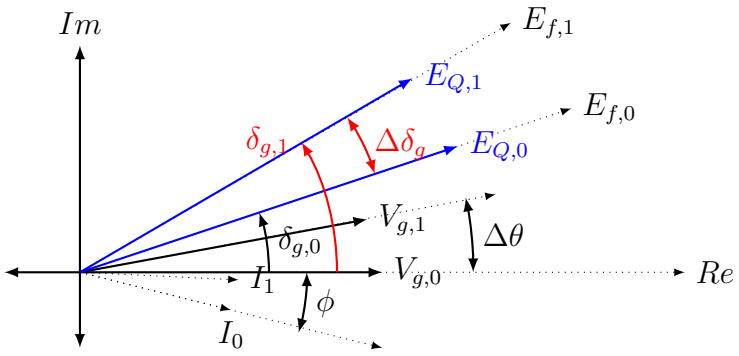

Figure A.2: Illustrative example showing what is discussed in the previous equations. The figure shows that when the terminal voltage magnitude $|\boldsymbol{V_g}|$, current $|\boldsymbol{I}|$ and power factor angle ϕ is held constant, the change in internal generator angle $\Delta\delta_g$ equals the change in terminal voltage angle $\Delta\theta$.

Although this relation could somehow be anticipated from Figure A.2, a mathematical deviation is deemed necessary in order to show it clearly. From the classical generator model being discussed in Section 4.4.1 connected to a stiff grid, one have the following

$$\boldsymbol{E_Q} = \boldsymbol{V_g} + jX_q\boldsymbol{I_g} = \boldsymbol{V_g} + jX_q\frac{\boldsymbol{S_g^*}}{\boldsymbol{V_g^*}}, \tag{A.7}$$

where the angle of E_Q is defining the generator voltage angle (state variable in the system), X_q is the q-axis reactance of the generator, $\boldsymbol{I_g}$ is the generator current given by $\boldsymbol{S_g}^*$ and $\boldsymbol{V_g}^*$ of which are the complex conjugate of the power provided by the generator and the generator terminal voltage respectively. The motivation behind this deviation is to show that when the terminal voltage angle changes, the generator angle changes with the same amount when assuming that the terminal voltage amplitude stays constant, the power provided by the generator is constant (no governor interaction). Thus, one have an analytical way of showing that the deviations between terminal voltage angles in the system will essentially be the same input signal as deviation between generator voltage angles.

Assuming the terminal voltage is constant at 1.0 p.u and denoting the complex constant number $jX_qS_q^*$ as $\boldsymbol{A} = |A|e^{j\alpha}$ and the generator terminal voltage angle as θ,

equation (A.7) might be rewritten as

$$\begin{aligned}\boldsymbol{E_Q}(\theta) &= 1.0e^{j\theta} + \frac{\boldsymbol{A}}{1.0e^{-j\theta}} = 1.0e^{j\theta} + \frac{|A|e^{j\alpha}}{1.0e^{-j\theta}} \\ &= [cos(\theta) + |A|cos(\alpha+\theta)] + j[sin(\theta) + |A|sin(\alpha+\theta)].\end{aligned} \tag{A.8}$$

Enforcing a small change in the terminal voltage angle of $\Delta\theta$, one can rewrite this into

$$\begin{aligned}\boldsymbol{E_Q}(\theta_0+\Delta\theta) =& [cos(\theta_0+\Delta\theta) + |A|cos(\alpha+\theta_0+\Delta\theta)] \\ &+ j[sin(\theta_0+\Delta\theta) + |A|sin(\alpha+\theta_0+\Delta\theta)],\end{aligned} \tag{A.9}$$

where θ_0 is the initial steady-state terminal voltage angle. The generator voltage angle δ is found to be $\angle\boldsymbol{E_Q}$ [56] and by using (A.9), it can be expressed as

$$\begin{aligned}\delta(\theta_0+\Delta\theta) = \angle\boldsymbol{E_Q}(\theta_0+\Delta\theta) &= \arctan(\frac{\Im(\boldsymbol{E_Q}(\theta_0+\Delta\theta))}{\Re(\boldsymbol{E_Q}(\theta_0+\Delta\theta))}) \\ &= \arctan\frac{sin(\theta_0+\Delta\theta) + |A|sin(\alpha+\theta_0+\Delta\theta)}{cos(\theta_0+\Delta\theta) + |A|cos(\alpha+\theta_0+\Delta\theta)} \\ &= \arctan\frac{cos\Delta\theta[sin\theta_0 + |A|sin(\alpha+\theta_0)] + sin\Delta\theta[cos\theta_0 + cos(\alpha+\theta_0)]}{cos\Delta\theta[cos\theta_0 + |A|cos(\alpha+\theta_0)] - sin\Delta\theta[sin\theta_0 + sin(\alpha+\theta_0)]},\end{aligned} \tag{A.10}$$

where one are making use of the trigonometric identities

$$\begin{aligned}sin(\alpha+\beta) &= sin(\alpha)cos(\beta) + cos(\alpha)sin(\beta) \\ cos(\alpha+\beta) &= cos(\alpha)cos(\beta) - sin(\alpha)sin(\beta).\end{aligned} \tag{A.11}$$

Dividing Equation (A.10) by $cos\Delta\theta(cos\theta_0 + cos(\alpha+\theta_0))$ and rearranging yields

$$\delta(\theta_0+\Delta\theta) = \arctan\frac{tan\Delta\theta + \frac{sin\theta_0+|A|sin(\alpha+\theta_0)}{cos\theta_0+|A|cos(\alpha+\theta_0)}}{1 - tan\Delta\theta\frac{sin\theta_0+|A|sin(\alpha+\theta_0)}{cos\theta_0+|A|cos(\alpha+\theta_0)}}. \tag{A.12}$$

Hence, by making use of the trigonometric identity

$$\arctan\alpha + \arctan\beta = \begin{cases}\arctan\frac{\alpha+\beta}{1-\alpha\beta} & \text{if } \arctan\alpha + \arctan\beta \in (-\frac{\pi}{2}, \frac{\pi}{2}) \\ \arctan\frac{\alpha+\beta}{1-\alpha\beta} + \pi & \text{if } \arctan\alpha + \arctan\beta \in (\frac{\pi}{2}, \pi) \\ \arctan\frac{\alpha+\beta}{1-\alpha\beta} - \pi & \text{if } \arctan\alpha + \arctan\beta \in (-\pi, -\frac{\pi}{2}),\end{cases} \tag{A.13}$$

one can rewrite Equation (A.12) into

$$\begin{aligned}\delta(\theta_0+\Delta\theta) &= \arctan\frac{sin\theta_0 + |A|sin(\alpha+\theta_0)}{cos\theta_0 + |A|cos(\alpha+\theta_0)} + \arctan(\tan\Delta\theta) + \psi \\ &= \delta_0 + \Delta\delta = \delta_0 + \Delta\theta\end{aligned} \tag{A.14}$$

where the value ψ is a constant taking a value of 0, π, or $-\pi$, as seen in Equation (A.13). Consequently, it can be concluded that under the assumptions that the voltage

magnitude stays constant and no governor interactions with the power being provided from the generator, the generator voltage angle δ follows the shift in the terminal angle $\Delta\theta$. This concludes the proof and shows that if the analysis is done using generator angle instead of generator terminal voltage angle, both of these signals will follow one another (given the ideal assumptions assumed here), and should therefore be a valid way of overcoming the problem of generator terminal voltages not being present in the state variable vector in the system. However, some small deviations should be expected for simulations utilizing the sixth-order generator model and not completely satisfying constant terminal voltage magnitude, but these are seen to only account for minor deviations from numerous simulations.

As a closing point for this deviation, a small simulation is carried out in a fictive and simple power system consisting of two generators. This allows for looking at how the deviation conducted in this thesis performs when the generator voltage magnitudes are held constant (as was assumed in the analytical deviation), while also gaining fundamental insight into the accuracy of the assumption $\Delta\theta \approx \Delta\delta$ when the voltage magnitudes are varying (representing more realistic behaviour). The generator terminal voltage angle is decaying with a frequency of 0.4 Hz for representing a somehow realistic behaviour of an inter-area mode. Figure A.3 shows the generator voltage angles δ_i and terminal voltage angles θ_i as a function of time.

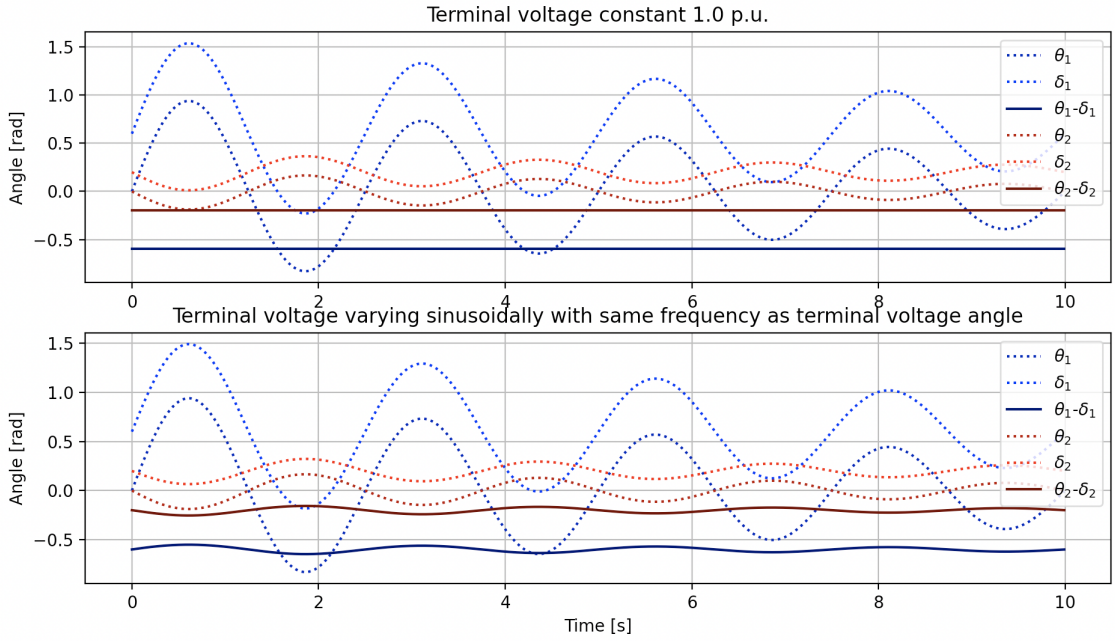

Figure A.3: Visual comparison of the terminal voltage angles θ_i and the generator voltage angles δ_i. It is clear that when the voltage magnitude is assumed constant, the difference between the local terminal voltage angle and generator voltage angle is constant, that is, they would provide the same magnitude of input signal. When the voltage magnitudes are varying as a decaying sinusoid, $|\boldsymbol{V_g}| = 1.0 + 0.05e^{-0.1t}sin(2\pi 0.4t)$, there are some slight deviations, but not really worrying. The amplitude of the change in angles at bus 2 is chosen to be 0.2, while it is 1.0 at bus 1. This is done in order to account for differences in observability vector present in more realistic power systems as discussed in Section 3.2.3.

One observes that for the upper Figure (constant voltage magnitudes) the deviation between the generator angle and terminal angle is a constant line (approximately at -0.6 rad), such that the relationship $\Delta\delta_i = \Delta\theta_i$ is withheld during the simulation for both generators. When the voltage magnitudes are varying sinusoidal with the same frequency as the terminal angles, the deviation between these signals are not constant anymore, and small oscillations (differences) are present. However, the magnitudes of these oscillations are small, such that both signals should in theory yield approximately the same response in a non-linear simulation for a larger and more complex system.

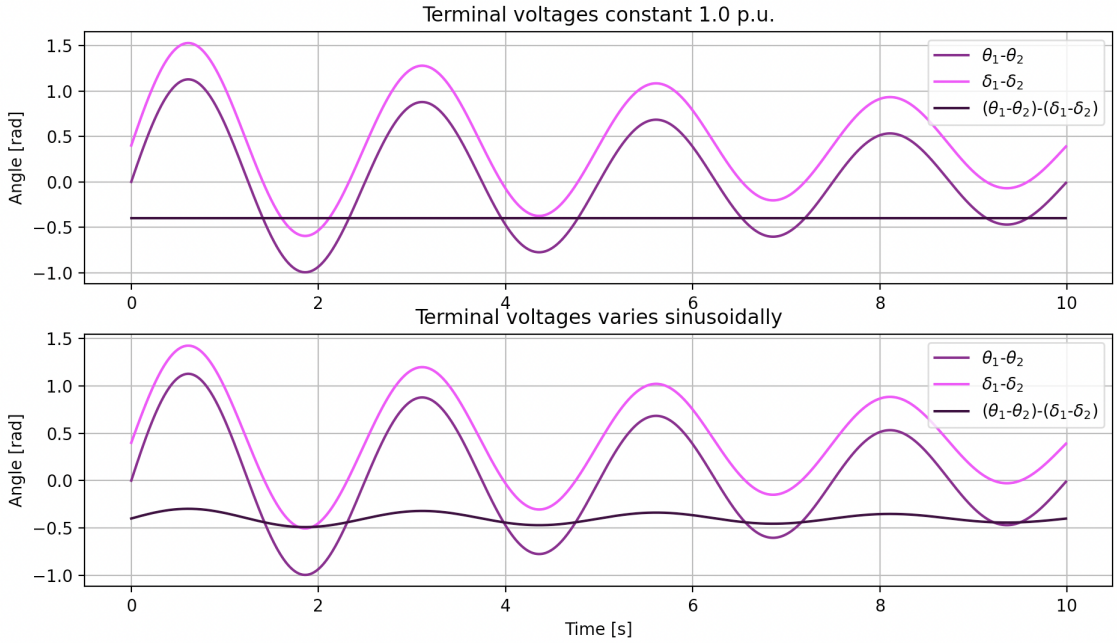

Figure A.4: Wide area measurements and signals. When the terminal voltage magnitudes are constant, one are obtaining the exact same input signal if one are using differences in terminal voltage angles or differences in generator voltage angles in the system, hence the constant line at -0.4 rad in the upper figure. When the voltage magnitudes are allowed to be changed (similar as for local signals in Figure A.3), small oscillations are present in the signal $(\theta_1 - \theta_2) - (\delta_1 - \delta_2)$.

The same justification goes for the wide-area signals presented in Figure A.4. When the terminal voltage magnitudes are constant, the difference between the signals is simply a constant line, such that whether one are using differences in generator angles or terminal angles in the system as feedback signal, the same controller action would be undertaken. Similarly, when the voltage magnitudes are being represented more realistically and allowed to vary, one sees small oscillations in the differences between the signals. Nevertheless, it should be evident from the simulation that the magnitude of these oscillations are rather small, which prove that using generator angles instead of terminal angles when designing controllers should be a valid way of tuning controllers employing terminal voltage angles as input signal.

A.5 Direct Quadrature Zero Transformation

In terms of implementing control systems in a power system, a common approach is to transform the coordinate systems for obtaining decoupled control of active and reactive power in the system. The general idea behind abc-dq0 transformations is to represent the three-phase quantities as constant values in steady-state for simplifying the controls. In a three-phase power system, one usually denotes voltage quantities as v_a, v_b, and

v_c, where the subscripts indicate the associated phase or axis. These voltages are in a balanced system phase shifted by 120 degrees, and one defines their reference axis likewise. The phase voltages vary in magnitude, from a maximum positive value to a minimum value during a half period, given that one is operating in a steady-state. The Clark transform, commonly known as $\alpha\beta$-transform transforms three-phase quantities into a single rotating vector, given that it is a balanced system, $v_a + v_b + v_c = 0$ [91]. For instance, if one is looking at the voltages measured at a bus, it is tempting to transform them into a single rotating vector, maintaining all the properties of the original quantities. This is made possible by the transform below, which defines two new orthogonal planes.

$$\begin{bmatrix} v_\alpha \\ v_\beta \\ v_\gamma \end{bmatrix} = \sqrt{\frac{2}{3}} \begin{bmatrix} 1 & -\frac{1}{2} & -\frac{1}{2} \\ 0 & \frac{\sqrt{3}}{2} & -\frac{\sqrt{3}}{2} \\ \frac{1}{\sqrt{2}} & \frac{1}{\sqrt{2}} & \frac{1}{\sqrt{2}} \end{bmatrix} \begin{bmatrix} v_a \\ v_b \\ v_c \end{bmatrix} \tag{A.15}$$

The last scalar, v_γ, will only be present if the condition $v_a + v_b + v_c = 0$ is not met, otherwise the vector to $\alpha\beta\gamma$ vector will be on the $\alpha - \beta$-plane [91]. The scalar in front of the matrix in Equation (A.15) is rather arbitrary. It can be chosen freely as long as one is accounting for this while doing the inverse transformation. However, the value of $\sqrt{2/3}$ makes the transformation power conservative. Another common choice is 2/3, which makes the voltage amplitudes consistent in both abc-reference frame and dq0. Suppose the newly created vector in the $\alpha - \beta$ plane is a rotating vector with constant length and speed. In that case, it should, in theory, account for this speed and make the vector stationary. This is made possible by the Park transformation, first proposed by Park in 1929 for use in synchronous machines [83]. The transformation takes the rotating vector defined in the $\alpha - \beta$-plane and takes advantage of the fact that one has preliminary information about the rotating speed of the quantities. The transformation from $\alpha\beta\gamma$ quantities to dq0 can be done by the following transformation [92]

$$\begin{bmatrix} v_d \\ v_q \\ v_0 \end{bmatrix} = \begin{bmatrix} cos(\theta) & sin(\theta) & 0 \\ -sin(\theta) & cos(\theta) & 0 \\ 0 & 0 & 1 \end{bmatrix} \begin{bmatrix} v_\alpha \\ v_\beta \\ v_\gamma, \end{bmatrix} \tag{A.16}$$

where the angle theta is given by

$$\theta(t) = \int_0^t \omega(\tau) d\tau + \theta_0, \tag{A.17}$$

where ω is the instantaneous fundamental angular frequency [93] and θ_0 is the angular position at t = 0 for the given transformation alignment [91]. This transformation allows for the three-phase quantities to be represented as constant values in steady-state, which makes the control significantly easier. Going from abc-quantities directly into dq0 components is also possible in one step, by using the appropriate transformation

matrix.

$$\begin{bmatrix} v_d \\ v_q \\ v_0 \end{bmatrix} = \boldsymbol{T_{dq0}} \begin{bmatrix} v_a \\ v_b \\ v_c \end{bmatrix}, \tag{A.18}$$

and the transformation matrix, $\boldsymbol{T_{dq0}}$ is then found to be, by combining equation (A.15) and (A.16)

$$\boldsymbol{T_{dq0}} = \sqrt{\frac{2}{3}} \begin{bmatrix} cos(\theta) & cos(\theta - 2\pi/3) & cos(\theta + 2\pi/3) \\ -sin(\theta) & -sin(\theta - 2\pi/3) & -sin(\theta + 2\pi/3) \\ \frac{1}{\sqrt{2}} & \frac{1}{\sqrt{2}} & \frac{1}{\sqrt{2}} \end{bmatrix} \tag{A.19}$$

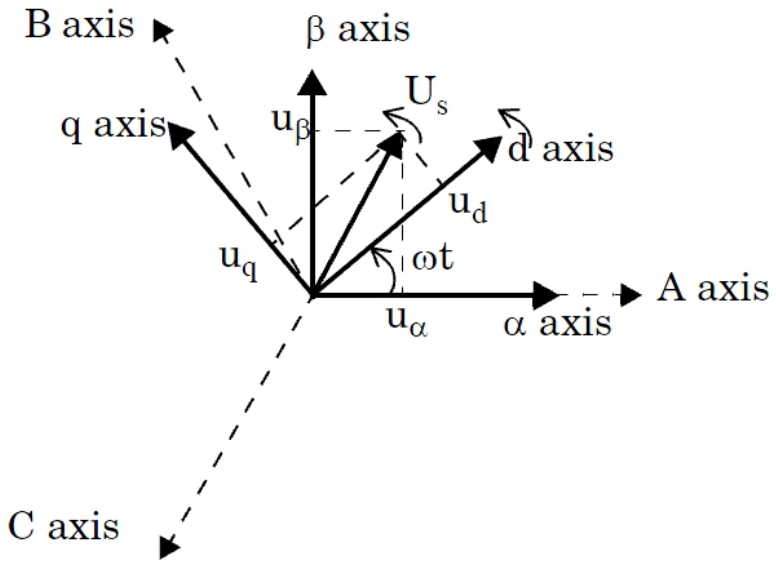

Figure A.5: Graphical representation of the abc-$\alpha\beta\gamma$-dq0 transforms. In this figures the q-axis is leading the d-axis by 90 degrees which is the chosen reference frame for the implementations used in the modelling for this report. The dq-axes are rotating with the grid frequency (ωt) yielding constant values for dq-components for balanced conditions in the phases. Source: Adapted from [94]

Figure A.5 provides a visual representation how the different quantities are related. It is evident that the $\alpha - \beta$ planes are defined as two new orthogonal axes, and one sees that the $\alpha - \beta$ vector is rotating with a rate given by ωt. This representation is assuming the frequency to be constant, which is why the angular position, given by the integral in Equation (A.17) is simplified. Transforming the system into equivalent quantities in the dq0 reference frame usually employed one of two possible alignments. One either chooses the angular position at t = 0 to be such that $v_d = 0$, or choose another reference alignment such that $v_q = 0$ in steady-state. Proceeding work is simplified substantionally if one can remove the impact of one of these, but the system dynamics are still intact.

A useful property of the transformation is that active and reactive power will be related to the dq0-components in a familiar way [83]

$$\begin{aligned} p &= v_d i_d + v_q i_q \\ q &= v_q i_d - v_d i_q, \end{aligned} \tag{A.20}$$

where p and q is the instantaneous active and reactive power respectively. As the transformation generally relies on reference frame alignment such that either v_d or v_q becomes zero, the active and reactive power can be controlled in a decoupled manner by the use of (A.20), which will be taken advantage of when designing a battery model together with its control[A.2], as well as demand response in the system[A.3].

B Supplementary Dynamic Models

B.1 Conventional Control Systems - Operation and Control

B.1.1 Governor (GOV)

Governors are essential for the operation of power systems. The governors are a control system included in the different generators in the system, which allows for adjustable power supply from the generating units. Consequently, one can control the overall system such that generation equals demand. Conventional governors usually take local speed/frequency deviation measurements as input and adjust the mechanical input power to the turbines based on this input and the droop characteristics of the control system.

There are several types of commonly used governors in power systems, and for this report two different models will be used. The first one is a conventional governor usually denoted TGOV1 and its schematic block diagram can be seen in Figure B.1.

[A.2] The battery model is presented in Section 4.5

[A.3] Demand response implementations is covered in Appendix B.2.

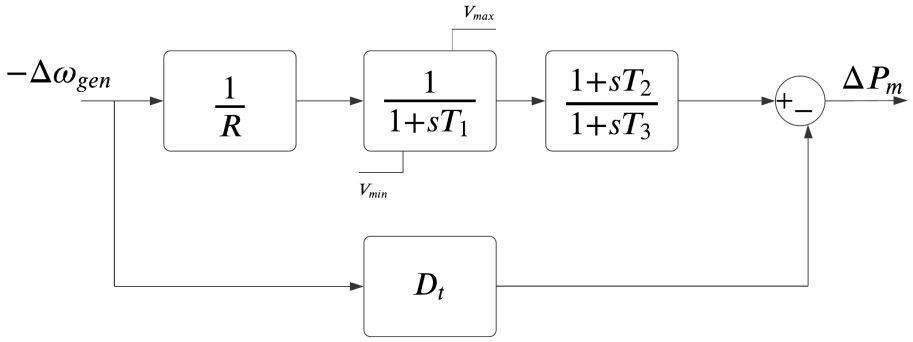

Figure B.1: Governor model TGOV1.

A second type of governor is also implemented in the simulation tool in order to replicate hydraulic turbine governing systems, and the implementation is based on the work presented in Machowski [56, p. 480]. The motivation for implementing this was to facilitate simulations using hydro-governor systems, which accounts for most of the generating units in Norway. Hydro-governor systems are characterized by transfer functions containing a zero in the right-half of the complex plane. This corresponds to a delayed response and is a consequence of the gate valve openings and the water pressures in the penstocks [58]. The flow rate of the water in the penstocks is incapable of changing instantaneously. Hence, immediately after a change in valve position is applied by the governor actions, the water velocity responds with an opposite effect, before gradually stabilizing and responding towards the desired response [56, p. 479].

This effect can be seen by the block diagram illustrating the turbine-governor in Figure B.2. The presence of a zero in the right-half plane for the transfer function between the change in valve position Δc and the output change in mechanical power reference ΔP_m corresponds to this undesired behavior. A transient feedback element aiming at reducing governor gain for fast-changing valve positions is included to compensate for this [56, p. 480]. A simplified model is implemented for the dynamic simulations, presented in Figure B.3. The relations between the block parameters seen in Figure B.2 and Figure B.3 together with typical values can be found in Machowski [56, p. 481].

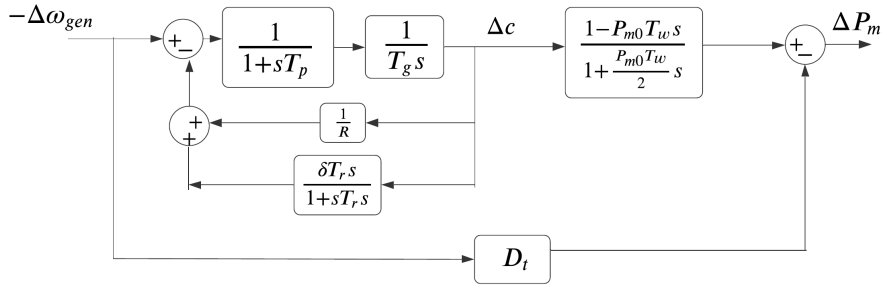

Figure B.2: Governor model HYGOV with Transient Gain Reduction (TGR).

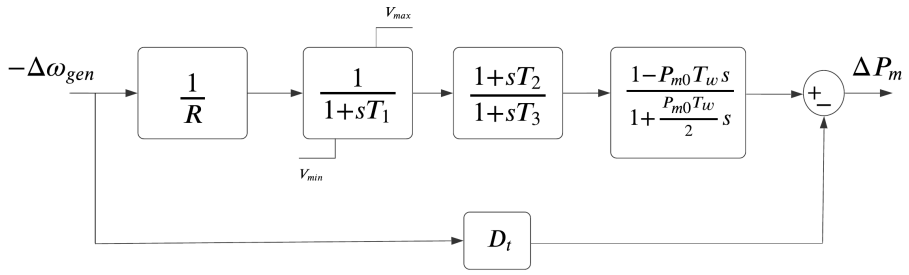

Figure B.3: Governor model HYGOV simplified. This configuration is essentially the same as the more detailed scheme shown in Figure B.2, where some simplifications are utilized to easify the implementation while the fundamental dynamics are maintained.

To visualize the effects of having Governors installed in the system, a small simulation is conducted. For this simulation, the AVRs are kept active such that the terminal voltages remain close to constant. The parameters for these control systems can be found in Appendix C.1. For the part using Governors, every generator in the system is equipped with a Hydro-governor, each having a droop constant of 5%. A similar but slower response could be observed by using the governor model TGOV1, which has a faster response, but hydro-governor is chosen to showcase the effect of the right-half zero in the open-loop transfer function seen in the block diagram in Figure B.3. The disturbance applied to the system is a reduction of power demand in Area 1 by 50MW, and one should expect the mechanical power input to the different generators in the system to be reduced as a response to this when the Governors are installed in the system.

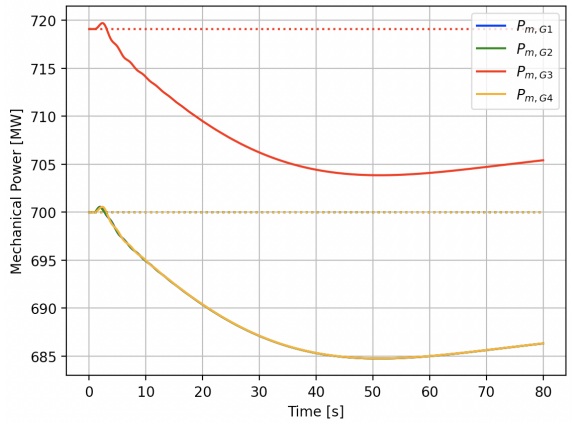

(a) Mechanical power input to the different generators. For the case without governors (dotted constant value lines), the mechanical input powers can be seen to be constant values, whereas when governors are active, the mechanical power input is reduced to account for the decrease in load-demand. The initial opposite response of the mechanical power associated with hydro-governors (seen approximately in the interval t=1.0s to t=3.0s) is observable from the plot.

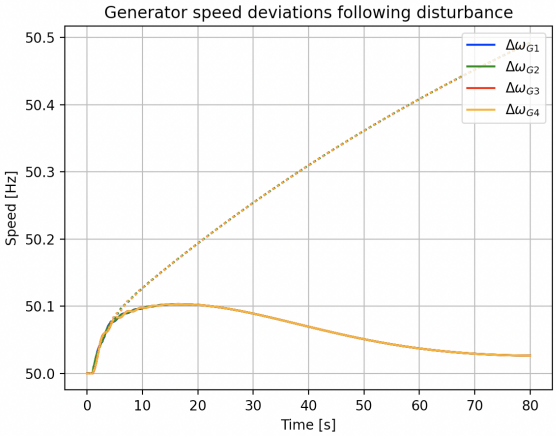

(b) Speed response in the system. For the case without governors in the system, the speed is not able to fall back to the initial value, and keeps on increasing. Thus, in order to reach the scheduled frequency in the system following a disturbance, the power provided by the generators needs to be adjusted by the help of governors. There are no integrator-effects in the governors, hence a small deviation away from the scheduled frequency is expected.

Figure B.4: Mechanical power input to the generators and speed response in the system following a reduction of L1 by 50MW at t = 1.0 seconds. The solid and dotted lines indicates the response with and without hydro-governors connected, respectively.

B.1.2 Automatic Voltage Regulator (AVR)

The generator's terminal voltage is controlled by controlling the excitation current [56] by the use of Automatic Voltage Regulators (AVRs). These are essentially used for all generators in the system, as keeping a somehow constant terminal voltage is of key interest for safe power system operation. The measured terminal voltage is compared to the reference terminal voltage, and based on the deviation between these signals; the AVRs aim at adjusting the exciter current for obtaining the desired terminal voltage. An additional input signal originating from a Power System Stabilizer (PSS) is often added for providing additional dampening torque in the system for improved transient stability. The fundamental principles behind the PSS will be discussed in Section B.1.3. A common practice is to equip control systems with limiters to reduce the number of controller interactions, keep the controlled components within safe operating limits, and avoid disastrous situations. For a standard AVR, these limiters are often included in order to reduce the magnitude of the excitation current, which can be seen in the

last block of the AVR model in Figure B.5

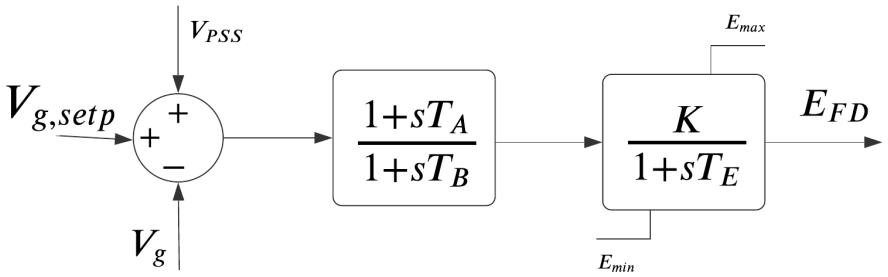

Figure B.5: Automatic Voltage Regulator (AVR) model SEXS.

Although the generator and its components may be able to withstand operation over their nominal values for a short duration, thermal limitations in equipment are what is being considered for steady-state safe operation [58, p. 554]. Therefore, in addition to the current limiters, the SEXS AVR model utilized for this thesis contains a lead-lag block and a low-pass filter for phase shifts and removing the influence of high-frequency input signals, respectively.

In practice, every generator is equipped with an AVR to maintain the terminal voltage close to its given reference point, but a fast-acting/responding AVR may cause the system to lose stability. In addition, AVRs introduce a detrimental effect on systems as the damping introduced by the field winding are weakened [56] which reduces the stability limits of the overall system. A more detailed and in-depth discussion about the working principles of these regulators can be found in Machowski [56]. A simulation is carried out to show the influence of having AVRs present in the system. The governors are active in both cases, but the AVRs are either included or not. Line L7-8-1 is disconnected for 0.1 seconds.

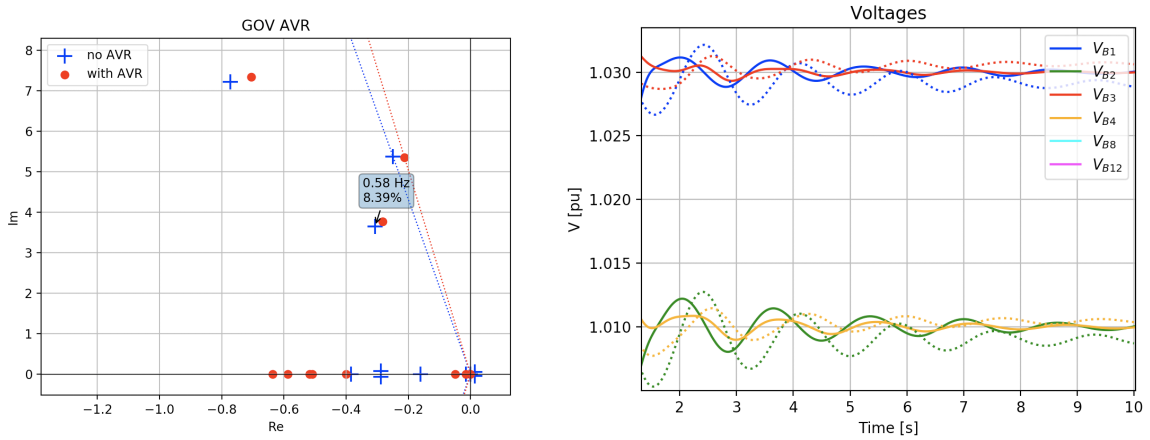

(a) The local modes and inter-area modes are shifted rightwards in the complex plane when AVRs are included, thereby reducing the damping of the oscillatory modes.

(b) Terminal voltages of generator buses in the system. The dotted lines indicates the voltages when the AVRs are disconnected. It is clear that including the AVRs have a stabilizing effect on the terminal voltages of the generator buses.

Figure B.6: Modal plot and terminal voltages for simulations carried out with and without AVRs active.

In Figure B.6b) the voltages at the generator buses are shown. The AVRs are undeniably making the terminal voltages more stable, which is their main task. However, they may turn out to decrease the damping in the system, which is evident from the calculated modes presented in Figure B.6a). The three modes of interest all end up with a weaker dampening after the introduction of the AVRs.

B.1.3 Power System Stabilizer (PSS)

Power System Stabilizers (PSSs) have gotten increased attention in the last decades. Lately, the majority of new generation units installed in power systems are being equipped with AVRs, and it has become evident that these have a detrimental impact on the dynamic stability of the systems [95]. PSSs were developed to address this by properly dampening the electromechanical oscillations for increased stability in the systems. It is commonly thought of to be one of the most cost-effective methods for enhancing stability [56] as it essentially only relies on providing the AVRs with an additional input signal. The block diagram for a widely used PSS referred to as STAB1 [96] is presented in Figure B.7.

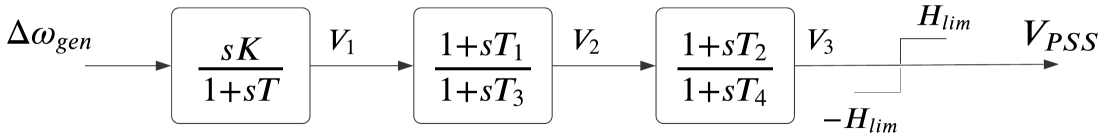

Figure B.7: Power System Stabilizer (PSS) model STAB1

This is the PSS used for all generators in this report where it is stated that "PSS is being used", or similar. Several different input signals could be used for obtaining desired responses from the PSSs, for instance, local speed measurements and terminal bus frequency [97] or accelerating power versus electrical power [98]. From Figure B.7 one sees that STAB1 uses local speed measurements at the individual generators as input signals which have been shown to increase PSSs mode dampening abilities [97]. The additional voltage signal provided by the PSS to the corresponding AVR helps to dampen the electromechanical oscillations in the system if the stabilizers parameter values are adequately selected. The input signal to the PSS is passed through a lowpass- and/or highpass-filter to remove the impact of noisy measurement and dc-offsets before the output of these filters is passed through lead-lag blocks for obtaining the desired phase shift of the signal. This phase shift is required as the PSS task is to add a signal that compensates for the voltage errors at the generator terminals while providing a damping component in phase with the generator speed deviation. A more in-depth explanation of these blocks and their fundamental principles can be found in Machowski [56]. Some limiters are included towards the end of the open-loop control diagram shown in Figure B.7 in order to limit the amount of controller action provided by the PSS during prominent disturbances [99]. Increasing these limits extends the PSS's ability to influence the system during disturbances. Previous research has shown that higher output limits can improve the performance of the PSS and enhance transient stability performance in the systems [99].

The effect of having PSSs in the system is illustrated in the modal plot and speed response shown in Figure B.8. A small-signal disturbance (disconnection of line 7-8-1) is applied for 0.1 seconds, and governors and AVRs with values listed in Appendix C.1 are used for both simulations (with and without PSSs included). For the simulation part where PSSs are employed, the values can be found in Table 12. The PSSs proportional gain constant and lead-lag parameters are not necessarily tuned as one would do for real-world applications, but the fundamental effect of having these stabilizers in the system is showcased.

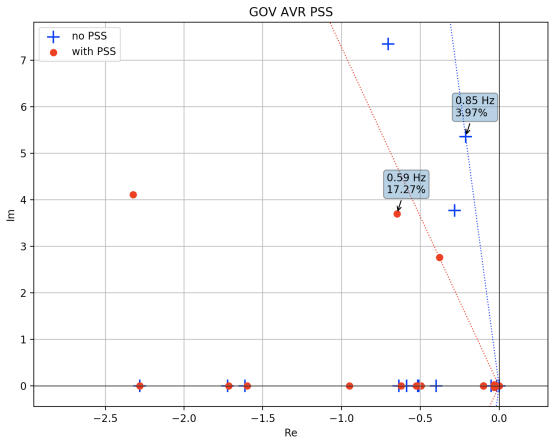

(a) Eigenvalues with and without PSSs. PSSs adds a significant amount of damping especially for local modes, but simultaneously the inter-area mode.

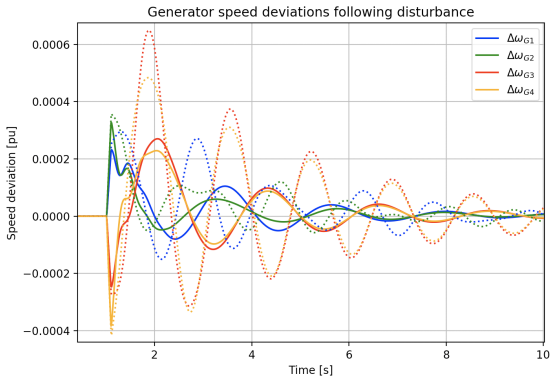

(b) Speed response to small disturbance with and without PSS's.

Figure B.8: Simulations showing the effect of PSSs on modes and speed response in the system. The dotted lines in Figure B.8b) indicates the response when the PSSs are not active, whereas the solid lines is the response when these are active. The simulation clearly indicates that the oscillatory response in the system is significantly damped when PSSs are included as the eigenvalues are moved from the blue crosses to the red dots. However, it should be mentioned that a usual design criterion for the PSS are to not alter the mode frequency too much, which is not really satisfied for the tuning employed here. Nevertheless, it should be evident from Figure B.8a) that the stabilizers are able to shift the modes leftwards, thus increasing the damping in the system which can be seen from the non-linear simulation results presented in Figure B.8b.

From the simulations carried out and visualized in Figure B.8 it is evident that the modes of interest are significantly more damped when PSSs are included, and the increased damping capabilities are validated by the non-linear system response in Figure B.8b).

B.2 Load Model and Demand Response Implementation

When running power system analysis, there are several options for modeling the loads in the system. The simplest load models can be thought of as a combination of constant power demand (P), constant current demand (I), and a constant impedance (Z) [56]. A combination of these can be said to be modeled as a ZIP Model. This model is commonly used for steady-state and dynamic studies but is usually unsatisfactory for transient analysis. The extent to which the load is characterized by either the Z, I, or P component might vary from analysis to analysis, depending on which types of

system loads one is trying to represent. For instance, electrical motor loads will have different characteristics when compared to lightning loads or other load types. In cases of rapid voltage drop, a load model based on piece-wise approximation might be the most accurate [56]. Several loads in a power system are also highly dependent on the grid's frequency, and some models are accounting for this.

In the simulations done in this report, all loads are modeled as constant impedance loads, which could be named Z-model. This type of model is reasonable for some lightning loads as the power consumption varies proportionally to the voltage squared but might have some downsides when modeling other system components [56]. Nevertheless, the voltage variations are pretty tiny in the analysis performed in this report, so the load model chosen might not be as significant.

Implementation of Demand Response by *Changing the Admittance Matrix*

The main objective of this control system was to use measurements in the system, which could be assumed to be PMU measurements, for regulating the load consumption at load buses in an attempt to damp inter-area oscillations in the system. A significant amount of time was spent trying to implement such a controller in the Python environment such that it complies and runs together with the rest of the code. Aiming for a PID-controller would include $2n$ new state variables in the system, where n is the number of loads being controlled. The first attempt in doing so resulted in a PID controller acting on an input signal, either local frequency measurement or speed deviations in the system, for regulating the impedance at the load bus. The need to regulate the impedance at the load bus is inherited because the Z-modelling approach modeled all the loads. It turned out that adjusting the power demands at those buses by making changes to the impedance was a bit more unpredictable than one would like. Firstly, changing the impedance would influence the bus admittance matrix in the system. In the dynamic simulations performed, the admittance matrix was transformed into a reduced admittance matrix using Kron-reduction. The latter was done to reduce the computational time for each simulation but proved to complicate the load controller approach. With this way of controlling it, it was evident that every call to the ordinary differential equation describing the system would have to modify the admittance matrix. From then, calculate the new reduced admittance matrix representation.

Although some controller parameter settings were yielding promising results related to damping, this was rather inconvenient. It made it difficult to get any numerical values on the extent of load changes at the buses. It was also clear that in terms of the linearization done in order to compute the eigenvalues, changes in eigenvalues did not replicate the actual amount of damping present in the speed responses. Very high gains were needed in order to see changes at all. It was later figured out that since

the numerical solver algorithm for solving the differential equations were based on the Runge-Kutta method proposed by Bogacki-Shampine [100], the ordinary differential equation was called a different number of times for each step in the simulation, and the step sizes are adaptive. Consequently, with the given structure and functioning of the proposed load controller, the admittance matrix was changed a significant amount of times during each simulation time-step, which in turn gave results differing from the expected responses anticipated by the modal plots.

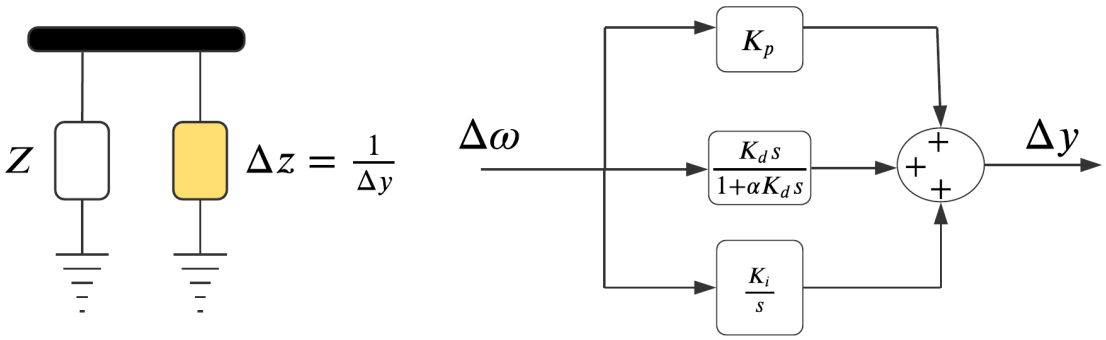

Figure B.9: Demand response implemented by changing the admittance matrix. Z is the pre-defined impedance value defining the load of interest, while Δz is the change in impedance based on input signal and the PID-controller.

Implementation of Demand Response by the use of *Controlled Current Source Injections*

A second approach for modeling and simulation time response was later developed. The Z-model still models the loads in this approach. However, the demand response is modeled using current source injections at the controlled loads. Thus, the controlled loads can kind of be thought about as Z-models with varying current injection for this purpose, as they consist of the constant impedance part, and at the same time, have a varying current source reflecting the changes due to the regulation.

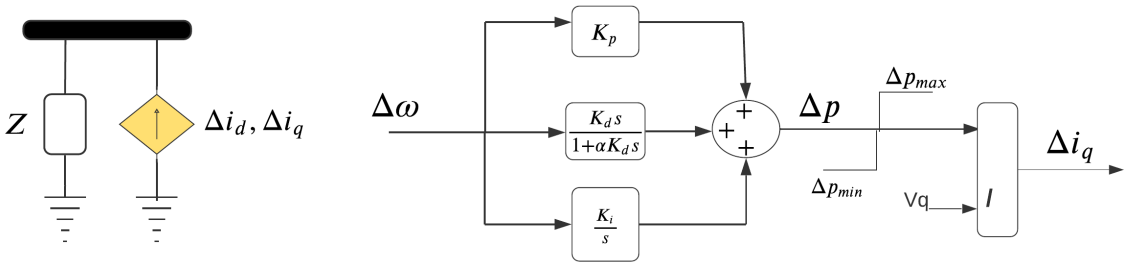

Figure B.10: Demand response implemented as controlled current source injection. The impedance Z corresponds to the predefined loading at the given bus given by the corresponding system initialization and represent as a Z-model load, while the controlled current source are accounting are modelling demand response at the given load.

This proved to be a somewhat decent approach, and a descriptive model is shown in Figure B.10. For instance, in cases where the loads is supposed to be reduced based on the measurements in the system, this is simulated by having the current source inject positive current to the system, which in turn adjust the net power demand at this bus. For cases where an increase in the load demand is needed, injection of negative current to the grid represents increased power demand at the current bus. This approach of modeling the demand response gave much more anticipated results both for the state variables responses in the system, while at the same time being reflected accurately in the eigenvalue calculations on the system in that sense that the observed damping in the speed responses correlated with the expected behavior when looking at the system eigenvalues and mode shapes. The implementation is very similar to the approach used for designing the battery model in Section 4.5, without the use of the inner dynamics of the battery. Basically, it used a PID-regulator for obtaining the desired power demand change at the given bus and then injected dq-axes current components based on a reference frame alignment made such that $v_d = 0$.

B.3 Secondary Control - Load Frequency Control and Area Control Error

In an attempt to reduce the time used developing and implementing for potential future students, a secondary control system developed during the work of this thesis is presented in this section. As it turned out, this model and its behavior were out of the scope for the topics covered in this thesis. Nevertheless, someone might find it helpful.

The general idea behind secondary control is to remove frequency deviations in the grid and keep the tie-line flows at their scheduled values. Secondary control is of major

interest for real-world operation and control of power systems. It is briefly introduced in Appendix A.1, but more information and an in-depth description of secondary control can be found in Machowski [56, p. 341-345], which also served as the inspiration for the implementation of secondary control in the first place. A general block diagram representation of the central regular associated with secondary-control/load-frequency-control is provided in Figure B.11. The idea is to remove the Area Control Errors (ACEs) with the use of a central regulator equipped with a PI-regulator, whose output ΔP_{ref} is distributed to the different generators participating in the secondary control with the weighting factors α_i.

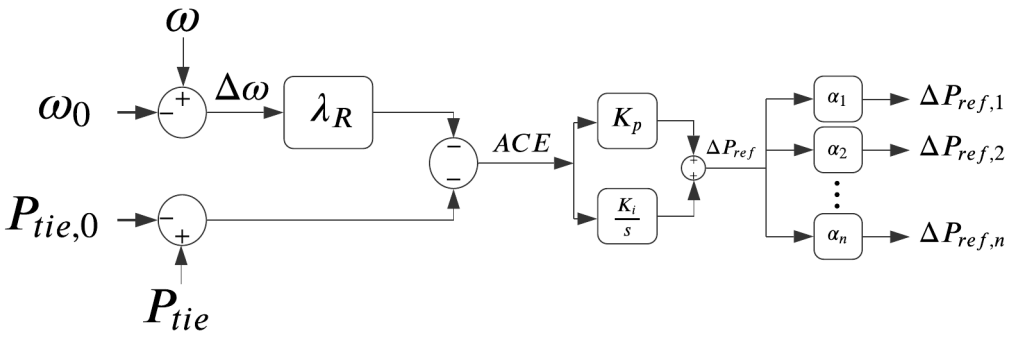

Figure B.11: Block diagram showing a standard control system associated with secondary control and Area Control Error. $P_{tie,0}$ and ω_0 corresponds to the reference/scheduled values of tie-line flow and rotational speed, respectively.

Figure B.11 shows that the ACE is a sum of the errors in the frequency/speed and tie-line flows. The parameter λ_R is usually called the *frequency bias factor* [56, p. 343] and is essentially a constant value amplifying the speed-deviation signal $\Delta\omega$. Machowski provides an intuitive explanation of the importance of the choice of this factor [56, p. 343], but it is practically a measure of whether the most important objective is to keep to the frequency at its scheduled value or the tie-line flows. Implementing the central regulator in Python does not require that much code when built into the dynamic simulation tool. This is inherently a fact due to the simplicity of the block diagram shown in Figure B.11. Hence, due to the few amounts of lines required, the code is provided in Figure B.12.

```python
import numpy as np
class ACE:
    def __init__(self):
        self.state_list = ['x_1'] # integrator
        self.int_par_list = ['Ptie0', 'f']
        self.input_list = ['speed_dev', 'p_tie']
        self.output_list = ['P_ace']

    @staticmethod
    def _update(dx, x, input, output, p, int_par):
        # The speed-deviation is defined negatively in dynamic.py
        speed_dev = input['speed_dev']
        p_tie = input['p_tie']

        # Compute ACE and find delta_p_ref
        ace = p['lambda']*speed_dev - (p_tie - int_par['Ptie0'])
        s_1 = p['K_p']*ace
        s_3 = p['K_i']*x['x_1']
        delta_p_ref = s_1 + s_3

        # Add power reference signal change. Including limitations.
        output['P_ace'][:] = np.minimum(np.maximum(-1.0, p['alpha']*delta_p_ref), 1.0)

        # Update the state variable
        dx['x_1'][:] = ace

        # Returns ace and p_tie solely for plotting purposes
        return ace, p_tie
```

Figure B.12: The Implementation in DynPSSimpy. To include such a system, some changes are needed in the dynamic file as well, but the correlation between the block diagram presented in Figure B.11 should be observable in the code.

It should be made clear that implementing new blocks requires several changes in the dynamic.py file. This file is somewhat large and consequently not shown here. However, by looking at the implementations of the other models in the file dynamic.py, it is assumed to be a manageable part, where the most challenging part is to distribute the output signal ΔP_{ref} (or output['P_{ace}'][:] in the code in Figure B.12) to the different generators participating in the secondary control. A relatively straightforward way to work around this problem in an initial attempt to see whether the control system is working as expected is to equip each generator with its own "central regulator", all of which are using the same input signals and controller parameters. However, if used extensively for future work, one should aim to find a way to remove the necessity of this brute-force method.

For illustrating the performance of the secondary control and to get a better understanding of the working principles, a small simulation is carried out, and the results are provided in Figure B.13. The system used is the Kundor-two-area system using the values given in Appendix C.1 and all control systems active, and the disturbance in the system is a reduction in L2 of 200MW at t=10.0 seconds. The sole purpose is to see how the load-frequency control is performing and how the system's frequency and tie-line flows are improved during secondary control. In terms of parameters used for the

load-frequency controllers, these are chosen somehow justifiable concerning the theory presented in Machowski [56]. However, the exact parameter values are deemed unnecessary to include here. This simulation is solely meant to be an illustrative example showing the fundamental principles of the LFC. Figure B.13 shows the simulation results with and without LFC active, and a discussion around the results is provided in the caption of the figures.

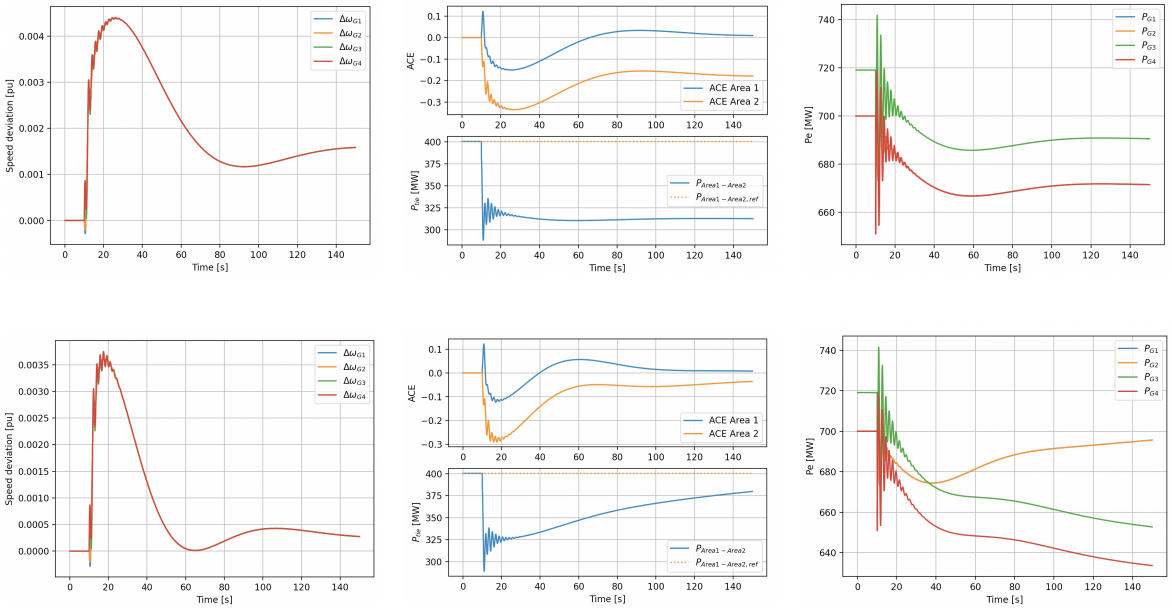

(a) Speed deviations in the system. For the case with LFC active (lower figure), one observes that the frequency is moving towards the scheduled value. For the case without LFC active (upper figure), the system reaches a new steady-state frequency differing from the reference value.

(b) ACEs (upper part of each sub-figure) and line flows (bottom part of each sub-figure) between the two regions. In the case of LFC active, one sees that the system is having a step-change in power flowing between the regions immediately after the disturbance, but it gradually moves towards the scheduled value (lowest plot).

(c) Power delivered by the generators. When LFC are active (bottom figure), the generators located in the faulted area (Area 2) have a change in the delivered power (green and red line). In contrast, generators located in Area 1 (orange line) approach their scheduled power production. Hence, generators located in the faulted area are responsible for covering the power deficit [56, p. 343]. Without LFC (upper figure), all generators change their power output to cover the power imbalance.

Figure B.13: Simulation showing the fundamentals behind load-frequency control (LFC). The upper plots show the system response without LFC active, and the lower plots show the response when LFC is active. The author is well aware that axis-ticks numbers are not entirely readable without zooming in. However, the sole purpose of this is to showcase the general behavior of the system and not the actual numerical values.

B.4 HVDC-implementation and Bifurcation Limit Cycle

HVDC-implementation in Python

During the work of this thesis, an HVDC model was developed and implemented. HVDC implementations are essentially relying on current injections to the system, thus having fundamental similarities to the Battery Model described in Section 4.5. Hence, it was chosen to exclude simulations with HVDC and HVDC for damping purposes for this thesis. The general results coincided to a prominent extent with the results obtained by using BESS.

However, future students might find it helpful to have a guideline and considerations about a proposed way of defining an HVDC-link in the Python Dynamic Power System Simulator (DynPSSimpy) or any dynamic simulator in general. With that in mind, the basic principles behind the HVDC model development and implementation conducted during the time spent working on this thesis are provided. The basic idea is to be able to represent a general HVDC-cable as shown in Figure B.14

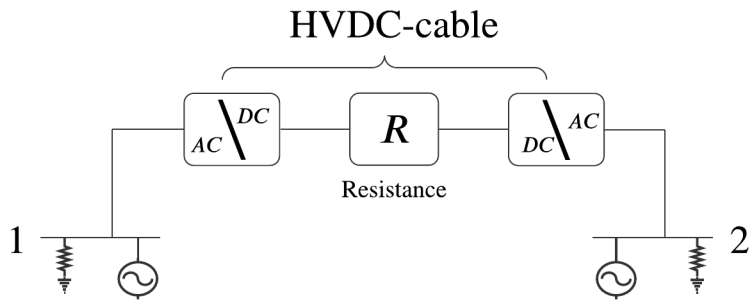

Figure B.14: HVDC-cable in a simple power system consisting of two areas where each area is represented by an equivalent generator and total loading. The power converters needed for a HVDC-cable is included, together with the ohmic cable resistance, R.

Hence, the question that arises is how to implement this into the dynamic system. The first thing that should be kept in mind is that an HVDC cable essentially is a positive power injection at the receiving bus and a negative power injection at the sending bus. This is illustrated in Figure B.15.

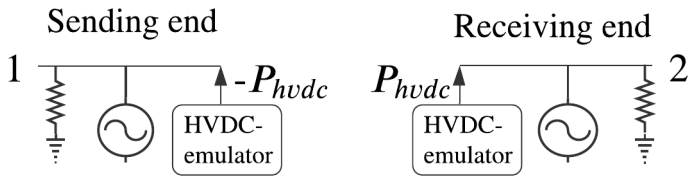

Figure B.15: Two-area power system, where the HVDC-cable from Figure B.14. For this case, the cable resistance is neglected for simplicity.

The generator models and system components utilized in the simulator are using the DQ0-transformation discussed in Appendix A.5. Hence, this is a natural way to implement the HVDC (although other methods could presumably give the same results). Thus, for such a case, the HVDC emulator from Figure B.15 will be a component that injects the desired amount of q-axis current into the system. Including the effect of the cable resistance, this is illustrated in Figure B.16.

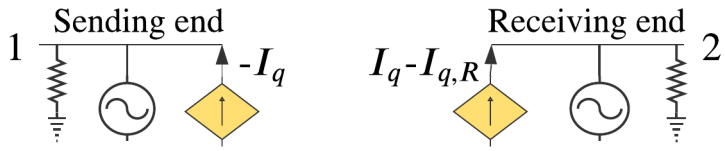

Figure B.16: Two-area power system where the HVDC-cable is represented as q-axis current injections. The sending end injects the negative of this component (-I_q), whereas the sending end injects I_q-$I_{q,R}$, where $I_{q,R}$ is reflecting the decrease in current due to cable power losses originating from the cable resistance R.

The Battery Model presented in Section 4.5 was built up injecting currents at a given bus, but for the HVDC-cable, as can be seen in Figure B.16. However, the fundamental principles behind both of them are the same. A lot of the inner dynamics of the Battery Model are neglected for the HVDC implementation. However, the HVDC-model does also contain a time-delay part, capturing the fact that when a reference current $I_{q,ref}$ is provided, there will be a short amount of time before the actual power converters can respond. The final model with an arbitrary chosen HVDC-controller (which could, for instance, be as simple as a proportional regulator) is presented in Figure B.17.

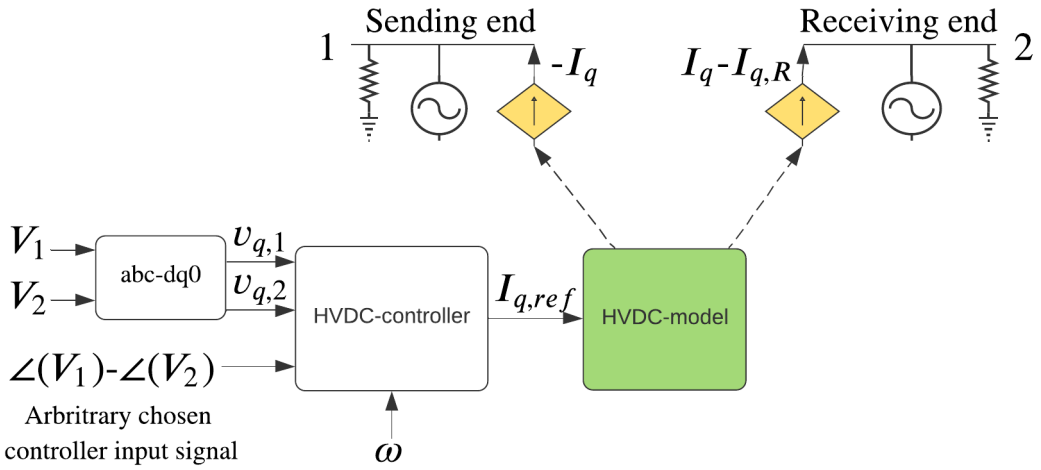

Figure B.17: Two-area system with HVDC-cable implementation visualized. The input signal to the controller is for this case chosen to be the difference in voltage angles between the connected buses, but this could in principle be any measurable signal in the system.

The code is appended to give an illustration behind the principles and the thought process behind the DQ0-transformation and the computation of the $I_{q,ref}$ current. It should also be valuable in terms of calculating the current component accounting for cable losses, $I_{q,R}$. The proposed implementation is found in Figure B.18, but some of the input variables are included solely for plotting and model verification purposes. Hence the model could arguably be simplified when used for simulations.

```python
class HVDC_SIMPLE:
    def __init__(self):
        self.state_list = ['i_inj_q_1'] # 1 is for the first bus, two is for the second bus
        self.input_list = ['V_t_abs_1', 'V_t_abs_2', 'V_t_angle_1', 'V_t_angle_2', 'p_ctrl', 'ang_dq1', 'ang_dq2']
        self.int_par_list = ['f', 's_n', 'p_ref', 'i_inj_q_1_ref', 'i_inj_q_2_ref', 'i_inj_q_2'] # p_ref is the sc
        self.output_list = ['P_e_1', 'P_e_2', 'I', 'i_inj_q_1_out', 'i_inj_q_2_out']

    @staticmethod
    def initialize(x_0, input, output, p, int_par):
        # DQ0 transfomration
        v_g_1 = input['V_t_abs_1']*np.exp(1j*input['V_t_angle_1'])
        angle_1 = input['ang_dq1']
        v_dq_1 = v_g_1 * np.exp(1j * (np.pi / 2 - angle_1))
        v_q_1 = v_dq_1.imag
        v_g_2 = input['V_t_abs_2']*np.exp(1j*input['V_t_angle_2'])
        angle_2 = input['ang_dq2']
        v_dq_2 = v_g_2 * np.exp(1j * (np.pi / 2 - angle_2))
        v_q_2 = v_dq_2.imag

        # Set to zero, only looking at deviations from the scheduled value
        x_0['i_inj_q_1'][:] = 0
        int_par['i_inj_q_2'] = 0

        output['P_e_1'] = int_par['p_ref']
        int_par['i_inj_q_1_ref'] = output['P_e_1']/v_q_1
        output['I'] = output['P_e_1']/input['V_t_abs_1']

        output['P_e_2'] = -(output['P_e_1']+np.abs(p['R']*output['I']))
        int_par['i_inj_q_2_ref'] = output['P_e_2']/v_q_2

        output['i_inj_q_1_out'] = x_0['i_inj_q_1']
        output['i_inj_q_2_out'] = int_par['i_inj_q_2']

    @staticmethod
    def _current_injections(x, int_par):
        return x['i_inj_q_1']+int_par['i_inj_q_1_ref'], int_par['i_inj_q_2']+int_par['i_inj_q_2_ref']

    @staticmethod
    def _update(dx, x, input, output, p, int_par):
        # DQ0 transformation, this must be done dynamically in the simulation
        v_g_1 = input['V_t_abs_1']*np.exp(1j*input['V_t_angle_1'])
        angle_1 = input['ang_dq1']
        v_dq_1 = v_g_1 * np.exp(1j * (np.pi / 2 - angle_1))
        v_q_1 = v_dq_1.ima
        v_g_2 = input['V_t_abs_2']*np.exp(1j*input['V_t_angle_2'])
        angle_2 = input['ang_dq2']
        v_dq_2 = v_g_2 * np.exp(1j * (np.pi / 2 - angle_2))
        v_q_2 = v_dq_2.imag

        u = input['p_ctrl']/v_q_1
        output['P_e_1'] = v_q_1 * x['i_inj_q_1'] + int_par['p_ref']
        output['I'] = output['P_e_1']/input['V_t_abs_1']
        # Positive P_e_1 -> power flowing to this bus -> higher power magnitude at bus 2
        # If opposite, want lower absolute value of power at bus 2
        output['P_e_2'] = -(output['P_e_1'] + np.abs(p['R'] * output['I']))

        delta_i = v_q_1*x['i_inj_q_1']/input['V_t_abs_1']
        int_par['i_inj_q_2'] = -(v_q_1*x['i_inj_q_1'] + np.abs(p['R'] * delta_i))/v_q_2
        output['i_inj_q_1_out'] = x['i_inj_q_1'] # x['i_inj_q_1']
        output['i_inj_q_2_out'] = int_par['i_inj_q_2']

        dx['i_inj_q_1'] = 1/p['T']*(p['K']*u-x['i_inj_q_1'])
```

Figure B.18: Code for implementing the HVDC model. This implementation should be somehow following Figure B.17. However, the HVDC-controller is chosen to be a separate model supplying the HVDC-model with a power reference signal named "p_{ctrl}". In principle, this control system could be any appropriate controller, for instance, a simple P-regulator acting on voltage angle deviations in the system. The important part is that the HVDC controller should supply the HVDC model with a power reference. It should be mentioned that the code presented as-is is implemented for the authors' use only, hence not been cleaned up before presented, and some of the parameters are solely used for plotting purposes. Nevertheless, it should serve as a decent example of how to model an HVDC cable.

Boiled down, it simply is a matter of injecting the desired amount of power at two

buses connected by the HVDC cable, and the power calculation together with the power losses due to the cable resistance is calculated in dq-components by the use of equation (A.20).

Bifurcation Limit Cycle simulation

In terms of operation and controller performance capabilities, the HVDC implementation and its controller exhibits similar characteristics as the BESS model used for the simulations conducted in this thesis. However, when running simulations using the HVDC-cable present in the system between buses 3020 and 7010 [B.1] in Nordic 44, see Figure 4.5, an interesting phenomenon usually known as Hopf Bifurcation arises. Historically, the Hopf Bifurcation has been the cause of significant disturbances in power systems [102]. When this phenomenon arises, the person implementing the dynamic model might assume an implementation error. Being aware of this phenomenon could be rather valuable for avoiding confusion during model and controller development. The simulation is carried out by disconnecting one of the lines between bus 3100 and 3200 without re-connection. Without re-connection, the system topology changes significantly; hence, the eigenvalues obtained by doing a linearization around the steady-state initial operating point might not be valid anymore.

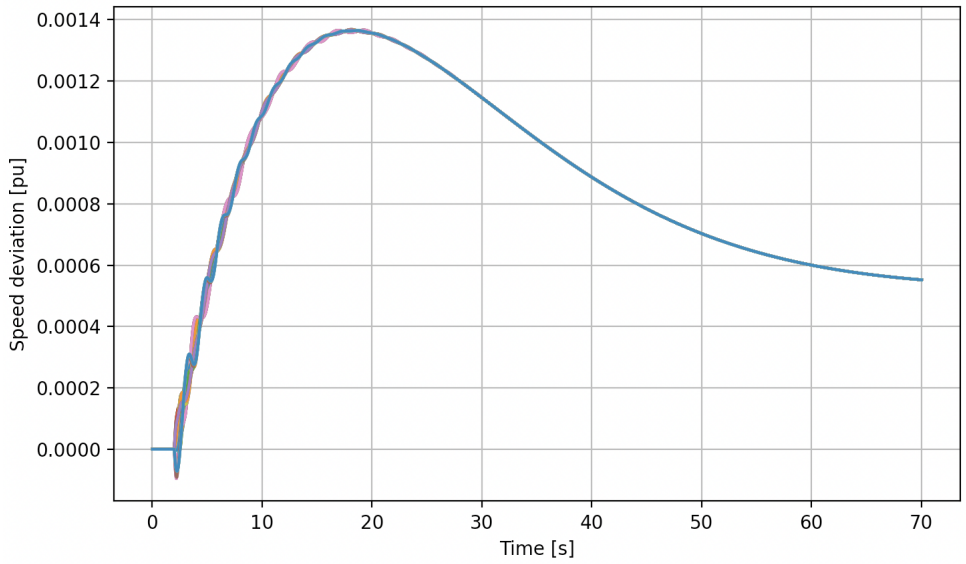

Figure B.19: Speed response after disconnection of L3100-3200-1 without HVDC-cable present in the system. The frequency of the grid is increasing following the disturbance, as the system impedance is increased, hence by the swing equation (3.2) and power transfer for a synchronous machine (3.3), the electrical power P_e injected by the generators is slightly decreasing the equivalent d-axis reactance x_d have increased.

[B.1] The HVDC-cable terminal buses is chosen based on the LCC-HVDC connection "Fenno-Scan" present in the real-world Nordic power system [101] between Northern Norway and Western Sweden.

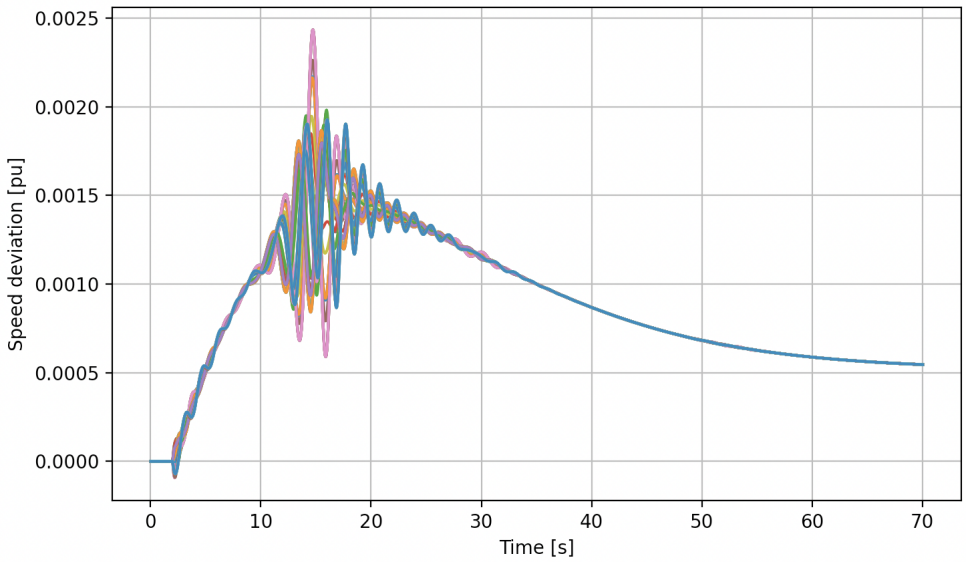

Figure B.20: Speed response when HVDC is present in the system as described in the text. The response is similar to the response without HVDC present in the system as seen in Figure B.19, but oscillations starts occurring at t = 10.0 seconds, before gradually dying out at approximately t = 30.0 seconds.

By comparing the response without HVDC in Figure B.19 with the response with HVDC present in Figure B.20, one notices the appearing oscillations around t = 10.0 seconds. This response is the major reason for presenting this simulation. Oscillations like this are highly unwanted but maybe appearing for certain types of faults. When working with HVDC, one should be aware of the possibility of responses like this being present. The fundamental reason is the eigenvalue movement during the simulation. It might be easier to look at the injected HVDC-power at the HVDC terminals in the system to explain this. This is shown in Figure B.21. It is evident that oscillations increasing in amplitude start at approximately t = 10.0 seconds, t = 25.0 seconds, and t = 50.0 seconds (although small-amplitude oscillation for the last one). Figure B.22 shows a zoomed-in version of the last two cycles containing a noticeable increase in oscillations.

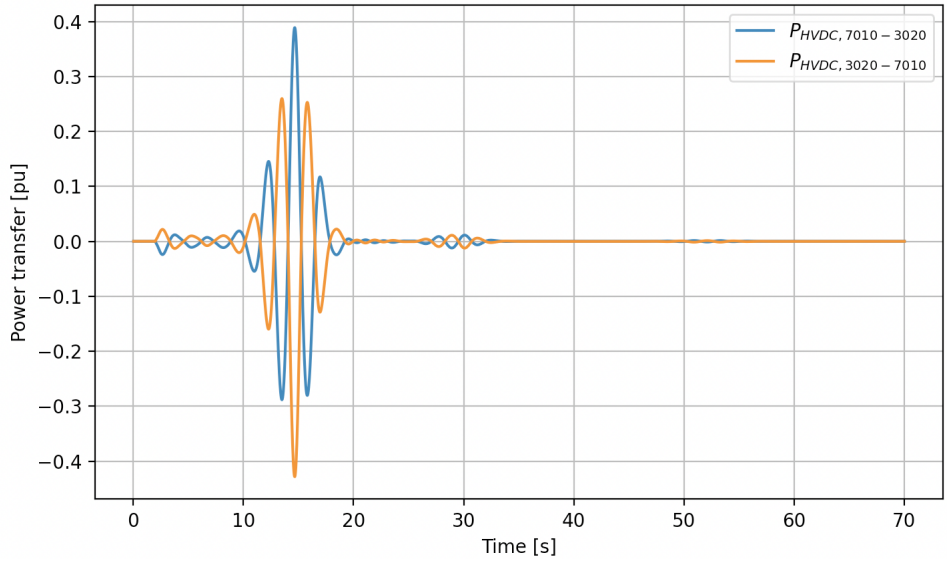

Figure B.21: Power injected at the HVDC terminals following the disturbance. Notice how the negative injection (sending side) amplitude is greater than the receiving end. This is due to the inclusion of a cable resistance of 0.1 p.u. (which is larger than the values in real-world systems but is made for making the cable losses observable in the simulation).

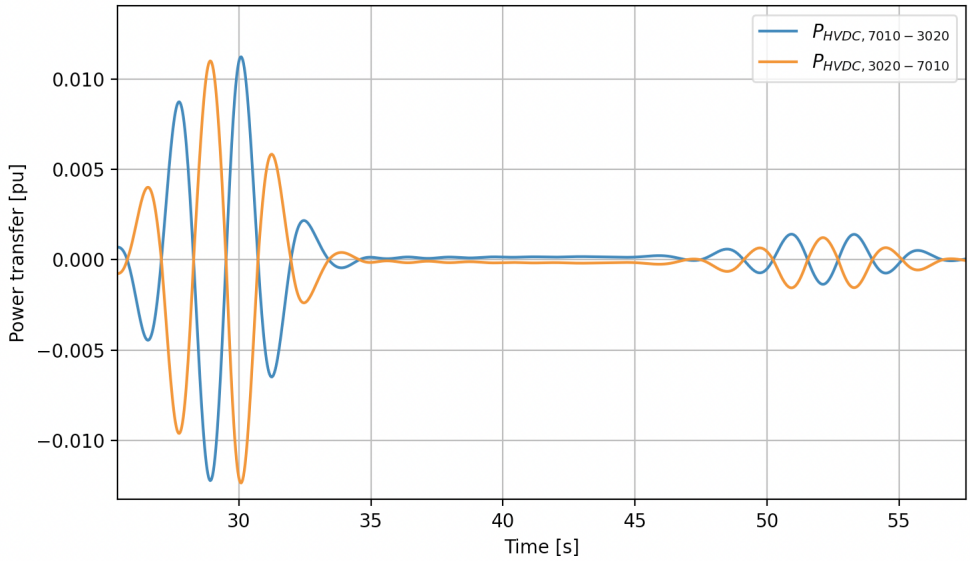

Figure B.22: Zoomed in version of the power injections at the HVDC-terminals towards the end of the simulation period. The results clearly indicated that the oscillations almost dies out, before suddenly starting to increase in amplitude several times during the simulation.

This phenomenon could be described as the Bifurcation Limit Cycle. Bifurcation can occur in power systems and cause the nominal equilibrium of the system to lose its

stability [103]. Several different phenomena can lead to bifurcations, for instance, improperly tuned control parameters and non-linear loads [103]. The HVDC-cable model presented here can represent non-linear loads at the HVDC-terminal buses, which might explain why this phenomenon arises here. Without going further into detail on this phenomena[B.2], this simulation was included to showcase some of the problems that may arise when working with self-developed models, and the results might not be unrealistic. However, it might look like an implementation error initially. While reading literature for this thesis, some examples of this phenomenon happening without explicitly discussing it was seen. In a paper written by Li et al. [104] it is clear that for some of their simulations, the oscillations decrease in amplitude before gradually increasing later in the simulation. Although their simulations do not show it as clearly as Figure B.22[B.3], it is still present.

C System Parameters

C.1 Kundur's Two-Area System Parameters

Include the base case system paramters in Kundur two-area system here.

Table 5: K2A - GENERATOR MODEL PARAMETERS

Gen	Bus	S_n	V_n	P	V	H	D	X_d	X_q	X'_d	X'_q	X''_d	X''_q	T'_{d0}	T'_{q0}	T''_{d0}	T''_{q0}
G1	B1	900	20	700	1.03	7.0	0.0	1.2	0.9	0.3	0.55	0.25	0.25	5.0	0.1	0.03	0.05
G2	B2	900	20	700	1.01	7.0	0.0	1.2	0.9	0.3	0.55	0.25	0.25	5.0	0.1	0.03	0.05
G3	B3	900	20	719	1.03	5.0	0.0	1.8	1.7	0.3	0.55	0.25	0.25	8.0	0.4	0.03	0.05
G4	B4	900	20	700	1.01	5.0	0.0	1.8	1.7	0.3	0.55	0.25	0.25	8.0	0.4	0.03	0.05

Table 6: K2A - LINE PARAMETERS

From	To	Length	$S_n[MVA]$	$V_n[kV]$	unit	R	X	B
B5	B6	25	100	230	pu	0.0001	0.001	0.00175
B6	B7	10	100	230	pu	0.0001	0.001	0.00175
B7	B8	110	100	230	pu	0.0001	0.001	0.00175
B7	B8	110	100	230	pu	0.0001	0.001	0.00175
B8	B9	110	100	230	pu	0.0001	0.001	0.00175
B8	B9	110	100	230	pu	0.0001	0.001	0.00175
B9	B10	10	100	230	pu	0.0001	0.001	0.00175
B10	B11	25	100	230	pu	0.0001	0.001	0.00175

[B.2]There is much available literature on this, especially related to voltage stability issues in power systems.

[B.3]The proportional controller gain was set satisfactory high such that the phenomena were easily observable, although a lower gain might be used for an actual real-world control system.

Table 7: K2A - TRANSFORMERS PARAMETERS

From	To	$S_n[MVA]$	$V_1[kV]$	$V_2[kV]$	R [Ω]	X [Ω]
B1	B5	900	20	230	0.0	0.15
B2	B6	900	20	230	0.0	0.15
B3	B11	900	20	230	0.0	0.15
B4	B10	900	20	230	0.0	0.15
B9	B12	100	230	0.4	0.0	0.30

Table 8: K2A - LOADS

Bus	$V_n[kV]$	P [MW]	Q [MVAr]	Model
B7	230	967	100	Z
B9	230	1767	100	Z

Table 9: K2A - SHUNTS

Bus	$V_n[kV]$	Q [MVAr]	Model
B7	230	200	Z
B9	230	350	Z

Table 10: K2A - GOVERNOR MODEL PARAMETERS

Gen	Model	R	D_t	V_{min}	V_{max}	T_1	T_2	T_3	P_{m0}	T_w
G1	HYGOV	0.06	0.0	0.0	1.0	0.36	6.0	67.6	0.777	1.0
G2	HYGOV	0.06	0.0	0.0	1.0	0.36	6.0	67.6	0.777	1.0
G3	TGOV1	0.12	0.0	0.0	1.0	0.1	0.09	0.2	-	-
G4	TGOV1	0.12	0.0	0.0	1.0	0.1	0.09	0.2	-	-

Table 11: K2A - AVR MODEL PARAMETERS

Gen	Model	K	T_A	T_B	T_E	E_{min}	E_{max}
G1	SEXS	250	2.0	10.0	0.05	-3.0	3.0
G2	SEXS	250	2.0	10.0	0.05	-3.0	3.0
G3	SEXS	250	2.0	10.0	0.05	-3.0	3.0
G4	SEXS	250	2.0	10.0	0.05	-3.0	3.0

Table 12: K2A - PSS MODEL PARAMETERS

Gen	Model	K	T	T_1	T_2	T_3	T_4	H_{lim}
G1	STAB1	50	10.0	0.5	0.5	0.05	0.05	0.03
G2	STAB1	50	10.0	0.5	0.5	0.05	0.05	0.03
G3	STAB1	50	10.0	0.5	0.5	0.05	0.05	0.03
G4	STAB1	50	10.0	0.5	0.5	0.05	0.05	0.03

C.2 Nordic 44 System Parameters

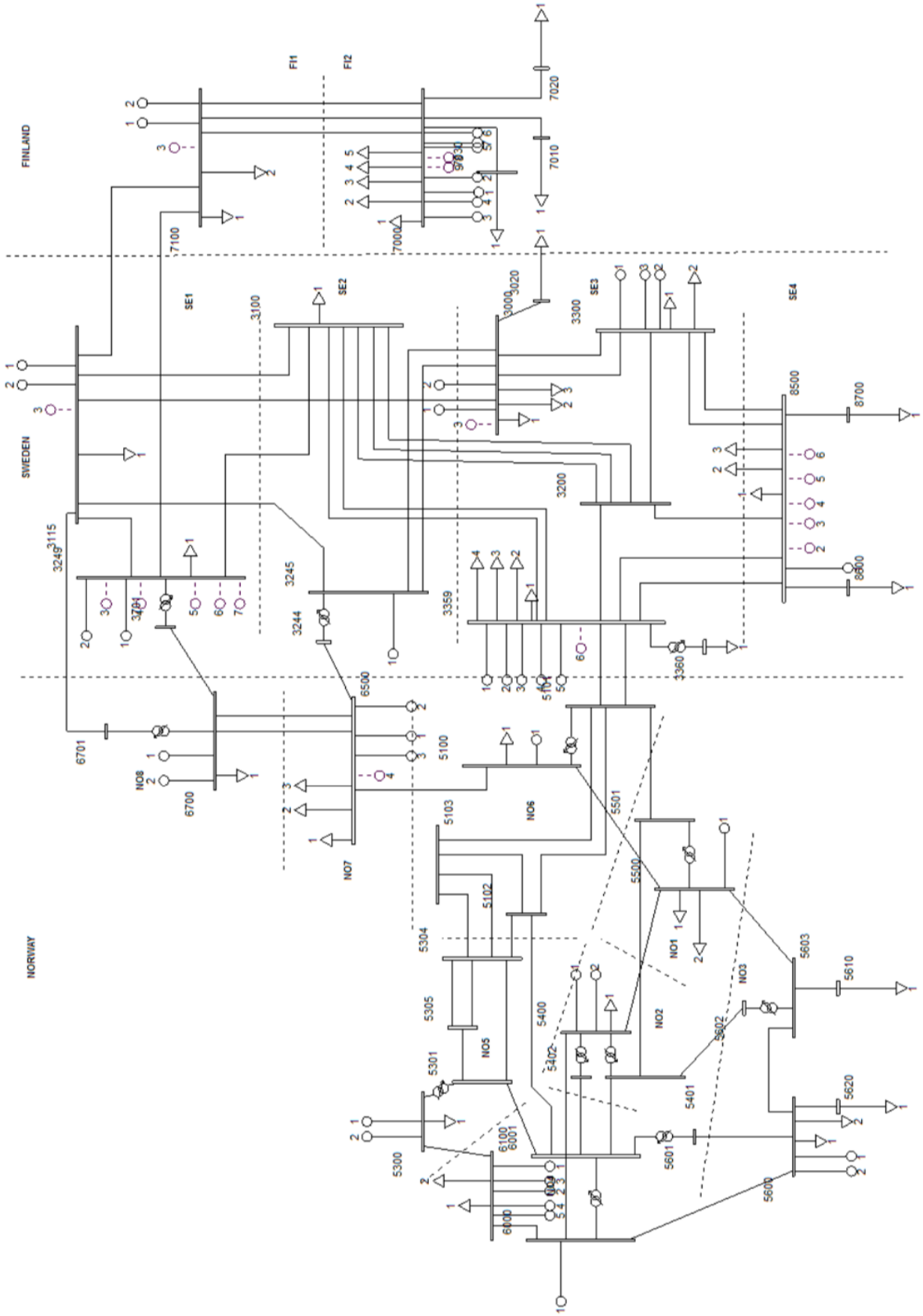

Figure C.1: The Nordic 44 test network in an enlarged version. Source: Adapted from [74].

Table 13: N44 - GENERATOR PARAMETERS

name	bus	S_n	V_n	P	V	H	D	X_d	X_q	X_d_t	X_q_t	X_d_st	X_q_st	T_d0_t	T_q0_t	T_d0_st	T_q0_st
G3000-1	3000	1300.000	0	550.000	1.000	5.9700	0	2.2200	2.13000	0.36000	0.46800	0.22500	0.22500	5.0000	1	0.050	0.05
G3000-2	3000	1300.000	0	550.000	1.000	5.9700	0	2.2200	2.13000	0.36000	0.46800	0.22500	0.22500	5.0000	1	0.050	0.05
G3000-3	3000	1300.000	0	0.000	1.000	5.9700	0	2.2200	2.13000	0.36000	0.46800	0.22500	0.22500	5.0000	1	0.050	0.05
G3115-1	3115	1450.620	0	1175.000	1.000	4.7410	0	0.9460	0.56500	0.29000	0.56500	0.23000	0.23000	7.5700	1	0.045	0.10
G3115-2	3115	1450.620	0	1175.000	1.000	4.7410	0	0.9460	0.56500	0.29000	0.56500	0.23000	0.23000	7.5700	1	0.045	0.10
G3115-3	3115	1450.620	0	1175.000	1.000	4.7410	0	0.9460	0.56500	0.29000	0.56500	0.23000	0.23000	7.5700	1	0.045	0.10
G3245-1	3245	1234.570	0	1000.000	1.000	3.3000	0	0.7500	0.50000	0.25000	0.50000	0.15385	0.15385	5.0000	1	0.060	0.10
G3249-1	3249	1357.000	0	1042.000	1.000	4.5430	0	1.0360	0.63000	0.28000	0.63000	0.21000	0.21000	10.1300	1	0.060	0.10
G3249-2	3249	1357.000	0	1042.000	1.000	4.5430	0	1.0360	0.63000	0.28000	0.63000	0.21000	0.21000	10.1300	1	0.060	0.10
G3249-3	3249	1357.000	0	1042.000	1.000	4.5430	0	1.0360	0.63000	0.28000	0.63000	0.21000	0.21000	10.1300	1	0.060	0.10
G3249-4	3249	1357.000	0	1042.000	1.000	4.5430	0	1.0360	0.63000	0.28000	0.63000	0.21000	0.21000	10.1300	1	0.060	0.10
G3249-5	3249	1357.000	0	1042.000	1.000	4.5430	0	1.0360	0.63000	0.28000	0.63000	0.21000	0.21000	10.1300	1	0.060	0.10
G3249-6	3249	1357.000	0	1042.000	1.000	4.5430	0	1.0360	0.63000	0.28000	0.63000	0.21000	0.21000	10.1300	1	0.060	0.10
G3249-7	3249	1357.000	0	1042.000	1.000	4.5430	0	1.0360	0.63000	0.28000	0.63000	0.21000	0.21000	10.1300	1	0.060	0.10
G3300-1	3300	1100.000	0	998.734	1.000	6.0000	0	2.4200	2.00000	0.23000	0.41080	0.16000	0.16000	10.8000	1	0.050	0.05
G3300-2	3300	1100.000	0	998.734	1.000	6.0000	0	2.4200	2.00000	0.23000	0.41080	0.16000	0.16000	10.8000	1	0.050	0.05
G3300-3	3300	1100.000	0	998.734	1.000	6.0000	0	2.4200	2.00000	0.23000	0.41080	0.16000	0.16000	10.8000	1	0.050	0.05
G3359-1	3359	1350.000	0	1110.000	1.000	4.8200	0	2.1300	2.03000	0.31000	0.40300	0.19370	0.19370	4.7500	1	0.050	0.05
G3359-2	3359	1350.000	0	1100.000	1.000	4.8200	0	2.1300	2.03000	0.31000	0.40300	0.19370	0.19370	4.7500	1	0.050	0.05
G3359-3	3359	1350.000	0	1100.000	1.000	4.8200	0	2.1300	2.03000	0.31000	0.40300	0.19370	0.19370	4.7500	1	0.050	0.05
G3359-4	3359	1350.000	0	0.000	1.000	4.8200	0	2.1300	2.03000	0.31000	0.40300	0.19370	0.19370	4.7500	1	0.050	0.05
G3359-5	3359	1350.000	0	0.000	1.000	4.8200	0	2.1300	2.03000	0.31000	0.40300	0.19370	0.19370	4.7500	1	0.050	0.05
G3359-6	3359	1350.000	0	0.000	1.000	4.8200	0	2.1300	2.03000	0.31000	0.40300	0.19370	0.19370	4.7500	1	0.050	0.05
G5100-1	5100	1200.000	0	972.437	1.000	3.9871	0	1.1332	0.68315	0.24302	0.68315	0.15135	0.15135	4.9629	1	0.050	0.15
G5300-1	5300	1574.890	0	1275.661	1.000	3.5000	0	1.1400	0.84000	0.34000	0.84000	0.26000	0.26000	6.4000	1	0.050	0.15
G5300-2	5300	1574.890	0	1275.661	1.000	3.5000	0	1.1400	0.84000	0.34000	0.84000	0.26000	0.26000	6.4000	1	0.050	0.15
G5400-1	5400	1611.516	0	1305.328	1.007	4.1000	0	1.0200	0.63000	0.25000	0.63000	0.16000	0.16000	6.5000	1	0.050	0.15
G5400-2	5400	1611.516	0	1305.328	1.007	4.1000	0	1.0200	0.63000	0.25000	0.63000	0.16000	0.16000	6.5000	1	0.050	0.15
G5500-1	5500	1450.000	0	1131.563	1.004	3.0000	0	1.2364	0.65567	0.37415	0.65567	0.22825	0.22825	7.1980	1	0.050	0.15
G5600-1	5600	1538.265	0	1245.995	1.010	3.5000	0	1.0000	0.51325	0.38000	0.51325	0.28000	0.28000	7.8500	1	0.050	0.15
G5600-2	5600	1538.265	0	1245.995	1.010	3.5000	0	1.0000	0.51325	0.38000	0.51325	0.28000	0.28000	7.8500	1	0.050	0.15
G6000-1	6000	896.590	0	735.730	1.005	3.5000	0	1.2800	0.94000	0.37000	0.94000	0.28000	0.28000	9.7000	1	0.050	0.15
G6100-1	6100	1634.960	0	1329.061	1.000	3.0000	0	1.2000	0.73000	0.37000	0.73000	0.18000	0.18000	9.9000	1	0.050	0.15
G6100-2	6100	1634.960	0	1329.061	1.000	3.0000	0	1.2000	0.73000	0.37000	0.73000	0.18000	0.18000	9.9000	1	0.050	0.15
G6100-3	6100	1634.960	0	1329.061	1.000	3.0000	0	1.2000	0.73000	0.37000	0.73000	0.18000	0.18000	9.9000	1	0.050	0.15
G6100-4	6100	1634.960	0	1329.061	1.000	3.0000	0	1.2000	0.73000	0.37000	0.73000	0.18000	0.18000	9.9000	1	0.050	0.15
G6100-5	6100	1634.960	0	1329.061	1.000	3.0000	0	1.2000	0.73000	0.37000	0.73000	0.18000	0.18000	9.9000	1	0.050	0.15
G6500-1	6500	1100.000	0	814.333	1.000	3.5580	0	1.0679	0.64200	0.23865	0.64200	0.15802	0.15802	5.4855	1	0.050	0.15
G6500-2	6500	1100.000	0	814.333	1.000	3.5580	0	1.0679	0.64200	0.23865	0.64200	0.15802	0.15802	5.4855	1	0.050	0.15
G6500-3	6500	1100.000	0	814.333	1.000	3.5580	0	1.0679	0.64200	0.23865	0.64200	0.15802	0.15802	5.4855	1	0.050	0.15
G6500-4	6500	1100.000	0	0.000	1.000	3.5580	0	1.0679	0.64200	0.23865	0.64200	0.15802	0.15802	5.4855	1	0.050	0.15
G6700-1	6700	2144.444	0	1753.000	1.020	3.5920	0	1.1044	0.66186	0.25484	0.66186	0.17062	0.17062	5.2400	1	0.050	0.15
G6700-2	6700	2144.444	0	1753.000	1.020	3.5920	0	1.1044	0.66186	0.25484	0.66186	0.17062	0.17062	5.2400	1	0.050	0.15
G7000-1	7000	1278.000	0	1085.500	1.000	5.5000	0	2.2200	2.13000	0.36000	0.46800	0.22500	0.22500	10.0000	1	0.050	0.05
G7000-2	7000	1278.000	0	1085.500	1.000	5.5000	0	2.2200	2.13000	0.36000	0.46800	0.22500	0.22500	10.0000	1	0.050	0.05
G7000-3	7000	1278.000	0	1085.500	1.000	5.5000	0	2.2200	2.13000	0.36000	0.46800	0.22500	0.22500	10.0000	1	0.050	0.05
G7000-4	7000	1278.000	0	1085.500	1.000	5.5000	0	2.2200	2.13000	0.36000	0.46800	0.22500	0.22500	10.0000	1	0.050	0.05
G7000-5	7000	1278.000	0	1085.500	1.000	5.5000	0	2.2200	2.13000	0.36000	0.46800	0.22500	0.22500	10.0000	1	0.050	0.05
G7000-6	7000	1278.000	0	1085.500	1.000	5.5000	0	2.2200	2.13000	0.36000	0.46800	0.22500	0.22500	10.0000	1	0.050	0.05
G7000-7	7000	1278.000	0	0.000	1.000	5.5000	0	2.2200	2.13000	0.36000	0.46800	0.22500	0.22500	10.0000	1	0.050	0.05
G7000-8	7000	1278.000	0	0.000	1.000	5.5000	0	2.2200	2.13000	0.36000	0.46800	0.22500	0.22500	10.0000	1	0.050	0.05
G7000-9	7000	1278.000	0	0.000	1.000	5.5000	0	2.2200	2.13000	0.36000	0.46800	0.22500	0.22500	10.0000	1	0.050	0.05
G7100-1	7100	1000.000	0	715.333	1.000	3.2000	0	0.7500	0.50000	0.25000	0.50000	0.15385	0.15385	5.0000	1	0.060	0.10
G7100-2	7100	1000.000	0	715.333	1.000	3.2000	0	0.7500	0.50000	0.25000	0.50000	0.15385	0.15385	5.0000	1	0.060	0.10
G7100-3	7100	1000.000	0	715.333	1.000	3.2000	0	0.7500	0.50000	0.25000	0.50000	0.15385	0.15385	5.0000	1	0.060	0.10
G8500-1	8500	1300.000	0	994.000	1.020	7.0000	0	2.4200	2.00000	0.23000	0.41080	0.17062	0.17062	10.0000	1	0.050	0.05
G8500-2	8500	1300.000	0	0.000	1.020	7.0000	0	2.4200	2.00000	0.23000	0.41080	0.17062	0.17062	10.0000	1	0.050	0.05
G8500-3	8500	1300.000	0	0.000	1.020	7.0000	0	2.4200	2.00000	0.23000	0.41080	0.17062	0.17062	10.0000	1	0.050	0.05
G8500-4	8500	1300.000	0	0.000	1.020	7.0000	0	2.4200	2.00000	0.23000	0.41080	0.17062	0.17062	10.0000	1	0.050	0.05
G8500-5	8500	1300.000	0	0.000	1.020	7.0000	0	2.4200	2.00000	0.23000	0.41080	0.17062	0.17062	10.0000	1	0.050	0.05
G8500-6	8500	1300.000	0	0.000	1.020	7.0000	0	2.4200	2.00000	0.23000	0.41080	0.17062	0.17062	10.0000	1	0.050	0.05

Table 14: N44 - LINE PARAMETERS

name	from_bus	to_bus	length	S_n	V_n	unit	R	X	B
L3000-3020	3000	3020	1	0	0	p.u.	0.00000	0.0060	0.000
L3000-3115	3000	3115	1	0	0	p.u.	0.04500	0.5400	0.500
L3000-3245	3000	3245	1	0	0	p.u.	0.00480	0.0720	0.050
L3000-3245	3000	3245	1	0	0	p.u.	0.01080	0.1200	0.050
L3000-3300	3000	3300	1	0	0	p.u.	0.00360	0.0480	0.030
L3000-3300	3000	3300	1	0	0	p.u.	0.00540	0.0600	0.025
L3100-3115	3100	3115	1	0	0	p.u.	0.01800	0.2400	0.110
L3100-3200	3100	3200	1	0	0	p.u.	0.02400	0.1440	0.200
L3100-3200	3100	3200	1	0	0	p.u.	0.02400	0.1440	0.200
L3100-3200	3100	3200	1	0	0	p.u.	0.02400	0.1440	0.200
L3100-3249	3100	3249	1	0	0	p.u.	0.01800	0.2580	0.160
L3100-3359	3100	3359	1	0	0	p.u.	0.04800	0.3000	0.250
L3100-3359	3100	3359	1	0	0	p.u.	0.02400	0.1380	0.240
L3115-3245	3115	3245	1	0	0	p.u.	0.02700	0.3000	0.140
L3115-3249	3115	3249	1	0	0	p.u.	0.00900	0.1200	0.080
L3115-6701	3115	6701	1	0	0	p.u.	0.02400	0.2400	0.100
L3115-7100	3115	7100	1	0	0	p.u.	0.02400	0.0780	0.130
L3200-3300	3200	3300	1	0	0	p.u.	0.01200	0.1200	0.060
L3200-3359	3200	3359	1	0	0	p.u.	0.00600	0.1200	0.070
L3200-8500	3200	8500	1	0	0	p.u.	0.00600	0.1020	0.060
L3244-6500	3244	6500	1	0	0	p.u.	0.00600	0.1200	0.060
L3249-7100	3249	7100	1	0	0	p.u.	0.01200	0.0450	0.078
L3300-8500	3300	8500	1	0	0	p.u.	0.01200	0.1380	0.060
L3300-8500	3300	8500	1	0	0	p.u.	0.00720	0.1620	0.100
L3359-5101-1	3359	5101	1	0	0	p.u.	0.00960	0.1560	0.090
L3359-5101-2	3359	5101	1	0	0	p.u.	0.01200	0.1320	0.060
L3359-8500	3359	8500	1	0	0	p.u.	0.00720	0.1620	0.100
L3359-8500	3359	8500	1	0	0	p.u.	0.01500	0.1920	0.090
L3701-6700	3701	6700	1	0	0	p.u.	0.15000	1.2000	0.030
L5100-5500	5100	5500	1	0	0	p.u.	0.01620	0.1560	0.044
L5100-6500	5100	6500	1	0	0	p.u.	0.04800	0.5400	0.060
L5101-5102	5101	5102	1	0	0	p.u.	0.00480	0.0600	0.090
L5101-5103	5101	5103	1	0	0	p.u.	0.00600	0.0840	0.040
L5101-5501	5101	5501	1	0	0	p.u.	0.00600	0.0900	0.550
L5102-5103	5102	5103	1	0	0	p.u.	0.00240	0.0420	0.030
L5102-5304	5102	5304	1	0	0	p.u.	0.01020	0.1440	0.070
L5102-6001	5102	6001	1	0	0	p.u.	0.01800	0.2760	0.130
L5103-5304	5103	5304	1	0	0	p.u.	0.01200	0.1500	0.070
L5103-5304	5103	5304	1	0	0	p.u.	0.00780	0.1200	0.060
L5300-6100	5300	6100	1	0	0	p.u.	0.01260	0.1320	0.010
L5301-5304	5301	5304	1	0	0	p.u.	0.00600	0.1200	0.060
L5301-5305	5301	5305	1	0	0	p.u.	0.00420	0.0720	0.031
L5301-6001	5301	6001	1	0	0	p.u.	0.00780	0.1200	0.050
L5304-5305	5304	5305	1	0	0	p.u.	0.00600	0.0900	0.050
L5304-5305	5304	5305	1	0	0	p.u.	0.00780	0.0102	0.040
L5400-5500	5400	5500	1	0	0	p.u.	0.00540	0.5640	0.050
L5400-6000	5400	6000	1	0	0	p.u.	0.01980	0.2160	0.025
L5401-5501	5401	5501	1	0	0	p.u.	0.01050	0.1620	0.080
L5401-5602	5401	5602	1	0	0	p.u.	0.00960	0.1530	0.090
L5401-6001	5401	6001	1	0	0	p.u.	0.00384	0.0600	0.028
L5402-6001	5402	6001	1	0	0	p.u.	0.00042	0.0060	0.003
L5500-5603	5500	5603	1	0	0	p.u.	0.03000	0.3600	0.050
L5600-5601	5600	5601	1	0	0	p.u.	0.01800	0.2040	0.020
L5600-5603	5600	5603	1	0	0	p.u.	0.01200	0.1320	0.020
L5600-5620	5600	5620	1	0	0	p.u.	0.00000	0.0060	0.000
L5600-6000	5600	6000	1	0	0	p.u.	0.01200	0.1200	0.070
L5603-5610	5603	5610	1	0	0	p.u.	0.00000	0.0060	0.000
L6000-6100	6000	6100	1	0	0	p.u.	0.02040	0.2520	0.030
L6500-6700	6500	6700	1	0	0	p.u.	0.10200	1.0800	0.100
L6500-6700	6500	6700	1	0	0	p.u.	0.06000	0.7800	0.120
L7000-7010	7000	7010	1	0	0	p.u.	0.00000	0.0060	0.000
L7000-7020	7000	7020	1	0	0	p.u.	0.00000	0.0060	0.000
L7000-7100	7000	7100	1	0	0	p.u.	0.02400	0.0720	0.130
L7000-7100	7000	7100	1	0	0	p.u.	0.02400	0.0720	0.130
L7000-7100	7000	7100	1	0	0	p.u.	0.02400	0.0840	0.130
L8500-8600	8500	8600	1	0	0	p.u.	0.00000	0.0060	0.000
L8500-8700	8500	8700	1	0	0	p.u.	0.00000	0.0060	0.000

Table 15: N44 - LOAD PARAMETERS

name	bus	P	Q	model
L3000-1	3000	1420.656	567	Z
L3000-2	3000	1420.656	567	Z
L3000-3	3000	1420.656	567	Z
L3020-1	3020	1219.000	616	Z
L3100-1	3100	621.000	110	Z
L3115-1	3115	621.000	650	Z
L3249-1	3249	2265.000	650	Z
L3300-1	3300	1217.358	400	Z
L3300-2	3300	1217.358	400	Z
L3359-1	3359	1460.829	600	Z
L3359-2	3359	1460.829	600	Z
L3359-3	3359	1460.829	600	Z
L3359-4	3359	1460.829	600	Z
L3360-1	3360	-330.000	262	Z
L5100-1	5100	1154.170	70	Z
L5300-1	5300	2651.000	-70	Z
L5400-1	5400	1149.765	100	Z
L5500-1	5500	2203.415	200	Z
L5500-2	5500	2203.415	200	Z
L5600-1	5600	674.862	125	Z
L5600-2	5600	674.862	125	Z
L5610-1	5610	1412.000	363	Z
L5620-1	5620	414.000	175	Z
L6100-1	6100	1199.755	400	Z
L6100-2	6100	1199.755	400	Z
L6500-1	6500	1013.000	333	Z
L6500-2	6500	1013.000	333	Z
L6500-3	6500	1013.000	333	Z
L6700-1	6700	2489.000	150	Z
L7000-1	7000	1593.526	70	Z
L7000-2	7000	1593.526	70	Z
L7000-3	7000	1593.526	70	Z
L7000-4	7000	1593.526	70	Z
L7000-5	7000	1593.526	70	Z
L7010-1	7010	-1219.000	600	Z
L7020-1	7020	343.000	-4	Z
L7100-1	7100	1431.684	200	Z
L7100-2	7100	1431.684	200	Z
L8500-1	8500	1240.000	433	Z
L8500-2	8500	1240.000	433	Z
L8500-3	8500	1240.000	433	Z
L8600-1	8600	546.000	10	Z
L8700-1	8700	628.000	0	Z

Table 16: N44 - TRANSFORMER PARAMETERS

name	from_bus	to_bus	S_n	V_n_from	V_n_to	R	X	ratio
T3244-3245	3244	3245	1000	0	0	0.0050	0.0200	1
T3701-3249	3701	3249	1000	0	0	0.0200	0.5000	1
T3359-3360	3359	3360	1000	0	0	0.0050	0.0200	1
T5101-5100	5101	5100	1000	0	0	0.0008	0.0305	1
T5300-5301	5300	5301	1000	0	0	0.0016	0.0610	1
T5400-5401	5400	5401	1000	0	0	0.0032	0.1200	1
T5400-5402	5400	5402	1000	0	0	0.0004	0.0150	1
T5500-5501	5500	5501	1000	0	0	0.0004	0.0150	1
T5601-6001	5601	6001	1000	0	0	0.0002	0.0076	1
T5603-5602	5603	5602	1000	0	0	0.0008	0.0305	1
T6000-6001	6000	6001	1000	0	0	0.0004	0.0150	1
T6700-6701	6700	6701	1000	0	0	0.0050	0.0200	1

Table 17: N44 - GOVERNOR PARAMETERS

name	gen	R	D_t	V_min	V_max	T_2	T_3	T_4	P_m0	T_w
GOV2	G3000-1	0.05	0	0	1	0.36	6	67.6	0.424	1
GOV3	G3000-2	0.05	0	0	1	0.36	6	67.6	0.424	1
GOV4	G3000-3	0.05	0	0	1	0.36	6	67.6	0.100	1
GOV5	G5400-1	0.05	0	0	1	0.36	6	67.6	0.810	1
GOV6	G5400-2	0.05	0	0	1	0.36	6	67.6	0.810	1
GOV7	G6700-1	0.05	0	0	1	0.36	6	67.6	0.820	1
GOV8	G6700-2	0.05	0	0	1	0.36	6	67.6	0.820	1
GOV9	G7100-1	0.05	0	0	1	0.36	6	67.6	0.715	1
GOV10	G7100-2	0.05	0	0	1	0.36	6	67.6	0.715	1
GOV11	G7100-3	0.05	0	0	1	0.36	6	67.6	0.715	1

Table 18: N44: AVR PARAMETERS

name	gen	K	T_a	T_b	T_e	E_min	E_max
AVR2	G3000-1	100	2.0	10.0	0.5	-3	3
AVR3	G3000-2	100	2.0	10.0	0.5	-3	3
AVR4	G3000-3	100	2.0	10.0	0.5	-3	3
AVR5	G5400-1	100	2.0	10.0	0.5	-3	3
AVR6	G5400-2	100	2.0	10.0	0.5	-3	3
AVR7	G6700-1	100	2.0	10.0	0.5	-3	3
AVR8	G6700-2	100	2.0	10.0	0.5	-3	3
AVR9	G7100-1	100	2.0	10.0	0.5	-3	3
AVR10	G7100-2	100	2.0	10.0	0.5	-3	3
AVR11	G7100-3	100	2.0	10.0	0.5	-3	3
AVR18	G6100-1	100	2.0	10.0	0.5	-3	3
AVR19	G6100-2	100	2.0	10.0	0.5	-3	3
AVR20	G6100-3	100	2.0	10.0	0.5	-3	3
AVR21	G6100-4	100	2.0	10.0	0.5	-3	3
AVR22	G6100-5	100	2.0	10.0	0.5	-3	3

D Supplementary Simulations and Results

D.1 Local Mode - Signal and Location Selection

This thesis is focusing on adding additional damping to the lowest damped inter-area mode. However, in a general case, one might be interested in adding damping to a local mode in the system. The approach used for deciding the feedback signal combination in Section 5.3.1 and BESS location in 5.3.2 is equally applicable for such cases.

D.1.1 Feedback Signal Selection

Aiming at finding the optimal feedback signal for appending damping to the 0.92Hz mode from the base system presented in Section 5.1, the following colormap showing the magnitude of the corresponding residue for the different feedback signal combinations is shown in Figure D.1.

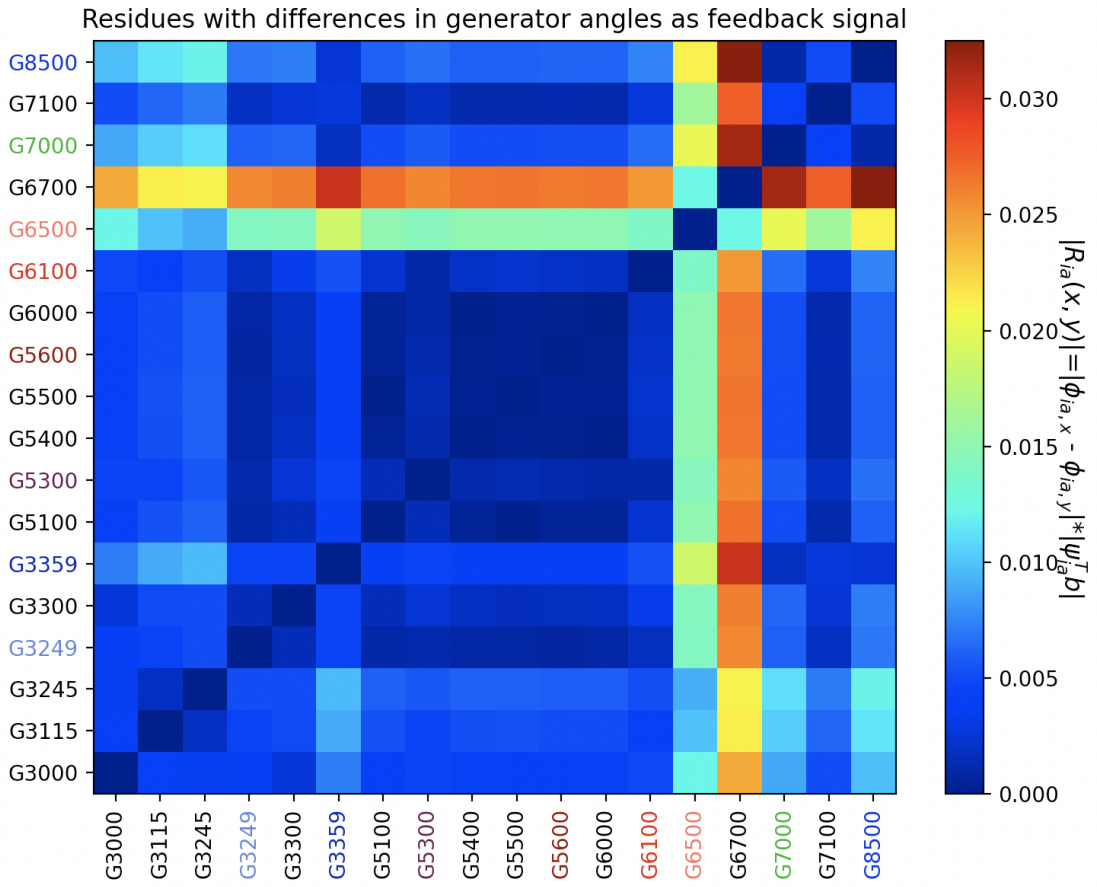

Figure D.1: Colormap showing the absolute values of residues for different feedback signal combinations when considering the local-area mode having a frequency of 0.92Hz.

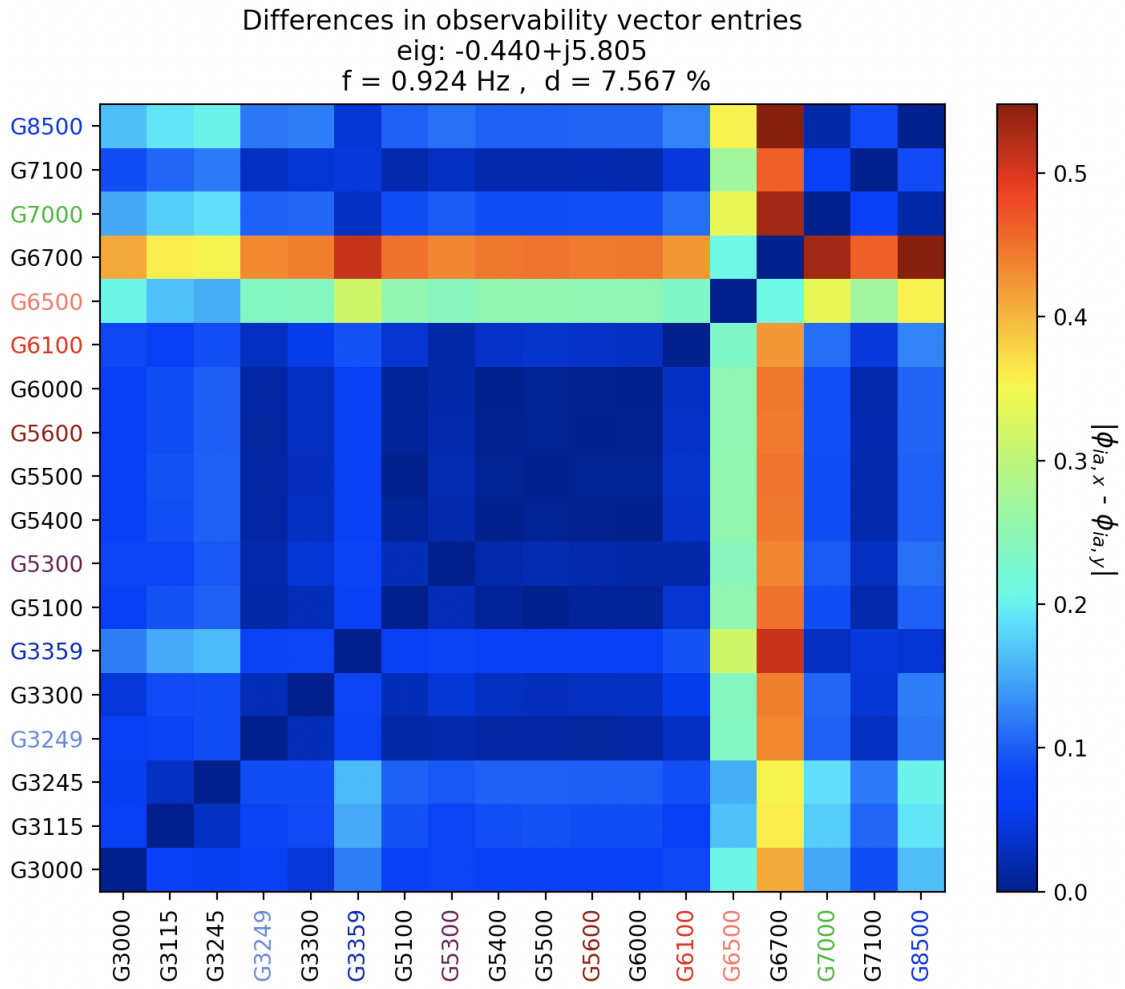

Figure D.2: Colormap showing the absolute values of differences in right eigenvector entries for different feedback signal combinations.

For this case, it is evident from the colormap plot that this is a local-area mode, as the two most suitable voltage angle signals are related to bus 6500 and 6700 (in combination with another voltage angle). It is also evident that a majority of the possible combinations will have a negligible effect as feedback signals for dampening the 0.92Hz mode, as most of them are having a residue absolute value close to zero (signal combinations having blue colors in Figure D.1.1). Similarly as seen when selecting feedback signal for dampening the poorliest damped mode in Section 5.3.1, the difference in mode shapes (Figure D.2) contains the same information about the relative difference between the residue magnitudes for a given feedback signal combination, such that Figure D.1 and D.2 looks exactly the same, but have a different scaling.

D.1.2 BESS location selection

To follow up the feedback signal selection from Appendix D.1.1, a small check is done to verify the optimal BESS location when the feedback signal is chosen such that damping

of the 0.92 Hz is what's of interest. The theory behind this is presented in Section 3.4.2, and is essentially covering the same topics as in the simulations conducted in Section 5.3.2, but this time the local-area mode of 0.92 Hz is what is being targeted.

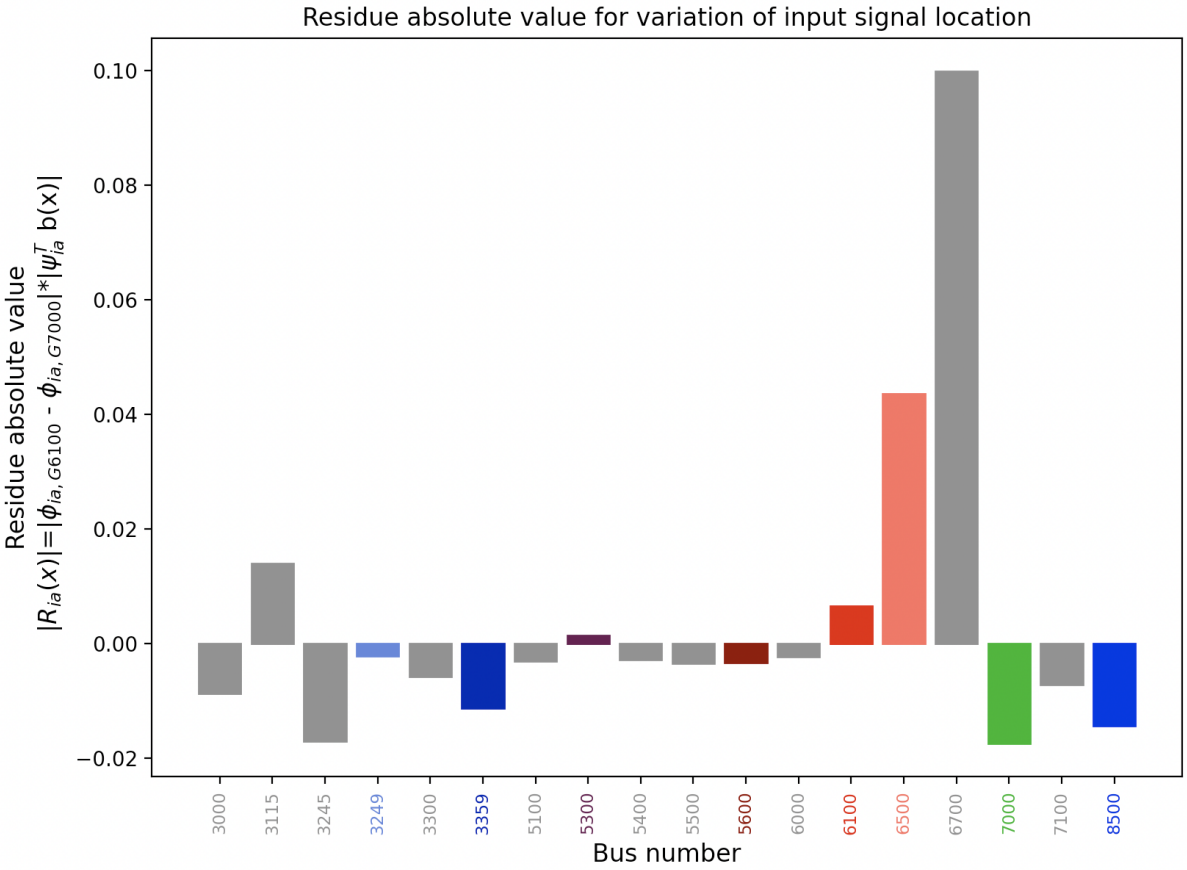

Figure D.3: Residue magnitudes for variation in BESS location when aiming at damping the local mode of 0.92Hz. From the plot it is evident that two locations is significantly better than the other possible locations, which is expected as it is a local-area mode.

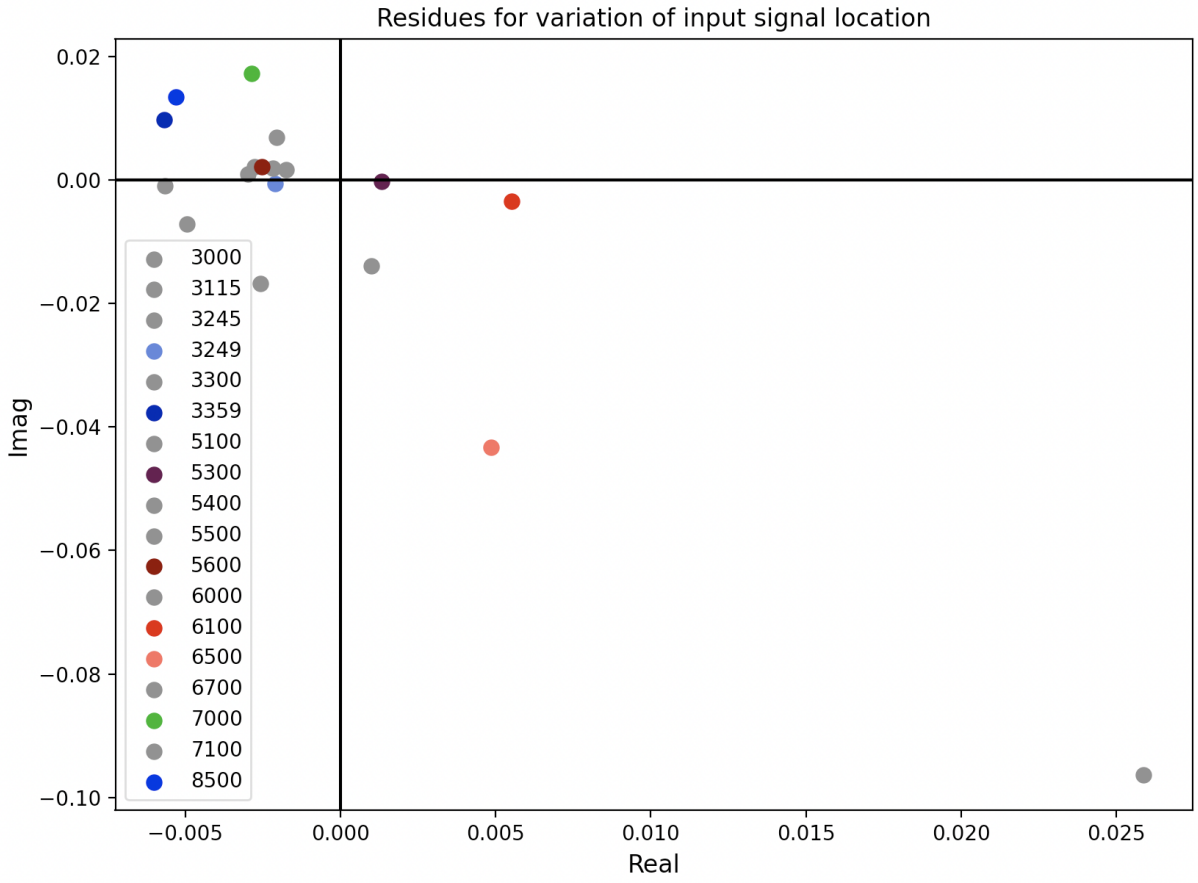

Figure D.4: Residues capturing both magnitudes and directions for variations in BESS location aiming at damping the local area mode. The feedback signal is chosen to be θ_{6700}-θ_{7000} which from Appendix D.1.1 is seen to be the optimal feedback signal when aiming at damping this mode. The grey dot with largest magnitude (bottom right) is corresponding to BESS placed at Bus 6700, which is evident by comparing the plot with Figure D.3

Hence, if the objective were to damp this mode, the optimal location would be to place the BESS at Bus 6700. This would have the largest dampening capabilities for the given local-area-mode.

D.2 Validating the Selection Procedure in a Slightly Modified System

To validate the proposed method of selecting feedback signals to the controller and an appropriate location of the BESS, the same analysis conducted for the base case system is performed in a slightly modified system. In the original system, bus 6100 seems to strongly influence the results, as could be observed initially from the participation factors in the system. Therefore, the new modified system attempted to remove some

of the influence of this bus to create a system that has another optimal solution than the previously discussed system.

Hence, some changes are applied to the system, which is listed below and illustrated in Figure D.5.

1. Three of the generators located at bus 6100 are taken out of the system, and for the remaining two, the inertia constant is reduced by a factor of three.
2. The power production at bus 7000 is reduced by an amount equivalent to three generators. The inertia constant of the generators at this bus is reduced by a factor of three.
3. Load located at bus 5300 (close to bus 6100), one of the loads at bus 6100 and two of the loads at bus 7000 are **set to zero**. This is done to account for the loss in generation capacity and have a steady-state operational point with power production equal to demand.
4. The previously used HYGOVs are replaced by TGOV1 which is discussed in Section B.1.1. This is done to make the system more stable, thereby notably different from the base case system.

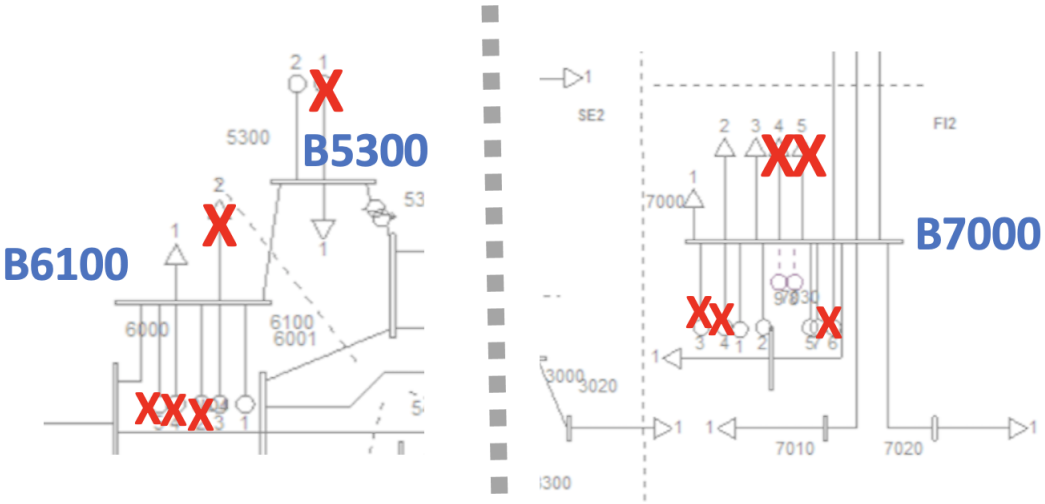

Figure D.5: Highlighting the major modifications made on the base case system seen in Figure 4.5 for creating the new and modified system.

Doing so, the *inter-area mode of interest* is now having a frequency of $0.53Hz$ and relative damping of 7.33%. This mode is still the lowest damped mode in the system, but the overall stability is significantly increased. Thus, if the results are valid for this system, one has a clear indication of the proposed method of figuring out the optimal

controller signals, location, and parameters.

The general procedure is the same as for the base case system, which was presented quite in detail. However, for this system, a more compact presentation of the results is provided. Suppose more information about the algorithm is needed. In that case, the reader can quickly return to the results presented for the base case system, where the results are discussed in more detail.

D.2.1 Signal Selection

Firstly, the feedback controller signals is to be determined, and the results are presented in Figure D.6.

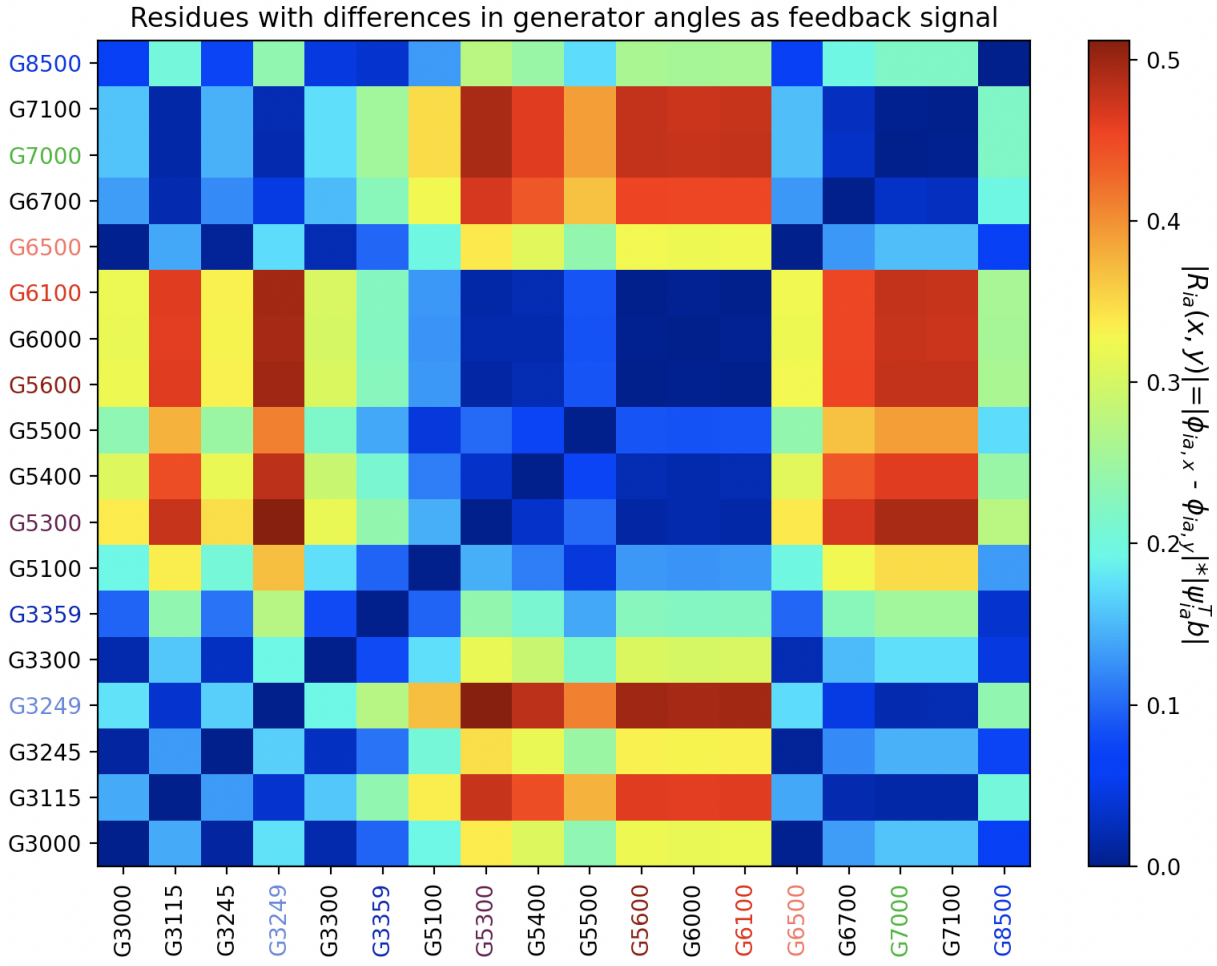

Figure D.6: Residues for feedback signal selection in the new system.

For this system, the feedback signal combination yielding the largest residue is the difference between the voltage angles at bus 5300 and 3245, such that the feedback signal is chosen to be θ_{5300}-θ_{3249}. However, it can be seen that the feedback signal is chosen for the original system, θ_{6100}-θ_{7000}, is still yielding a large value of the residue, but not the largest.

D.2.2 Location Selection

Secondly, the BESS location should be selected and the results are presented in Figure D.7.

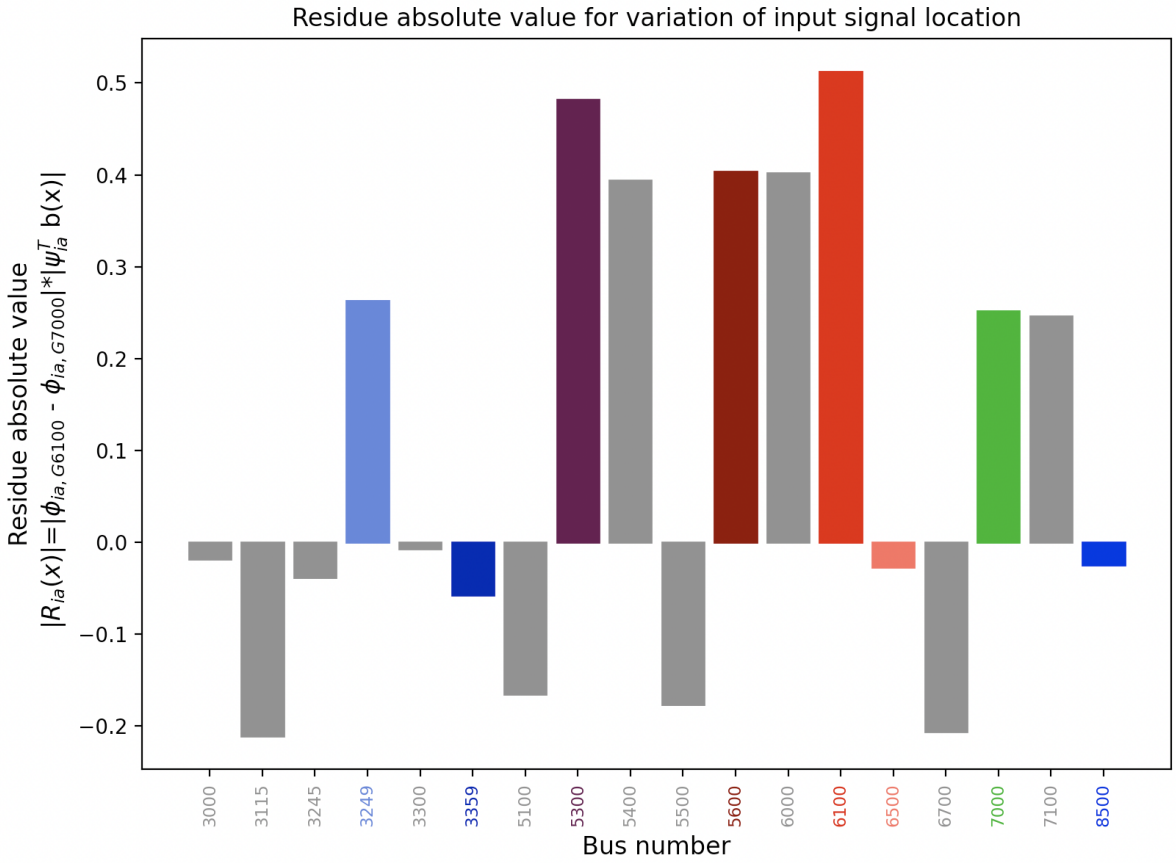

Figure D.7: BESS location selection.

Similarly, as for the base case system, bus 6100 turns out to yield the optimal placement of the BESS. Placing it at bus 5300 would presumably yield decent results, but not as good as locating it at bus 6100. The residues with their corresponding directions in the complex plane are shown in Figure D.8.

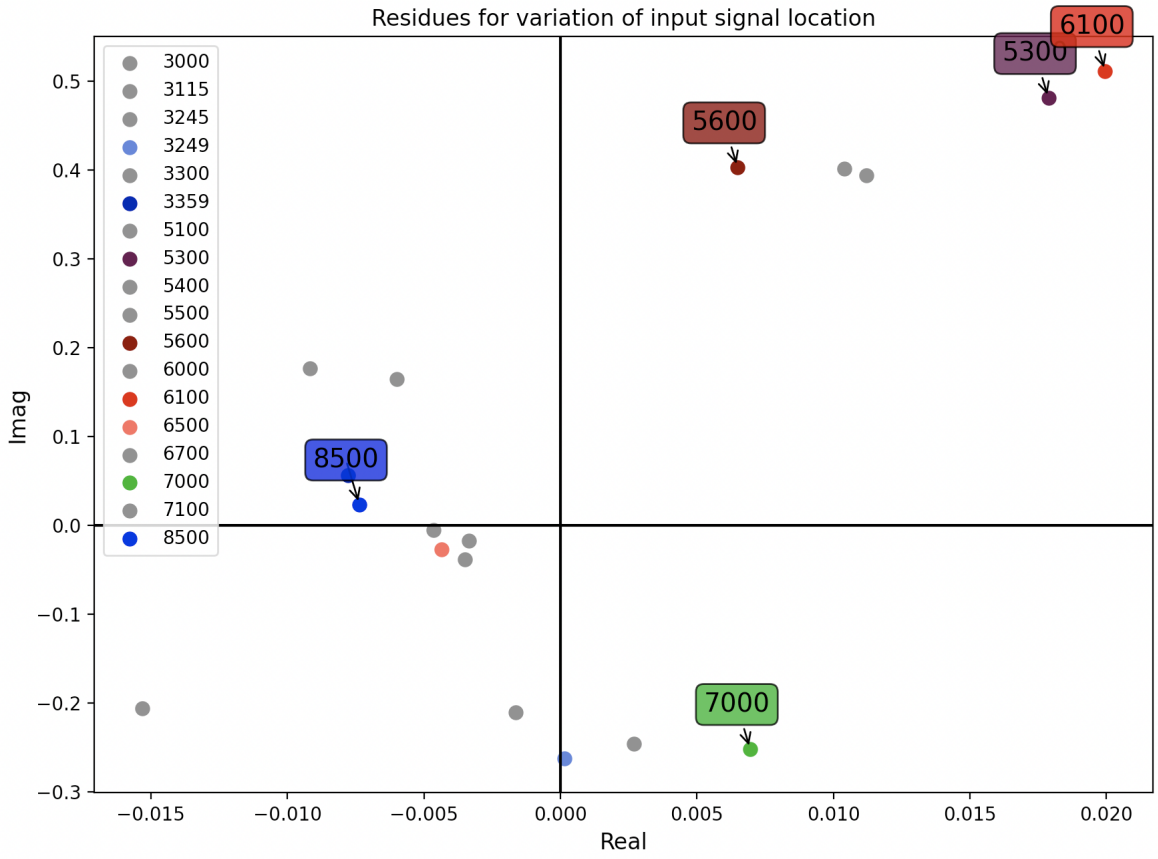

Figure D.8: Residues and their corresponding directions for different BESS locations in the system. The feedback signal (θ_{5300}-θ_{3249}) is held constant during the residue calculations. Bare in mind the scaling of the axis, that is, the residues are located approximately at a straight line parallel and close to the imaginary axis.

For the base case system, the residues for different locations of the BESS ended up approximately on a straight line. Although it might not seem like this for this case, notice how the real values and scaling of the x-axis are significantly smaller than the imaginary values in Figure D.8, such that this is still the case for this new system. To summarize, for this system, one have:

1. **Optimal feedback signal combination**: θ_{5300}-θ_{3249}.
2. **Optimal BESS location:** Bus 6100.

It turns out that the optimal feedback signal is not correlating with the BESS placement in the investigated system. This is made possible after introducing PMUs in the system, allowing controllers to effectively use remotely located signals in the system, and could therefore be a potential solution for a real-world system for given operating conditions.

D.2.3 Controller Parameters Selection

Lastly is the tuning of the controller. The eigenvalues sensitivity for different gains and phase shifts are shown in Figure D.9.

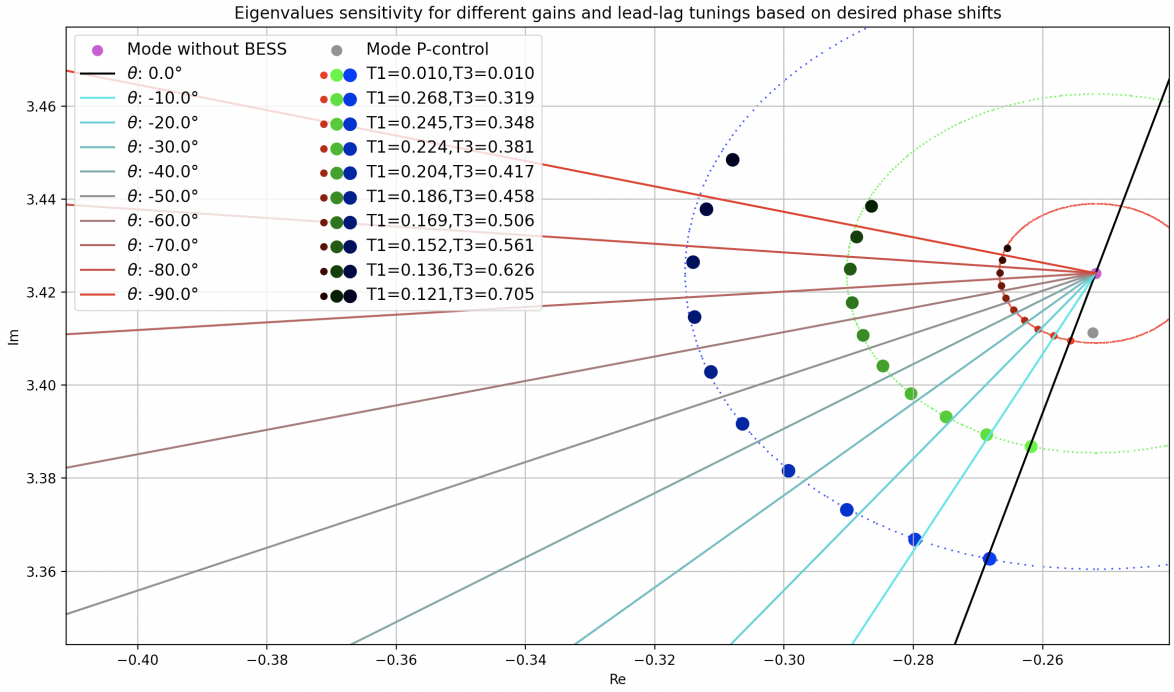

Figure D.9: Eigenvalues for the new system for different gains and phase compensation utilized on the BESS controller. The colored circles indicates constant controller amplitude gains, $K_p|H(j\omega_{ia})|$.

Notice how the phase shifts for this case is negative, whereas they were defined positively in the base case. This is done in order to account for the fact that for the given feedback signal combination, the residues are located in the right-half plane; hence a phase compensation larger than $\pm 90°$ is needed. One can quite straightforwardly get a $180°$ phase compensation by reverting the sign of the input signal. In contrast, the rest of the needed shift is captured by the two lead-lag blocks depending on the needed compensation. From Figure D.9, it seems likely that the desired phase compensation by the lead-lag blocks should be in the region of $[-60°, -70°]$. A choice of selecting $-65°$ is taken as it is previously seen (for instance, in Figure **??**) that the error between the desired and actual phase compensation increases for larger gains.

The next step would be to determine the proportional gain factor K_p, and the calculation of this utilizes the same formula as used for the base case system, given in equation (5.3). Most of the terms occurring in the Equation are the same for this system.

- The internal gain of the BESS-model is the same as previously (see Section 5.4),

namely 0.00402.

- The washout filter provides a gain even closer to unity compared to the base case when the inter-area mode frequency is increased[D.1].
- When the lead-lag blocks are aiming for a 65° phase compensation, one have that $T_1 = 0.160$ and $T_2 = 0.532$, given a total amplitude gain of these blocks of 0.301.
- The absolute value of the residue is found to be 0.51 by looking at the numerical values used for establishing Figure D.7.
- For a desired inter-area mode relative damping of 10%, the real value of the new modal position is calculated to being $\alpha_{ia,new} = -0.3437$ by using Equation (5.4), yielding a change in the mode of $|\Delta\lambda_{ia}| = |\Delta\alpha_{ia}| = 0.092$.
- Thus, the proportional gain factor is calculated to $K_p = 149$ by Equation (5.3).

Selecting the proportional gain factor, washout filter and lead-lag filters with these parameters, yields to modal plot shown in Figure D.10.

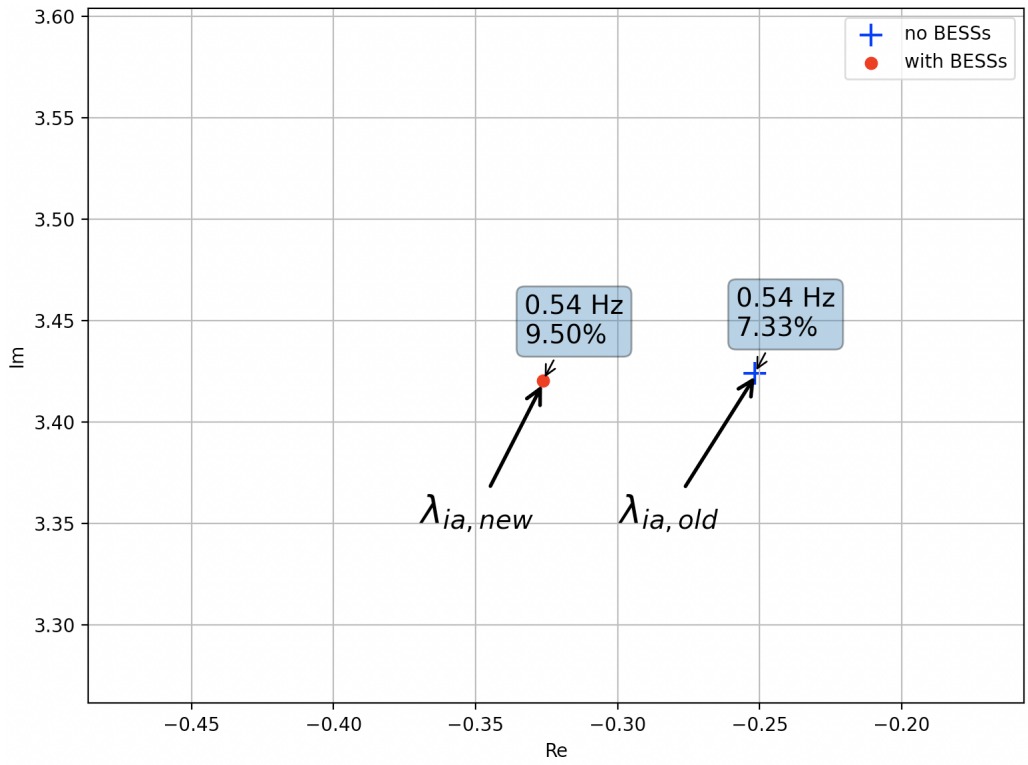

Figure D.10: Inter-area mode of interest for system without and with BESS tuned with the aforementioned parameters aiming for a straight left-wards shift in the complex plane and a targeted damping of 10%.

[D.1] Since $lim_{s\to\infty}|\frac{sT}{1+sT}| = 1$ yields a washout filter gain closer to unity when the frequency of the inter-area mode is larger.

It can be seen that the mode is moved left-wards in the complex plane as expected. However, the desired relative damping is not met as accurately as was the case for the base case system in Section 5.4. The Relative Residue Index could explain the mismatch between the targeted and actual gain in damping (see Appendix A.3). For this case, the residue value is lower than the case for the base case system (0.51 vs. 0.80), which intuitively could be interpreted as the residue ratio to the rest of the residues in the considered control loop system is smaller. Thus, it seems evident that the interaction with other modes in the system is greater for this case, thereby increasing the amount of error present when designing the controller for targeting a desired value of the relative damping.

D.2.4 Validation of Optimality

Similarly as for the base case system, the validity of the supposedly optimal feedback signal combination and location is checked further. This is done by selecting three different locations and three different feedback signal combinations, and see whether one of them outperforms the selected location/signal combination.

Table 19: Frequency f_{ia} and relative damping ζ_{ia} of the inter-area mode for different locations of the BESS using different feedback signals in the second system. Without BESS in the system, the eigenvalue is having a frequency of 0.54 Hz and relative damping of 7.33%.

BESS LOCATION	FEEDBACK SIGNAL	f_{ia}	ζ_{ia}	$\Delta\zeta_{ia}$
B6100	θ_{3249}-θ_{5300}	0.54 Hz	9.50 %	2.17 %
	θ_{3249}-θ_{6100}	0.54 Hz	9.43 %	2.10 %
	θ_{7000}-θ_{6100}	0.54 Hz	9.39 %	2.06 %
B5300	θ_{3249}-θ_{5300}	0.54 Hz	9.45 %	2.12 %
	θ_{3249}-θ_{6100}	0.54 Hz	9.39 %	2.06 %
	θ_{7000}-θ_{6100}	0.54 Hz	9.36 %	2.03 %
B3249	-(θ_{3249}-θ_{5300})	0.54 Hz	8.52 %	1.19 %
	-(θ_{3249}-θ_{6100})	0.54 Hz	8.39 %	1.06 %
	-(θ_{7000}-θ_{6100})	0.54 Hz	8.35 %	1.02 %

From Table 19, it seems evident that the selected location and feedback signal provides the largest amount of additional damping in the system. Notice the small difference in performance by selecting either $B6100$ or $B5300$ in combination with the feedback signal θ_{3249}-θ_{5300}, an increase in damping of 2.17% and 2.12% respectively. This could be anticipated from the residue plot for variations in BESS locations provided in Figure

D.7. The difference between the bar corresponding to $B6100$ and $B5300$ is almost negligible, thus being reflected as similar performance in terms of damping the mode. In addition, the residue corresponding to placing the BESS at $B3249$ is slightly larger than half of the two others, thereby yielding an approximated halving of the additional damping $\Delta\zeta_{ia}$ for all three different feedback signals considered. Similarly, as for the base case, the proposed method of selecting feedback signals and BESS location seems to identify the optimal combination for this system having a fundamentally different system topology. One also notices that the optimal feedback signals (θ_{3249}-θ_{5300}) do not correspond to quantities measurable at the optimal placement location $B6100$. Hence, this example illustrates that in terms of wide-area damping controllers, the best-suited controller signals might be remotely located in the system and not associated with the actual controller location.

D.3 Validating the Selection Procedure in a Highly Modified System Containing a Line Between Western Norway and Eastern Sweden

A somehow unrealistic system is created to investigate the proposed method for signal and location selection and justify the validity further. The motivation is to reduce the impact of bus 6100, such that, most likely, a new feedback signal and BESS location will yield the optimal solution. The system is fundamentally the same as the system analyzed in Section D.2, but an additional low impedance line between the west-coast of Norway (bus 6100) to Forsmark (bus 3300) is included. The modification is illustrated in Figure D.11.

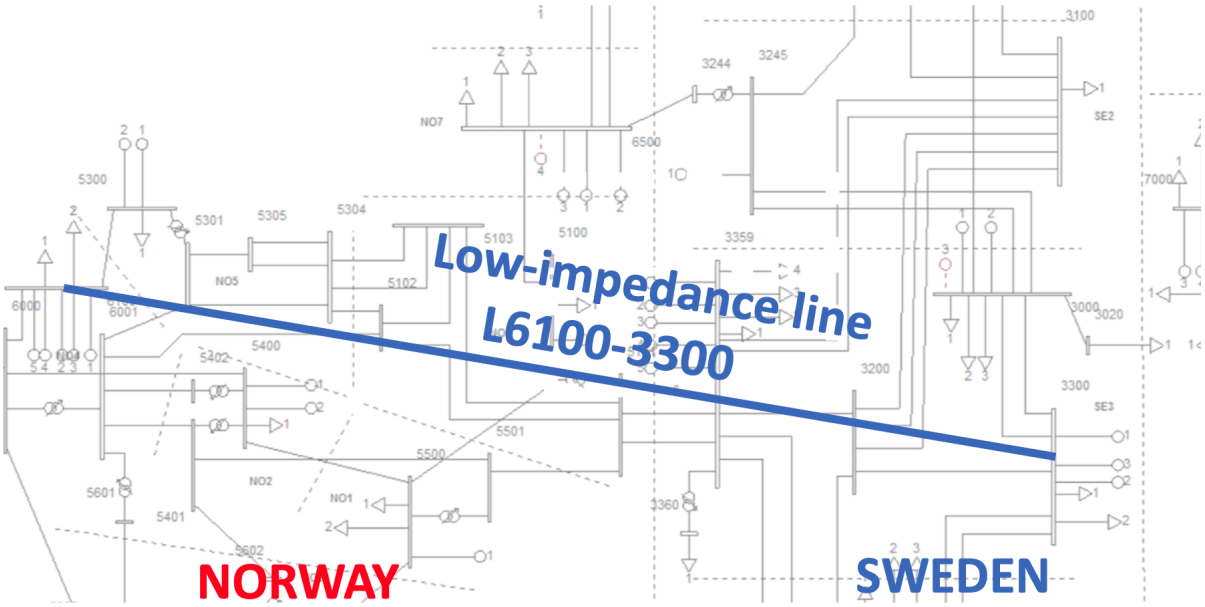

Figure D.11: Illustrating the change made to the system for obtaining a fundamentally different system topology by inserting a highly unrealistic line between Norway and Sweden.

In reality, one would never build this line due to the geographical distance separating the buses. However, it could, in principle, be a suitable solution in some countries for lowering the total system impedance from production cites and high-demand areas. However, it fundamentally changes the system topology, thereby influencing the optimal feedback signal and BESS location significantly and yielding an exciting system for a "what if" scenario. For this analysis, the proportional gain factor will be considered neither tuned for applying specific additional damping. This aims to showcase how another solution is the optimal solution for a system where the topology has changed significantly. Hence, only the relative difference between the gains obtained for the different feedback signals and BESS location selections will be considered.

D.3.1 Signal Selection

The residue magnitude plot used for selecting the optimal signal for this system is presented in Figure D.12, which naturally[D.2] suggest that the impact of signals associated with Bus 6100 is significantly reduced compared to the base case system in Figure 5.11 and the second investigated system in Figure D.6.

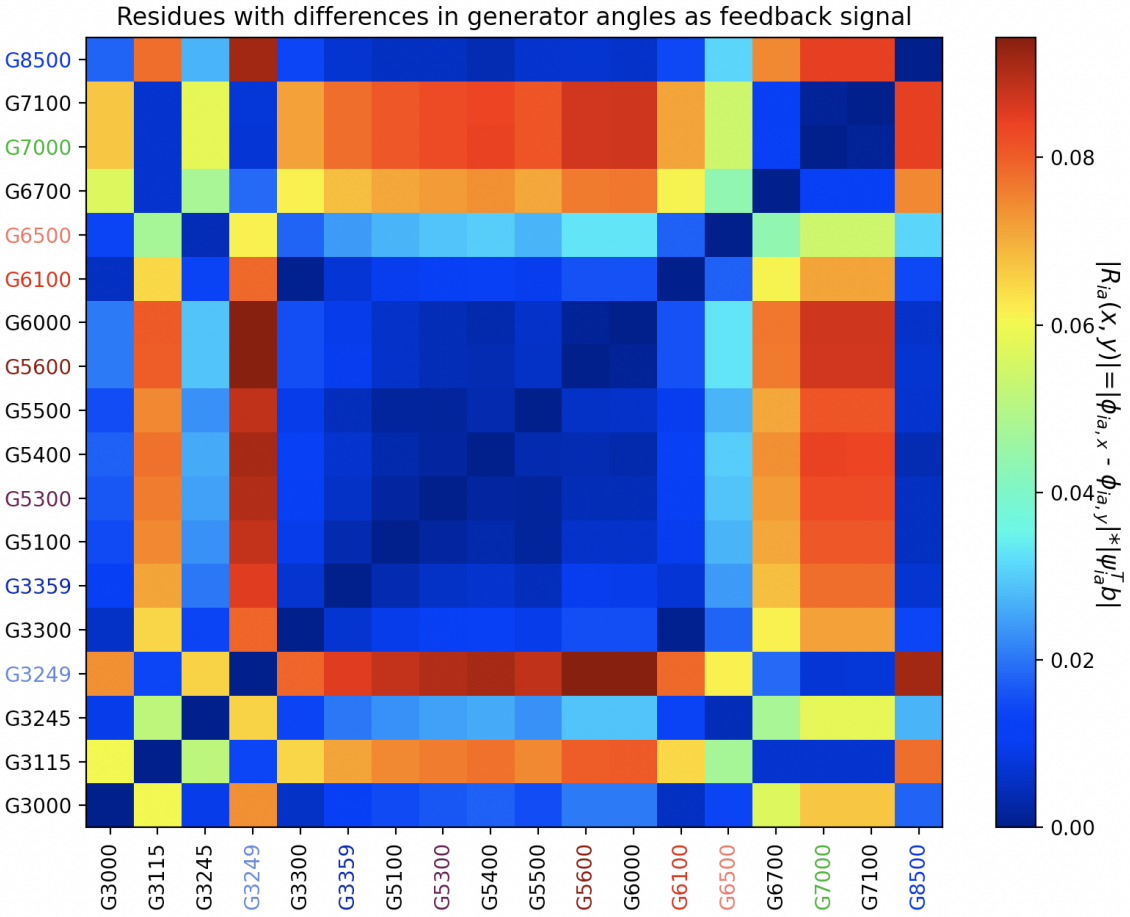

Figure D.12: Residues for feedback signal selection for the 3rd system.

For this system, the optimal feedback signal is a combination of the voltage angle at bus 6000 and bus 3249. This is not easy to see when looking at Figure D.12 but is evident from looking at the actual numbers used for creating the plot. When the feedback signal is determined, the next step is to determine the optimal BESS location.

[D.2] Removing some of the impacts of Bus 6100 was a design criterion when creating the system.

D.3.2 Location Selection

When deciding the optimal BESS location, the result shown in Figure D.13 are used.

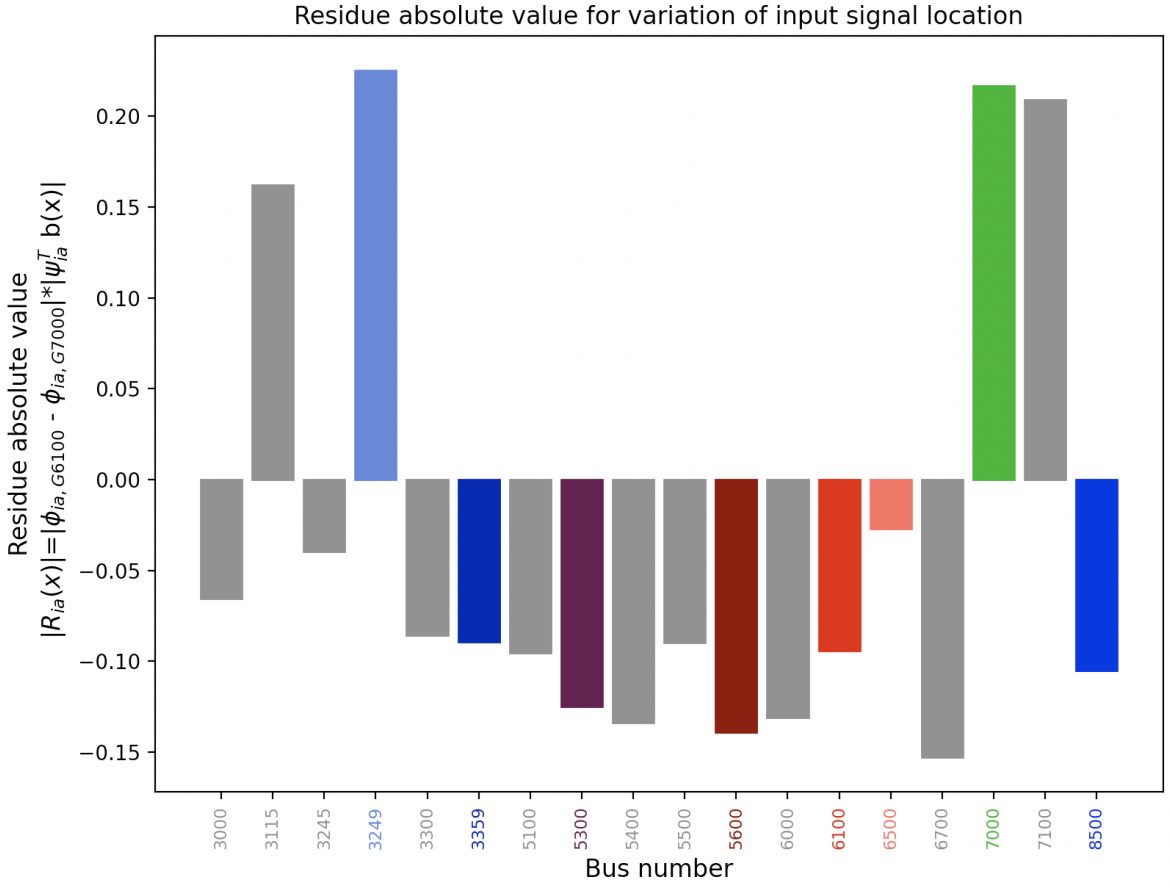

Figure D.13: Selecting optimal BESS location for the 3rd system.

For this system, it seems like several candidate locations would be appropriate locations. However, Bus 3249 stands out by having a slightly larger value of the residue compared to Bus 7000 and Bus 7100.

D.3.3 Controller Parameters Selection

A further look is taken into the phase shifts of the residues for the different locations.

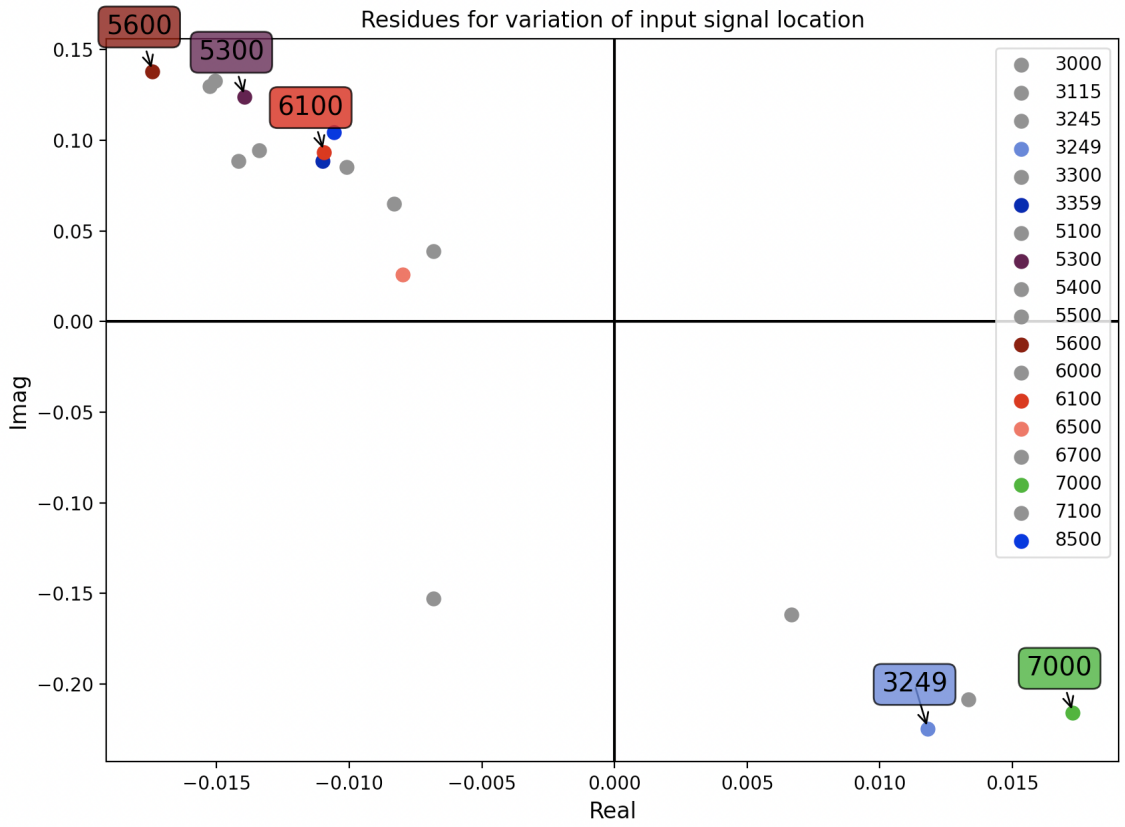

Figure D.14: Residues for different BESS location. Bare in mind the scaling of the axis.

From Figure D.14 one have that the residues for the different locations investigated seem to be laying on an approximately straight line[D.3].

Without providing the details behind the tuning of the parameters and proportional gain factor[D.4], the lead-lag filter is aiming at providing a phase shift of $-70°$, and the proportional gain factor is chosen to $K_p = 200$. The purpose of analyzing this system is to see further the validity of the proposed method for selecting feedback control signal and BESS location. The shift in the eigenvalue when using the selected optimal feedback signal and BESS location is shown in Figure D.15.

[D.3] Notice the scaling of the axis. The values on the real axis are significantly smaller than the values in the imaginary axis.

[D.4] The same procedure used for the other systems are applied.

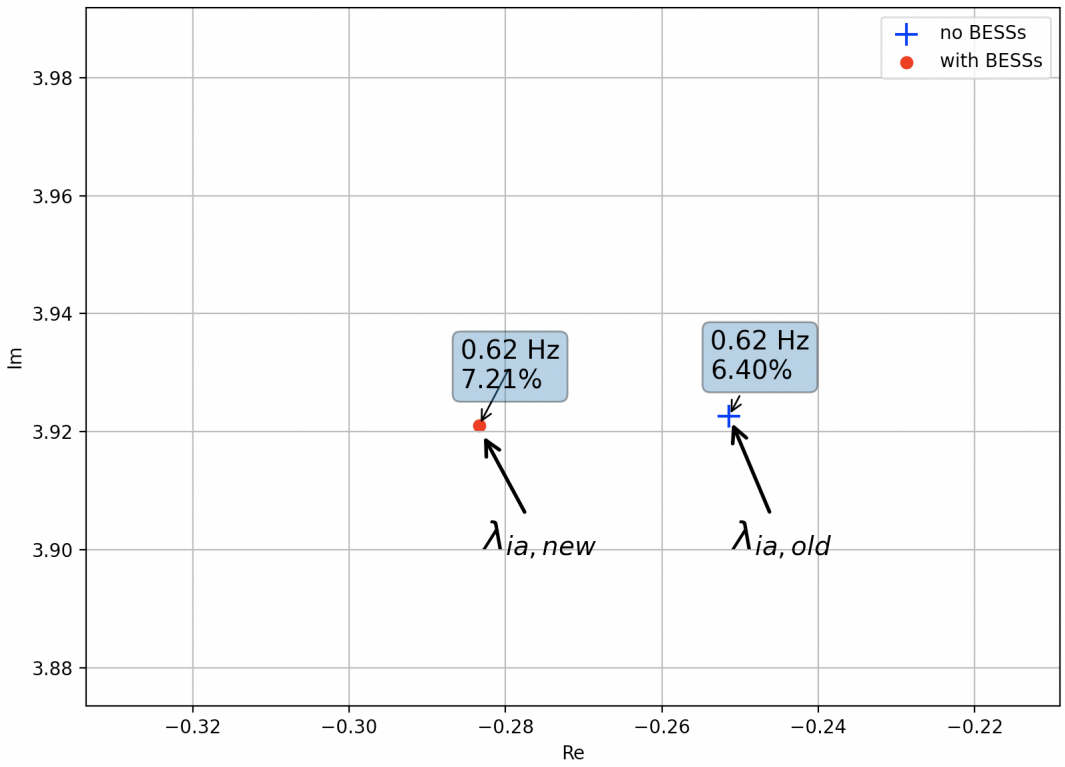

Figure D.15: Inter-area mode of interest for system without and with BESS tuned with the aforementioned parameters aiming for a straight left-wards shift in the complex plane in the 3rd system

It can be seen from Figure D.15 that the mode is shifted left-wards in the complex plane, and the damping has increased. Due to the low value of the residue for this system, together with the small amplitude gain of the lead-lag blocks for a $-70°$ targeted phase compensation, the K_p would have to be increased further if more damping is desired in this system. However, this is not looked further into, as the relative difference between the different feedback signals and BESS locations is of interest when validating that the chosen signals are the optimal solution.

D.3.4 Validation of Optimality

In order to validate that the chosen signal and location is the optimal, analysis are carried out by investigating three different locations, together with three different feedback signal combinations, in a similar matter that is conducted for the base case system in Section 5.4.5 and the modified system in Section D.2. For this system containing the unrealistic line between Norway and Sweden, $B3249$ is the suggested optimal placement of the BESS. In addition, $B5300$ and $B6100$ are also considered, both of which showed promising solutions in the other systems considered. The feedback signals looked further into for this case corresponds to the signal yielding the maximum residue value for this given system $\pm(\theta_{6000}\text{-}\theta_{3249})$, and the two feedback signals yielding the optimal

solution in the other systems, $\pm(\theta_{6100}\text{-}\theta_{7000})$ and $\pm(\theta_{5300}\text{-}\theta_{3249})$ respectively. The results are presented in Table 20.

Table 20: Frequency and relative damping of the inter-area mode for different locations of the BESS using different feedback signals. Without BESS in the system, the eigenvalue is having a frequency of 0.62 Hz and relative damping of 6.40%.

BESS LOCATION	FEEDBACK SIGNAL	f_{ia}	ζ_{ia}	$\Delta\zeta_{ia}$
	$\theta_{6000}\text{-}\theta_{3249}$	0.62 Hz	7.21 %	0.81 %
B3249	$\theta_{5300}\text{-}\theta_{3249}$	0.62 Hz	7.17 %	0.77 %
	$\theta_{6100}\text{-}\theta_{7000}$	0.62 Hz	6.91 %	0.51 %
	$-(\theta_{6000}\text{-}\theta_{3249})$	0.62 Hz	6.95 %	0.55 %
B5300	$-(\theta_{5300}\text{-}\theta_{3249})$	0.62 Hz	6.93 %	0.53 %
	$-(\theta_{6100}\text{-}\theta_{7000})$	0.62 Hz	6.84 %	0.44 %
	$-(\theta_{6000}\text{-}\theta_{3249})$	0.62 Hz	6.83 %	0.43 %
B6100	$-(\theta_{5300}\text{-}\theta_{3249})$	0.62 Hz	6.81 %	0.41 %
	$-(\theta_{6100}\text{-}\theta_{7000})$	0.62 Hz	6.75 %	0.35 %

Similarly, as for the other systems considered, the suggested optimal feedback signal combination and BESS locations yield the largest change in the relative damping $\Delta\zeta_{ia}$ of the mode of interest for the different combinations presented in Table 20[D.5]. In addition, it can be seen from Table 20 that for a given feedback signal, the magnitude of the additional damping of the mode is larger the greater the magnitude of the residue for the corresponding Bus is in Figure D.13. Furthermore, by keeping the BESS location fixed, it is evident that the amount of damping provided is correlated with the residue value for the given feedback signal combination seen in Figure D.12. The suggested optimal feedback signal combination $\pm(\theta_{6000}\text{-}\theta_{3249})$ only slightly outperforms the alternative feedback signal $\pm(\theta_{5300}\text{-}\theta_{3249})$, which could be anticipated from the residue magnitudes from Figure D.12. Hence, even for this system having a fundamentally different system topology than the other systems analyzed, employing residue magnitudes for choosing the feedback signal combination and BESS location seems to yield the optimal solution. The validity of the proposed method for signal and location selection is thus strengthened even further. Interestingly, for all of the investigated systems, the optimal combination of signal and location is different, strengthening the proposed method's credibility.

[D.5] A large amount of other seemingly suitable combinations are also checked, although not presented in the table. None of them outperformed the suggested optimal solution.

Bibliography

[1] A. Chakrabortty and P. P. Khargonekar, 'Introduction to wide-area control of power systems', in *2013 American Control Conference*, 2013, pp. 6758–6770. DOI: 10.1109/ACC.2013.6580901.

[2] S. Sivaranjani and D. Thukaram, 'A networked control systems perspective for wide-area monitoring control of smart power grids', in *2013 IEEE Innovative Smart Grid Technologies-Asia (ISGT Asia)*, 2013, pp. 1–6. DOI: 10.1109/ISGT-Asia.2013.6698775.

[3] V. Yari, S. Nourizadeh and A. M. Ranjbar, 'Wide-area frequency control during power system restoration', in *2010 IEEE Electrical Power Energy Conference*, 2010, pp. 1–4. DOI: 10.1109/EPEC.2010.5697202.

[4] A. G. Phadke, 'Synchronized phasor measurements-a historical overview', in *IEEE/PES Transmission and Distribution Conference and Exhibition*, vol. 1, 2002, 476–479 vol.1. DOI: 10.1109/TDC.2002.1178427.

[5] T. Bi, H. Liu, D. Zhang and Q. Yang, 'The pmu dynamic performance evaluation and the comparison of pmu standards', in *2012 IEEE Power and Energy Society General Meeting*, 2012, pp. 1–5. DOI: 10.1109/PESGM.2012.6345328.

[6] M. Kabiri and N. Amjady, *IEEE Transactions on Instrumentation and Measurement*, vol. 68, no. 9, pp. 3078–3089, 2019. DOI: 10.1109/TIM.2018.2872446.

[7] B. Pierre, R. Elliott, D. Schoenwald, J. Neely, R. Byrne, D. Trudnowski and J. Colwell, 'Supervisory system for a wide area damping controller using pdci modulation and real-time pmu feedback', in *2016 IEEE Power and Energy Society General Meeting (PESGM)*, 2016, pp. 1–5. DOI: 10.1109/PESGM.2016.7741594.

[8] M. Alsarray and R. A. McCann, 'Consensus damping of inter-area oscillations using utility-scale solar-battery generation', in *2018 IEEE Electronic Power Grid (eGrid)*, 2018, pp. 1–6. DOI: 10.1109/eGRID.2018.8598665.

[9] Y. Zhang and A. Bose, 'Pmu-based wide-area damping control system design', in *2012 IEEE Power and Energy Society General Meeting*, 2012, pp. 1–7. DOI: 10.1109/PESGM.2012.6344736.

[10] Y. Li, C. Rehtanz, S. Ruberg, L. Luo and Y. Cao, 'Assessment and choice of input signals for multiple hvdc and facts wide-area damping controllers', *IEEE Transactions on Power Systems*, vol. 27, no. 4, pp. 1969–1977, 2012. DOI: 10.1109/TPWRS.2012.2189865.

[11] S. B. Swathi and N. G. Poothullil, 'Analysis of active power control of hvdc in damping power oscillations', in *2016 International Conference on Next Generation Intelligent Systems (ICNGIS)*, 2016, pp. 1–5. DOI: 10.1109/ICNGIS.2016.7854074.

[12] L. Harnefors, N. Johansson, L. Zhang and B. Berggren, 'Interarea oscillation damping using active-power modulation of multiterminal hvdc transmissions', *IEEE Transactions on Power Systems*, vol. 29, no. 5, pp. 2529–2538, 2014. DOI: 10.1109/TPWRS.2014.2306826.

[13] R. Preece, A. M. Almutairi, O. Marjanovic and J. V. Milanović, 'Damping of inter-area oscillations using wams based supplementary controller installed at vsc based hvdc line', in *2011 IEEE Trondheim PowerTech*, 2011, pp. 1–8. DOI: 10.1109/PTC.2011.6019173.

[14] Trudnowski, Donnelly and Lightner, 'Power-system frequency and stability control using decentralized intelligent loads', in *2005/2006 IEEE/PES Transmission and Distribution Conference and Exhibition*, 2006, pp. 1453–1459. DOI: 10.1109/TDC.2006.1668732.

[15] M. W. Tsang and D. Sutanto, 'Damping inter-area oscillation using a battery energy storage system', in *1997 Fourth International Conference on Advances in Power System Control, Operation and Management, APSCOM-97. (Conf. Publ. No. 450)*, vol. 2, 1997, 409–414 vol.2. DOI: 10.1049/cp:19971869.

[16] Y. Zhu, C. Liu, K. Sun, D. Shi and Z. Wang, 'Optimization of battery energy storage to improve power system oscillation damping', *IEEE Transactions on Sustainable Energy*, vol. 10, no. 3, pp. 1015–1024, 2019. DOI: 10.1109/TSTE.2018.2858262.

[17] S. B. Karanki and D. Xu, 'Optimal capacity and placement of battery energy storage systems for integrating renewable energy sources in distribution system', in *2016 National Power Systems Conference (NPSC)*, 2016, pp. 1–6. DOI: 10.1109/NPSC.2016.7858983.

[18] K. Prasertwong, M. Nadarajah and D. Thakur, 'Understanding low-frequency oscillation in power systems', *International Journal of Electrical Engineering Education*, vol. 47, Jul. 2010. DOI: 10.7227/IJEEE.47.3.2.

[19] M. Chenine, K. Zhu and L. Nordstrom, 'Survey on priorities and communication requirements for pmu-based applications in the nordic region', in *2009 IEEE Bucharest PowerTech*, 2009, pp. 1–8. DOI: 10.1109/PTC.2009.5281956.

[20] X. Zhang, C. Lu, S. Liu and X. Wang, 'A review on wide-area damping control to restrain inter-area low frequency oscillation for large-scale power systems with increasing renewable generation', *Renewable and Sustainable Energy Reviews*, vol. 57, pp. 45–58, 2016, ISSN: 1364-0321. DOI: https://doi.org/10.1016/j.rser.2015.12.167. [Online]. Available: http://www.sciencedirect.com/science/article/pii/S1364032115015506.

[21] G. M. Masters, *Renewable and efficient electric power systems*, 2nd ed. John Wiley Sons Inc., 2013, ISBN: 978-1-118-63350-2.

[22] M. Tsebia and H. Betarzi, 'Improve monitoring system of interconnected oscillation power system based on pmu technology', in *2020 International Conference on Electrical Engineering (ICEE)*, 2020, pp. 1–6. DOI: 10.1109/ICEE49691.2020.9249857.

[23] J. W. Nilsson and S. A. Riedel, *Electric circuits*, 9th ed. Pearson, 2015, ISBN: 9780136114994.

[24] E. O. Schweitzer, A. Guzmán, H. J. Altuve, D. A. Tziouvaras and J. Needs, 'Real-time synchrophasor applications in power system control and protection', in *10th IET International Conference on Developments in Power System Protection (DPSP 2010). Managing the Change*, 2010, pp. 1–5. DOI: 10.1049/cp.2010.0343.

[25] R. Wilson, 'Pmus [phasor measurement unit]', *IEEE Potentials*, vol. 13, no. 2, pp. 26–28, 1994. DOI: 10.1109/45.283885.

[26] M. Maheswari, N. Suthanthira Vanitha and N. Loganathan, 'Wide-area measurement systems and phasor measurement units', in *Wide Area Power Systems Stability, Protection, and Security*, H. Haes Alhelou, A. Y. Abdelaziz and P. Siano, Eds. Cham: Springer International Publishing, 2021, pp. 105–126, ISBN: 978-3-030-54275-7. DOI: 10.1007/978-3-030-54275-7_4. [Online]. Available: https://doi.org/10.1007/978-3-030-54275-7_4.

[27] A. Kumar and G. Priya, 'Power system stability enhancement using facts controllers', in *2012 International Conference on Emerging Trends in Electrical Engineering and Energy Management (ICETEEEM)*, 2012, pp. 84–87. DOI: 10.1109/ICETEEEM.2012.6494448.

[28] S. A. Jumaat, I. Musirin, M. M. Othman and H. Mokhlis, 'Optimal placement and sizing of multiple facts devices installation', in *2012 IEEE International Conference on Power and Energy (PECon)*, 2012, pp. 145–150. DOI: 10.1109/PECon.2012.6450195.

[29] J. M. Ramirez, R. J. Davalos and V. Valenzuela, 'Coordination of facts-based stabilizers for damping oscillations', *IEEE Power Engineering Review*, vol. 20, no. 12, pp. 46–49, 2000. DOI: 10.1109/39.890376.

[30] A. Kazemi and M. V. Sohrforouzani, 'Power system damping using fuzzy controlled facts devices', in *2004 International Conference on Power System Technology, 2004. PowerCon 2004.*, vol. 2, 2004, 1623–1628 Vol.2. DOI: 10.1109/ICPST.2004.1460263.

[31] M. Klein, G. J. Rogers and P. Kundur, 'A fundamental study of inter-area oscillations in power systems', *IEEE Transactions on Power Systems*, vol. 6, no. 3, pp. 914–921, 1991. DOI: 10.1109/59.119229.

[32] H. M. Long and J. C. Smith, 'Load management on the electric power system', in *1979 18th IEEE Conference on Decision and Control including the Symposium on Adaptive Processes*, vol. 2, 1979, pp. 273–273. DOI: 10.1109/CDC.1979.270179.

[33] Trudnowski, Donnelly and Lightner, 'Power-system frequency and stability control using decentralized intelligent loads', in *2005/2006 IEEE/PES Transmission and Distribution Conference and Exhibition*, 2006, pp. 1453–1459. DOI: 10.1109/TDC.2006.1668732.

[34] Q. Shi, F. Li, G. Liu, D. Shi, Z. Yi and Z. Wang, 'Thermostatic load control for system frequency regulation considering daily demand profile and progressive recovery', *IEEE Transactions on Smart Grid*, vol. 10, no. 6, pp. 6259–6270, 2019. DOI: 10.1109/TSG.2019.2900724.

[35] G. M. Jonsdottir, M. S. Almas, M. Baudette, M. P. Palsson and L. Vanfretti, 'Rt-hil hardware prototyping of synchrophasor and active load-based power system oscillation damping controllers', in *2016 IEEE Power and Energy Society General Meeting (PESGM)*, 2016, pp. 1–5. DOI: 10.1109/PESGM.2016.7741307.

[36] A. Oudalov, R. Cherkaoui and A. Beguin, 'Sizing and optimal operation of battery energy storage system for peak shaving application', in *2007 IEEE Lausanne Power Tech*, 2007, pp. 621–625. DOI: 10.1109/PCT.2007.4538388.

[37] B. Singh and Z. Hussain, 'Application of battery energy storage system (bess) in voltage control and damping of power oscillations', in *2010 5th International Conference on Industrial and Information Systems*, 2010, pp. 514–519. DOI: 10.1109/ICIINFS.2010.5578649.

[38] J. C. Neely, R. H. Byrne, R. T. Elliott, C. A. Silva-Monroy, D. A. Schoenwald, D. J. Trudnowski and M. K. Donnelly, 'Damping of inter-area oscillations using energy storage', in *2013 IEEE Power Energy Society General Meeting*, 2013, pp. 1–5. DOI: 10.1109/PESMG.2013.6672775.

[39] V. M. Dileepan, K. T. Madhavan and J. Jayakumar, 'Performance analysis of lithium polymer battery and super capacitor', in *2017 International Conference on Energy, Communication, Data Analytics and Soft Computing (ICECDS)*, 2017, pp. 2029–2033. DOI: 10.1109/ICECDS.2017.8389805.

[40] K. Ogata, *Modern control engineering*, 5th ed. Pearson, 2010, ISBN: 9780137133376.

[41] Y. Chompoobutrgool and L. Vanfretti, 'A fundamental study on damping control design using pmu signals from dominant inter-area oscillation paths', in *2012 North American Power Symposium (NAPS)*, 2012, pp. 1–6. DOI: 10.1109/NAPS.2012.6336336.

[42] K. Uhlen, L. Vanfretti, M. M. de Oliveira, A. B. Leirbukt, V. H. Aarstrand and J. O. Gjerde, 'Wide-area power oscillation damper implementation and testing in the norwegian transmission network', in *2012 IEEE Power and Energy Society General Meeting*, 2012, pp. 1–7. DOI: 10.1109/PESGM.2012.6344837.

[43] Y. Ge, W. Du and T. Littler, 'Co-ordinated design of phase measurement unit and power system stabilizers in large scale power systems', in *2nd IET Renewable Power Generation Conference (RPG 2013)*, 2013, pp. 1–5. DOI: 10.1049/cp.2013.1768.

[44] S. Ray, B. Chaudhuri and R. Majumder, 'Appropriate signal selection for damping multi-modal oscillations using low order controllers', in *2008 IEEE Power and Energy Society General Meeting - Conversion and Delivery of Electrical Energy in the 21st Century*, 2008, pp. 1–7. DOI: 10.1109/PES.2008.4596564.

[45] Y. Lin, Z. Xu and Y. Huang, 'Power oscillation damping controller design for tcsc based on the test signal method', in *IEEE Power Engineering Society General Meeting, 2005*, 2005, 1671–1675 Vol. 2. DOI: 10.1109/PES.2005.1489379.

[46] Feng Xiao, Yuanzhang Sun, Fang Yang and Lin Cheng, 'Inter-area damping controller design based on mode controllability and observability', in *2007 International Power Engineering Conference (IPEC 2007)*, 2007, pp. 95–99.

[47] A. Paul, M. Bhadu, N. Senroy and A. R. Abhyankar, 'Study of effect of local pss and wadc placement based on dominant inter-area paths', in *2015 IEEE Power Energy Society General Meeting*, 2015, pp. 1–5. DOI: 10.1109/PESGM.2015.7285955.

[48] M. Aboul-Ela, A. Sallam, J. McCalley and A. Fouad, 'Damping controller design for power system oscillations using global signals', *IEEE Transactions on Power Systems*, vol. 11, no. 2, pp. 767–773, 1996. DOI: 10.1109/59.496152.

[49] A. Prakash, K. Kumar and S. K. Parida, 'Design of damping controller based on the wide-area signal strength', in *2020 21st National Power Systems Conference (NPSC)*, 2020, pp. 1–6. DOI: 10.1109/NPSC49263.2020.9331866.

[50] M. Mustafa and N. Magaji, 'Design of power oscillation damping controller for svc device', in *2008 IEEE 2nd International Power and Energy Conference*, 2008, pp. 1329–1332. DOI: 10.1109/PECON.2008.4762681.

[51] K. Uhlen, S. Elenius, I. Norheim, J. Jyrinsalo, J. Elovaara and E. Lakervi, 'Application of linear analysis for stability improvements in the nordic power transmission system', in *2003 IEEE Power Engineering Society General Meeting (IEEE Cat. No.03CH37491)*, vol. 4, 2003, 2097–2103 Vol. 4. DOI: 10.1109/PES.2003.1270938.

[52] R. K. Pandey and N. K. Singh, 'An analytical approach for control design of upfc', in *2008 Joint International Conference on Power System Technology and IEEE Power India Conference*, 2008, pp. 1–6. DOI: 10.1109/ICPST.2008.4745186.

[53] J. Morsali, R. Kazemzadeh and M. R. Azizian, 'Coordinated design of mpss and tcsc-based damping controller using pso to enhance multi-machine power system stability', in *2013 21st Iranian Conference on Electrical Engineering (ICEE)*, 2013, pp. 1–6. DOI: 10.1109/IranianCEE.2013.6599804.

[54] A. Adamczyk, R. Teodorescu, F. Iov and P. C. Kjær, 'Evaluation of residue based power oscillation damping control of inter-area oscillations for static power sources', in *2012 IEEE Power and Energy Society General Meeting*, 2012, pp. 1–8. DOI: 10.1109/PESGM.2012.6343981.

[55] B. Chaudhuri, R. Majumder and B. C. Pal, 'Wide-area measurement-based stabilizing control of power system considering signal transmission delay', *IEEE Transactions on Power Systems*, vol. 19, no. 4, pp. 1971–1979, 2004. DOI: 10.1109/TPWRS.2004.835669.

[56] J. Machowski, J. W. Bialek and J. R. Bumby, *Power system dynamics: stability and control*, 2nd ed. Wiley, 2008, ISBN: 9780470725580.

[57] E. Kreyszig, *Advanced engineering mathematics*, 10th ed. John Wiley Sons, 2011, ISBN: 9780470646137.

[58] J. G. Balchen, T. Andresen and B. A. Foss, *Reguleringsteknikk*, 6th ed. NTNU, Institutt for teknisk kybernetikk, 2016.

[59] NTNU, *Differential equations, linear algebra and its applications*, 2nd ed. Custom Publishing, 2015, ISBN: 9781784480202.

[60] M. R. Djalal, A. Imran and I. Robandi, 'Optimal placement and tuning power system stabilizer using participation factor and imperialist competitive algorithm in 150 kv south of sulawesi system', in *2015 International Seminar on Intelligent Technology and Its Applications (ISITIA)*, 2015, pp. 147–152. DOI: 10.1109/ISITIA.2015.7219970.

[61] B. J. Shah, G. N. Pillai and P. Agarwal, 'Power oscillation damping in multi-machine power system using psss considering various load models', in *2013 Nirma University International Conference on Engineering (NUiCONE)*, 2013, pp. 1–6. DOI: 10.1109/NUiCONE.2013.6780165.

[62] G. Rogers, *Power System Oscillations*, eng, 1st ed. 2000., ser. Power Electronics and Power Systems. New York, NY: Springer US : Imprint: Springer, 2000, ISBN: 1-4615-4561-7.

[63] A. Jalilvand and M. D. Keshavarzi, 'Adaptive svc damping controller design, using residue method in a multi-machine system', in *2009 6th International Conference on Electrical Engineering/Electronics, Computer, Telecommunications and Information Technology*, vol. 01, 2009, pp. 160–163. DOI: 10.1109/ECTICON.2009.5136986.

[64] H. Nguyen-Duc, L.-A. Dessaint, A. F. Okou and I. Kamwa, 'Selection of input/output signals for wide area control loops', in *IEEE PES General Meeting*, 2010, pp. 1–7. DOI: 10.1109/PES.2010.5589788.

[65] V. S. Perić and L. Vanfretti, 'Optimal pmu placement for power system ambient data-based mode estimation applications', in *2016 IEEE PES Innovative Smart Grid Technologies Conference Europe (ISGT-Europe)*, 2016, pp. 1–6. DOI: 10.1109/ISGTEurope.2016.7856239.

[66] H. Haugdal and K. Uhlen, 'An open source power system simulator in python for efficient prototyping of wampac applications', Jan. 2021.

[67] Hallvar Haugdal, *Dynpssimpy*, [Online; accessed 19-June-2021], 2021. [Online]. Available: https://github.com/hallvar-h/DynPSSimPy.

[68] Simulink, *General control*, [Online; accessed 11-May-2021], 2021. [Online]. Available: https://www.mathworks.com/help/physmod/sps/general-control.html?s_tid=CRUX_lftnav.

[69] Y. Zhu, B. Wang and K. Sun, 'Damping control for power systems using energy storage', in *2017 29th Chinese Control And Decision Conference (CCDC)*, 2017, pp. 3730–3735. DOI: 10.1109/CCDC.2017.7979153.

[70] Y. Zhu, C. Liu, B. Wang and K. Sun, 'Damping control for a target oscillation mode using battery energy storage', *Journal of Modern Power Systems and Clean Energy*, vol. 6, no. 4, pp. 833–845, 2018. DOI: 10.1007/s40565-017-0371-3.

[71] W. Yao, L. Jiang, J. Wen, Q. H. Wu and S. Cheng, 'Wide-area damping controller of facts devices for inter-area oscillations considering communication time delays', *IEEE Transactions on Power Systems*, vol. 29, no. 1, pp. 318–329, 2014. DOI: 10.1109/TPWRS.2013.2280216.

[72] S. Jakobsen and E. Solvang, 'The nordic 44 test network', Dec. 2018. DOI: 10.6084/m9.figshare.7464386.v1.

[73] Sigurd Hofsmo Jacobsen, *Nordic44-nordpool/nordic44/models*, [Online; accessed 15-December-2020], 2016. [Online]. Available: https://github.com/ALSETLab/Nordic44-Nordpool/tree/master/nordic44/models.

[74] S. M. Hamre, 'Inertia and fcr in the present and future nordic powersystem. master's thesis', *Norwegian University of Science and Technology,Trondheim, June 2015*, Jun. 2015.

[75] M. T. Lawder, B. Suthar, P. W. C. Northrop, S. De, C. M. Hoff, O. Leitermann, M. L. Crow, S. Santhanagopalan and V. R. Subramanian, 'Battery energy storage system (bess) and battery management system (bms) for grid-scale applications', *Proceedings of the IEEE*, vol. 102, no. 6, pp. 1014–1030, 2014. DOI: 10.1109/JPROC.2014.2317451.

[76] TESLA, *Powerpack - utility and business energy storage*, [Online; accessed 18-June-2020], 2021. [Online]. Available: https://www.tesla.com/powerpack.

[77] DIgSILENT GmbH, *Digsilent powerfactory application example battery energy storing systems bess*, [Online; accessed 14-December-2020], 2010. [Online]. Available: https://www.academia.edu/34763216/DIgSILENT_PowerFactory_Application_Example_Battery_Energy_Storing_Systems.

[78] H. Yang, 'Effects of aging and temperature on supercapacitor peukert constant', in *2019 IEEE 7th Workshop on Wide Bandgap Power Devices and Applications (WiPDA)*, 2019, pp. 349–353. DOI: 10.1109/WiPDA46397.2019.8998793.

[79] Y. Gong, X. Zhang, H. Li, H. Liao, Z. Meng, Y. Liu and Z. Huang, 'Estimation of peukert constant of lithium-ion batteries and its application in battery discharging time prediction', in *2020 IEEE Energy Conversion Congress and Exposition (ECCE)*, 2020, pp. 905–910. DOI: 10.1109/ECCE44975.2020.9236241.

[80] L. Patnaik and S. Williamson, 'A five-parameter analytical curvefit model for open-circuit voltage variation with state-of-charge of a rechargeable battery', in *2018 IEEE International Conference on Power Electronics, Drives and Energy Systems (PEDES)*, 2018, pp. 1–4. DOI: 10.1109/PEDES.2018.8707806.

[81] B. M. Prabhakar, J. Ramprabhakar and V. Sailaja, 'Estimation and controlling the state of charge in battery augmented photovoltaic system', in *2016 Biennial International Conference on Power and Energy Systems: Towards Sustainable Energy (PESTSE)*, 2016, pp. 1–6. DOI: 10.1109/PESTSE.2016.7516431.

[82] B. Han, 'Battery soc-based dc output voltage control of bess in stand-alone dc microgrid', in *2016 IEEE Region 10 Conference (TENCON)*, 2016, pp. 1445–1449. DOI: 10.1109/TENCON.2016.7848254.

[83] R. H. Park, 'Two-reaction theory of synchronous machines generalized method of analysis-part i', *Transactions of the American Institute of Electrical Engineers*, vol. 48, no. 3, pp. 716–727, 1929. DOI: 10.1109/T-AIEE.1929.5055275.

[84] Simulink, *Power (dq0, instantaneous)*, [Online; accessed 18-June-2021], 2021. [Online]. Available: https://www.mathworks.com/help/physmod/sps/powersys/ref/powerdq0instantaneous.html.

[85] R. Visakhan, R. Rahul, K. R. Hridya and A. A. Kurian, 'Analysis of power oscillation damping capability of statcom-pod and optimal placement of pmus in ieee-14 bus system', in *2015 International Conference on Power, Instrumentation, Control and Computing (PICC)*, 2015, pp. 1–7. DOI: 10.1109/PICC.2015.7455748.

[86] J. Qi, Q. Wu, Y. Zhang, G. Weng and D. Zhou, 'Unified residue method for design of compact wide-area damping controller based on power system stabilizer', *Journal of Modern Power Systems and Clean Energy*, vol. 8, no. 2, pp. 367–376, 2020. DOI: 10.35833/MPCE.2018.000370.

[87] Wikipedia contributors, *Battery storage power station*, [Online; accessed 07-June-2021], 2020. [Online]. Available: https://en.wikipedia.org/wiki/Battery_storage_power_station.

[88] D. P. Kothari, *Electric machines*, 5th ed. McGraw Hill Education (India), 2018, ISBN: 9789352606405.

[89] H. Jabir, J. Teh, D. Ishak and H. Abunima, 'Impacts of demand-side management on electrical power systems: A review', *Energies*, vol. 11, Apr. 2018. DOI: 10.3390/en11051050.

[90] W. Yang, F. Reis, Y. Xu, X. Zhang, Y. Li, X. Tian and R. Pestana, 'Study on the demand and requirements of renewable energy primary frequency control', in *2019 Chinese Control And Decision Conference (CCDC)*, 2019, pp. 5804–5808. DOI: 10.1109/CCDC.2019.8832858.

[91] J. Pou, *Lecture notes in ee6501 - power electronic converters, nanyang technological university*, Oct. 2019.

[92] Wikipedia contributors, *Direct-quadrature-zero transformation*, [Online; accessed 07-June-2021], 2020. [Online]. Available: https://en.wikipedia.org/wiki/Direct-quadrature-zero_transformation#cite_note-Park-40.

[93] Q. Xiao, P. Mattavelli, A. Khodamoradi and F. Tang, 'Analysis of transforming dq impedances of different converters to a common reference frame in complex converter networks', *CES Transactions on Electrical Machines and Systems*, vol. 3, no. 4, pp. 342–350, 2019. DOI: 10.30941/CESTEMS.2019.00046.

[94] Simulink, *Alpha-beta-zero to dq0, dq0 to alpha-beta-zero*, [Online; accessed 17-November-2020], 2020. [Online]. Available: https://www.mathworks.com/help/physmod/sps/powersys/ref/alphabetazerotodq0dq0toalphabetazero.html.

[95] A. A. Ba-muqabel and M. A. Abido, 'Review of conventional power system stabilizer design methods', in *2006 IEEE GCC Conference (GCC)*, 2006, pp. 1–7. DOI: 10.1109/IEEEGCC.2006.5686203.

[96] M. Rabbani, M. A. Mahmud and A. M. T. Oo, 'A comparative study of different power system stabilizers for dynamic stability analysis', in *2015 Australasian Universities Power Engineering Conference (AUPEC)*, 2015, pp. 1–5. DOI: 10.1109/AUPEC.2015.7324886.

[97] G. J. Rogers, 'The application of power system stabilizers to a multigenerator plant', *IEEE Transactions on Power Systems*, vol. 15, no. 1, pp. 350–355, 2000. DOI: 10.1109/59.852143.

[98] K. E. Bollinger, W. Gu and E. Norum, 'Accelerating power versus electrical power as input signals to power system stabilizers', *IEEE Transactions on Energy Conversion*, vol. 6, no. 4, pp. 620–626, 1991. DOI: 10.1109/60.103634.

[99] K. E. Bollinger and S. Z. Ao, 'Pss performance as affected by its output limiter', *IEEE Transactions on Energy Conversion*, vol. 11, no. 1, pp. 118–124, 1996. DOI: 10.1109/60.486585.

[100] P. Bogacki and L. Shampine, 'A 3(2) pair of runge - kutta formulas', *Applied Mathematics Letters*, vol. 2, no. 4, pp. 321–325, 1989, ISSN: 0893-9659. DOI: https://doi.org/10.1016/0893-9659(89)90079-7. [Online]. Available: http://www.sciencedirect.com/science/article/pii/0893965989900797.

[101] J. C. Gonzalez-Torres, J. Mermet-Guyennet, S. Silvani and A. Benchaib, 'Power system stability enhancement via vsc-hvdc control using remote signals: Application on the nordic 44-bus test system', in *15th IET International Conference on AC and DC Power Transmission (ACDC 2019)*, 2019, pp. 1–6. DOI: 10.1049/cp.2019.0078.

[102] K. Kim, H. Schattler, V. Venkatasubramanian, J. Zaborszky and P. Hirsch, 'Methods for calculating oscillations in large power systems', *IEEE Transactions on Power Systems*, vol. 12, no. 4, pp. 1639–1648, 1997. DOI: 10.1109/59.627870.

[103] M. Jazaeri and M. Khatibi, 'A study on hopf bifurcations for power system stability analysis', in *2008 IEEE Canada Electric Power Conference*, 2008, pp. 1–6. DOI: 10.1109/EPC.2008.4763323.

[104] Y. Li, C. Rehtanz, S. Ruberg, L. Luo and Y. Cao, 'Assessment and choice of input signals for multiple hvdc and facts wide-area damping controllers', *IEEE Transactions on Power Systems*, vol. 27, no. 4, pp. 1969–1977, 2012. DOI: 10.1109/TPWRS.2012.2189865.

Johannes Kalland Tjoland

Small-Signal Stability Enhancement by Wide-Area Damping Control

NTNU
Norwegian University of
Science and Technology